Universitat Autònoma de Barcelona

IMMUNOTHERAPY FOR ALZHEIMER'S DISEASE: from antibody engineering to combined therapy with apolipoproteins

Laia Montoliu Gaya

Universitat Autònoma de Barcelona

Departament de Bioquímica i Biologia Molecular

IMMUNOTHERAPY FOR ALZHEIMER'S DISEASE:

from antibody engineering to combined therapy with apolipoproteins.

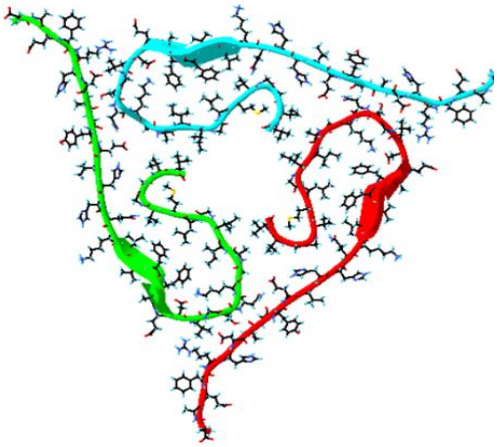

Doctoral Thesis

Laia Montoliu Gaya

2017

Universitat Autònoma de Barcelona

Departament de Bioquímica i Biologia Molecular

IMMUNOTHERAPY FOR ALZHEIMER'S DISEASE:

from antibody engineering to combined therapy with apolipoproteins.

Doctoral Thesis presented by Laia Montoliu Gaya for the Degree of Ph.D in Biochemistry, Molecular Biology and Biomedicine, supervised by Dra. Sandra Villegas.

Laia Montoliu Gaya **Sandra Villegas**

Bellaterra, June 2017

CONTENTS

LIST OF TABLES AND FIGURES

FIGURES

TABLES

ABBREVIATIONS

AD	Alzheimer's Disease
AICD	APP Intracellular C-terminal Domain
APH1	Anterior Pharynx Defective Phenotype
apoE	Apolipoprotein E
apoJ	Apolipoprotein J
APP	Amyloid Precursor Protein
ARIA	Amyloid-related Imaging Abnormalities
ARIA-E	ARIA-edema/effusions
ARIA-H	ARIA-microhemorrhage
Aβ	Amyloid-β
BACE	β-site APP-cleaving Enzyme
BBB	Blood Brain Barrier
CAA	Cerebral Amyloid Angiopathy
CD	Circular Dichroism
CDR	Complementary Determining Region
CEX	Cation Exchange chromatography
CSF	Cerebrospinal Fluid
C-terminal	Carboxy-terminal
D_2O	Deuterated water
Da	Daltons
DAB	Diaminobenzidine
deg	Ellipticity
DMEM	Dulbecco's Modified Eagle's Medium
DMSO	Dimethyl sulfoxide
DNA	Deoxyribonucleic acid
dNTP	Deoxynucleotide
DSC	Differential Scanning Calorimetry
DTI	Diffusion tensor imaging
ELISA	Enzyme-Linked Immunoabsorbent Assay
EOAD	Early-onset Alzheimer's Disease
EU	Endotoxin Units
Fab	Fragment antigen-binding
FBS	Fetal Bovine Serum
Fc	Fragment Crystallizable region
FR	Framework Region
FTIR	Fourier Transformed Infrared Spectroscopy
g	Relative centrifugal force
GFAP	Glial Fibrillary Acidic Protein
GndCl	Guanidine hydrochloride
HCl	Hydrochloric acid
HDL	High-Density Lipoproteins
HFIP	1,1,1,3,3,3-hexafluoro-2-isopropanol
HSPG	Heparan Sulfate Proteoglycans
IPTG	Isopropyl β-D-1-thiogalactopyranoside
LDLR	Low-density Lipoproteins Receptor

LOAD	Late-onset Alzheimer's Disease
LPS	Lipopolysaccharides
LRP1	LDL-related Protein Receptor 1
mAb	Monoclonal Antibody
MAC	Membrane Attack Complex
MALDI	Matrix Assisted Laser Desorption Ionization
MCI	Mild Cognitive Impairment
MP	Mimetic Peptides
MRE	Mean Residue Ellipticity
MRI	Magnetic Resonance Imaging
MTT	3-(4, 5-dimethylthiazolyl-2)-2, 5-diphenyltetrazolium bromide
NFTs	Neurofilament tangles
NMR	Nuclear Magnetic Resonance
N-terminal	Amino-terminal
OD_{600}	Optical Density at 600nm
PCR	Polymerase Chain Reaction
PDB	Protein Data Bank
PIB-PET	Positron emission tomographic imaging using Pittsburgh compound B
PMF	Peptide mass fingerprinting
PSEN	Presenilin
RAGE	Receptor for Advanced Glycation End-products
RT	Room Temperature
scFv	Single-chain variable Fragment
SDM	Site-Directed Mutagenesis
SEM	Standard Error of the Mean
TEAEs	Treatment-emergent Adverse Events
TEM	Transmission Electron Microscopy
TEV	Tobacco Etch Protein
TOF	Time of Flight
Trx	Thioredoxin
V_H	Heavy variable domain
V_L	Light variable domain
VLDLR	Very-low-density Lipoproteins Receptor
WL	Worm-like

ABSTRACT

ScFv-h3D6 is a single chain variable fragment, derived from the monoclonal antibody bapineuzumab, that prevents Aβ-induced cytotoxicity by withdrawing Aβ oligomers from the amyloid pathway towards the worm-like one. In addition, it was shown to be effective at the behavioral, cellular, and molecular levels in the treatment of the mouse model of Alzheimer's disease (AD), 3xTg-AD.

Although its great potential, scFv-h3D6 production was limited by some bottlenecks like the presence of scrambled conformations generated in the refolding process and its contamination with endotoxins, which dramatically reduce the production yield and increase the cost. In the current work, several ways to improve protein production and thermodynamic stability have been explored. Firstly, disulphide bridges were eliminated to avoid scrambled conformations and, in this way, improve the protein purification yield and assure an homogenous protein conformation. Elimination of the disulphide bridge of the most stable domain, V_H, solved the scrambling problem and doubled the production yield. Notably, it also changed the aggregation pathway from the protective worm-like morphology to an amyloid one. Then, we stabilized the scFv-h3D6 fold by introducing the mutation V_H-K64R and combined it with the previously described elongation of the V_L domain (C3). The stabilities of the different scFv-h3D6 constructs resulted in the order C3 > K64R/C3 > V_H-K64R ≥ scFv-h3D6, showing that combination of both mutations was not additive but rather they partially canceled each other. Cytotoxicity assays showed that all the mutants recovered cell viability of Aβ-treated neuroblastoma cell cultures in a dose-dependent manner and with efficiencies that correlated with stability, therefore improving the therapeutic ability of this antibody. Finally, a change in the expression system of the scFv-h3D6 was performed. The novel protein obtained in the eukaryotic system *Pichia Pastoris* maintained the same thermodynamic properties as the protein obtained from *Escherichia coli*. However, other properties were improved: homogeneity of the sample, absence of scrambled conformations, endotoxin free sample, better protein yield, easy purification and extrapolation to a larger scale. Therapeutic effectiveness was also demonstrated *in vitro* and *in vivo*.

On the other hand, Aβ-Immunotherapy has long been studied in the treatment AD, but not how other molecules involved in the disease can affect antibody performance. To completely understand the possible interactions and effects among Aβ, scFv-h3D6, apolipoprotein E (apoE) and apoJ, we performed a complete study from all different perspectives: biophysical, cellular and *in vivo*. Instead of full-length apolipoproteins, we combined scFv-h3D6 with apoE

and apoJ mimetic peptides (MP), composed of essential structures within these apolipoproteins for binding to other molecules. Biophysical studies showed that apoE-MP precluded the formation of protective WL fibrils by the scFv-h3D6/Aβ complex, and partially interfered with the scFv-h3D6-induced reduction in Aβ-uptake by astrocytes; whereas apoJ-MP allowed the formation of WL fibrils and did not interfere with the reduction in Aβ uptake. When looking at the inflammation associated with AD, apoE-MP developed an anti-inflammatory role in cell culture and in the 3xTg-AD mouse model; while apoJ-MP showed an anti-inflammatory profile only when combined with scFv-h3D6. ScFv-h3D6 alone did not induce microglial activation, as previously shown with complete antibodies, but rather reduced it. ApoE and apoJ levels were reduced by scFv-h3D6, but increased by apoE-MP and apoJ-MP, affecting each other.

As a general conclusion, scFv-h3D6 treatment decreases Aβ burden, decreases astrocytic Aβ uptake, restores endogenous apoE and apoJ levels and ameliorates inflammation. Although, combined therapy with MPs should be further analyzed, this work demonstrates that all the effects of scFv-h3D6 are addressed to preclude AD pathology, without eliciting the detrimental effects shown by bapineuzumab in clinical trials.

I- INTRODUCTION

1. ALZHEIMER'S DISEASE

Alzheimer's disease (AD) is the major cause of dementia, affecting some 44 million people globally; this number is expected to almost double in the next 15 years, and more than triple by 2050 [1]. AD is a neurodegenerative disorder associated with progressive damage in brain functions including memory, language, spatial orientation, behavior and personality. The clinical manifestation of AD is generally preceded by a silent preclinical phase [2], the prodromal phase, after which the first clinical symptoms appear as mild cognitive impairment (MCI) [3]; the disease finally results in dementia, which implies the existence of multiple cognitive symptoms severe enough to interfere with daily functioning [4]. These phases are accompanied by biochemical changes in the brain, which are reflected in the cerebrospinal fluid (CSF) [5].

Extracellular plaques, containing various forms of amyloid-β (Aβ) peptide, and intracellular neurofibrillary tangles (NFTs), composed of hyper-phosphorylated tau protein, are the two major pathological hallmarks of the AD brain (Figure I-1). According to the amyloid cascade hypothesis, first established by Selkoe and his research group in 1991, cerebral Aβ accumulation is the critical early step in the disease pathogenesis that subsequently leads to neurofibrillary tangle formation, neuroinflammation, synaptic loss, neuron death and ultimately, dementia [6].

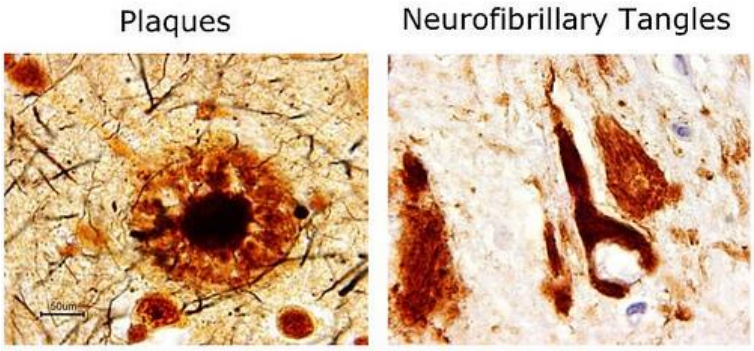

Figure I-1. Extracellular Aβ plaques and intracellular neurofibrillary tangles (NFTs) are the two major pathological hallmarks of the AD brain. Adapted from http://alz101.blogspot.com.es/2015/09/the-tangles-of-tau-labyrinthine-tau.html.

2. AMYLOID CASCADE HYPOTHESIS

Aβ is a soluble metabolite of ~4 kDa that is produced by the processing of APP, a large transmembrane glycoprotein [7]. APP can be processed by either of two distinct membrane-anchored proteases, α-secretase (thought to consist of one or more members of the ADAM family of metalloproteases) or β-secretase (an aspartyl protease of the pepsin family, also called β-site APP-cleaving enzyme (BACE-1)) [8]. Depending on which enzyme initially processes the APP, two cleavage pathways are possible: the non-amyloidogenic and amyloidogenic, respectively

(Figure I-2). In both cases, the γ-secretase complex, containing a special type of aspartyl protease called presenilin, performs sequential cleavage to the membrane-anchored generated product. The γ-secretase complex is composed of presenilin-1 (PS1) or PS2, nicastrin, anterior pharynx defective phenotype (APH1) and presenilin enhancer 2 [9].

In the prevalent non-amyloidogenic pathway, APP is cleaved by α-secretase at a position 83 amino acids away from the carboxy (C)-terminus, producing a large amino (N)-terminal ectodomain (sAPPα) that is secreted into the extracellular medium [10]. The resulting 83-amino acid C-terminal fragment (C83 or CTFα) is retained in the membrane and subsequently cleaved by the γ-secretase complex, producing a short fragment termed p3 [11]. In this pathway, cleavage by α-secretase occurs within the Aβ region, thereby avoiding Aβ formation.

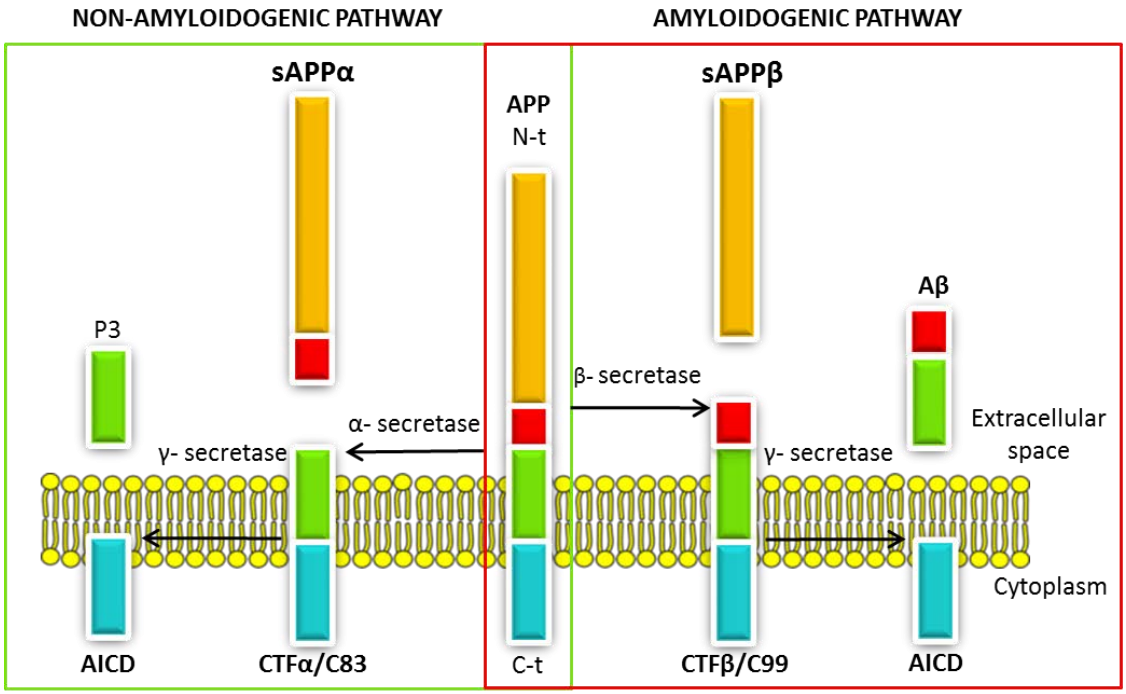

Figure I-2. APP processing. APP can be processed by two different pathways: the non-amyloidogenic and the amyloidogenic one. In the non-amyloidogenic pathway (left) APP is cleaved by α-secretase at a position 83 residues away from the carboxy (C)-terminus, producing a large amino (N)-terminal ectodomain (sAPPα), which is secreted into the extracellular space, and an 83-residue C-terminal fragment (C83, also CTFα), which is retained in the membrane. In the amyloidogenic pathway (right), the cleavage of APP by β-secretase at a position located 99 residues from the C-terminus generates the release of sAPPβ into the extracellular space, and leaves a 99-residue C-terminal fragment (C99, also CTFβ) within the membrane. In both cases, the γ-secretase complex does a sequential cleavage in the fragments retained in the membrane: in the non-amyloidogenic case by producing a short fragment termed p3 and the APP intracellular domain (AICD), and in the amyloidogenic one by cleaving the CTFβ fragment at different positions releasing Aβ peptides of different lengths and the AICD. Reproduced from Montoliu-Gaya, L. & Villegas, S. ABB (2015) [12].

In the amyloidogenic pathway, the cleavage of APP by β-secretase at a position located 99 residues away from the C-terminus generates the release of sAPPβ into the extracellular space, and leaves the resulting 99-amino acid C-terminal fragment (C99 or CTFβ) within the membrane,

with the newly generated N-terminus corresponding to the first amino acids of Aβ. Subsequent cleavage of this fragment by the γ-secretase complex (between residues 38 and 43) liberates the Aβ peptide [13].

2.1 Aβ generation by the γ-secretase complex

The γ-secretase cleavage of the transmembrane domain of the βCTF (Figure I-2) is heterogeneous, generating a variety of peptides of various lengths [14]. The cleavage site has a great influence in the aggregation potential and consequently in the pathogenicity of Aβ. Most of the Aβ produced has a length of 40 residues ($Aβ_{40}$), but a little fraction (approximately 10%) is the $Aβ_{42}$ variant [15]. The additional two hydrophobic residues in $Aβ_{42}$ increase its ability to aggregate, providing the scaffold for oligomeric and fibrillar forms, thus it is considered to be the most neurotoxic one [16]. However, some studies suggest that the ratio of $Aβ_{42}$ to $Aβ_{40}$, rather than the total amount of Aβ, exhibits better correlation with cognitive decline [17].

The γ-secretase complex cleaves the βCTF in a sequential manner: first at the ε-site, followed by the ζ-site and then, the γ-site (Figure I-3A). The ε cleavage site is located in close proximity to the cytoplasm, where water is available [18]. This cleavage is heterogeneous and generates two types of fragments: AICD50-99 and AICD49-99. Aβ peptides generated in these cleavages are $Aβ_{49}$ and $Aβ_{48}$, so they must undergo further processing to obtain the predominant $Aβ_{40}$ and the more pathogenic $Aβ_{42}$. Then, ζ-site is cleaved, apparently generating two divided groups: the sites relevant to $Aβ_{40}$ production ($Aβ_{43}$, $Aβ_{46}$, $Aβ_{49}$) and those relevant to $Aβ_{42}$ production ($Aβ_{45}$, $Aβ_{48}$). The cleavage at a three-residue interval is a prominent property of both groups. Finally, the γ-site cleavage generates $Aβ_{40}$ and $Aβ_{42}$ [18,19].

Interestingly, there is a link between $Aβ_{40}$ and AICD50-99 and between $Aβ_{42}$ and AICD49-99. In cells expressing wild-type APP and/or wild-type PS1/2, $Aβ_{40}$ and AICD49-99 were predominant, but when various forms of APP or PS1/2 mutants were expressed, the proportion of $Aβ_{42}$ as well as of AICD49-99 increased [20].

2.2 Amyloid-β (Aβ) peptide

At physiological concentrations the amyloid-β peptide is an enhancer of learning and retention, as it has been demonstrated by Morley's group in several studies [21]. Low doses of amyloid-β produce presynaptic enhancement [22], arborisation of dendritic-like processes, increase neurite outgrowth and cell survival [23]. Therefore, it is not Aβ itself, but its accumulation what is pathological.

In the earlier AD studies, it was thought that only the Aβ peptide composing the amyloid plaques was toxic. However, it has been a long time since it was demonstrated, and now widely accepted, that the oligomeric and protofibril forms of Aβ are the crucial toxic species. In addition, recent work has clearly established that the main neurotoxic species of Aβ are the soluble oligomers, and fibrils *per se* are relatively less toxic, although they serve as a source for the shedding of soluble oligomers [24]. Consequently, soluble Aβ is the responsible for triggering the pathophysiological cascade leading to AD, rather than its deposition as plaques. This idea has been well-established since several studies pointed out that soluble Aβ levels were better correlated with cognitive deficits than the amount of amyloid plaques [25,26]. Moreover, these observations demonstrated that degeneration starts before, and no as a consequence, of amyloid deposition [27].

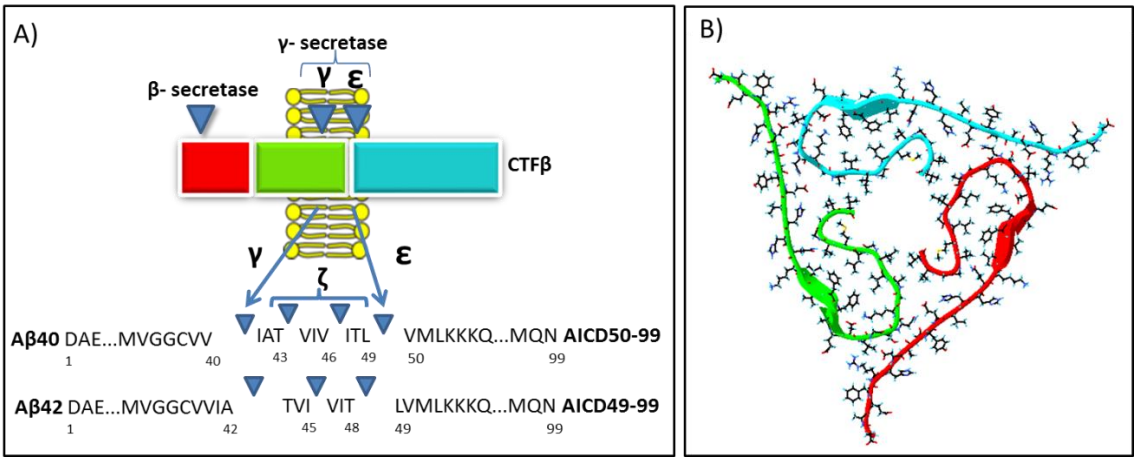

Figure I-3. Aβ peptide generation and 3D-structure of its trimers. A) Once the CTFβ fragment is produced by β-secretase cleavage, it is processed in a sequential manner by different γ-secretase activities (ε, ζ and γ) to obtain the common $Aβ_{40}$ and $Aβ_{42}$ species. The ε cleavage produces, on the one hand, the AICD50-99 and AICD49-99 fragments and, on the other, the $Aβ_{49}$ and $Aβ_{48}$ peptides, respectively. Then, ζ-activity cleaves the $Aβ_{49}$ and $Aβ_{48}$ peptides generating two different groups: the sites relevant to $Aβ_{40}$ production ($Aβ_{43}$, $Aβ_{46}$, $Aβ_{49}$) and those relevant to $Aβ_{42}$ production ($Aβ_{45}$, $Aβ_{48}$). Finally, the γ-site cleavage generates $Aβ_{40}$ and $Aβ_{42}$, respectively. Consequently, there is a link between $Aβ_{40}$ and AICD50-99 and between $Aβ_{42}$ and AICD49-99. B) As demonstrated by NMR and EM, in the human brain $Aβ_{40}$ peptide monomers tends to aggregate in oligomers multiple of three units (trimers, hexamers, nonamers and dodecamers), where the N-termini (DAEFR, residues 1-5) are exposed to the solvent, while the C-termini, highly hydrophobic, are buried in the trimer core (PDB 2M4J, first conformer). Cartoon representation was generated by Swiss-PdbViewer 4.1.0. Monomers are arbitrarily colored. Reproduced from Montoliu-Gaya, L. & Villegas, S. ABB (2015) [12].

The Aβ peptide appears to produce its effect through oxidative damage, possibly mediated by mitochondrial dysfunction and/or due to generalized neuroinflammation [21]. The increased Aβ aggregation and burden can stimulate the immune system and induce inflammatory stress. Cellular immune components, such as microglia or astrocytes, mediate the release of inflammatory molecules, including tumor necrosis factor, growth factors, adhesion molecules, or chemokines. Over- and under-expression of pro- and anti-inflammatory molecules,

respectively, may result in neuroinflammation and thus disease initiation and progression [28]. In addition, levels of several inflammatory factors were reported to be altered in the brain or body fluids of patients with AD, reflecting their neuropathological changes [29–31].

The biophysics of Aβ assembly and compaction into neurotoxic oligomers has been extensively studied by several approaches. As described recently by Lu *et al.* by using seeded fibril growth from human brain extract and data from solid-state nuclear magnetic resonance (NMR) and electron microscopy (EM), $A\beta_{40}$ peptide monomers tend to aggregate in oligomers multiple of three units (trimers, hexamers, nonamers and dodecamers), where the N-termini (DAEFR, residues 1-5) are exposed to the solvent, while the C-termini, highly hydrophobic, are buried in the trimer core (Figure I-3B, pdb 2M4J). Likewise, 0.5nm-twisted hydrophobic package of the trimers leads to the formation of amyloid fibrils, in such a way that all of the N-termini within the fibril are solvent-exposed [32].

3. GENETICS OF AD

The lines of evidence supporting the key role of Aβ in triggering the disease include the fact that patients with familial early-onset AD (EOAD) carry mutations in the Aβ region of the APP gene, as well as in other genes related with Aβ processing (*PSEN1, PSEN2*) [8,14]. All the roughly 180 mutations in *PSEN1*, 20 mutations in *PSEN2* and 36 mutations in *APP* lead to elevation of total Aβ, its aggregation, or shift Aβ production from $A\beta_{40}$, the most common species, to the more aggregation-prone $A\beta_{42}$ [17].

However, in the most prevalent form of the disease, the late-onset sporadic AD (LOAD), decreased Aβ clearance rather than increased production is initiating the disease process [33]. Genetically, *APOE*, which encodes the lipid/cholesterol carrier apolipoprotein E (apoE) is the only well-established locus that affects the risk of developing LOAD. *ε*4 allele of the *APOE* gene, is the strongest risk factor for LOAD, compared to the more common ε3 allele, whereas the presence of the ε2 allele is protective [34,35]. Recently, high-throughput genotyping analyses have been successful in the characterization of the *APOJ* (also *CLU*), *CR1*, *PICALM*, *BIN1*, *ABCA7* and *CD33* loci as new genetic determinants of AD (in addition to the well-established *APOE ε4* allele) [36], with at least one independent genome-wide association study replication for each major candidate [37]. The proteins codified by these newly identified genes are involved in vesicular protein trafficking, lipid metabolism and inflammation [38], which are thought to be related to Aβ clearance.

Thus, both forms of the disease, EOAD and LOAD, show very similar clinical and neuropathological features, leading to the assumption that both diseases share a molecular basis: accumulation of Aβ, whether it is by an overproduction or a deficiency in the clearance mechanisms.

4. APOLIPOPROTEINS AND AD

With *APOE* as the main risk factor for developing LOAD and the predominance of lipid-related genes in the list of new genetic determinants of AD, it is evidenced that there is a relation between AD and lipid metabolism. Moreover, apolipoproteins have been shown to play a key role in AD pathogenesis, especially in terms of Aβ aggregation and clearance. Both fibrillar and diffuse plaques include components that co-localize with Aβ-deposits [39] and modulate fibril formation [40], known as amyloid-associated proteins (AAPs), which include apolipoproteins E and J.

4.1 Apolipoprotein E (APOE)

Because of the low permeability of the Blood Brain Barrier (BBB) to peripheral cholesterol, most of the cholesterol present in the brain derives from *de novo* synthesis. In the central nervous system (CNS) apoE, in partnership with apoJ and apoC1, plays a pivotal role in cholesterol delivery during the membrane modeling associated with synaptic turnover and dendritic organization [41]. ApoE is normally synthesized and secreted by astrocytes and microglia in the brain and binds to high-density lipoproteins (HDLs) to facilitate cholesterol and phospholipids mobilization and transport between glia and neurons [36]. ApoE interacts with a variety of cell-surface receptors of the high-density lipoproteins receptor (LDLR) family to allow particle uptake, including low-density lipoproteins receptor (LDLR), LDL-related protein receptor 1 (LRP1), very-low-density lipoproteins receptor (VLDLR) and apoEr2 [42]. Internalization of the apoE-HDL particles by members of the LDL receptor family occurs primarily in specific clathrin-coated pit structures in the plasma membrane, where both *BIN1* and *PICALM* gene products (also identified in GWAS as genetic determinants for developing LOAD) were shown to facilitate endocytosis of large complexes. Once internalized via endocytic processes, the HDL complex is degraded and the released cholesterol can be used for synapse formation, terminal proliferation or for medium-term storage purposes [36].

ApoE is synthesized with an 18-residue N-terminal peptide that undergoes intracellular processing before secretion of a mature 35kDa glycoprotein containing 299 residues [43,44]. The 3D-structure of the full-length human apoE3 was solved by NMR in solution (pdb 2L7B) [45],

whereas available information for apoE4 and apoE2 is just from the crystal structures of the N-terminal 22kDa domain (pdb 1B68 and 1NFO, respectively). ApoE has two separate N-terminal and C-terminal domains joined by a flexible hinge region (see scheme in Figure I-4). The N-terminal domain contains the receptor-binding region and the C-terminal domain the lipid-binding region. The three isoforms apoE2, apoE3, apoE4, differ only at positions 112 and/or 158. ApoE3 contains a cysteine at position 112 and an arginine at 158, while apoE2 contains cysteine residues at both positions and apoE4 contains arginine residues [46] (Figure I-4). The differences of one or two residues among isoforms significantly alter the apoE's folding structure and change its ability to bind lipids and receptors.

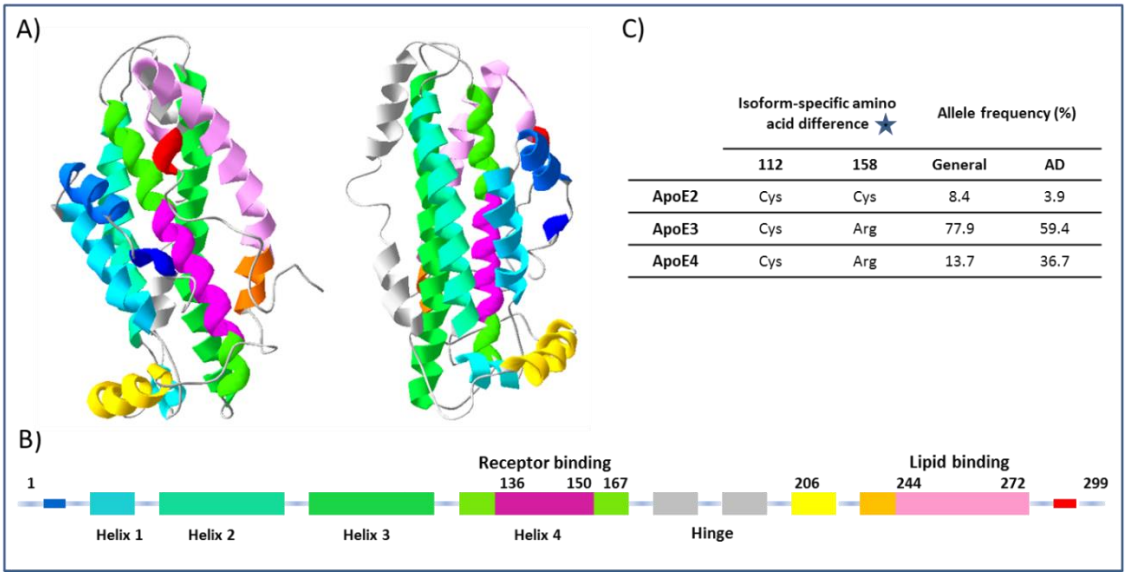

Figure I-4. ApoE3 NMR 3D-structure and isoforms. A) Two different orientations of the first conformer in PDB 2L7B (residues K1-H299) show the receptor binding site (magenta), the lipid binding (pink) site, and the flexible hinge region joining the N- and C-terminal domains (gray). Cartoon representations are coloured as secondary structure succession and were generated by Swiss-PdbViewer 4.1.0. B) Scheme of the main secondary structures and domains. The N-terminal domain has four main helices, with the receptor-binding region located at the fourth one (magneta). The C-terminal domain is shorter and contains the lipid-binding region (pink). C) The three isoforms apoE2, apoE3 and apoE4, differ only at positions 112 and/or 158 (labeled with a star in B)). The differences of one or two residues among isoforms significantly alter the apoE's folding structure, which has been demonstrated to have a direct effect in the incidence of LOAD. Reproduced from Montoliu-Gaya, L. & Villegas, S. ABB (2015) [12].

While transporting cholesterol is its primary function, apoE also regulates Aβ metabolism, aggregation and deposition [47]. The presence of apoE4 contributes to the pathogenesis of AD probably by both loss-of-function in neuroprotection and gain-of-function in neurotoxicity compared to apoE3 [34,48]. Although several pathways underlying the risk associated with apoE4-linked AD have been defined through *in vitro* and *in vivo* studies, the exact mechanisms are still not completely understood [47].

One method of clearance of Aβ is the efflux across the BBB to the periphery, where Aβ is rapidly degraded in the plasma [49]. In fact, it has been described that LRP1 is the main responsible receptor for Aβ efflux, whereas RAGE (Receptor for Advanced Glycation End-products, a key element in diabetes, atherosclerosis, cancer and AD) is responsible for Aβ influx. The 3D-structure of the ectodomain for this relevant receptor has just been solved (pdb 4LP5).

Epitope mapping of the apoE-Aβ complex revealed that Aβ can interact with both the lipid-binding site and the receptor-binding site within apoE [50]. Not only apoE and Aβ can interact with each other, but they also share common receptors including LRP1, LDLR and HSPG (heparan sulfate proteoglycans) on cell surface [51]. ApoE likely competes with Aβ for their receptor binding but can also facilitate cellular Aβ uptake by forming apoE/Aβ complexes depending on their concentrations, the apoE isoform involved, lipidation status, Aβ aggregation level and receptor distribution patterns [47,52]. Furthermore, receptor-mediated clearance of Aβ through the BBB is affected by apoE isoform: while apoE2 and apoE3 use both LRP1 and VLDLR to cross the BBB, apoE4 shifts Aβ transport from LRP1 to the VLDL receptor [53], resulting in a slower rate of Aβ clearance, as it has been described that LRP1 has the higher endocytic rate [51]. The only 3D-structural information available is the solution NMR structure of the complex between the complement repeat CR17 from LRP1 and a peptide of apoE corresponding to the α-helix involved in binding (α-helix 4, residues 130-149) (pdb 2KNY), but this relevant interaction may give light on the clearance mechanism.

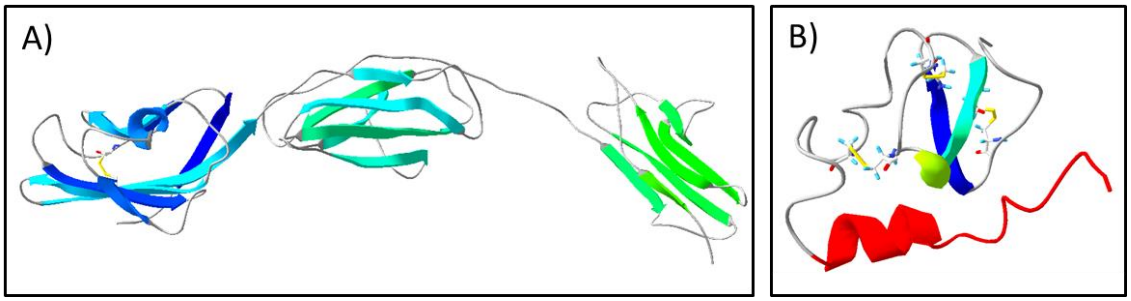

Figure I-5. Three-dimensional structure of some proteins related to Aβ clearance. A) RAGE ectodomain (residues G20-I321, PDB 4LP5, chain A). B) NMR structure of a fusion construct of CR17 from LRP1 (residues G2770-T2817) and apoE (residues S190-L149, PDB 2KNY, first conformer). ApoE region is shown in red. Adapted from Montoliu-Gaya, L. & Villegas, S. ABB (2015) [12].

Although not known at the molecular level, the interaction between apoE and Aβ is evident, but the effect of apoE in Aβ aggregation, whether it is facilitated or inhibited, is controversial [49]. On the one hand, high concentrations of apoE form high molecular weight co-aggregates with Aβ, where apoE4 is likely to promote Aβ aggregation more than apoE3 [54]. In addition, apoE increases the level of Aβ oligomers in an isoform dependent manner (apoE4> apoE3> apoE2), and apoE4 stabilizes preformed Aβ oligomers more than apoE3 [55]. ApoE is also known to aggregate with

irregular protofilament-like morphology, where the aggregates are formed at substantially different rates depending on the isoform (apoE4> apoE3> apoE2) [56]. So, it seems that apoE may be able to produce more co-aggregates with Aβ through its own aggregation propensity.

In contrast, it has been reported that apoE decreases Aβ fibrillogenesis, as it prefers to interact with Aβ peptides that are in β-sheet structure [57], probably by capturing Aβ nuclei and preventing their seeding effects [58]. In this case, apoE3 appears to interact with Aβ more tightly than apoE4, so it is possible that apoE4 is less effective in the inhibition of Aβ fibril formation [47]. Even though the apparent contradiction, in both cases, it is shown that it is apoE4 isoform which leads to the pathological hallmarks of AD.

The relevance of apoE as a genetic risk factor for developing LOAD, as well as the newly discovered list of genes related to lipid metabolism, and the fact that γ-secretase cleavage is carried in lipid rafts, point out the strong relationship between AD and cholesterol. Experiments performed in cell cultures and on animal models have consistently demonstrated that hypercholesterolemia is associated with an increased deposition of cerebral Aβ peptides [59]. If cholesterol levels are elevated, there is an increase in the number of lipid rafts and a consequent enhancement in γ-secretase activity. In the case of apoE, the presence of apoE4 results in higher plasma cholesterol levels [59], as apoE3 and apoE2 isoforms display a preference for HDL, whereas apoE4 is frequently associated with VLDL and LDL [60]. Moreover, cholesterol is an essential component of cell membranes and plays a crucial role in the development and maintenance of neuronal plasticity and function, which are deeply compromised in AD [61].

4.2 Apolipoprotein J /Clusterin (APOJ/CLU)

As previously mentioned, *APOJ* (or *CLU*, clusterin) has been determined as an important genetic risk factor for developing AD. Surprisingly, although clusterin has been reported to be abundantly expressed in the CNS, at similar concentrations to apoE, very little is known about the role this apolipoprotein plays in AD pathogenesis. There are at least five isoforms expressed in human, the canonical isoform 1 has a molecular weight of 53kDa, but obtaining its 3D-structure remains challenging.

ApoJ is thought to act as an extracellular chaperone with the capacity for interacting with a wide range of molecules [62], modulating the membrane attack complex (MAC) and preventing the inflammatory response associated with complement activation after protein aggregation [63]. ApoJ binds to ApoER2 and VLDLR, and is internalized by cells expressing either one of these receptors [62].

It has been proven that apoJ expression is increased in AD, where it is associated with Aβ plaques. Although some authors have pointed out that clusterin expression facilitates, but is not required, for Aβ fibril formation [64], others have shown that it inhibits Aβ fibril formation *in vitro* and promotes the clearance of protein aggregates via endocytosis [65]. As a consequence of such different observations, the role of apoJ is undetermined and further research is needed to find out the precise mechanism this apparently important molecule plays in AD pathogenesis.

5. IMMUNOTHERAPY

With our current worldwide aging population and the increase in the disease incidence, preventing or, at least, blocking AD progression, is necessary for both social and economic reasons [66]. Current approaches used to treat Alzheimer's patients are only capable of temporarily slow down the cognitive decline of AD, as they are focused on ameliorating symptoms instead of targeting its underlying causes [67].

Findings on the specific pathogenicity of the oligomeric forms of the Aβ peptide have raised the question of directly attempting to target them. Developing therapies based on the reduction of these species has become a challenge in treating the underlying pathogenic causes of AD. Immunotherapy is one approach that has been advanced recently for its ability to reduce the accumulation of Aβ. In addition, the immune system participates in AD pathogenesis and it has been demonstrated that naturally-produced antibodies against Aβ occur in humans, and AD patients have lower levels of these antibodies compared to healthy individuals [68].

The primary aim of immunotherapy to treat Alzheimer's disease is to reduce the Aβ burden by using antibodies against the Aβ peptide. This can be achieved either by inducing production by the patient (active immunization) or by administering monoclonal antibodies (mAbs) to the patient (passive immunotherapy).

5.1 Active immunotherapy

The basic concept of active immunization is to prime the immune system to recognize an antigen as a foreign protein in order to generate a response against it [69]. Active Aβ-immunotherapy uses synthetic full-length Aβ peptide, or a fragment. It aims to stimulate B cells to generate specific antibodies to sequester amyloid from the brain in the peripheral system, destroy plaques and inhibit further deposit of amyloid into plaques [70].

On the one hand, active immunotherapy is attractive because it can induce long-term antibody production while being cost effective and requiring only a few visits to the doctor [71]. On the other, some disadvantages could be that the polyclonal response is established to varying degrees with variable specificity of the antibodies produced and, in some cases, meaningful titers are not produced. Especially in the older population such as the late-onset AD group, age-related attenuation of the immune system will affect the efficacy of active immunotherapy. In addition, the specificity of the generated antibodies can be tough to predict, and adverse reactions may be persistent and difficult to reverse [72].

The first Phase IIa clinical trial for an active AD vaccine, AN1792, was performed in 2002 (ELAN & Wyeth). It enrolled patients with moderate-to-severe AD and tested an aggregated full-length $A\beta_{42}$ peptide with an adjuvant (QS-21) that preferably promotes T cell-mediated responses [73]. Administrations were halted due to the development of meningoencephalitis in ~6% (18/300) of the treated group, likely due to activation of pro-inflammatory T cells. Considering that activation of Aβ-specific T cells was potentially harmful, second generation vaccines seek to induce a humoral immune response to generate anti-Aβ antibodies while avoiding Aβ T cell epitopes [74]. To do so, they have been restricted to the B cell epitopes of the Aβ peptide located at the N-terminus, while avoiding the T cell epitopes located at the C-terminus (which were exposed by polysorbate-80 in the AN1792 trial) [69]. Two of such vaccines, AD03 and CAD106, consist of the 1-6 N-terminal fragment of the Aβ peptide, whereas Vanutidecridificar (ACC-001) uses the 1-7 N-terminal fragment. AD03 (MimoVax) Phase I clinical trial, completed in 2011, has not been published and subsequent studies have been terminated for organizational reasons [75]; CAD106 Phase II trial showed a favorable safety profile in subjects with mild AD [76]; and Vanutidecridificar (ACC-001, Janssen and Pfizer) Phase II trials reported a variety of treatment-emergent adverse events (TEAEs) from most subjects during the studies [77].

5.2 Passive immunotherapy

One way to overcome the main drawback of active immunotherapy, i.e. having varying amounts and specificities of the polyclonal antibodies produced by each patient, is to treat the patients with *ex vivo* produced monoclonal antibodies (mAbs) [69]. Passive immunotherapy allows for stopping the treatment whenever an adverse effect occurs, apart from targeting a specific epitope. Its main drawbacks are the high cost of mAb production and the necessary long-term administration [71,78]. For a long time, mAbs have been studied to be used as therapies for different diseases, as they have been found to be an excellent paradigm for the design of high-affinity, protein-based binding reagents [79]. They have been successful in the clinic for a number of

diseases, including autoimmune disorders (anti-TNF Humira and anti-IL-6 Actemra), cancer (anti-HER2 receptor Herceptin and anti-CD20 Rituxan), transplant rejection (anti-CD25 Zenapax and Simulect)[80] and cardiovascular diseases (anti-CD41 ReoPro) [79].

Full-length mAbs designed to bind Aβ peptide were the first molecules tested for passive immunotherapy to treat AD. Some of them showed promising results *in vitro* and in AD mouse models and advanced to clinical trials. Bapineuzumab is described as an example of these antibodies, but many others have been developed (Table I-1).

Table I-1: Passive anti-Aβ immunotherapies for Alzheimer's disease beyond clinical Phase I. Adapted from Montoliu-Gaya L & Villegas S. Expert Reviews in Molecular Medicine (2016) [81].

DRUG	TYPE OF ANTIBODY	COMPANY	AB EPITOPE	CLINICAL STAGE
Bapineuzumab	Humanized monoclonal IgG1	Pfizer/Janssen	N-terminal (all forms)	Two Phase III studies completed
Solanezumab	Humanized monoclonal IgG1	Eli Lilly	Mid-domain (monomers)	Two Phase III studies completed. Other Phase III studies ongoing
Ganterezumab	Humanized monoclonal IgG1	Hoffman-La Roche	N-terminal and mid-domain (aggregates)	Phase III
Crenezumab	Humanized monoclonal IgG4	Genentech	Mid-domain (oligomers and fibrils)	Phase II
Ponezumab	Humanized monoclonal IgG2	Pfizer	C-terminal (plasmatic monomer)	Phase II repurposed for CAA
BAN2401	Humanized monoclonal IgG1	BioArtic/ Eisai	E22G "arctic" mutation (protofibrils)	Phase II
Aducanumab	Human Monoclonal IgG1	Biogen Idec	N-terminal and mid-domain (aggregated)	Phase III
Octagam IVIG	Human polyclonal	Octapharma	Multiple sites on conformational Aβ epitopes	Phase II completed
Gammagard IVIG	Human polyclonal	Baxter	Multiple sites on conformational Aβ epitopes	Phase III completed
Newgam	Humanized monoclonal IgG1	Sutter Health	Multiple sites on conformational Aβ epitopes	Phase II

5.2.1 Mabs: *Bapineuzumab (AAB-001 & AAB-003, Pfizer/Janssen)*

In 2000, Bard and colleagues demonstrated that peripheral administration of an IgG1 mAb specific for the five N-terminal residues of Aβ, 3D6-mAb, into AD Tg-mice resulted in the transfer of the antibody into the brain, binding of the antibody to plaques and induction of the Fc receptor-mediated microglial-phagocytosis of Aβ deposits [82]. 3D6-mAb binds all forms of the Aβ peptide (monomeric, oligomeric and fibrillar).

This antibody is the precursor of the humanized bapineuzumab (AAB-001), which has been tested up to Phase III [83]. In a Phase I study, bapineuzumab appeared safe and overall well-tolerated in patients with mild-to-moderate AD, but MRI monitoring showed microhemorrhages in three out of ten patients on the highest dose. This finding lead to the new term amyloid-related imaging abnormalities (ARIA) and, more specifically, ARIA-edema/effusions (ARIA-E) to refer to vasogenic edema and ARIA-H to refer to microhemorrhage [84]. ARIAs are thought to result from transient leakiness of cerebral vessels following vascular amyloid clearance.

In the subsequent Phase II trial, the highest dose was lowered (from 5 mg/kg to 2 mg/kg). Although no significant differences were seen by two different cognitive assessments (ADAS-Cog and DAD), a considerable reduction in amyloid was shown by PIB-PET (positron emission tomographic imaging using Pittsburgh compound B) as well as reduced CSF phospho-tau. However, the occurrence of ARIA-E in *APOE ε4* allele carriers led to recruiting *APOE ε4* and non-*APOE ε4* carriers separately for Phase III. CSF analyses showed a reduction in phospho-tau with treatment only in the *APOE ε4* group, while the Aβ concentration was maintained in all the cohorts. Volumetric magnetic resonance imaging (MRI) did not show any differences between treated and untreated groups, but amyloid PET scans demonstrated the clearance of some fibrillar cerebral Aβ. Diffusion tensor imaging (DTI, a variant of MRI) showed that ARIA-E occurred in at least 5% of the bapineuzumab-treated patients, especially in the *APOE ε4* carrier cohort, and this lead to the discontinuation of the study at the highest dose. Diminished levels of CSF phospho-tau were also seen exclusively in this cohort. These facts were attributed to the increased Aβ burden, including vascular amyloid, in *APOE ε4* carriers. Because bapineuzumab did not improve clinical outcomes in patients with AD, despite treatment differences in biomarkers observed in *APOE ε4* carriers, the trial was stopped in August 2012. The commonly cited explanation for the failure of this trial points to the recruitment of patients with mild-to-moderate AD, a stage at which brain amyloid deposition has been occurring for many years. Thus, the main thing learned from this study is that clinical trials for AD must be performed on patients in the prodromal phase. Pfizer and Janssen have been working on an improved version

of bapineuzumab (AAB-003), which has been tested in two recently completed Phase I trials [85]. This version has a redesigned Fc region, aiming to prevent ARIAs [86].

Due to the severe side-effects observed in the clinical trials with complete monoclonal antibodies, some other immunotherapeutic approaches targeting Aβ peptide have been developed with the aim of improving properties as efficacy and safety. These are based on natural polyclonal IgGs and on antibody fragments derived from those mAbs mentioned above. Although this work is based on an anti-Aβ scFv, many other structures have been developed (Table I-2).

5.2.2 Single-chain variable fragment (ScFv)

Single chain Fvs (scFvs) are a recombinant format in which the V_H and V_L domains of immunoglobulins are joined with a flexible polypeptide linker that prevents dissociation. Antibody Fab and scFv fragments, comprising both V_H and V_L domains, usually retain the specific, monovalent, antigen-binding affinity of the parent IgG, while showing improved pharmacokinetics regarding tissue penetration [79]. In addition, and as is desirable for a therapeutic agent against a brain disease, these fragments do not induce Fc-mediated activation of microglia.

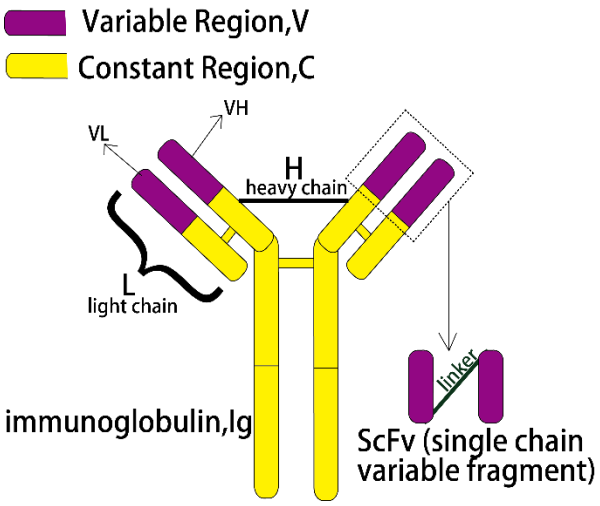

Figure I-6. ScFvs are a recombinant format in which the V_H and V_L domains of immunoglobulins are joined with a flexible polypeptide linker. Adapted from http://2014hs.igem.org/Team:Shenzhen_SFLS.

Several Aβ specific scFvs have been developed for several purposes, such as interfering with Aβ aggregation [87–90], attenuating Aβ neurotoxicity [88–91], increasing specificity for the oligomer conformation [92], inhibiting β-secretase cleavage [93], and having α-secretase-like activity[94] or Aβ-hydrolyzing activity [95]. With this latter aim, in 2008 Taguchi *et al.* described a phage display-derived scFv capable of hydrolyzing peptide bonds within Aβ molecules via serine protease-like

activity [96,97]. Aβ fragments were less aggregation-prone than intact Aβ. Such a catalytic function may reduce the negative effects of conventional Aβ binding IgGs, like the occurrence of cerebral microhemorrhages as a consequence of opsonisation of Aβ deposits in blood vessels [96]. One of the main properties of this type of molecule, commonly named catalytic antibodies, must be a high specificity for binding to Aβ, thus avoiding the proteolysis of other proteins. For this purpose, in 2010 Kasturirangan *et al.* improved the specificity for Aβ of the previously designed scFv using affinity maturation [98].

In terms of interfering with Aβ aggregation and attenuating Aβ neurotoxicity, the single-chain variable fragment scFv-h3D6, derived from the mAb bapineuzumab, has been shown to be a promising approach to treat AD.

6. ScFv-h3D6

6.1 ScFv-h3D6 characterization

Given the evidence for the use of immunotherapy as a tool to treat AD and the potential of scFvs, the Protein Folding and Stability Group at UAB, headed by Dr. Sandra Villegas, developed a scFv derived from the humanized monoclonal antibody bapineuzumab (h3D6-mAb). This new antibody, the scFv-h3D6, consisted of the variable domains of the heavy (V_H) and light chains (V_L), linked by a fused connector $(Gly_4Ser)_3$. The scFv-h3D6 was designed to target the N-terminal 1-5 residues of the Aβ peptide, which are exposed to the solvent when Aβ peptide monomers aggregate in oligomers as multiples of three units (trimers, hexamers, nonamers and dodecamers) [32]. In addition, as it lacks the Fc region of complete antibodies, it is supposed to reduce Aβ burden on patients without generating any inflammatory response.

The expression of scFv-h3D6 was achieved by Argany-Marín, Rivera-Hernández *et al*. [99] using Origami2 strain of *E. coli* (DE3). Protein purification was carried out from the insoluble fraction containing a precursor: scFv-h3D6 was fused with thioredoxin, a protein with chaperone and disulfuroisomerase activity in order to favor the native folding. Tag of the precursor was eliminated thanks to the presence of a target for digestion with protease TEV (tobacco etch virus).

Table I-2: Passive immunotherapeutic approaches targeting Aβ peptide. Adapted from Montoliu-Gaya L & Villegas S. Expert Reviews in Molecular Medicine (2016) [81].

ENGINEERED ANTIBODY	TYPE OF ANTIBODY	MOLECULAR WEIGHT (KDa)	PROPERTIES	EXAMPLES
Monoclonal antibody	Complete antibody	150	-High stability, low aggregation tendency. -Low efficiency crossing BBB. -Fc-mediated immunoreactivity. -Many in clinical trials.	bapineuzumab solanezumab
Fab	IgG devoid of Fc portion	55	-Non Fc-mediated glial activation or inflammation. -Very few developed.	hWO-2 rFab
ScFv	V_H and V_L domains joined with a flexible linker	25	-Non-Fc-mediated glial activation or inflammation. -High tissue penetration. -Difficult to produce due to low stability.	scFv-h3D6
V domain	V_H, V_HH, V-NAR	15	-From humans: prone to aggregation, poor solubility. -From camelids, sharks: high solubility, plasticity, stability.	V_HH V31-1
DARPins	Ankyrin repeats	15	-High solubility, stability, and low aggregation tendency. -No immune response associated with immunoglobulins. -No disulfide bonds: intracellular and extracellular applications. -Lack of endogenous receptors.	Amyloid-β peptide-specific DARPins
IVIG	Polyclonal antibodies	150	-No immunoreactivity. -Differences in their levels of anti-Aβ antibodies. -Difficult and expensive to obtain and purify. -Not shown to recover cognitive impairment but other applications.	octagammard gammagard
Catalytic antibodies	ScFv with catalytic activity	25	-ScFv capable of hydrolyzing Aβ peptide bond. -Aβ fragments are less aggregation-prone than intact Aβ. -No protofibril and fibril formation.	Asec-1 scFv
Bispecific antibodies	ScFv/mAb+ shuttle	-	-Transport through the BBB via receptor. -Treat aggregation in the brain.	anti-Aβ mAb-Tfr

To test the effectiveness of the antibody fragment in protecting against the toxic effects of Aβ, experiments with human neuroblastoma cell line SH-SY5Y were performed. A range of Aβ concentrations was used to test the toxic effects of Aβ oligomers, being 10 μM the lowest concentration with the maximum toxicity (60% viability) (Figure I-7A). Then, a fixed concentration of Aβ (10 μM) and a range of scFv-h3D6 concentrations were used. MTT toxicity tests showed that the scFv-h3D6 was able to recover cell viability when used at an equimolar concentration with the Aβ peptide (Figure I-7B).

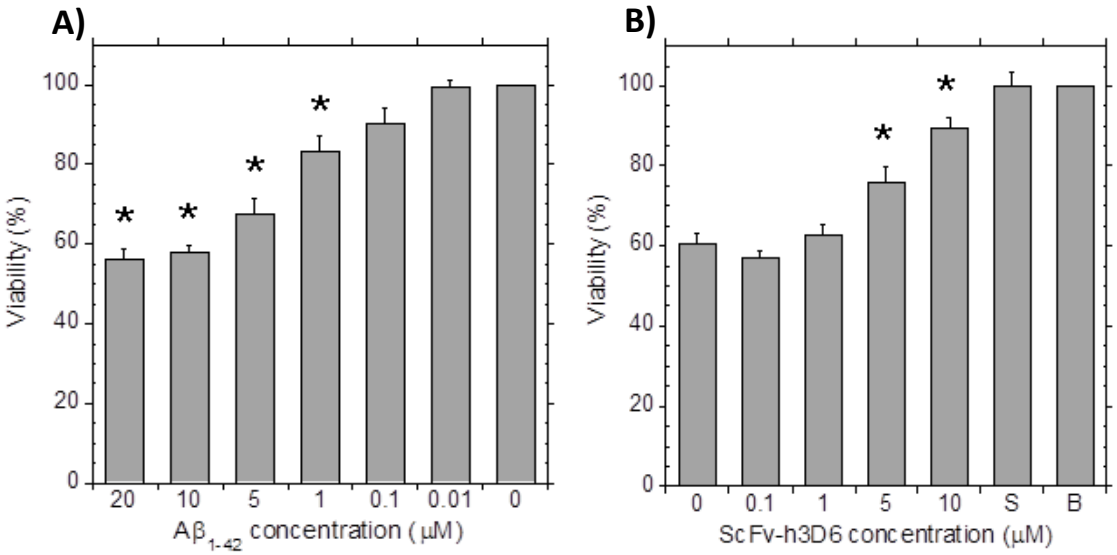

Figure I-7. MTT toxicity assays with the SH-SY5Y human neuroblastoma cell-line. (A) Toxicity induced by different concentrations of the Aβ peptide. **P*< 0.068 compared with 0 μM Aβ. (B) Recovery of cell viability in the presence of 10 μM of Aβ peptide by adding different concentrations of scFv-h3D6. S, 10μM scFv-h3D6 alone (without Aβ peptide); B, buffer (without Aβ peptide and scFv). * *P*<0.068 compared with 0 μM scFv-h3D6. Results are mean±S.E.M. Significance was calculated using the Wilcoxon signed-rank test for four independent experiments (six replicas for each condition per experiment). Reproduced from Marín-Argany, M. *et al.*, Biochemical Journal (2011) [99].

Once effectiveness in cell culture had been demonstrated, experiments addressed to determine which was the molecular mechanism behind the therapeutic effect of the scFv-h3D6 were performed. To do so, scFv-h3D6 aggregation pathway was characterized by circular dichroism (CD), fluorescence spectroscopy (Trp and Tht/ANS) and infrared spectroscopy (FTIR) (Figure I-8). It was observed that thermal treatment initiated an aggregation pathway characterized by a β-sheet conformation rich intermediate that eventually aggregated as worm-like (WL) fibrils. These fibrils are short and curved, different than amyloid fibrils especially in terms of toxicity.

In addition, it was demonstrated that the formation of WL fibrils by scFv-h3D6 was kinetically and thermodynamically favored when it was bound to Aβ oligomers, explaining why this antibody fragment is able to withdraw Aβ oligomers from the amyloid pathway and therefore reduce their toxicity.

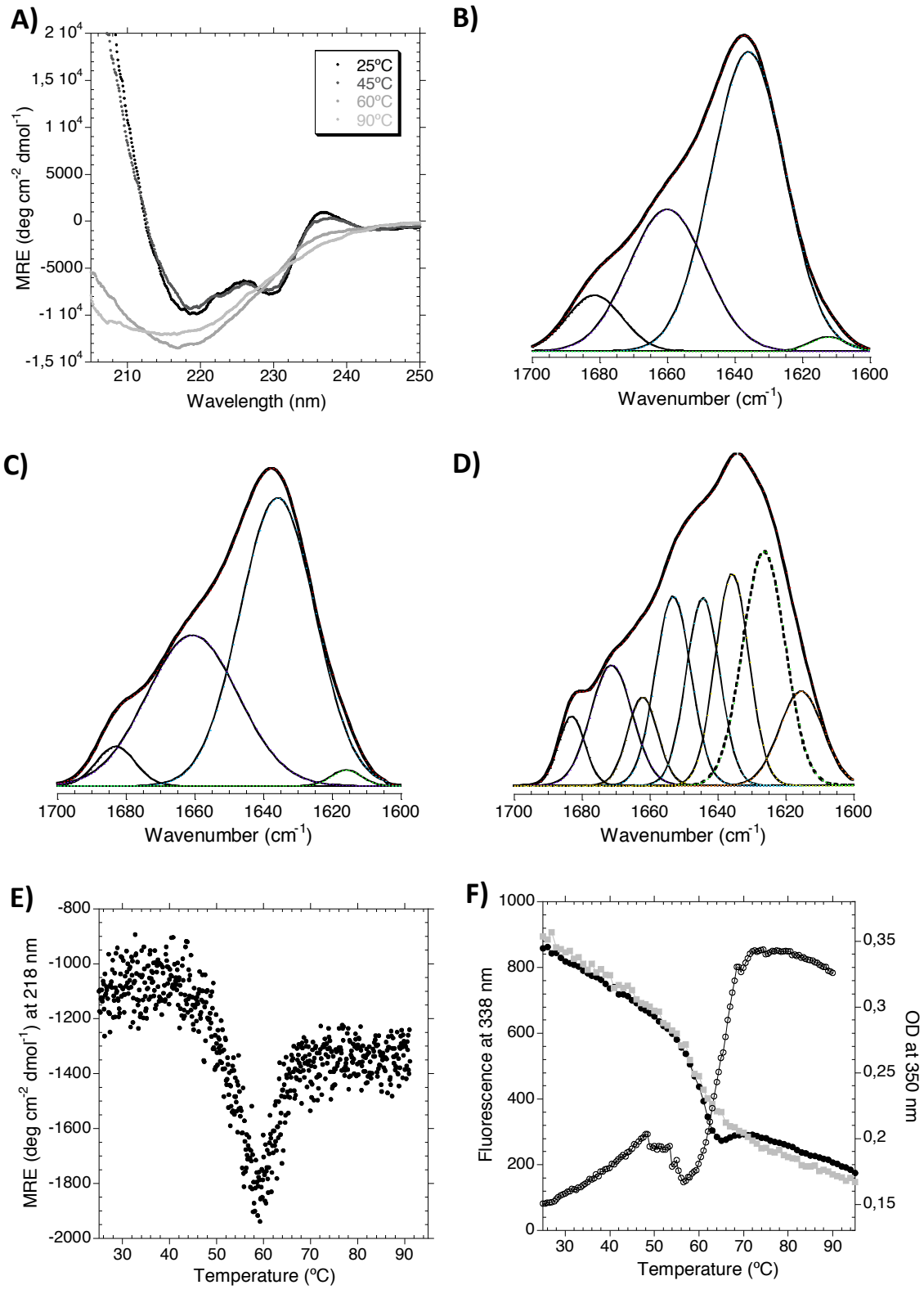

Figure I-8. Secondary structure and thermal denaturation of scFv-h3D6. (A) Far-UV CD spectra at different temperatures. The spectrum at 25˚C shows two ellipticity minima (218nm and 230nm), an ellipticity maximum (200nm) and a positive shoulder (237nm). This particular shape of the spectra is lost at 60˚C in favor of a canonical β-sheet conformation (ellipticity minimum at 215nm). (B–D) Band decomposition of the FTIR amide I' spectra at relevant temperatures. (B) 25˚C; (C)37˚C; (D)60˚C. Decomposition at 25˚C and 37˚C generated four components, whereas at 60˚C, eight components

contributed to the spectrum. The dotted line indicates the 1626 cm^{-1} component. (E) Thermal denaturation followed by CD (ellipticity at 218nm). (F) Thermal denaturation followed by tryptophan fluorescence (338nm) and turbidity (A_{350}). Reproduced from Marín-Argany, M. *et al.*, Biochemical Journal (2011) [99].

In order to better study the formation of WL fibrils by the scFv-h3D6, TEM analysis was performed (Figure I-9). It could be demonstrated that scFv-h3D6 tendency to form WL fibrils was increased with temperature, but especially when the interaction with Aβ oligomers occurred.

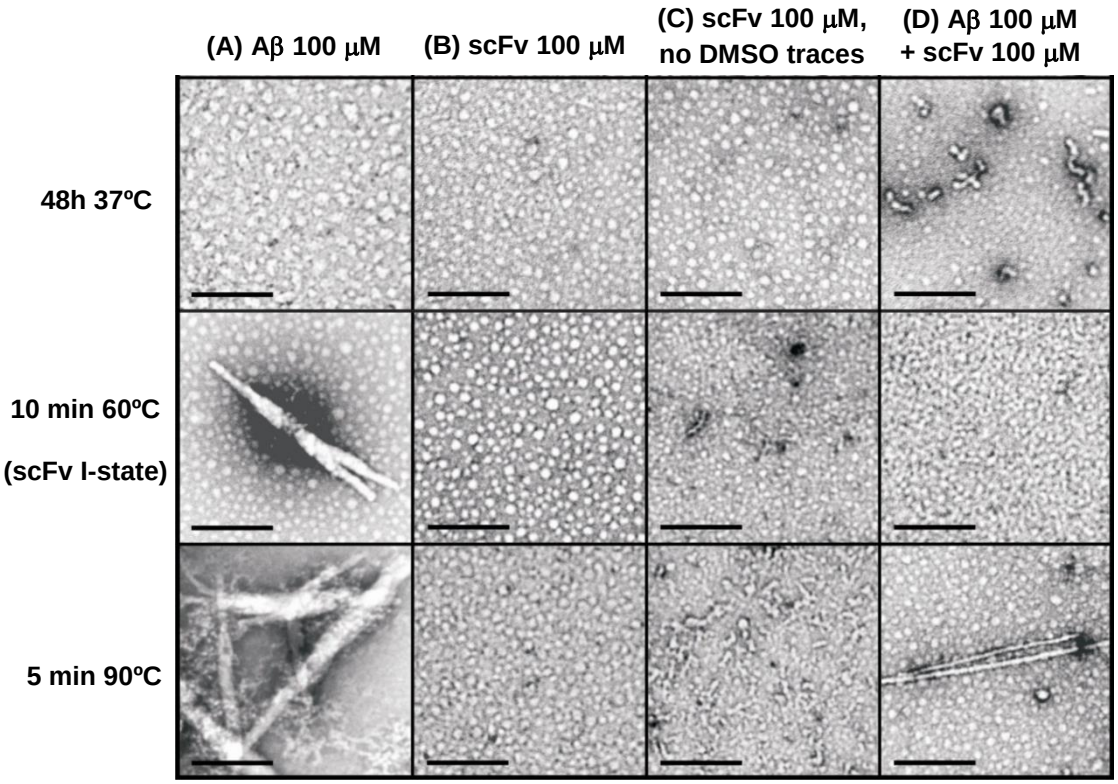

Figure I-9. TEM of amyloid and WL fibrils by Aβ and scFv-h3D6. 100 μM Aβ (A), 100 μM scFv-h3D6 (B), 100μM scFv-h3D6 in the absence of DMSO (C), and 100μM Aβ plus 100 μM scFv-h3D6 (D), at different incubation conditions. (A) The cytotoxic oligomers of the Aβ peptide are visualized at 37˚C, and heating at a higher temperature is mandatory to obtain amyloid fibrils. (B) ScFv-h3D6 does not form WL fibrils in the presence of DMSO. (C) ScFv-h3D6 in the absence of DMSO forms small oligomers at 37˚C, and at 60˚C initiates the formation of WL fibrils; these WL fibrils are better structured after treatment at 90˚C. (D) The Aβ/scFv-h3D6 complex directly forms WL fibrils at 37˚C and heating disrupts them. Reproduced from Marín-Argany, M. *et al.*, Biochemical Journal (2011) [99].

6.2 In vivo *validity of scFv-h3D6.*

ScFv-h3D6 was demonstrated to be effective in the triple transgenic 3xTg-AD mouse model of Alzheimer's disease at both the behavioral and molecular levels [100,101]. Prior to the treatment, five-old-month female animals, corresponding to the early stages of the disease, showed the first behavioral and psychological symptoms of dementia-like traits (BPSD). Cognitive deficits included short- and long-term learning and memory deficits, and high navigation speed. After a single intraperitoneal dose of scFv-h3D6, the swimming speed was the same as the control non-

transgenic mice and learning and memory deficits were ameliorated. Western analysis of brain areas extracts from treated 3xTg-AD animals revealed a global decrease in Aβ oligomers in the cortex and the olfactory bulb, not seen in the hippocampus, plausibly because the study was performed at an early stage of disease progression (Figure I-10A). Indeed, scFv-h3D6 showed great potential in treating other molecular features of AD. In the untreated 3xTg-AD animals, an increase in the concentrations of both apoJ and apoE in the cortex, as well as apoE in the hippocampus were observed. Treatment significantly recovered the non-pathological levels of these apolipoproteins [100] (Figure I-10B).

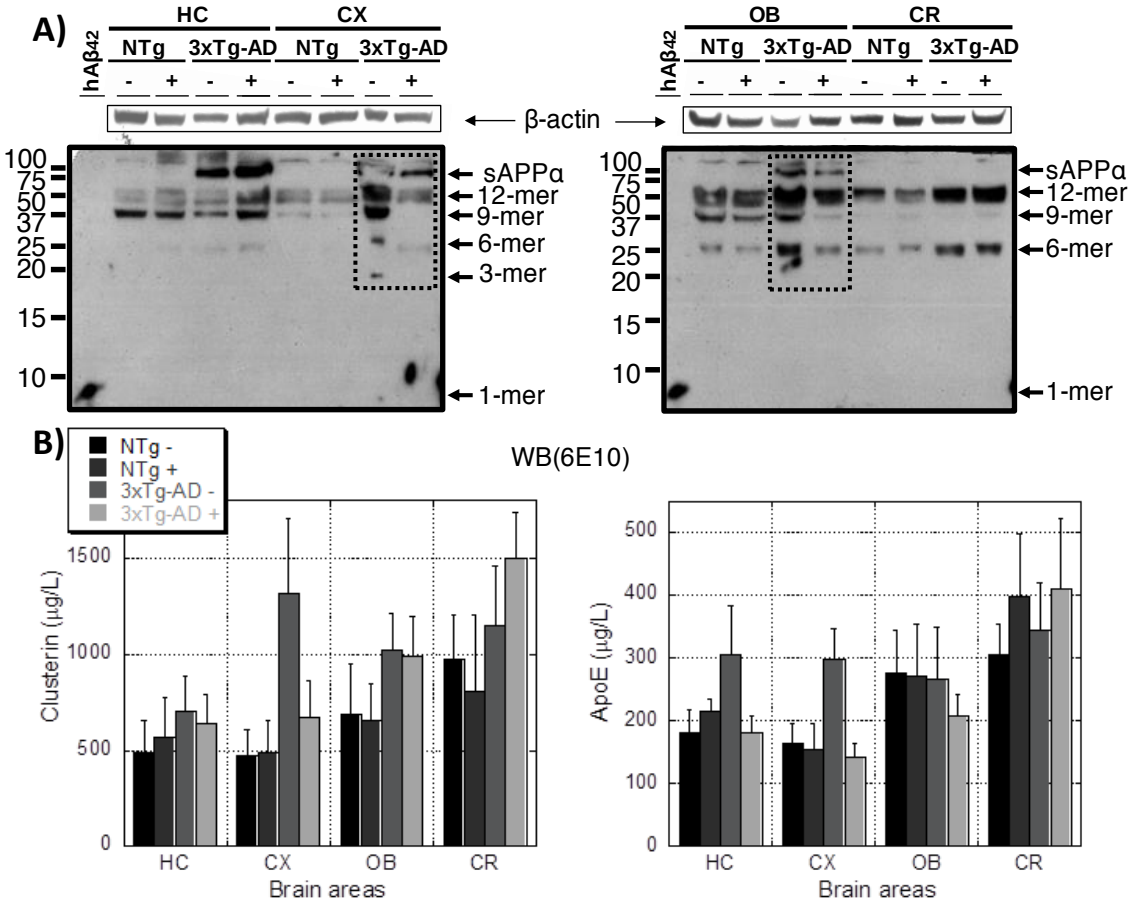

Figure I-10. (A) Immunoblotting analysis of the soluble Aβ-amyloid oligomers from extracellular extracts of 5-mo-old NTg and 3xTg-AD mice. Extracellular extracts from several brain subregions (HC, hippocampus; CX, cortex; OB, olfactory bulb and CR, cerebellum), from non-transgenic (NTg) and triple transgenic (3xTg-AD) mice i.p. treated with 85 µg of scFv-h3D6 (+) and i.p. treated with PBS (−), were analyzed. Profiles for NTg mice did not change upon scFv-h3D6 treatment. The profiles for 3xTg-AD mice of extracellular soluble Aβ oligomers in CX and OB showed a clear decrease of the dodecameric, nonameric, hexameric and trimeric Aβ-species upon treatment (squared), while in HC and CR remained the same. Arrows indicate respective migration position of monomers (1-mer), trimers (3-mer), hexamers (6-mer), nonamers (9-mer), dodecamers (12-mer), sAPPα and sAPPβ (secreted form of APP that has been cleaved by α- and β-secretase, respectively). Synthetic human Aβpeptide (hAβ42) was used as a positive control (left lanes). Total protein applied to each lane was 45 µg. Blots were normalized by β-actin concentration. **(B) Clusterin (apoJ) and apoE concentrations in extracellular extracts determined by ELISA.** Mean ± SD, n = 5, Mann-Whitney U test, **P* < 0.05 vs. untreated NTg mice. #*P* < 0.05 vs. untreated 3xTg-AD mice. Adapted from Giménez-Llort, L. *et. al*, mAbs (2013) [100].

6.3 Improvement of scFv-h3D6 stability.

In a posterior work, Rivera-Hernández, Marín-Argany *et al.* [102] analyzed the scFv-h3D6 chemically induced unfolding. This follows a three state transition (native, unfolding intermediate and unfolded), like is the case for other scFvs (Figure I-11A). The intermediate state is composed of the unfolded V_L domain and the folded V_H domain, suggesting that V_L domain could be a good target to redesign in order to increase the thermodynamic stability.

Plünckthun and his colleagues proposed a model for classifying scFvs depending on the stability of the interface between the domains and the intrinsic stability of each domain [103,104]. The scFv-h3D6, included in Class I, is characterized by the fact that the intrinsic stability of a domain is significantly greater than the sum of the stabilities of the other domain and the interface. Consequently, an intermediate state in the folding pathway would be present in equilibrium and would be detected in the unfolding curve, as in the case of scFv-h3D6.

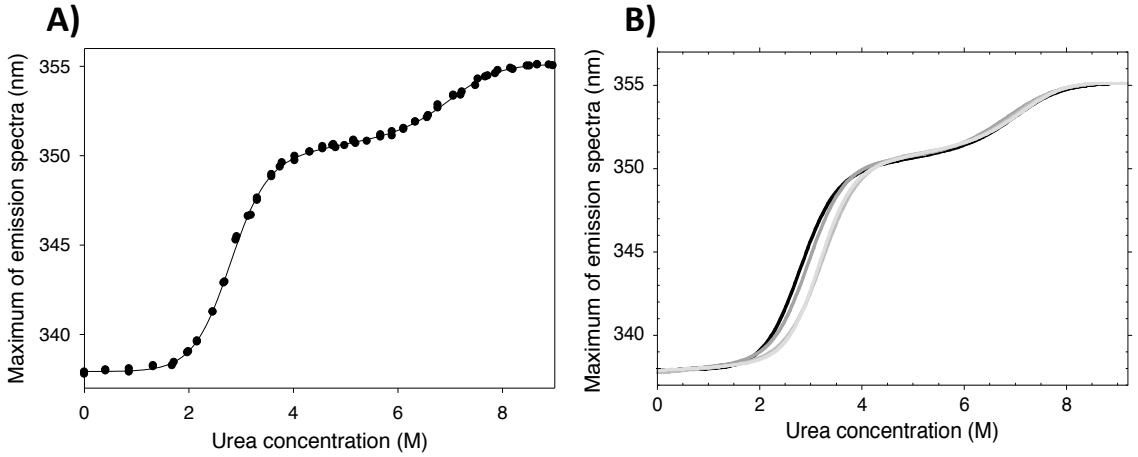

Figure I-11. Urea denaturation of scFv-h3D6 WT and its variants. The maximum of the Trp-fluorescence emission-spectra is plotted as a function of urea concentration. (A) WT, (B) Comparison of WT and C1, C2 and C3 mutants. Two transitions are observed during the red-shift. The plateau in the 4-6M urea region is indicative of the occurrence of an intermediate state. WT, black; C1, dark grey; C2, mild gray; C3, light grey. Adapted from Rivera-Hernández G. *et al*., mAbs (2013) [102].

In order to redesign the molecule as to increase its thermodynamic stability, the group modeled the 3D-structure of scFv-h3D6 and observed that the V_L domain, located at the C-terminal end of the molecule, finished before its last β-sheet is completed. C-terminal residues of twenty-four scFv molecules were analyzed by structural alignment and three new mutants were designed: V_L-R108G (C1), V_L-R108 (C2) and V_L-R108T109 (C3). All three showed an increase in the thermodynamic stability, as seen in urea denaturation experiments (Figure I-11B), and reduced aggregation tendency, as determined by FTIR spectroscopy and Trp-fluorescence (data not shown). Moreover, cooperativity was maintained in the mutants with the extension of one residue, but in the case of the C3 mutant, which was the most stable one, was increased.

6.4 The scrambling problem

One of the main disadvantages of scFv-h3D6 production is the low yield obtained in the protein purification. The fact that the molecule presents two disulphide bridges, one in the core of each domain, can lead to the formation of non-native disulphide bonds during the refolding process carried out in the protein purification from the insoluble fraction. The therapeutic application of this protein does not allow the coexistence of different conformations in the sample. Then, scrambled conformations must be fractioned from the native state, dramatically reducing the production yield and increasing the cost.

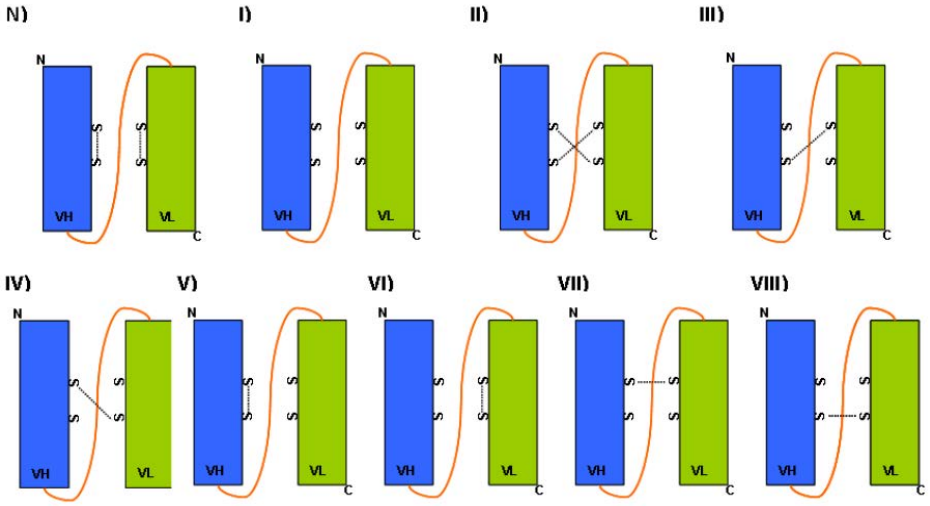

Figure I-122. Representation of native (N) and scrambled conformations (I-VIII) of scFv-h3D6. Native disulphide bridges are formed between cysteines C22-C92 in the V_H domain and C23-C88 in the V_L domain.

II- GENERAL AIMS

Although its great therapeutic potential, scFv-h3D6 production presents some limitations like the presence of disulphide scrambled conformations generated in the refolding process and the contamination with endotoxins, which dramatically reduce the production yield and increase the cost. The current Thesis aims to improve the folding and stability properties of the scFv-h3D6, as well as to establish an efficient production with a higher yield. To do so, several approaches have been explored: elimination of disulfide bridges to avoid scrambled conformations (Chapter 1), mutation of protein sequence to improve thermodynamic stability (Chapter 2) and a change in the expression system from *Escherichia coli* to *Pichia Pastoris* (Chapter 3).

On the other hand, albeit Aβ-immunotherapy has long been studied in the treatment of AD, how other molecules involved in the disease could affect the antibody action remains elusive. The second part of this Thesis aims to test the influence of apolipoproteins E and J, key players in AD development, on scFv-h3D6 action. This has been studied from different perspectives: biophysical (Chapter 4), cellular (Chapter 5) and *in vivo* (Chapter 6).

III- GENERAL METHODS

Due to the wide range of techniques used in the current Thesis, a general description of the basis of each one is given. The aim of this section is to present how a general procedure is performed or what information can be obtained from a concrete technique. The reader can always come back to this part in case any of the chapters include approaches that are not of his/her field of expertise. Concrete conditions for each experiment are detailed in the Materials and Methods section of each chapter.

1. RECOMBINANT PROTEIN PRODUCTION

Recombinant protein production is based on the use of a host microorganism or eukaryotic cells to express a desired protein in high amounts and then isolate the protein to obtain it pure. Essentially, DNA encoding a target protein is cloned downstream of a promoter in an expression vector. This vector is then introduced into a host cell, and the cell's protein synthesis machinery produces the protein.

Recombinant DNA techniques to obtain the DNA construct with the protein sequence, expression of the target protein and purification are the main steps of the process.

1.1 Polymerase Chain Reaction (PCR)

PCR is a revolutionary method developed by Kary Mullis in the 1980s. PCR is based on using the ability of DNA polymerase to synthesize new strand of DNA complementary to the offered template strand. Because DNA polymerase can add a nucleotide only onto a preexisting 3'-OH group, it needs a primer to which it can add the first nucleotide. This requirement makes possible to delineate a specific region of template sequence that the researcher wants to amplify. At the end of the PCR reaction, the specific sequence will be accumulated in billions of copies (amplicons) [105] .

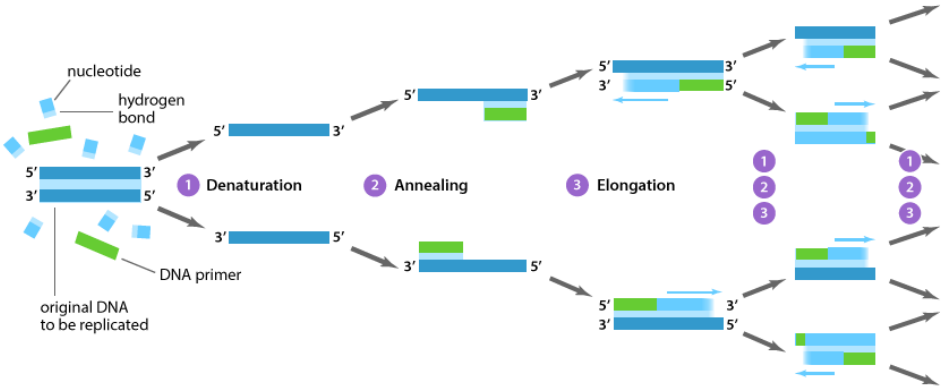

Figure M-1. **How Polymerase Chain Reaction works:** 1) Denaturation: the reaction is heated to 94–98 °C for 20–30 seconds to break the hydrogen bonds between the template DNA strands. 2) Annealing: the reaction temperature is lowered to 50-65 °C for 20-40 seconds to allow primers to anneal to the template strands. 3) Elongation: the temperature is increased (optimal temperature is dependent on DNA Polymerase used, i.e. 72-78 °C for Taq Polymerase) to allow for the addition of dNTPs. The amount of

target sequence doubles with each thermal cycle which leads to an exponential amplification [106] . Extracted from www.abmgood.com/marketing/knowledge_base/polymerase chain reaction. php

Site-directed mutagenesis (SDM) is one of the PCR approaches in which a few residues within the protein sequence are mutated. SDM is a method to create specific, targeted changes in double stranded plasmid DNA (insertions, deletions and substitutions). In this work, SDM has been used to generate concrete mutations in order to:

- Change Cys residues to eliminate disulphide bridges (Chapter 1)
- Substitute one amino acid for another to improve protein stability (Chapter 2)
- Delete a couple of residues to have the protein sequence closer to a protease target (Chapter 3).

1.2 Protein expression

Table M-1. Host microorganisms used in the current work.

MICROORGANISM	STRAIN	GENOTYPE	USED FOR
Escherichia coli	**XL-1Blue**	*recA1 endA1 gyrA96 thi-1mhsdR17 supE44 relA1 lac [F' proAB lacI^{q}ZΔM15 Tn10 (Tet^R)]*	Cloning
	XL-10 Gold	*Tet^{R}Δ(mcrA)183 Δ(mcrCB-hsdSMR-mrr)173 endA1 supE44 thi-1 recA1 gyrA96 relA1 lac Hte [F' proAB lacI^{q}ZΔM15 Tn10 (Tet^R) Amy Cam^R]*	
	Origami 2 (DE3)	*Δ(ara-leu)7697 ΔlacX74 ΔphoA PvuII phoR araD139 ahpc gale galK rpsL [F' proAB lacI^{q}pro] (DE3) gor 522::Tn10 trxB (Str,^{R} Tet^R)*	Protein expression
	BL21 (DE3)	*E. coli* str. B F$^-$ *ompT gal dcm lon hsdS$_B$*(r_B^- m_B^-) λ(DE3 [*lacI lacUV5-T7p07 ind1 sam7 nin5*]) [*malB*$^+$]$_{K-12}$(λ^S)	
Pichia pastoris	**KM71H**	*arg4 aox1::ARG4* genotype; Mut^S, His$^+$, Arg$^+$ phenotype	Protein expression

Once the desired DNA sequence is obtained, the plasmid is inserted in a microorganism able to express the target protein. Among microorganisms, host systems that are available include bacteria, yeast, filamentous fungi, unicellular algae and eukaryotic cells. All have strengths and weaknesses and their choice may be subject to the protein of interest [107,108]. For example, if eukaryotic post-translational modifications (like protein glycosylation) are needed, a prokaryotic expression system may not be suitable [109]. In the current work the gram negative bacteria *Escherichia coli* and the methylotrophic yeast *Pichia Pastoris* have been used (Table M-1).

Induction of expression

Vectors used here for protein expression in *E.coli* have the protein gene under the control of the lac operon. In the absence of lactose, the lac repressor binds to the operator sequence on DNA and blocks the access of T7 RNA polymerase to the promoter site, preventing gene transcription. When lactose binds to to the repressor, it induces a conformational change in the protein that renders it incapable of binding to the operator DNA sequence. IPTG (isopropyl β-D-1-thiogalactopyranoside) is a structural mimic of lactose (it resembles the galactose sugar) that also binds to the lac repressor and induces a similar conformational change that greatly reduces its affinity for DNA. But unlike lactose, IPTG is non-hydrolyzable by the cell, preventing the cell from metabolizing or degrading the inducer. This ensures that the concentration of IPTG added remains constant, making it a more useful inducer of the lac operon than lactose itself. The best moment to induce protein expression is the exponential phase of the growing culture (OD_{600}=0.7). Then, IPTG is added to a final concentration of 1 mM.

Table M-2 Vectors used in the current work.

MICROORGANISM	VECTOR	PROPERTIES
Escherichia coli	**pET1a-trx**	Kanamycin resistance. Protein is expressed fused with thioredoxin (trx), a chaperone with disulfure isomerase activity. It also has an Histidine tag and a TEV target. His(6x)-Trx-Tev-Protein
	pET28a	Kanamycine resistance. Protein is expressed alone, without any other fused element.
	pCri05a	Kanamycin resistance. Protein is expressed fused with NusA, an enhancer of protein solubility. It also has an Histidine tag and a TEV target. His(6x)-NusA-Tev-Protein
Pichia pastoris	**pPicZαA**	Zeocine resistance. Protein is expressed fused with α-factor secretion signal (α-MF) that allows for efficient secretion of most proteins. When protein is translocated to the extracellular space Kex2 and STE13 proteases separate the protein from the α-MF.

As a methylotrophic yeast *P. pastoris* is capable of metabolizing methanol as its sole carbon source. The strong promoter for alcohol oxidase, *AOX1,* is tightly regulated and induced by methanol, and it is used for the expression of the gene of interest. Accordingly, the expression of the foreign protein can be induced by adding methanol to the growth medium. The vector used here (pPICZαA) contains the *AOX1* promoter for tightly regulated, methanol-induced expression of the gene of interest.

1.3 Protein purification

Having found an assay and chosen a source of protein, the cell must be fractionated into components and determine which component is enriched in the protein of interest. It can be expressed in the extracellular or the intracellular space, and in this case, it can be expressed in the soluble or in the insoluble fraction. After the protein expression, cell culture is centrifuged. If protein is expressed in the extracellular fraction, it will remain in the supernatant. For proteins expressed in the intracellular space, cell membrane must be disrupted. A *homogenate* is formed and the mixture is fractionated by centrifugation. Soluble proteins are located in the supernatant, while insoluble proteins forming inclusion bodies are in the pellet. This pellet has to be solubilized by denaturing agents and proteins need to be refolded.

Proteins can be purified from a complex mixture on the basis of characteristics such as solubility, size, charge, and specific binding affinity. Usually, protein mixtures are subjected to a series of separations, each based on a different property to yield a pure protein (Table M-3).

Table M-3. Types of chromatography used in the current work.

CHROMATOGRAPHY TECHNIQUE	SEPARATION PRINCIPLE	USE IN THE CURRENT WORK
Ion exchange chromatography	Ionic interaction	Last step of purification scFv-h3D6 and its variants. Fractionation of scrambled conformations from the native state.
Gel Filtration	Size of the molecule	Last step for final purification or buffer exchange.
Affinity chromatography	Ligand affinity	Separation of scFv-h3D6 from Trx or NusA (which have an HisTag) after cleavage with TEV protease, when the protein was obtained as a fusion protein (vectors pET-1a-trx and pCri5a). Removal of LPS from proteins by affinity columns for endotoxins.

2. PROTEIN CHARACTERIZATION

2.1 Circular Dichroism (CD)

CD is an excellent method of determining the secondary structure of proteins. The most widely used applications of protein CD are to determine whether an expressed, purified protein is folded, or if a mutation affects its conformation or stability. In addition, it can be used to study protein interactions [110]. Briefly, circular dichroism is defined as the unequal absorption of left-handed and right-handed circularly polarized light. A beam of light has time dependent electric and magnetic fields associated with it. If the light is polarized by passing through suitable prisms or filters its electric field, E, will oscillate sinusoidally in a single plane. When viewed from the front, the sinusoidal wave can be visualized as the resultant of two vectors of equal length, which trace out circles, one which rotates clockwise (E_R) and the other which rotates counterclockwise (E_L). The two circularly polarized waves have physical existence. When asymmetric molecules interact with light, they may absorb right and left handed circularly polarized light to different extents (hence the term circular dichroism) and also have different indices of refraction for the two waves. The result is that the plane of the light wave is rotated and that the addition of the E_R and E_L vectors results in a vector that traces out an ellipse and the light is said to be elliptically polarized (Figure M-2A). CD is reported either in units of ΔE, the difference in absorbance of E_R and E_L by an asymmetric molecule, or in degrees ellipticity, which is defined as the angle whose tangent is the ratio of the minor to the major axis of the ellipse. [θ], the molar ellipticity in deg cm^2/dmol = 3298ΔE.

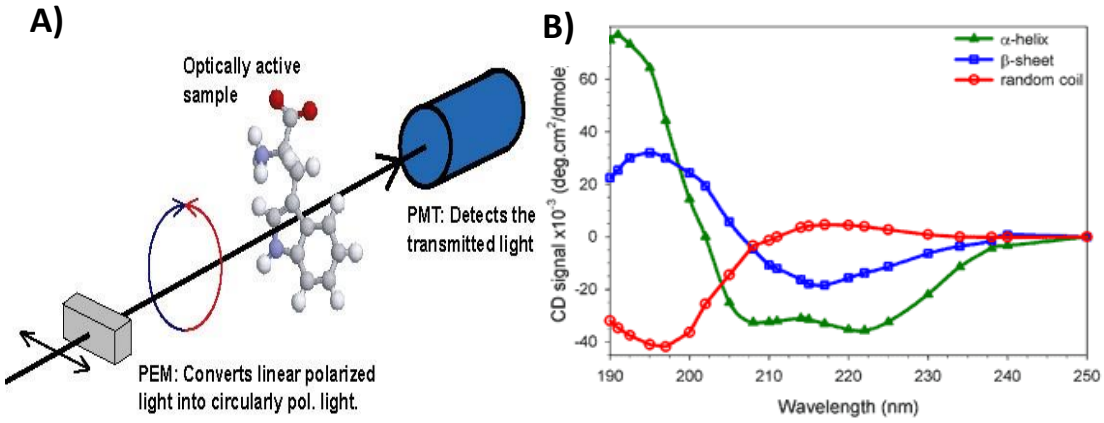

Figure M-2. Circular Dichroism. (A) The principle behind CD spectroscopy. Monochromatised light from the AU-CD beam line is passed through a Photo Elastic Modulator (PEM) which converts the linear polarised light into alternating left and right handed polarised light. The two polarisations are differently absorbed, and the difference in absorption is detected with a Photo Multiplier Tube (PMT); (B) CD spectrum of protein secondary structure elements. Reproduced from www.isa.au.dk/facilities/astrid2/beamlines/AU-cd/.asp and http://www.fbs.leeds.ac.uk/facilities/cd/.

In the case of protein secondary structure, canonical curves have been stablished. For example, α-helical proteins have negative bands at 222 nm and 208 nm and a positive band at 193 nm[111]. Proteins with well-defined antiparallel β-pleated sheets (β-strands) have negative bands at 218 nm and positive bands at 195 nm [112], while disordered proteins have very low ellipticity above 210 nm and negative bands near 195 nm [113] (Figure M-2B) . In addition, the presence of aromatic residues and disulphide bridges within the protein sequence have been reported to importantly contribute to the protein far-UV-CD spectrum (below 260nm) [114].

Protein interactions can also be studied by CD. One of the advantages of CD spectroscopy is that the arithmetic sum of two spectra may overlap the experimental spectrum of the equimolar mixture if there is no interaction. If strong interaction exists, the docking of both molecules may change their conformation so that the experimental and the arithmetic spectra would differ. On the other hand, differences between the experimental CD-spectrum and the arithmetic sum are indicative of aggregation of the complex if the experimental spectrum is similar in shape but less intense than the sum.

Thermal denaturation of protein can also be followed by CD. A determined wavelength is fixed and changes in the secondary structure can be observed with increasing temperatures.

Circular Dichroism has been used to study the secondary structure and the aggregation process of scFv-h3D6 and its variants (Chapter 1, 2 and 3). In addition, interactions among scFv-h3D6, apoE-MP, apoJ-MP and Aβ have been studied by CD (Chapter 4).

2.2 Fluorescence spectroscopy

A fluorescent compound absorbs light energy over a range of wavelengths that is characteristic for that compound. This absorption of light causes an electron in the fluorescent compound to be raised to a higher energy level. The excited electron quickly decays to its ground state, emitting the excess energy as a photon of light. This transition of energy is called fluorescence. The range over which a fluorescent compound can be excited is termed its excitation spectrum. The range of emitted wavelengths for a particular compound is termed its emission spectrum. Fluorescence spectroscopy (also known as fluorometry or spectrofluorometry) is a type of electromagnetic spectroscopy that analyzes fluorescence from a sample [115].

There are three amino acids with intrinsic fluorescence properties, phenylalanine (Phe), tyrosine (Tyr) and tryptophan (Trp) but only Tyrosine and tryptophan are used experimentally because their quantum yields (emitted photons/exited photons) is high enough to give a good fluorescence signal. So this technique is limited to protein having either Trp or Tyr or both. For

an excitation wavelength of 280 nm, both Trp and Tyr will be exited. To selectively excite Trp only, 295 nm wavelength is appropriated. Those residues can be used to follow protein folding because their fluorescence properties (quantum yields) are sensitive to their environment which changes when protein folds/unfolds. In the native folded state, Trp and Trp are generally located within the core of the protein, whereas in a partially folded or unfolded state, they become exposed to solvent. In a hydrophobic environment (buried within the core of the protein), Trp and Tyr have a high quantum yield and therefore a high fluorescence intensity. In contrast in a hydrophilic environment (exposed to solvent) their quantum yield decreases leading to low fluorescence intensity. For Trp residue, there is strong stoke shifts dependent on the solvent, meaning that the maximum emission wavelength of Trp will differ depending on the Trp environment. Therefore, Trp-fluorescence intensity not always increases upon unfolding since the environment of the Trp in the denatured state can be even more hydrophobic than in the core of the native state. This means that when a protein has more than one Trp, while one residue can increase its signal during the unfolding process, another can decrease it. Then, analyzing changes in intensity has no sense but a red shift is what gives the reliable information[116].

There are several means to unfold a protein based on the disturbance of the weak interactions that maintain the protein folded (hydrogen bonding, electrostatic interactions and hydrophobic interactions). The most common ways of unfolding a protein are chaotropic agents (urea, guanidium hydrochloride), the change of pH (acid, base) or the rise of temperature.

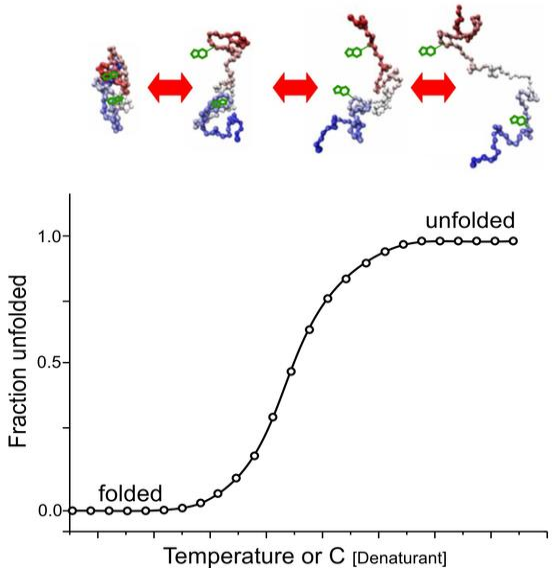

Figure M-3. Thermal or chemical denaturation of a protein. At low temperatures or low denaturant concentration, the protein is perfectly folded. A rise in these parameters leads to the unfolding of the protein. Reproduced from http://www.nanotemper-technologies.com/technologies/nanodsf/.

In temperature induced denaturation, the protein is unfolded by increasing temperature, so at each temperature the protein undergoes unfolding and reach an equilibrium state corresponds to a partially folded or fully unfolded state depending on the conditions. For each temperature, the fluorescence emission of Trp is measured if changes in the three-dimensional packing are to be detected, whereas the CD signal at a concrete wavelength will be used to follow changes in secondary structure.

In the case of chemical induced denaturation, urea is one of the most common denaturing agents. At each urea concentration, the maximum emission of the spectrum is measured and a curve is obtained. Apart from protein properties such as a the number of states during unfolding or the occurrence of an earlier or later red-shift, fitting the curve to an equation permits to determine some thermodynamic parameters: $[D]_{50\%}$ (concentration of the denaturing agent at which 50% of the protein is denatured), AG_{N-U} (folding free energy), m_{N-U} (difference in accessibility to solvent between native and unfolded states).

Thermal and chemical denaturation followed by Trp fluorescence have been used in order to determine the thermodynamic properties of the scFv-h3D6 and its variants (Chapter 1, 2 and 3).

2.3 Fourier Transformed Infrared Spectroscopy (FTIR).

Infrared spectroscopy is one of the classical methods to determine protein structure, due to its high sensitivity to chemical composition and changes in the protein environment. Infrared radiation absorption generates a vibration of the covalent bonds of proteins that renders up to 9 amide bands. The main one is amide I, between 1700 and 1600 cm^{-1} wavenumbers. Vibrational frequency of amide I is due to the carbonyl group (C=O) of each peptide bond of the protein and its intensity depends on the conformation of the polypeptide bone, related to secondary structure.

FTIR is one of the few techniques that permits to study aggregated samples and, in addition, differentiates β-strands depending on the strength of their packing. It is known that the most common structure in proteins with aggregation tendency is β-sheet, so that during the aggregation process the amide I maximum shifts to lower wavelengths due to the increase in the number of hydrogen bonds, β-strand length or the number of β-strands [117].

One of the limiting steps of FTIR is assignation of the components of amide I to secondary structure elements to get an appropriate interpretation of the results[118,119] (Table M-4).

Infrared spectroscopy requires high protein concentrations to obtain a reliable signal/noise ratio. In addition, vibration of O-H bonds of water molecules, located at amide II region (at

1545cm^{-1}), overlaps the absorption region of amide I. To avoid this problem, water in samples is changed for deuterated water (D_2O) using MINI Dialysis Units or lyophilizing the sample and resuspending in D_2O. Amide I band in deuterated sample is called amide I'.

For acquisition, samples were deposited between two CaF_2 windows separated by 50 µm (reflex analytical). Spectrums were obtained with Varian Resolutions Pro. Concrete parameters of the acquisition as well as the data analysis are detailed in Chapters 1 and 2.

Table M-4. Assignation of components of amide I to secondary structure protein elements.

SECONDARY STRUCTURE	WAVELENGTH (nm)
β turns	1690
β turns/High frequency antiparallel β-sheet	1684-1680
β turns	1670
β turns/loops/helix$_{3-10}$	1660
α-helix	1654-1650
Random coil	1650-1640
Low frequency antiparallel β-sheet	1640-1630
Worm-Like	1630-1620
Amyloid	1620-1615
Side chains	1610

Sometimes FTIR shows some disadvantages like: the presence of air bubbles in the cells, the facts that liquid cells are not easy to clean and difficult to mount, the sample can be turbid and the baseline of the resulting spectrum is drifted due to the influence of the stray light, the interference of water molecules is strong, etc. ATR (Attenuated Total Reflection) mode is simpler to use than the conventional transmission mode. All types of samples (i.e. solids, liquids, powders, pastes, pellets, slurries, fibers etc.) are placed undiluted on the ATR crystal and then usually air- or N_2-dried. The measurement is typically performed within a few minutes. One advantage of ATR-IR over transmission-IR, is the limited pathlength through the sample. This avoids the problem of strong attenuation of the IR signal in highly absorbing media, such as aqueous solutions. However, the resolution of ATR is typically lower than that of transmission-IR. In this work, ATR has been used in Chapter 4 to determine the secondary structure of the molecules used in the study.

2.4 Transmission Electron microscopy (TEM)

The electron microscope is a type of microscope that uses a beam of electrons to create an image of the specimen. It is capable of much higher magnifications and has a greater resolving power than a light microscope, allowing it to see much smaller objects in finer detail.

TEM involves a high voltage electron beam emitted by a cathode and formed by magnetic lenses. The electron beam that has been partially transmitted through the very thin (and so semitransparent for electrons) specimen carries information about the structure of the specimen. The spatial variation in this information (the "image") is then magnified by a series of magnetic lenses until it is recorded by hitting a fluorescent screen, photographic plate, or light sensitive sensor such as a CCD (charge-coupled device) camera. The image detected by the CCD may be displayed in real time on a monitor or computer. TEMs are the most powerful electron microscopes: we can use them to see things just 1 nanometer in size, so they effectively magnify by a million times [120].

Negative staining

In negative stain microscopy, the stain surrounds the sample but is excluded from the volume occupied by the sample. When the electron beam primarily passes through the sample, the deflection of the electron beam through sample (i.e. protein) is less than that through the stain rich regions. Electrons that are highly deflected by the stain are then filtered out by the objective aperture located below the sample. Depending on the size of the aperture, the quantity of electrons that are culled out will vary and determine the contrast and resolution of the image [121].

In the current work, electron microscopy has been used to observe the formation of WL fibrils by scFv-h3D6 (Chapters 1,2,3 and 4) or the formation of amyloid fibrils (Chapter 1) using 1% uranyl acetate for negative staining.

2.5 Differential scanning calorimetry (DSC)

DSC is a technique widely used to study thermally induced phase transitions and conformational changes in biological systems, such as proteins, nucleic acids and lipid membranes. DSC measures the difference in heat capacity between both the sample and the reference solutions as a function of temperature. This is obtained by measuring the power required to keep the sample solution at the same temperature as that of the reference solution, as the temperature of both is increased in a linear manner. So, as the temperature changes during a calorimetric

scanning, the protein in the sample solution undergoes a transition in a cooperative fashion. This transition arises from the destruction of numerous small forces that stabilize the native structure. Since the process is usually endothermic, the changes observed in the enthalpy of the system, resulting from such disruption, give rise to a drop in the temperature. Thus, the calorimeter will provide energy to the sample to maintain its temperature at the same value as the one of the reference solution. The energy is measured as a power input and the raw output is a data set of power *vs.* temperature. In modern calorimeters the power is converted, by using internal calibrations, into partial molar heat capacity values. The main parameters that can be determined from a calorimetric scan are: the temperature of the maximum of the transition peak, T_m. This temperature will correspond to the temperature where 50% of the protein molecules are unfolded in the case of a pure two-state unfolding transition without any coupled association/dissociation process; the heat of the transition or calorimetric enthalpy, $\Delta H_{m,exp}$, which is the area of the heat capacity curve centered at the temperature T_m; and the difference between the extrapolated pre- and post-transitional baselines at the transition temperature, ΔCp_{N-U}, that is, the difference between the heat capacities of the unfolded, Cp_U, and native, Cp_N, states of the protein [122].

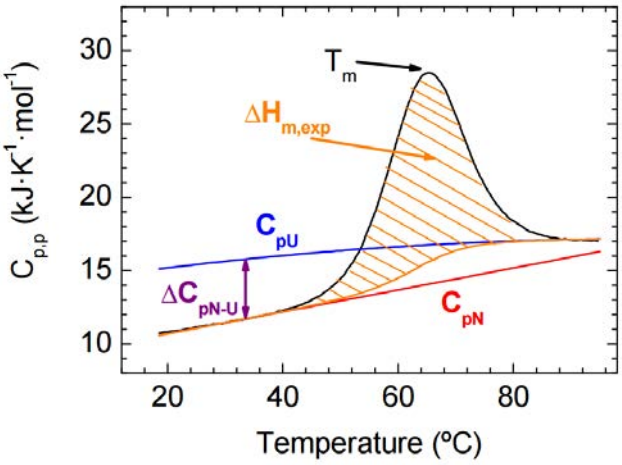

Figure M-4. An example of a DSC calorimetric scan. Black line, experimental data already baseline subtracted and dynamically corrected; red and blue lines correspond to the heat capacities of the native (Cp_N) and unfolded (Cp_U) protein states respectively. The main parameters of the calorimetric scan are shown: temperature of the maximum of the transition peak (T_m), area under the curve corresponding to the calorimetric enthalpy ($\Delta H_{m,exp}$) and the difference between the extrapolated pre- and post-transitional baselines at the transition temperature, ΔCp_{N-U}, that is, the difference between the heat capacities of unfolded, Cp_U (blue line), and native, Cp_N (red line), states of the protein. Reproduced from [122].

Calorimetry experiments have been performed by Dr. Jose C. Martinez at Universidad de Granada. They have been used to describe the thermodynamic properties of the scFv-h3D6 and its variants in Chapter 2.

2.6 Mass spectrometry

Mass spectrometry is an analytical technique in which chemical compounds are ionized into charged molecules and the ratio of their mass to charge (m/z) is measured. In matrix-assisted laser-desorption-ionization (MALDI), peptides are converted into ions by either addition or loss of one or more than one protons. The sample for analysis by MALDI MS is prepared by mixing or coating with a solution of an energy-absorbent, organic compound called matrix. When the matrix crystallises on drying, the sample entrapped within the matrix co-crystallises. The sample within the matrix is ionized in an automated mode with a laser beam. Desorption and ionization with the laser beam generates singly protonated ions from analytes in the sample. The protonated ions are then accelerated at a fixed potential, where these separate from each other on the basis of their mass-to-charge ratio (m/z). The charged analytes are then detected and measured using different types of mass, here, by time of flight (TOF) analyzers. During MALDI-TOF analysis, the m/z ratio of an ion is measured by determining the time required for it to travel the length of the flight tube. Based on the TOF information, a characteristic spectrum is generated for analytes in the sample [123].

Mass spectrometry can be used to determine the molecular weight of a protein but also to identify a protein. Peptide mass fingerprinting (PMF) (also known as protein fingerprinting) is an analytical technique for protein identification in which the unknown protein of interest is first specifically cleaved into smaller peptides, whose absolute masses can be accurately measured with a mass spectrometer such as MALDI-TOF. Then, the peptide masses are compared to a database with the theoretical peptides predicted from the known sequence of the protein.

Mass spectrometry analyses presented in this work were carried out in the Proteomics facility at the UAB (Chapter 3).

3. CELL CULTURE

In vitro models provide the opportunity to study the cellular response in a closed system, where the experimental conditions are maintained. Such models provide preliminary information for outcome of an experiment *in vivo* [124] and in some cases can replace animal tests.

3.1 SH-SY5Y neuroblastoma cell line

Originally derived from a metastatic bone tumor biopsy, SH-SY5Y (ATCC® CRL-2266™) cells are a subline of the parental line SK-N-SH (ATCC®HTB-11™). SK-N-SH were subcloned three times; first to SH-SY, then to SH-SY5, and finally to SH-SY5Y. SH-SY5Y were deposited to the ATCC® in 1970 by June L. Biedler [125]. SH-SY5Y cells are often used as *in vitro* models of neuronal function and differentiation. They are adrenergic in phenotype but also express dopaminergic markers.

SH-SY5Y cell line has been used to determine the therapeutic effect of the scFv-h3D6 and its variants of protecting against Aβ oligomers-induced toxicity. To do so, viability assays were performed (Chapters 2 and 3).

3.2 Viability assays

Measurement of cell viability and proliferation are widely used in cell biology for the study of growth factors, cytokines and nutrients; and for the screening of cytotoxic or chemotherapeutic agents. The most common assay for cell proliferation is the reduction of tetrazolium salts. The yellow tetrazolium MTT (3-(4, 5-dimethylthiazolyl-2)-2, 5-diphenyltetrazolium bromide) is reduced by metabolically active cells, in part by the action of dehydrogenase enzymes, to generate reducing equivalents such as NADH and NADPH. This reduction process requires functional mitochondria, which are inactivated within a few minutes after cell death. The resulting intracellular purple formazan can be solubilized and quantified by spectrophotometric means[126].

However, the early tetrazolium salts did have some disadvantages, such as the insolubility of the resulting formazan products and toxicity of tetrazolium salts. Although the assay procedure was made easier by soluble dyes, in practice the use was limited due to the instability of the formazan dye and a relatively low absorbance of the end product as compared to the classical MTT assay. The BIOMEDICA research department has solved both problems and created an easy to use, rapid and reliable non-isotopic cell proliferation assay (EZ4U). Furthermore, there is no need for the removal of culture medium before or after the addition of the chromogenic substrate and

neither solubilizing nor harvesting procedures are necessary[127], so that experimental error decreases.

This assay has been used to test the protection against Aβ oligomers-induced toxicity by scFv-h3D6 and its variants (Chapters 2 and 3).

3.3 Human primary astrocyte cell culture

Cells can be isolated directly from human or animal tissue using enzymatic or mechanical methods. Once isolated, they are placed in an artificial environment in plastic or glass containers supported with specialized medium containing essential nutrients and growth factors to support proliferation. Cell cultures directly derived from an intact tissue are called primary cells. These cells have undergone very few population doublings and are therefore more representative of the main functional component of the tissue from which they are derived, in comparison to continuous (tumor or artificially immortalized) cell lines, thus constituting a more representative model to the *in vivo* state [128].

Adult primary human astrocytes have been used to study the effects of scFv-h3D6 and apoE and apoJ mimetic peptides (Chapters 4 and 5). Astrocytes were isolated from brain specimens obtained at surgery (medication-refractory epilepsy patients) as described before [129]. The tissue had to be removed to reach the epileptic focus and was not needed for diagnostic purposes. Permission for the use of human brain tissue for *in vitro* research was granted by the Ethical Medical Committee of the VU University Medical Center (VUmc) in Amsterdam, where the operations took place. Brain tissue specimens were obtained with written informed consent and patient information was treated in accordance with the Declaration of Helsinki.

3.4 Flow cytometry

Flow cytometry is a technology that simultaneously measures and then analyzes multiple physical characteristics of single particles, usually cells, as they flow in a fluid stream through a beam of light. The properties measured include a particle's relative size, relative granularity or internal complexity, and relative fluorescence intensity. These characteristics are determined using an optical-to-electronic coupling system that records how the cell or particle scatters incident laser light and emits fluorescence [130].

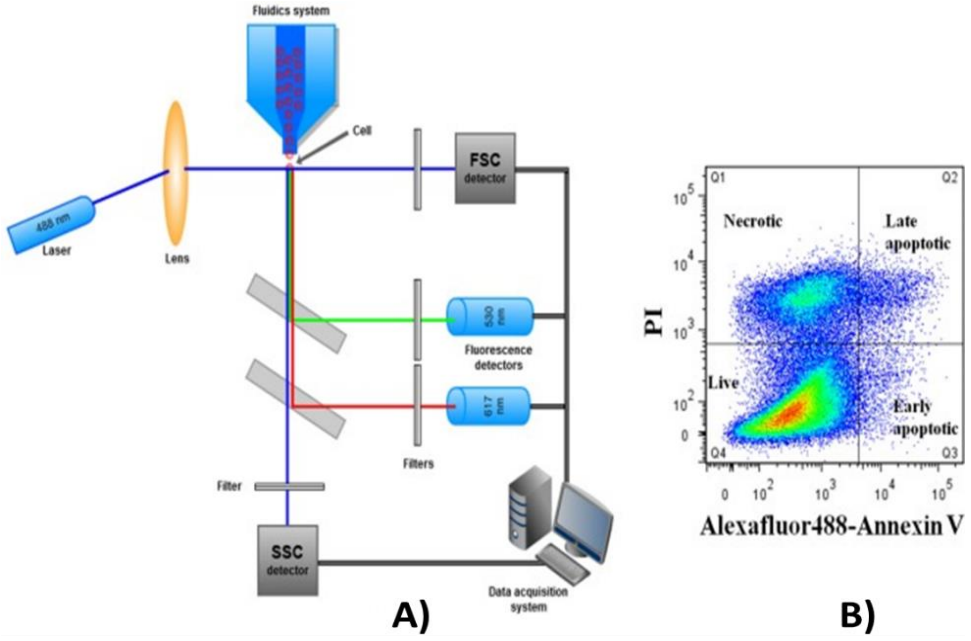

Figure M-5. **Flow cytometry**. A) Ray-diagram, illustrating the schematic of flow cytometer and its working principle. B) Representation of flow cytometry results, showing the live, early apoptotic, late apoptotic, and necrotic cells.

In the flow cytometer, particles are carried to the laser intercept in a fluid stream. Any suspended particle or cell from 0.2–150 µm in size is suitable for analysis. When particles pass through the laser intercept, they scatter laser light and in case any fluorescent is present, it emits fluorescence. The scattered and fluorescent light is collected by appropriately positioned lenses. A combination of beam splitters and filters steers the scattered and fluorescent light to the appropriate detectors. The detectors produce electronic signals proportional to the optical signals striking them. The characteristics or parameters of each event are based on its light scattering and fluorescent properties. This data can be analyzed to provide information about subpopulations within the sample [131].

In this work, flow cytometry has been used to quantify uptake of Aβ oligomers and fibrils (labeled with a fluorophore) by human primary astrocytes (Chapter 4 and 5).

3.5 Enzyme-linked immunosorbent assay (ELISA)

ELISA is a plate-based assay technique designed for detecting and quantifying substances such as peptides, proteins, antibodies and hormones. The ELISA type used in the current work is known as Sandwich ELISA. Sandwich ELISAs typically require the use of matched antibody pairs, where each antibody is specific for a different, non-overlapping part (epitope) of the antigen molecule. The basic procedure is: (1) the plate is coated with a capture antibody; (2) the sample is added, and any antigen present binds to the capture

antibody; (3) the detecting antibody is added, and binds to the antigen; (4) the enzyme-linked secondary antibody is added, and binds to detecting antibody; (5) the substrate is added, and is converted by the enzyme to a detectable form [132].

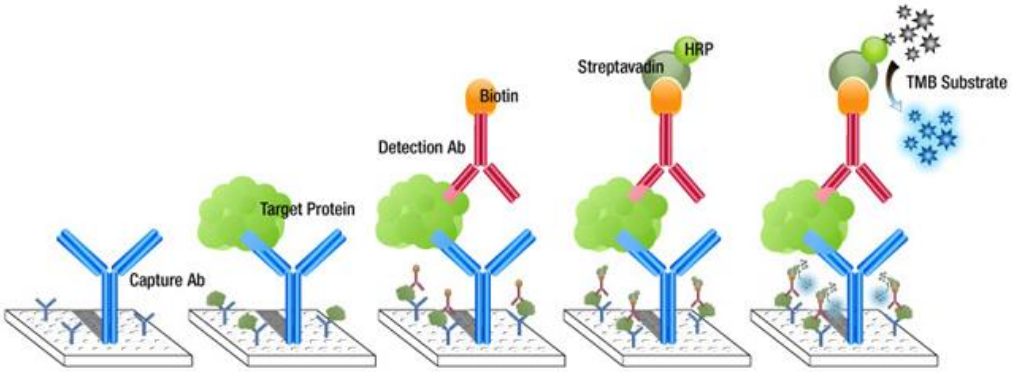

Figure M-6. **Schematic representation of the basic procedure performed in an ELISA**. Reproduced from http://keywordsuggest.org/gallery/400988.html.

All the ELISAs used in the current work are commercial kits. In the case of cell culture supernatants, IL-6 and MCP-1 release levels were analyzed. (Chapter 5)

4. *IN VIVO* STUDIES

4.1 Mice: 3xTg-AD

The mice strain used in the current work for *in vivo* experiments is the transgenic line 3xTg-AD. These mice contain two mutations associated with familial Alzheimer's disease (APP Swedish, and PSEN1 M146V) and one associated with a form of familial frontotemporal dementia (MAPT P301L). The mice are viable, fertile, and display no initial gross physical or behavioral abnormalities. Translation of the overexpressed transgenes appears restricted to the central nervous system, including the hippocampus and cerebral cortex. These mice display both plaque and tangle pathology. Aβ deposition is progressive, with intracellular immunoreactivity detected in some brain regions as early as three to four months of age. Extracellular Aβ deposits appear by six months in the frontal cortex and become more extensive by twelve months. Changes in tau occur later, by 12 to 15 months aggregates of conformationally-altered and hyperphosphorylated tau are detected in the hippocampus [133–135].

This mouse model has been used to test the efficacy of scFv-h3D6 purified from *E. coli* and scFv-h3D6 purified from *P. pastoris* to reduce Aβ burden in brain (Chapter 3). It has also been used to determine how apoE and apoJ mimetic peptides modulate scFv-h3D6 action (Chapter 6).

4.2 Enzyme-linked immunosorbent assay (ELISA)

ELISA has also been used to detect Aβ (Chapters 3 and 6), IL-33, apoE and apoJ (Chapter 6) levels in brain extracts. Also in this part the performed ELISAs are commercial kits.

4.3 Immunohistochemistry (IHC)

IHC refers to the process of selectively imaging (i.e. proteins) in cells of a tissue section by exploiting the principle of antibodies binding specifically to antigens in biological tissues. This requires proper tissue collection, fixation and sectioning. In this work mice brains have been fixed with a solution of paraformaldehyde, which is often used to fix tissue. Once fixed, tissue was embedded in paraffin, then sliced (10µm) with a microtome and mounted on slides. When the slices are used for IHC, they need to be deparaffined and rehydrated using alcohol washes of decreasing concentrations (xylene, ethanol 100%, 96%, 70%, 50%, H_2O).

Depending on the method of fixation and the antibody that is going to be used, the sample may require additional steps to make the epitopes available for antibody binding (antigen retrieval). This is often necessary, and involves pre-treating the sections with heat, formic acid 70% or proteases.

To detect the antigen of interest, an antigen specific antibody, which is usually unlabeled, is used. The secondary antibody is raised against the immunoglobulins of the primary antibody species and is the secondary antibody itself which is directly bound to the reporter molecule. It can be that the antibody is conjugated to an enzyme, such as peroxidase, that can catalyse a colour-producing reaction (immunoperoxidase staining) or the antibody can also be tagged to a fluorophore, such as fluorescein or rhodamine (immunofluorescence) [136].

Immunostaining has been used in the current work to detect several antigens in brain slices: Aβ, GFAP, Iba-1 (Chapter 3 and Chapter 6).

IV-CHAPTERS

CHAPTER 1:

Understanding the contribution of disulphide bridges to the folding and misfolding of scFv-h3D6.

AIMS

The most common problem when obtaining scFv molecules by recombinant protocols is the presence of two disulphide bridges, one in the core of each domain, which drives to scrambled conformations that must be fractionated from the native state [102]. Then, the yield of production is dramatically reduced and the cost is increased. Disulphide bridges are known to increase thermodynamic stability by lowering the conformational entropy of the unfolded state compared with the native state, which makes the *de novo* introduction of such linkages a strategy for protein stabilization [137]. The fact that several disulphide-free scFv molecules can reach the native state [138], allows using the removal of these linkages as the most straightforward strategy to preclude the appearance of scrambled conformations.

Here, we have separately get rid of both disulphide bridges to solve the scrambling problem. Because removing a covalent bond results on an overall destabilization of the fold, we also combined these single-disulphide variants with the stabilizing mutations derived from elongation of the V_L domain. To understand the effect of the elimination of each disulphide bridge and the combination with the stabilizing mutations, we have evaluated the stability and some structural features of the different constructs.

MATERIAL AND METHODS

Mutagenesis, protein expression and purification. Mutagenesis was performed by QuickChange Lightning Site-Directed Mutagenesis Kit (Agilent Technologies). Protein expression was carried out in *Escherichia coli* strain Origami 2 (DE3), as previously described for scFv-h3D6 [99]. In brief, pETtrx-1a was used for the reference scFv-h3D6, V_H-DF mutants, whereas for the V_L-DF mutants, expression in pCri5a was used. These vectors generated scFv variants fussed to Trx and NusA carriers, respectively. Carriers were removed by TEV proteolysis and purification was performed as previously described [102].

Secondary structure determination by Circular Dichroism (CD). Protein secondary structure was monitored at different temperatures by far-UV CD spectroscopy from 260 nm to 190 nm in a Jasco J-715 spectrophotopolarimeter. Protein concentration was 20 μM, and 20 scans were recorded at 50 nm min^{-1} (response 2s) in a 0.2 cm pathlength cuvette.

Secondary structure determination by Fourier Transformed Infrared Spectroscopy (FTIR). FTIR analysis was performed as described previously [99]. Briefly, protein at 100 μM was dialyzed at 4°C against deuterated-PBS. Spectra were acquired at different temperatures ranging 25°C-60°C in a Variant Resolutions Pro spectrometer using excavated cells with a 50 μm path (Reflex Analytical) and the series software licensed under OMNIC (Thermo Scientific).

Thermal denaturation. Thermal denaturation was followed up by far-UV CD spectroscopy at 218 nm and tryptophan fluorescence emission at 338 nm, both at 20 μM protein concentration and 1°C min^{-1} heating rate.

Chemical Denaturation. Chemical denaturation was performed by creating series of progressive urea concentrations with 2 μM final concentration of protein. Measurement of Trp-fluorescence was performed at 25˚C at an excitation wavelength of 290 nm and an emission spectrum recorded from 320 nm to 380 nm in a Varian Cary Elipse fluorimeter. Excitation slit was set to 5 nm and the emission one at 10 nm, and 5 scans were averaged. The maximum of each emission spectrum was obtained by fitting to a three-parametric polynomial, as described before [102].

Transmission Electron Microscopy (TEM). To visualize the aggregation extent and morphology of the variants incubation of 100 μM samples were carried out at 60°C for 10 min. Then, samples were diluted 1:10 in PBS and quickly adsorbed onto glow-discharge carbon-coated grids. Transmission electron microscopy was performed in a Jeol 120-kV JEM-1400 microscope, using 1% uranyl acetate for negative staining.

RESULTS

Elimination of the V_L disulphide bridge

First, we intended to eliminate the disulphide bridge of the V_L domain by generating scFv-h3D6 mutant V_L-C23V/C88A, for the sake of clarity henceforth referred to as V_L-DF (disulphide-free). Surprisingly, the first consequence of removing the disulphide bridge of the V_L domain was a dramatic decrease in the production yield. Then, it became evident that stability dramatically dropped upon mutation. In consonance, thermal denaturation showed that the conformational transition followed by fluorescence was advanced about 15˚C (Figure 1.1A). Although the native state of V_L-DF was only different in the minimum at 230 nm featuring the V_L domain, as seen by CD (Figure 1.1B), thermal denaturation showed a wide and dispersed signal (Figure 1.1C). This may reflect a low stability of the fold, but the protein is well folded since, apart from showing a native CD spectrum, thermal unfolding followed by Trp-fluorescence is cooperative. It is known that proteins subjected to a structural stress can be in a metastable, native-like conformation. Thus, although changes in the overall spectrum cannot be seen, instability can drive to misfolding. This native conformation partially unfolds upon thermal denaturation driving to aggregation, but this is not likely to occur through a β-rich intermediate as the spectra at 85˚C is not that of a pure β-conformation (Figure 1.1B).

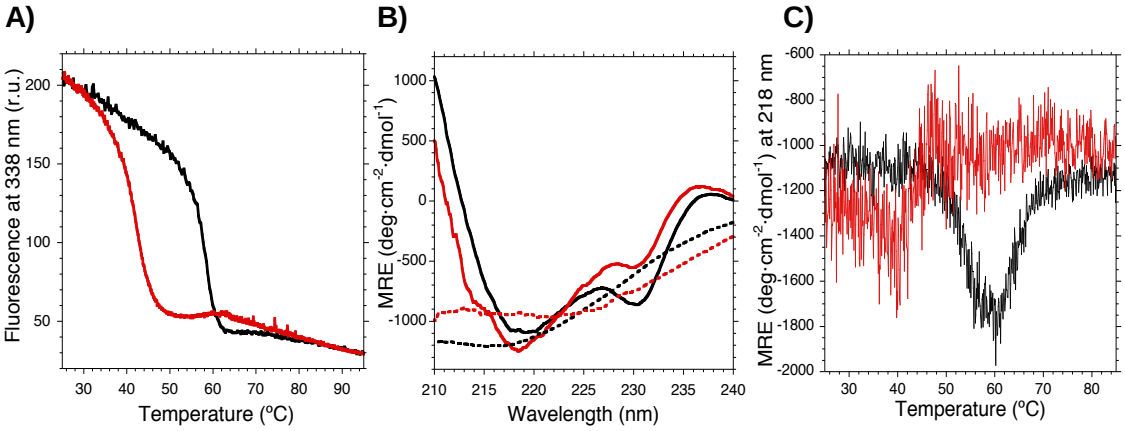

Figure 1.1. Thermal denaturation of V_L-DF followed by Trp-fluorescence and Circular Dichroism (CD). Black, scFv-h3D6, Red, V_L-DF. (A) Intensity of the fluorescence emission spectrum at 338 nm upon increasing temperature shows that the transition is advanced 15˚C for the mutant. (B) Far-UV CD spectra for the native states (25˚C) of scFv-h3D6 and V_L-DF mutant show differences in the V_L signature (230 nm), whereas for the thermal-denatured states (85˚C), scFv-h3D6 is in a β-conformation and V_L-DF mutant displays a singular spectrum (dotted lines). (C) Ellipticity signal at 218 nm upon increasing temperature shows that the mutant partially unfolds. Data for scFv-h3D6 are already published and are shown for comparative purposes [99], [102].

Because we know from previous work that elongation mutations mainly increase the stability of the V_L domain [102], we tried to combine these mutations with the V_L-DF mutation, but no stabilization could be achieved (not shown). This confirms the necessity of the disulphide bridge of the V_L domain to maintain a stable native fold and that the molecule does not endure the elimination of the disulphide bridge of the less stable domain. This may be also true for other class I scFv molecules [103,104].

Elimination of the V_H disulfide bridge

Since the intermediate state in the unfolding pathway of scFv-h3D6 is composed of the unfolded V_L domain and the folded V_H domain [102], we eliminated the disulphide bridge of the more stable domain, presuming that the loss of stability would not be as high as in the case of the less stable domain. For such a purpose, mutant V_H-C22V/C92A was generated. For the sake of clarity, this mutant will be henceforth referred to as V_H-DF (disulphide-free). In fact, the first consequence of these mutations was doubling the production yield, while ensuring conformational homogeneity without the presence of scrambled conformations as assessed by cationic exchange and thermal denaturation (not shown). Interestingly, these mutations not only affected the stability of the molecule, but also its folding and misfolding and, consequently, its ability to form WL fibrils, as the following subsections describe.

Changes in the unfolding pathway of V_H-DF

Concerning the unfolding pathway, a two-state model was enough to describe V_H-DF unfolding, instead of the more complex three-state one showed by scFv-h3D6 (Figure 1.2A) and its elongation mutants [102]. Thus, it seems that the intermediate state does not populate this pathway. This means that the lack of disulphide bridge in V_H domain affects its stability so that differences between both domains are not apparent. Despite this destabilization, the maximum of the Trp-fluorescence emission spectrum for the native state of V_H-DF was close to that of scFv-h3D6, indicating that mutant V_H-DF is well folded. There was, however, a red-shift of 1 nm in the native spectrum of the mutant, 339 nm *vs* 338 nm (Figure 1.2A). Such a small red-shift is likely to be due to experimental error, but could also be indicative of faint differences in the packing of Trp residues within the mutant. On the other hand, since in both profiles the final plateau reached the emission maximum considered for Trp-containing fully-unfolded proteins, 355 nm [139], the urea-denatured states were, in terms of tertiary structure, completely unfolded in both cases.

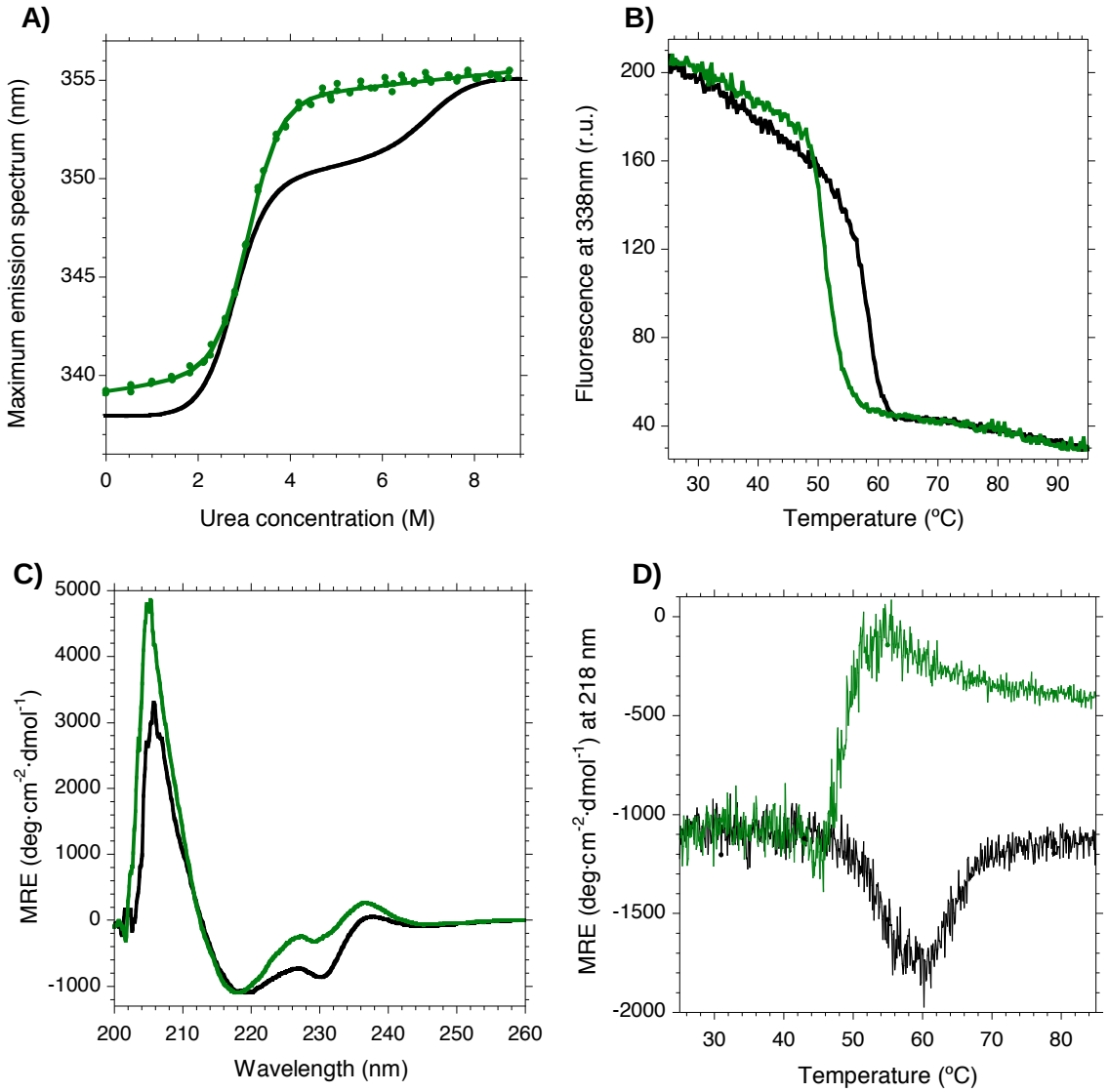

Figure 1.2. Changes in the unfolding pathway and the aggregation tendency of the V_H-DF mutant. Black, scFv-h3D6; Green, V_H-DF. (A) Urea denaturation curve fits to a two-state model for V_H-DF instead of the three-state for scFv-h3D6. (B) Thermal denaturation followed by Trp-fluorescence shows a decrease in the mid-point of about 6ºC upon mutation. (C) Circular dichroism shows that the native state of V_H-DF was slightly different to that of scFv-h3D6 in terms of secondary structure. (D) Thermal denaturation followed by CD indicates that V_H-DF unfolds before aggregation occurs, instead of directly reorganizing into a richer β-sheet conformation that drives to aggregation.

Opposite to the three-state behavior of scFv-h3D6, the urea-denaturation curve of V_H-DF does not show the two well-defined transitions (Figure 1.2A). In fact, the fitting of the urea-denaturation curve to the two-state model rendered a very nice convergence with a Gibbs energy for unfolding of 21.8 ± 0.8 kJ mol^{-1} and a cooperativity of 7.1 ± 0.2 kJ mol^{-1} M^{-1} (Table 1.1). Because there are different theories on the physical meaning and contribution of these values, differences seen in Table 1.1 should be just qualitatively considered. Since the first transition has been attained to the V_L domain and the second to V_H [102], it appears that the latter has been dramatically destabilized in the V_H-DF mutant, as it was foreseen. In any case, and despite this appreciable destabilization, the domain seems to keep its folded arrangement

according to the CD spectrum (Figure 1.2C; see next sub-section for further details). Thus, the native state spectrum is only different to the scFv-h3D6 in the minimum at 230 nm, which is featuring the V_L domain. In addition, the FTIR spectra show similar secondary structure distributions at 25˚C (see also next sub-section for further details). Perhaps, such a difference may indicate that elimination of the disulphide bridge of the V_H domain not only influences its intrinsic stability but also that of the neighboring domain, probably through perturbation of the interfacial forces between domains. This inter-domain cooperativity has been reported elsewhere studying other scFv molecules [140].

Table 1.1. Fitting of urea denaturation curves to the two-state model for protein folding of V_H-DF mutant and its elongation mutants. C1 (V_L-el-R108G), C2 (V_L-el-R108) and C3 (V_L-el-R108T109). ΔG in kJ mol^{-1}; *m* in kJ mol^{-1} M^{-1}. F = folded state; U= unfolded state; [D] between states = denaturant 50% in M.

Parameter / **Variant**	$\Delta G_{F\text{-}U}$	$m_{F\text{-}U}$	$[D]_{F\text{-}U}$
V_H-DF	-21.8 ± 0.8	7.1 ± 0.2	3.1
V_H-DF/C1	-21.5 ± 1.0	7.0 ± 0.3	3.1
V_H-DF/C2	-22.2 ± 0.8	7.1 ± 0.2	3.1
V_H-DF/C3	-23.0 ± 0.7	7.3 ± 0.2	3.2

Changes in the aggregation/misfolding pathway of V_H-DF

Thermal denaturation followed by Trp fluorescence showed that the conformational transition was advanced about 6˚C, despite it displays a single cooperative transition as scFv-h3D6 does (Figure 1.2B). To get insight into this transition circular dichroism was used. Figure 1.2C shows that the native state of V_H-DF was slightly different to that of scFv-h3D6. It is known that the scFv-h3D6 CD-spectrum is featured, apart from the 218 nm minimum and 205 nm maximum characteristic for an all-β fold, by a minimum at 230 nm and a positive shoulder at 237 nm [99]. In a previous study, the minimum at 230 nm was attributed to the contribution of the conserved Trp in the V_L domain, V_L-Trp 35, whereas the shoulder at 237 nm was attributed to the V_H domain without any information for discriminating between the possible contribution of its conserved Trp, V_H-Trp 36, and that of the cystinyl side-chain [114]. Because this shoulder was even increased in the V_H-DF mutant, it became evident that V_H-Trp 36 generates such interference. In consonance with the interpretation of the urea denaturation curve, the minimum at 230 nm featuring the V_L domain has been considerably decreased upon mutation, exhibiting that V_L-Trp 35 has also been reoriented upon eliminating the disulphide bridge within its neighboring domain.

The most salient feature comes from CD thermal unfolding curves. It was previously reported that thermal denaturation of scFv-h3D6, followed at 218 nm, the minimum characteristic for a β-fold, showed an increase in ellipticity starting at 45˚C and finishing at 60˚C; thus, a thermally-induced β-sheet rich intermediate state is maximally populated at 60˚C. This intermediate was also shown to lead to scFv-h3D6 aggregation as WL fibrils [99]. The behavior of V_H-DF emerges as "opposite" (Figure 1.2D), since the ellipticity decreases at mid-temperatures, indicating that the β-sheet rich intermediate does not populate. Surprisingly, the V_H-DF mutant aggregates at around 55˚C (Figure 1.2B).

To delve into these differences, additional thermal denaturation experiments were done using CD and FTIR as spectroscopic probes. We recorded a collection of CD spectra upon thermal unfolding (Figure 1.3A). In the case of scFv-h3D6, as the temperature increases the CD signals at 230 nm and 237 nm decrease, and the minimum at 218 nm corresponding to β-sheet increases. Up above 60˚C a transition to a prone-to-aggregation conformation is observed and aggregation could be appreciated from the signal dropping. Therefore, it is at 60˚C when the intermediary state is maximally populated. Opposite, in the V_H-DF mutant the intensity of the β-sheet minimum decreases from the beginning, so that a partial unfolding process occurs before the transition to a prone-to-aggregation conformation takes place. Therefore, we have clear evidence that the elimination of the disulfide of the V_H domain has changed the conformation of the intermediate state populating the aggregation pathway.

To gain structural insight of these intermediate states FTIR was used at the temperature at which they are maximally populated (60˚C for the scFv-h3D6, 55˚C for the V_H-DF mutant). One of the advantages of FTIR is its ability to differentiate among different β-sheet conformations because a shift to lower wavenumbers in the maximum of the amide I' spectrum can be interpreted as the result of increased hydrogen bonding within the β-strands, of a more planar sheet or of a larger number of strands [141]. Figure 1.3C shows that the spectra at 25˚C were quite similar for scFv-h3D6 and V_H-DF, with the maximum located at 1636 cm^{-1} for scFv-h3D6 and 1638 cm^{-1} for V_H-DF (both attributable to a native β-sheet main component), but the maximum in the spectra at 55-60˚C were located at 1630 cm^{-1} for scFv-h3D6 and 1624 cm^{-1} for V_H-DF. To delve in the differences of these spectra deconvolution was performed (Table 1.2). At 25˚C there are no differences but it becomes evident that at 55-60˚C the WL component is smaller for V_H-DF (5% versus 23%) and the amyloid component is rather bigger (24% versus 9%), as well as the random coil component (39% versus 14%). Therefore, it appears that the elimination of the disulphide bridge within the V_H domain shifts the aggregation pathway from the WL to the amyloid one through the formation of a partially unfolded intermediate.

Table 1.2. Band decomposition of FTIR amide I' band at different temperatures. [a] Data for the scFv-h3D6 are already published and are shown only for comparative purposes [99]. *These correspond to side-chains rather than to amyloid fibrils.

SECONDARY STRUCTURE	scFv-h3D6[a]				DF-V_H			
	25˚C		60˚C		25˚C		55˚C	
	Center (cm^{-1})	% Area	Center (cm^{-1})	% Area	Center (cm^{-1})	% Area	Center (cm^{-1})	% Area
↑ **Fr. antip. β-sheet**	1681	9	1683	4	1684	5	1683	6
↑ **Fr. loops/turns**	-	-	1671	11	-	-	1669	15
↓ **Fr. loops/turns**	1660	30	1662	6	1663	33	-	-
α-helix	-	-	1653	15	-	-	-	-
Random coil	-	-	1644	14	-	-	1648	39
↓ **Fr. antip. β-sheet**	1636	60	1636	16	1637	60	1633	12
WL fibril	-	-	1626	23	-	-	1627	5
Amyloid fibril	1612*	1	1615	9	1611*	2	1617	24

TEM analysis of scFv-h3D6 and V_H-DF samples incubated at 60˚C or 55˚C, respectively, confirmed the FTIR evidence, as seen in Figure 3E-F, where the WL fibrils formed by scFv-h3D6 (Figure 1.3E) and the amyloid fibrils formed by the V_H-DF mutant (Figure 1.3F) could be seen. Amyloid and WL fibrils populate different aggregation pathways: amyloid fibrils being straight and long, and forming through a nucleated-dependent kinetics; whereas WL fibrils being curved and short, and forming through a non-nucleation-dependent kinetics [99], [142].

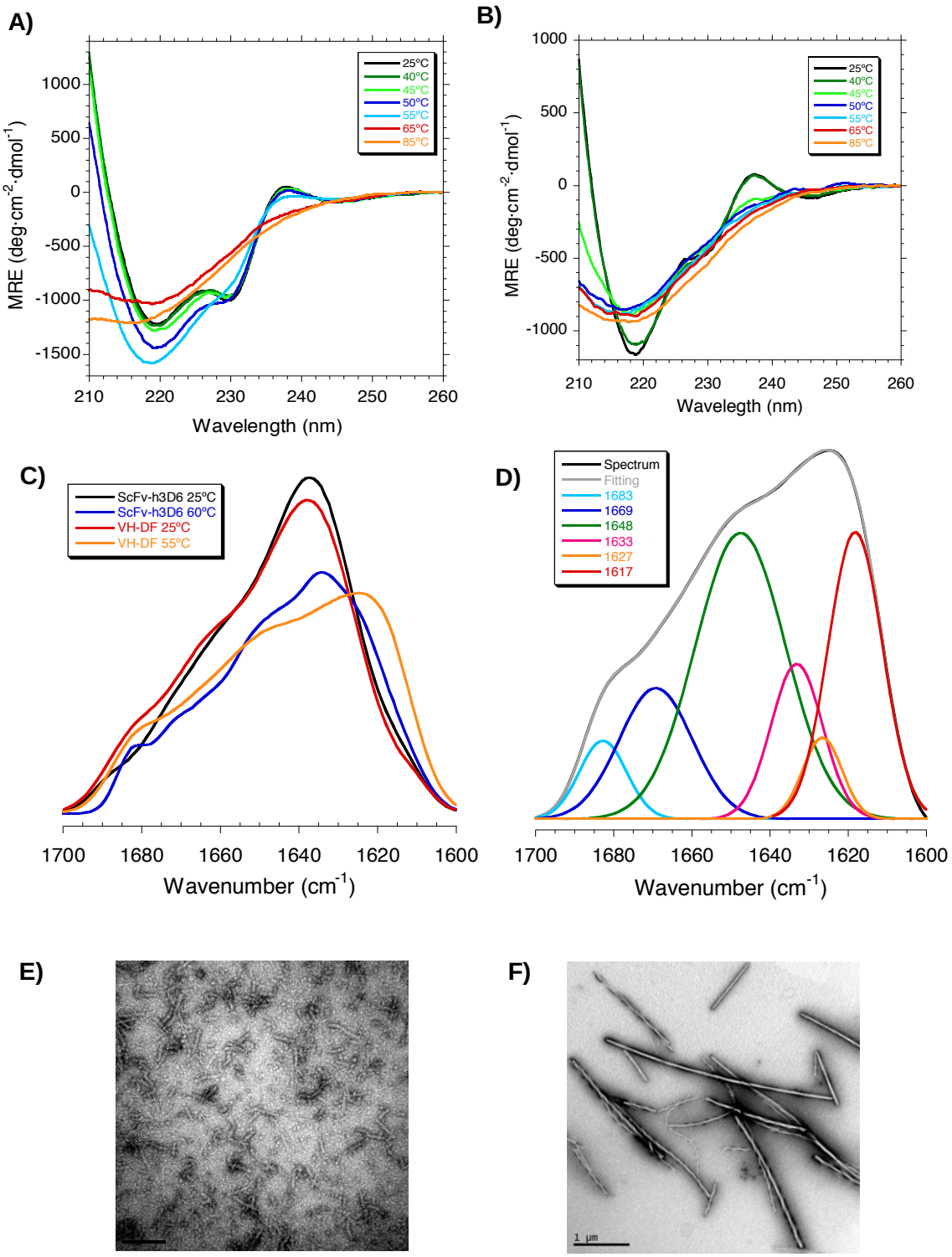

Figure 1.3. Changes in the aggregation pathway of V_H-DF. (A) CD at different temperatures of scFv-h3D6 indicates that a conformational transition occurs between 55 and 65˚C. (B) In the case of V_H-DF the conformational transition occurs from 45˚C and the intensity of the β-sheet minimum also decreases from the beginning, so that a partial unfolding process takes place before. (C) Amide I´ FTIR spectra at 25˚C shows no differences between scFv-h3D6 and V_H-DF but the shift to lower wavenumbers of the maximum of the spectra upon heating at around 60˚C is greater for V_H-DF. (D) Deconvolution of the V_H-DF spectrum reveals the presence of a prominent amyloid component at 1617 cm^{-1} at the temperature at which the intermediate state is maximally populated (55˚C) (see Table 1.2 for quantification). (E) TEM micrographs of scFv-h3D6 incubated at 60˚C for 5 min shows the presence of WL fibrils. (F) TEM micrographs of V_H-DF incubated at 55˚C for 5 min shows the presence of amyloid fibrils.

Combination of V_H-DF with elongation mutants

Combination of elongation mutations with V_H-DF rendered a good yield but no differences were found. Albeit these elongation mutations were reported to increase the stability of scFv-h3D6, this was not likely the case when combined with the V_H-DF mutant (Figure 1.4A). Table 1.1 shows that stability tend to slightly increase in the order C1, C2, C3, as described for the combination with scFv-h3D6, but these differences cannot be taken as reliable since they are within the experimental error.

Thermal denaturation followed by Trp-fluorescence was advanced 10˚C for all the combinations, instead of the 6˚C for the V_H-DF mutant (Figure 1.4B). This was also observed when following thermal denaturation by CD, where the unfolding before aggregation was even more evident (Figure 1.4D) and the initial spectra were more affected, both at the V_H and V_L CD signatures (Figure 1.4C). FTIR analysis confirmed the increase in the aggregation tendency to amyloid fibrils, as the maximum of the spectra is shifted to lower wavenumbers in the mutants (Figure 1.4E). Finally, TEM micrographs showed the formation of amyloid fibrils by such variants (Figure 1.4F).

Therefore, an increase in the aggregation tendency has occurred upon elongation of the V_H-DF mutant. This is indicative of the stabilization of the intermediate state in the amyloid aggregation pathway of V_H-DF rather than the stabilization of the native state, as was the case for the elongated scFv-h3D6 [102].

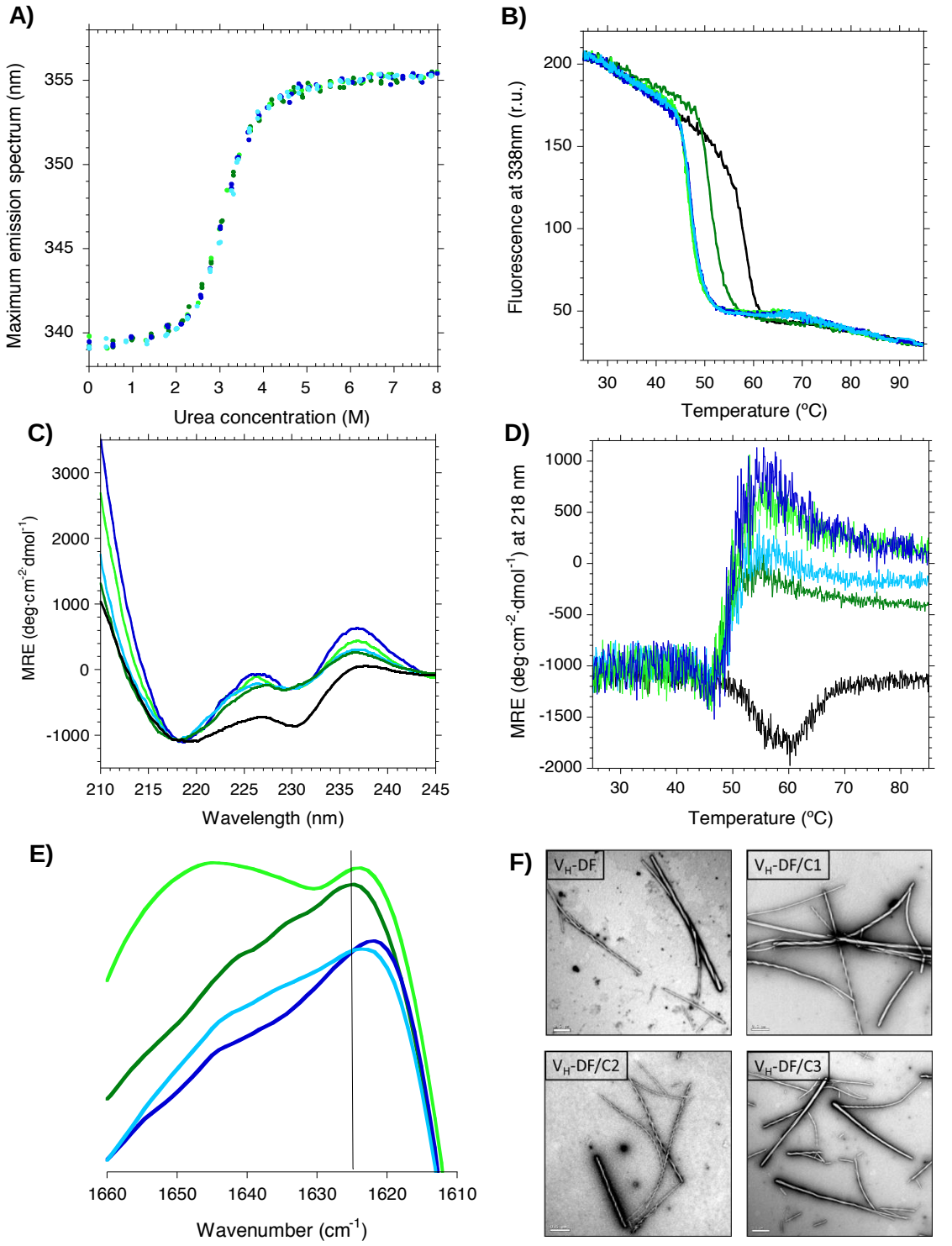

Figure 1.4. **Effect of elongation mutations on V_H-DF.** Black, scFv-h3D6; Dark green, V_H-DF; Light green, V_H-DF/C1; Dark blue, V_H-DF/C2; Light blue, V_H-DF/C3. (A) Urea denaturation curves show no differences with V_H-DF. (B) Thermal denaturation curves followed by Trp-fluorescence display a decrease in the mid-point of about 10˚C for all the combinations, instead of 6˚C for V_H-DF. (C) Circular dichroism shows that both the V_H and V_L signatures were more evident for the combined mutants. (D) Thermal denaturation followed by CD indicates that V_H-DF unfolds before aggregation occurs, instead of directly reorganizing into a richer β-sheet conformation that drives to aggregation as in the case of scFv-h3D6. (E) Amide I´ FTIR spectra at 55˚C shows that all elongation mutants on V_H-DF display a shift to lower wavenumbers of the maximum of the spectra, indicating that the aggregation tendency in the form of amyloid fibrils has increased. (F) TEM micrographs of V_H-DF and its elongation mutants incubated at 55˚C for 5 min show the presence of amyloid fibrils.

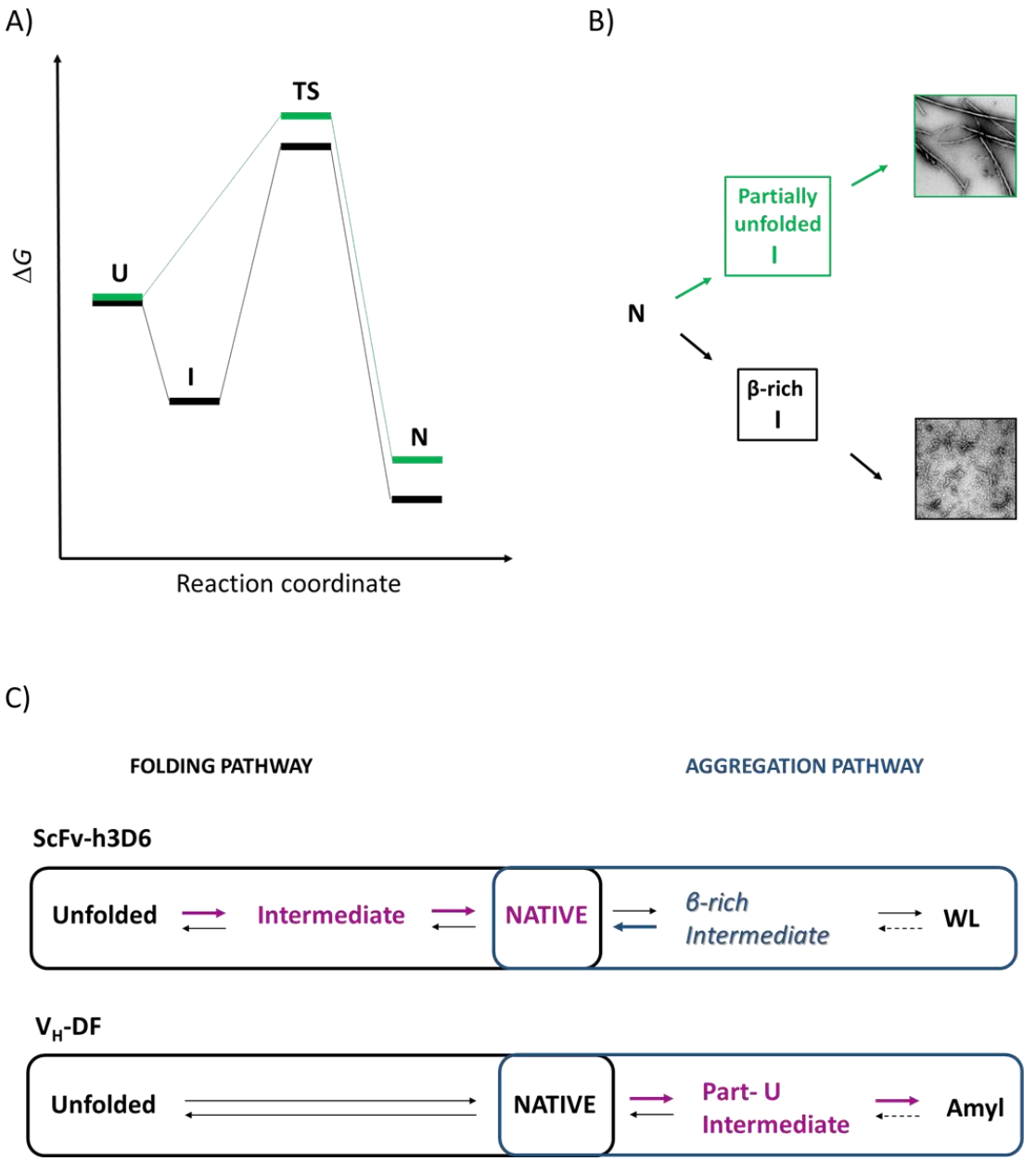

Figure 1.5. Diagrams for the folding and the aggregation pathways of scFv-h3D6 and V_H-DF. ScFv-h3D6, black, V_H-DF, grey, (A) Energy diagram for the folding reaction. ScFv-h3D6 follows a three-state folding reaction, whereas V_H-DF does not show any intermediate state. (B) Scheme of the aggregation pathway. ScFv-h3D6 aggregates as WL fibrils through the formation of a β-rich intermediate, whereas V_H-DF aggregates as amyloid fibrils through the formation of a partially unfolded intermediate. (C) Folding and aggregation pathways compete, such as at 25˚C the folding pathway is the predominant one whereas at 60˚C (scFv-h3D6) or 54˚C (V_H-DF) it is the aggregation pathway the one that predominates. The effect of the already described stabilizing mutations on scFv-h3D6 are indicated with bold arrows, the stabilized states in magenta, and the destabilized states in blue. These mutations stabilize the intermediate state in the folding pathway of scFv-h3D6 while destabilizing the β-rich intermediate driving to the formation of WL fibrils. In the case of V_H-DF stabilization of the partially unfolded intermediate driving to amyloid fibrils is the only effect observed.

DISCUSSION

ScFv-h3D6 is an antibody fragment that precludes Aβ peptide-induced toxicity by withdrawing Aβ oligomers from the amyloid pathway towards the WL pathway [99]. Because its therapeutic potential has been successfully assessed in the 3xTg-AD mouse model of Alzheimer's disease [100,101], it is worthy to improve the main drawback of its recombinant production. Here, we separately removed the disulphide bond of each domain and solved the scrambling problem, and then, we intended to compensate the loss of thermodynamic stability by adding three C-terminal elongation mutations previously described as stabilizing the native fold of scFv-h3D6.

ScFv-h3D6 does not endure the elimination of the disulphide bridge of the less stable domain, V_L. Apart from the compromised low-yield obtained, and although the CD spectrum was native-like, thermal denaturation showed an evident decrease in stability. It is generally accepted that proteins subjected to a structural stress, here removing the V_L disulphide bridge, can adopt a metastable conformation that do not change the overall structure but affects the stability and go to misfolding when subjected to environmental changes. Another consequence of removing this disulphide bridge was that aggregation did not occur through a β-rich intermediate state. This behavior indicates that the disulphide containing V_L domain is a structure involved in aggregation in the form of WL fibrils previously described for the scFv-h3D6. The involvement of structured domains in scFv aggregates was postulated by Plünckthun from the observation that the presence of a stable V_L domain in combination with a disulphide-free V_H domain was likely to promote aggregation [143]. On the other hand, introduction of the already known as elongation mutations, V_L-el-R108G (referred to as C1), V_L-el-R108 (C2) and V_L-el-R108T109 (C3), did not help to stabilize V_L-DF. It is calculated that the stabilizing contribution of the disulphide bridge in variable domains is around -19 kJ mol^{-1} [144] and we know that the most stable of the three introduced mutations, V_L-el-R108T109 (C3), stabilized the scFv-h3D6 fold in -5.1 kJ mol^{-1} [102], so that the combination of the elimination of the V_L disulphide bridge with the stabilized mutants was already expected to be challenging.

When removing the disulphide bond of the more stable V_H domain the fluorescence, CD and FTIR spectra were native-like and the yield was doubled because scrambling conformers were not present, so we achieved our main goal. Two main effects of removing V_H disulphide bridge were observed. Firstly, the folding behavior apparently changed from a three-state to a two-state (Figure 1.5A), so that the equilibrium intermediate was not detected. In addition, stability dropped much more than the calculated contribution of one disulphide bond in a variable domain, -19 kJ mol^{-1} [144]. The energy previously published for the folding of the scFv-h3D6 V_L

domain plus interface contribution is -19 kJ mol^{-1} and that for the folding of the V_H domain is -37 kJ mol^{-1}. Because a value of -22 kJ mol^{-1} is reported here as the energy required to fold the complete V_H-DF mutant, it can be concluded that the lack of a properly folded V_H domain also marginally affects V_L domain because the native interface is somehow affected. This concurs with the observation by CD of the hydrophobic environment of Trp-35 of V_L domain being different in the V_H-DF mutant. Mutual stabilization of V_L and V_H in scFvs is already known [140], and it reflects the relevance of the interface in the folding of these molecules. Therefore, we can conclude that destabilization of the V_H domain induced by the removal of its disulphide bridge has changed the folding behavior from a Class I scFv, with one domain much more stable than the sum of the other plus interface contribution, to a Class II, where the intrinsic stability of one domain is in the same range as the total stability of the other domain [103].

The second main effect of removing the V_H disulphide bridge was that the aggregation pathway changed from a WL morphology, through the formation of a β-rich intermediate, to an amyloid morphology, through the formation of a partially unfolded intermediate (Figure 1.5B), as demonstrated by CD, FTIR and TEM. Interestingly, the disulphide bridge in the V_L domain is also required for WL aggregation to occur. Therefore, it is likely that both disulphide bridges might stabilize the β-rich intermediate driving to aggregation in the form of WL fibrils. Folding and misfolding are competing pathways because kinetic partitioning occurs [145], similarly WL and amyloid pathways compete.

When adding the elongation mutations on V_H-DF the stabilization of the native fold failed, in contrast to what was already reported for scFv-h3D6 [102] (Figure 1.5C). These mutations stabilize the native fold by stabilizing the intermediate state in the folding pathway of scFv-h3D6, whereas on V_H-DF such an intermediate is not detected and no stabilization of the native state can be achieved. Stabilization of the folding intermediate favors the folding pathway at the expense of the aggregation one, as the β-rich intermediate driving to WL fibrils is destabilized. However, in the absence of the V_H disulphide bridge the partially unfolded intermediate driving to the formation of amyloid fibrils is the one that is stabilized.

As a general conclusion, the goals of getting rid of scrambling conformations and increasing the production yield have been achieved. The removal of the V_L disulphide bridge was not endured by the molecule, but the removal of the V_H disulphide bridge rendered a native-like conformation. Both the unfolding and the aggregation pathways have changed, and elongation of the C-terminus had not effect on the stability of the native state. Therefore, next step to further improve the molecule will be to explore evolutionary approaches on the V_H disulphide-free mutant [104].

CHAPTER 2:

Towards the improvement in stability of scFv-h3D6 as a way to enhance its therapeutic potential.

AIMS

Antibody-based therapeutics are only stable in a limited temperature range, so their beneficence *in vivo* depends on their capability for maintaining the proper fold in physiological conditions. The most stabilizing mutations for scFv molecules and other antibody fragments were found by molecular evolution methodologies in Plünckthun's lab [103,104,140,143,146]. These mutations are already introduced in most of the mAbs currently tested in clinical trials. ScFv-h3D6, therefore, contains them [147]. Among these stabilizing mutations, V_H-K66R is able to recover the stability of a disulphide-free scFv [146]. Similarly, here we have introduced the same mutation in another residue, V_H-K64R, intended to stabilize the βC''-βD loop within scFv-h3D6. Furthermore, we have combined this mutation with the elongation of the C-terminal domain (C3), i.e. the V_L domain, which was already proven to stabilize the scFv-h3D6 fold [102]. The relative stabilities and aggregation tendencies of the different scFv-h3D6 constructs were assessed from urea and thermal denaturation followed by Trp-fluorescence, Circular Dichroism (CD), and/or Differential Scanning Calorimetry (DSC). Transmission Electron Microscopy (TEM) was used to check if new variants maintained the worm-like aggregation pathway. Finally, cytotoxicity assays were performed to test the effectiveness of the mutants to recover cell viability of Aβ-treated neuroblastoma cell cultures.

MATERIAL AND METHODS

Mutagenesis, protein expression and purification. Mutagenesis was performed using a Quickchange Lightning Site-Directed Mutagenesis Kit (Agilent Technologies). Primers were designed to change residue V_H-K64 to R, and scFv-h3D6 and scFv-h3D6-C3 genes were used as templates. Protein expression was carried out using pET28a (+) vector and the *Escherichia coli* BL21 strain. Induction with 0.5 mM IPTG (isopropyl *β*-D-thiogalactopyranoside) was performed at D_{600} = 0.7 and incubation in the shaker at 20℃ for 18h. After three freeze–thaw cycles, the cellular pellet was sonicated for 5 min, at 70% duty cycle and output 9 (Sonifier 450, Branson). The protein was obtained by solubilizing the insoluble fraction in denaturing buffer (100 mM, Tris-HCl, 10 mM GSH, pH 8.5, and 8M urea) and refolding by dilution (1:10) in an ice-cold refolding buffer (100 Mm, Tris/HCl, 100 mM L-arginine, and 0.15mM GSSG, pH 8.5) for 48h. Then, a cationic exchange chromatography (Resource S6, GE Healthcare) was performed using 5 mM Na_2HPO_4, pH 6.5, buffer and a gradient until 15% of 5 mM Na_2HPO_4, 1M NaCl, pH 6.5. This chromatography was used to completely purify the protein and also fractionate the native state and the disulphide scrambled forms. Finally, because proteins purified from *E. coli* contain lipopolysaccharides that are toxic for cell cultures, these were removed from the protein by using Detoxi-Gel Endotoxin Removing columns (Thermo Scientific). The buffer was changed to PBS using PD-10 Desalting Columns (GE Healthcare), and protein aliquots were stored at −20ºC until further use.

Secondary structure determination by Circular Dichroism (CD). The protein secondary structure was monitored at different temperatures by far-UV CD spectroscopy from 260 nm to 190 nm in a Jasco J-715 spectrophotopolarimeter. The protein concentration was 20 µM, and 20 scans were recorded at 50 nm min^{-1} (response 2s) in a 0.2 cm pathlength cuvette.

Thermal denaturation. Thermal denaturation was followed up by far-UV CD spectroscopy in a Jasco J-715 spectrophotopolarimeter at 218 nm and tryptophan fluorescence emission in a Varian Cary Eclipse fluorimeter at 338 nm, both at 20 µM protein concentration and 1°C min^{-1} heating rate.

Chemical Denaturation. Chemical denaturation was performed by creating a series of progressive urea concentrations with a 2 µM final concentration of protein. Samples were allowed to denature for 12h at 4˚C. Measurement of Trp-fluorescence was performed at 25˚C at an excitation wavelength of 290 nm and an emission spectrum was recorded from 320 nm to 380 nm in a Varian Cary Eclipse fluorimeter. The excitation slit was set to 5 nm and the emission

slit at 10 nm; five scans were averaged. The maximum of each emission spectrum was obtained by fitting to a three-parametric polynomial, as described before [102]. The maximum of each spectrum, rather than intensity, was used because the changes in the intensity of the spectra can increase or decrease upon unfolding when more than one Trp residue is present, as is the case for scFv-h3D6, with five Trp residues.

Differential scanning calorimetry (DSC). DSC experiments were performed in a CAP-VP-DSC, as described previously [148]. The experiments were carried out in PBS buffer, with protein concentrations between 20-75 µM. All experiments were dynamically corrected. No appreciable effect of scan rate (in the range 0.5 and 2˚C min^{-1}) was observed on the DSC traces. Because of the total irreversibility of thermal unfolding, we subtracted the second DSC heating from the experimental traces in order to achieve a better description of the net heat capacity of the protein denaturation process in terms of excess heat capacity [149]. MicrocalOrigin software was used to treat the DSC traces.

Secondary structure determination by Fourier-transformed infrared spectroscopy (FTIR). FTIR analysis was performed as described previously [99]. Briefly, protein at 100 µM was dialyzed at 4°C against deuterated-PBS. Spectra were acquired at different temperatures ranging between25-60°C in a Variant Resolutions Pro spectrometer using excavated cells with a 50 µm path (Reflex Analytical) and the series software licensed under OMNIC (Thermo Scientific).

Aβ preparations. $A\beta_{1-42}$ synthetic lyophilized peptide (Bachem), was dissolved at 1 mM in HFIP (1,1,1,3,3,3-hexafluoro-2-isopropanol) (Sigma-Aldrich). Then, aliquots of 30 µL were prepared and HFIP was removed by drying in vacuum in a SpeedVac (Savant Instruments) and then stored at −20°C. When using the peptide, each aliquot was resuspended with 6 µL of DMSO (Sigma-Aldrich) and subsequently diluted to 150 µL (200 µM) with PBS (TEM analysis) or with phenol-red free DMEM (Gibco) (cell culture cytotoxicity assays).

Transmission Electron Microscopy (TEM). To visualize the aggregation extent at physiological conditions (used in the cell cultures, see below), incubation of scFv-h3D6 variants with Aβ (mixture at 100 µM each), was carried out at 37°C for 48h. Then, the samples were diluted 1:10 in PBS and quickly adsorbed on to glow-discharge carbon-coated grids. TEM was performed in a Jeol 120-kV JEM-1400 microscope, using 1% uranyl acetate for negative staining.

Cell culture and cytotoxicity assay. The SH-SY5Y human neuroblastoma cell line was grown in a serum-supplemented medium in 5% CO_2 at 37°C. DMEM/F-12 (1:1) +GlutaMAX™ (Gibco) was supplemented with 10% fetal bovine serum (Sigma), 1% MEM non-essential amino acids (Gibco)

and a 1% mix of antibiotics: penicillin, streptomycin and anti-fungal amphotericin (Gibco). 10,000 cells/well were plated in 96-well plates (Life Technologies) and incubated for 24h to allow cell attachment. The same day, Aβ was resuspended and incubated for 24h at 4˚C before addition to the cell cultures, as previously described to obtain Aβ oligomers [150], which are considered to be the crucial toxic species [26,27]. The next day, the medium was changed and the cells were treated with Aβ oligomers (10μM) and/or scFv-h3D6 mutants (0, 2.5, 5, 7.5 and 10 μM) for 48h at 37˚C. Because of the method of preparation of the Aβ peptide, 2% (v/v) DMSO remained in the initial solution (0.2% in the well); all samples, including controls, contained the same percentage of DMSO during incubation, as well as the same medium and buffer composition. Viability assay, EZ4U (Biomedica), was performed following the manufacturer's instructions. Each condition consisted of five replicas per experiment, and three independent experiments were performed. Data are presented as the percentage of viability for each condition, compared to untreated cells. Differences were statistically analyzed for significance, comparing viability results for each mutant and concentration with cells treated only with Aβ, when looking at viability recovery in the presence of scFv-h3D6 variants (Mann-Whitney test, Graphpad 6). The Kruskal-Wallis test (Graphpad 6) was also performed for each concentration to establish statistically significant differences among treatments.

RESULTS AND DISCUSSION

Redesign of V_H domain stability

A careful examination of the three-dimensional model for the structure of scFv-h3D6 (Figure 2.1A) showed that the amine group of V_H-K64 (Kabat numbering, [151]) interacts with the carboxyl group of V_H-D61 (Figure 2.1B). A similar interaction was previously described with V_H-K66, where the mutation to Arg increased stability by potentiating the interaction with V_H-D86 [146]. Residue K66 is part of a highly-conserved charge cluster within the V_H domain where it interacts with D86, both residues belonging to the FR3 (Framework Region) [146]. However, interacting residues K64 and D61 are located in the CDR2 (Complementary Determining Region). Thus, K66 potentiates a charge cluster in a conserved region, whereas K64 is involved in the stabilization of the βC''-βD loop within the specific CDR2 of scFv-h3D6. Similarly to the already-present mutation V_H-K66R, we decided to perform mutation V_H-K64R with the aim of obtaining an additional reinforcement of the stability of the antibody fragment.

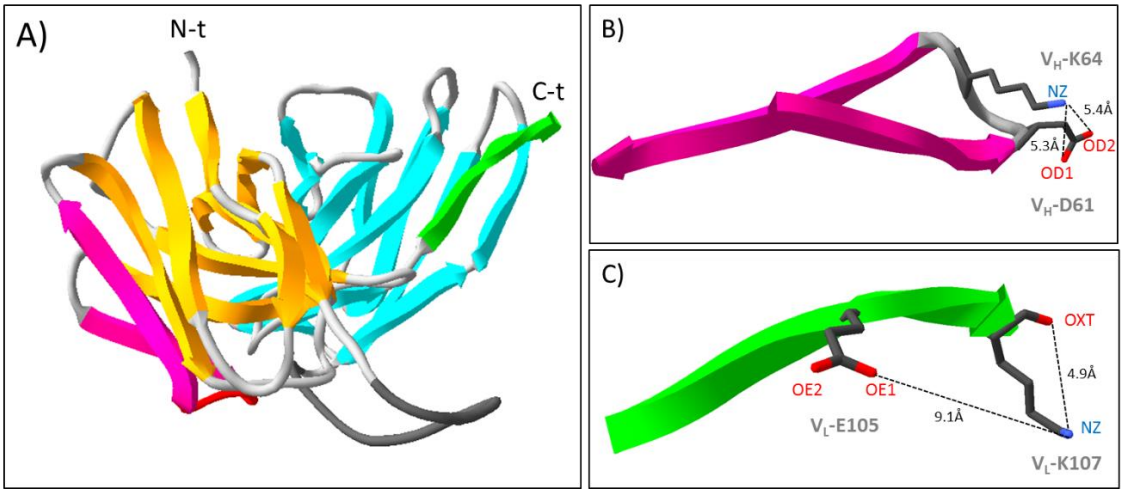

Figure 2.1. ScFv-h3D6 three-dimensional model and detail of the mutated sites. (A) ScFv-h3D6 model. Red, βC''-βD loop; Magenta, β-stands flanking the βC''-βD loop; Orange, the rest of the V_H domain; Blue, V_L domain with the exception of the last β-stand; Green, last β-stand; Grey, linker ($(G_4S)_3$). (B) Main interactions of V_H-K64 side-chain within the βC''-βD loop. The NZ group of K64 is at 5.3Å of the OD1 group of D61, and at 5.4Å of the OD2 one. Mutation V_H-K64R should potentiate this electrostatic interaction (C) C-terminus of scFv-h3D6 showing the detrimental interaction between V_L-K107-NZ group and the C-terminal oxygen (OXT), which are only 4.9Å apart. As a consequence, the last β-strand of scFv-h3D6 is destabilized because V_L-K107 and V_L-E105 cannot properly interact, as shown by the long distance (9.1Å) between V_L-K107-NZ and V_L-E105-EO1 groups. C3 mutant solves this problem by locating the OXT group apart, since it is two residues elongated (R108 and T109) [102].

In addition, we decided to combine the V_H-K64R mutation with the previously described C3 mutation [102]. In short, the C-terminal end of scFv-h3D6, which corresponds to V_L-K107, still belongs to the last β-strand of the fold (Figure 2.1C). Therefore, the side-chains of V_L-K107 and V_L-E105 should establish an electrostatic interaction, which cannot be performed properly since

the distance between the amine group of V_L-K107 and the carboxyl group of V_L-E105 is too long. This is a consequence of the attraction of the amine group of V_L-K107 to the C-terminal oxygen (OXT). Mutant C3 is elongated by two additional residues, R108 and T109, so that OXT is placed apart from the V_L-K107 side-chain.

Effect of V_H-K64R mutation in the stability, folding and aggregation of scFv-h3D6.

Our previous work with scFv-h3D6 and some elongation mutations described a three-state behavior for the urea unfolding curves [102,140]. As shown in Figure 2.2A, the V_H-K64R mutation kept the three-state scheme. Table 2.1 shows the results of the fitting of the urea denaturation curve to the three-state model. In the first transition, the unfolding of the V_L domain, stability has slightly increased ($\Delta\Delta G^\circ$= 1.5 kJ mol^{-1}), whereas cooperativity has remained more or less the same. The second transition, corresponding to the unfolding of the V_H domain where the mutation is localized, shows that stability has apparently increased ($\Delta\Delta G^\circ$= 1.9 kJ mol^{-1}), whereas cooperativity has also remained approximately the same. However, the difference between the maxima of the spectra for the intermediate and the unfolded states is only 4 nm, perhaps too low to make such small differences reliable.

Interestingly, the V_H-K64R mutation also affects the V_L domain, as seen by the urea denaturation curves, where the intrinsic stability of one domain affects the other. This effect is also seen by CD, since the intensity of the V_L signature at 230 nm is similar to that at 218 nm; whereas, when the mutation is not present, such a signature is less intense (Figure 2.2C). Mutual stabilization between domains in scFvs has already been described [140], and it is likely to be a common phenomenon in these chimeras.

Because, among the three C-terminal-elongation mutations previously described, C3 (V_L-el-R108T109) was the most stable [102], we combined this elongation mutant with V_H-K64R. Stability of the V_L domain has increased 3.5 kJ mol^{-1} with respect to scFv-h3D6. This increase is smaller than the 5.1 kJ mol^{-1} already reported for the elongation mutation C3 alone (Figure 2.2A and Table 2.1). Therefore, there is no additivity when combining V_H-K64R with the elongation mutations, but rather a negative effect that makes both mutations partially cancel each other.

Concerning thermal denaturation, driving to the formation of WL fibrils by scFv-h3D6 [99] and elongation mutants [102], it is known that mutation C3 rendered a denaturation curve with a mid-point temperature about 4˚C higher than that of scFv-h3D6 (Figure 2.2B), as followed by Trp-fluorescence. However, when the V_H-K64R mutation was introduced, alone or in combination with C3, such a thermostabilization was not observed and the transition became more complex

beyond 60˚C (Figure 2.2B). When following thermal denaturation by CD (Figure 2.2D), scFv-h3D6 showed a transition at 60˚C and the mutants at around 62-63˚C. This thermal denaturation drove towards the formation of WL fibrils by scFv-h3D6 [99] and its elongation mutants [102] and this transition was attributed to the triggering of aggregation. Similarly, it is likely that V_H-K64R mutation would decrease the aggregation tendency in the same way as that observed for the C3 mutation.

Table 2.1. **Fitting to the three-state model of equilibrium denaturation curves of scFv-h3D6 and its variants**. ΔG in KJ mol^{-1}; *m* in KJ mol^{-1} M^{-1}. N = native state; I = intermediate state; U= unfolded state; [D] between states = denaturant 50% in M. [a] These data have already been published and are shown for comparative purposes [102].

	FIRST TRANSITION			SECOND TRANSITION		
PARAMETER / **VARIANT**	ΔG_{I-N}	m_{I-N}	$[D]_{I-N}$	ΔG_{U-I}	m_{U-I}	$[D]_{U-I}$
ScFv-h3D6[a]	19.3 ± 0.7	7.0 ± 0.3	2.76	36.9 ± 5.7	5.2 ± 0.8	7.10
V_H-K64R	20.8 ± 0.9	7.2 ± 0.3	2.88	38.8± 7.4	5.3 ± 1.1	7.32
C3[a]	24.4 ± 0.5	7.7 ± 0.2	3.17	38.6 ± 3.9	5.3 ± 0.6	7.28
K64R/C3	22.7± 0.9	7.1 ± 0.3	3.20	34.0 ± 8.0	4.8± 1.2	7.08

DSC analysis of the contribution of mutations V_H-K64R and C3 to the thermal stability of scFv-h3D6.

As we previously found with spectroscopic probes, the thermal denaturation of all scFv-h3D6 constructs was totally irreversible. However, we decided to analyze the DSC experiments since no noticeable scan rate effects were found on the shapes of the traces. The differences found among the mutants can therefore be reliably interpreted [152].

Figure 2.2E shows the DSC traces, using as the experimental conditions the PBS buffer and 0.5-2 mg mL^{-1} (20-75 μM) protein concentration, of the four scFv-h3D6 variants represented as excess heat capacity. Two well-defined heat transitions can be distinguished, mainly in the cases where the C3 elongation is absent. The existence of two transitions indicates that at least one intermediate state populates upon denaturation. Nevertheless, previous proteolysis experiments showed that this intermediate is conformationally different to the one observed from urea denaturation [102]. Thus, in the urea denaturation, the V_H domain is roughly maintained, whereas partial unfolding of both V_L and V_H occurs in the thermal denaturation [102]. In any case,

the similar aspect of CD thermal transitions (Figure 2.2D) indicates that the heat-induced intermediate is conformationally similar in all scFv-h3D6 species studied here. In Figure 2.2C only the spectrum at 60˚C for scFv-h3D6 is shown, corresponding to a typical β-sheet, because the spectra for the other three variants perfectly overlapped.

These experiments demonstrate that the incorporation of mutation V_H-K64R does not generate a great change on the unfolding behavior of scFv-h3D6. However, a net increase of the maximum temperature of both heat transitions has been achieved in the mutants with respect to scFv-h3D6. Furthermore, when the C3 elongation is included, an increase in global cooperativity becomes evident and the two transitions are not so well separated. When considering these observations together with the urea experiments, we may hypothesize that the two transitions correspond to the denaturation of each single domain. Therefore, as the mutation V_H-K64R mainly affects the second transition and stabilizes the V_H domain, the V_L-C3 elongation seems to move the first transition to higher temperatures, thus stabilizing the V_L domain.

Despite the irreversible character of the thermal unfolding, from these DSC experiments the enthalpy change upon denaturation can be evaluated as the area under the heat capacity curve. Thus, scFv-h3D6 denaturation gives a value of 260 kJ mol^{-1}. To the best of our knowledge, this is the first time that DSC has been performed with isolated scFv constructs, so we cannot compare this value with others. There exists only one previous study in which DSC was carried out using a covalently linked pair of scFv molecules to emulate a Fab fragment, but the thermodynamic parameters were not evaluated [153]. Therefore, our results cannot be directly compared, although if we look at the values obtained for small protein domains, such as the 7-kDa SH3 [154], 260 kJ mol^{-1} is a very low enthalpy change for the denaturation of a protein of this size (26 kDa). The reason for such a difference may be that the thermal denaturation of scFv-h3D6 does not lead to an unfolded, or even partially unfolded, state [99,102]. Thermal denaturation followed by CD showed that the ellipticity at 218 nm, characteristic of a β-sheet conformation, is maintained until 50˚C and then suddenly increases until 60˚C, where the intermediate state is maximally populated (Figure 2.2D). From Figure 2.2C it is also evident that the denatured state reached at above 60ºC cannot be considered as fully unfolded but rather folded in a β-sheet conformation. Therefore, the observation of residual structure in the thermally-induced intermediate is complemented by the calorimetric experiments. The theoretical heat capacity functions of the native and unfolded states can be reliably estimated from the molecular weight and amino acid composition, respectively [155,156]. In the case of scFv-h3D6, the theoretical heat capacity function of the unfolded state has lower values than the experimental post-transition heat capacity shown in Figure 2.2F, indicating that a residual structure remains.

The incorporation of V_H-K64R mutation does not seem to produce any appreciable enthalpic effect, perhaps a small increase among errors. However, the C3 incorporation gives rise to an enthalpic increase of 100 kJ mol^{-1}, which constitutes almost one third of the total heat exchanged. Interestingly, enthalpic effects are not additive, since the combination of both mutations in the protein increases only 30 kJ mol^{-1} with respect to scFv-h3D6, a much lower increase than incorporating both separately.

The comparison between DSC and the spectroscopic experiments is quite difficult due to the kinetic character of the calorimetric traces and the experimental errors, together with the fact that the mid-point temperatures are not sufficiently different. Whatever the case, the spectroscopic experiments also show that thermal denaturation cannot be described by a simple two-state scenario characterized by typical S-shaped transitions (Figure 2.2 B,D).

In order to estimate the relative stabilities of our different constructs with our DSC experiments, we can assume that Tm values are roughly similar. Also, based on the evaluation from the difference between the heat capacities of the native and denatured states (Figure 2.2E), the unfolding heat capacity change of all the traces is approximately the same. Consequently, we can establish that the enthalpy values might correlate with the relative stabilities of the different scFv-h3D6 constructs, with the order C3 > K64R/C3 > V_H-K64R ≥ scFv-h3D6.

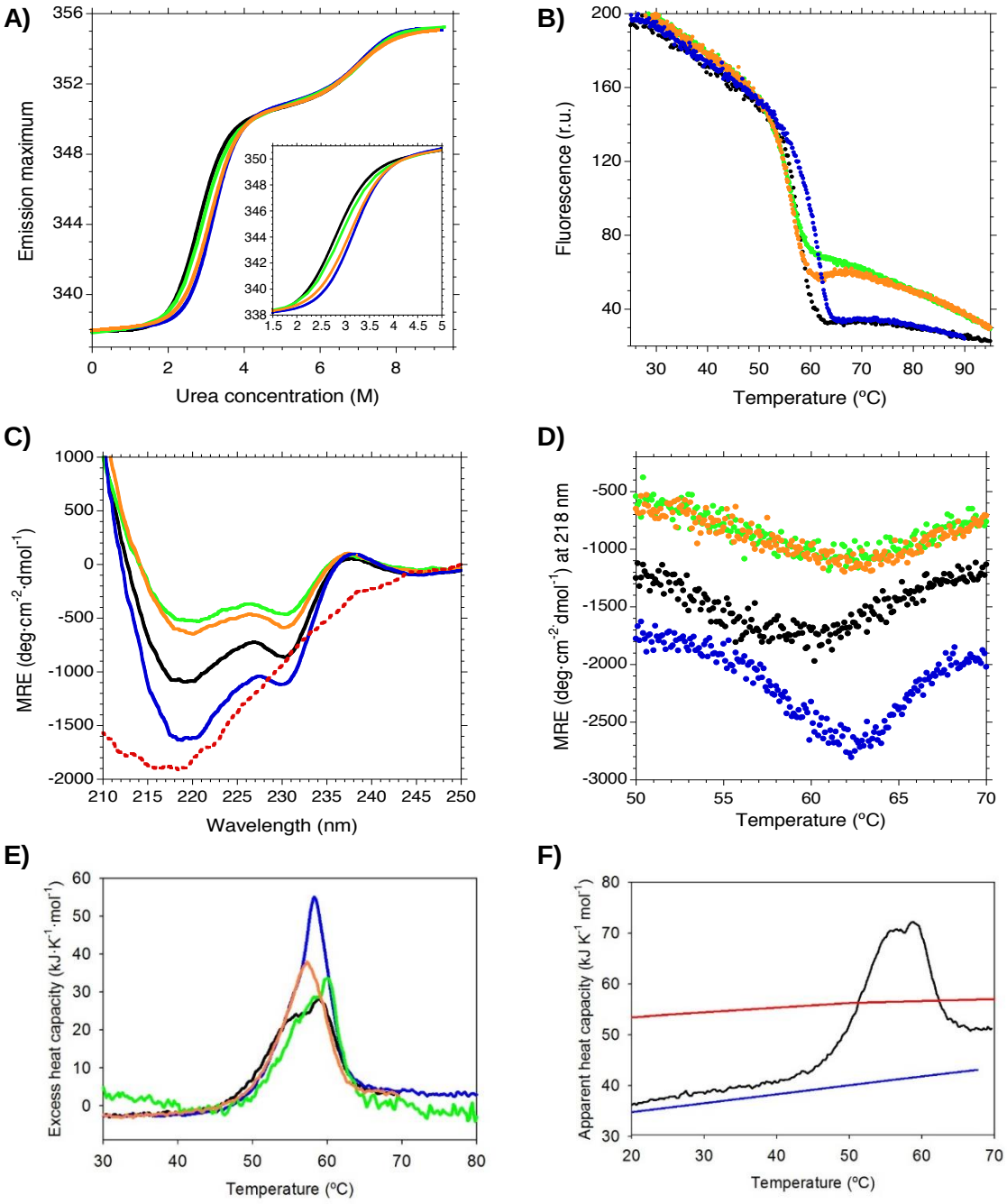

Figure 2.2. Conformational study of the effects of K64R mutation alone or in combination with the V_L elongation (C3). (A) Urea denaturation curve for ScFv-h3D6 (Black), V_H-K64R (Green), K64R/C3 (Orange) and C3 (Blue). The inset shows an enlargement of the first transition. (B) Thermal denaturation curve by following the intensity of the fluorescence at 338 nm. (C) Far-UV CD spectra for the native states (25˚C, continuous line; same result at 37˚C, not shown) and thermally-induced intermediate state (60˚C, dashed line; only one representative spectrum is shown because all the variants showed overlapped spectra). (D) Thermal denaturation by following the ellipticity signal at 218 nm. Denaturation in the transition region (50-70˚C) is shown. In C-D, spectra have been translocated by applying a factor to allow comparison (V_H-K64R and K64R/C3, x0.5; C3, x1.5). (E) The excess heat capacity profiles for the four scFv variants obtained from DSC experiments. (F) The apparent heat capacity of scFv-h3D6 (Black line). The blue line represents the apparent heat capacity of the native state estimated from molecular weight [155,156] whereas the red one the respective for the unfolded state estimated from the additive contribution of amino acids.

Analysis of the aggregation pathway of scFv-h3D6 variants and therapeutic effects.

FTIR shows that the amide I' spectra at 60˚C for all the mutants is slightly shifted to higher frequencies with respect to that for scFv-h3D6 (Figure 2.3A). Since a shift to lower frequencies is expected when aggregation occurs [141], it can be concluded that mutations decrease the aggregation tendency. However, when thermally-denatured mutants are analyzed by TEM (same samples as in Figure 2.3A) they maintain the characteristic WL morphology (not shown). In addition, they also render this morphology when incubated with the Aβ peptide at 37˚C for 48h (Figure 2.3B). As previously mentioned, it is the ability of the scFv-h3D6 to aggregate in a WL pathway that enables it to withdraw Aβ oligomers in a protective manner. This aggregation does not occur when incubating scFv-h3D6 alone at 25 or 37˚C, being the presence of the intermediate state populating the aggregation pathway at 60˚C required to adopt this morphology. However, when scFv-h36 and Aβ are placed together, the scFv-h3D6/Aβ complex immediately forms and adopts the WL morphology without the necessity for heat treatment [99]. The fact that all the mutants follow the same aggregation pathway as scFv-h3D6, indicates that they should also display therapeutic properties.

To corroborate this, we performed cytotoxicity assays in the human neuroblastoma SH-SY5Y cell line in the presence of Aβ peptide and/or sFcv-h3D6 mutants (Figure 2.3C). Cells were exposed to Aβ oligomers (10 μM), which are considered the crucial toxic species in the development of AD [26,27], and different concentrations (0, 2.5, 5, 7.5 and 10 μM) of scFv-h3D6, V_H-K64R, K64R/C3 and C3 in order to determine differences among the mutants. Treatments were incubated with cell cultures for 48h at 37˚C before viability assays were performed. Data are presented as the percentage of viability for each condition, compared to the untreated cells. A Mann-Whitney statistical analysis was performed comparing Aβ alone with each mutant concentration to determine significance in cell viability recovery in the presence of scFv-h3D6, V_H-K64R, K64R/C3 or C3 (*P<0.05, **P<0.01, ***P<0.001) (Figure 2.3C).

Treatment with Aβ alone reduces viability to approximately 60%, showing the toxic properties of Aβ oligomers; the presence of scFv-h3D6 variants increases this percentage, but differently, depending on the mutant. Both C3 and K64R/C3 show 100% viability at 10 μM (equimolar ratio with Aβ), but with C3 being more efficient at lower concentrations (i.e. at 5 μM: C3 87.1%±2.6 and K64R/C3 77.1%±0.7). In the cases of scFv-h3D6 and V_H-K64R, at 10 μM they show a viability percentage around 90%, but V_H-K64R is better at lower concentrations (i.e. at 5 μM: V_H-K64R 77.8%±2.9 and scFv-h3D6 68.5%±3.6). The Kruskal-Wallis test was also performed to establish differences among treatments; all concentrations, except for 2.5 μM, showed statistical

significance. The Kruskal-Wallis statistic values, which are considered to indicate significance when are higher than 7.0, are: 7.4 (for 2.5 μM), 12.8 (for 5 μM), 11.3 (for 7.5 μM) and 12.9 (for 10 μM).

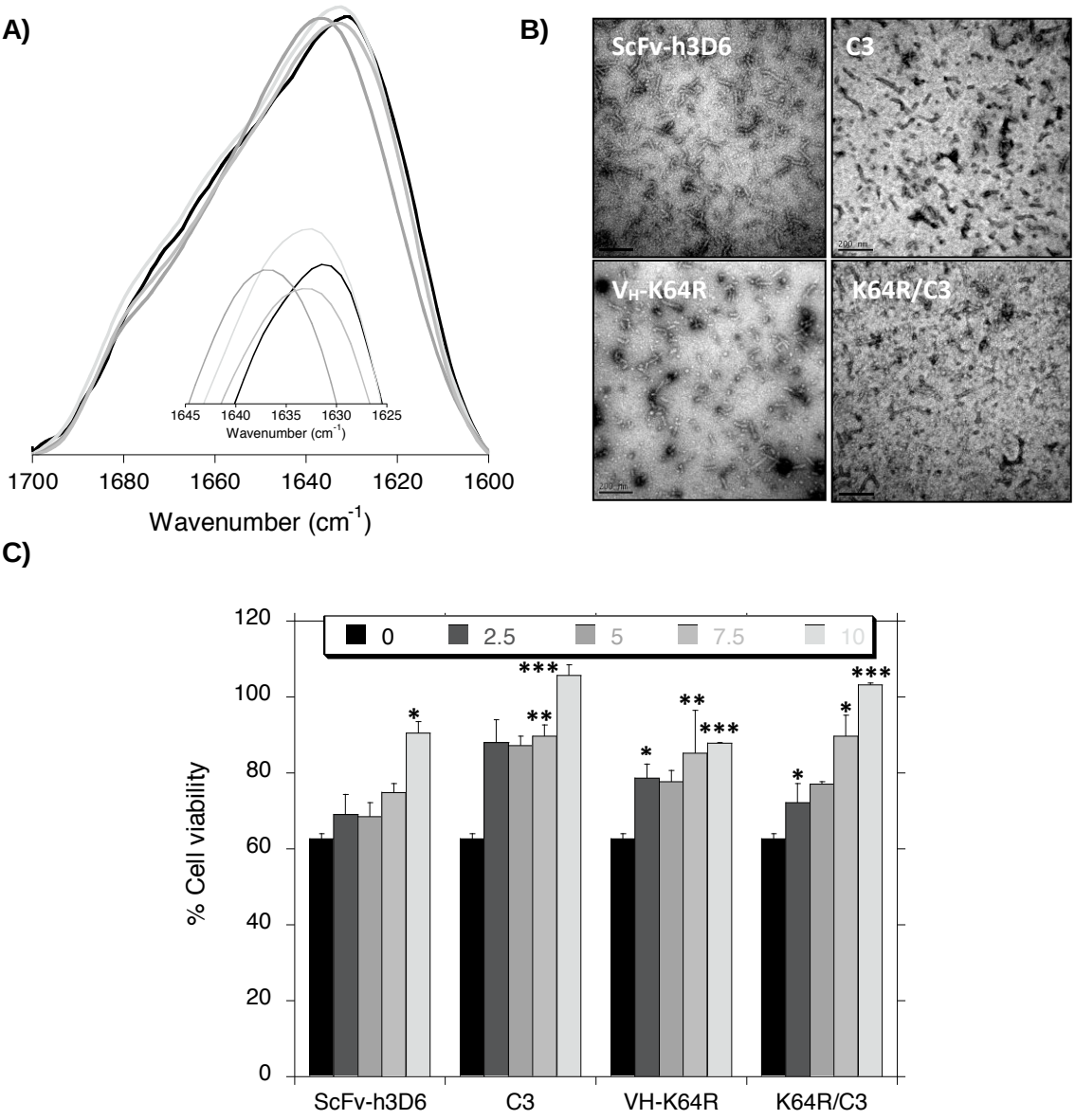

Figure 2.3. Analysis of the aggregation pathway. (A) FTIR amide I' spectra at 60˚C is slightly shifted to higher frequencies for the mutants than for scFv-h3D6, which concurs with a faint decrease in the aggregation tendency. The inset shows an enlargement of the maxima of the spectra. Black, scFv-h3D6; Dark grey, V_H-K64R; Mild grey, K64R/C3; Light grey, C3. (B) TEM analysis show that the mutants containing K64R and C3 aggregate in the form of WL fibrils, as it was previously reported for scFv-h3D6 [102]. It is the ability of the scFv-h3D6 to aggregate in a worm-like pathway what enables it to withdraw Aβ oligomers in a protective manner. The fact that all the mutants follow the same aggregation pathway as scFv-h3D6 indicates that they should also display therapeutic properties. (C) Cytotoxicity assay in SH-SY5Y cell-cultures in the presence of 10 μM Aβ peptide and increasing concentrations of scFv-h3D6 and its mutants (0, 2.5, 5, 7.5 and 10 μM). Y axis shows the % of viable cells compared to untreated ones. Results from a minimum of three individual cultures are presented as means with standard error. Mann-Whitney test was performed. **P*<0.05, ***P*<0.01, ****P*<0.001.

These results indicate that there is a correlation between the stability properties described by the biophysical analysis and the ability of the mutants to prevent Aβ cytotoxicity in cell culture. Putting all the results together, we could list the mutants in terms of stability and therapeutic potential as follows: C3 > K64R/C3 > V_H-K64R ≥ scFv-h3D6.

CONCLUSIONS

Stabilization of the V_H βC''-βD loop by mutating V_H-K64R increased stability and decreased aggregation tendency. However, its introduction into the elongation mutant V_L-el-R108T109 (C3) was not additive; instead, both mutations partially canceled their effects. Finally, the differences in stability of scFV-h3D6 and the three mutants assayed correlated with their efficiency to recover cell viability in Aβ-treated neuroblastoma cell cultures. Therefore, these improved variants are of high therapeutic interest and, consequently, worth to testing *in vivo.*

CHAPTER 3:

A simple *Pichia pastoris* production of scFv-h3D6 and *in vitro* and *in vivo* validation of its therapeutic effect.

AIMS

Although the scFv format is aglycosylated and suitable for expression in *Escherichia coli* [157], disulphide scrambling is favored in the reducing bacterial cytoplasm and proteins expressed in the insoluble fraction require a refolding process that can also generate disulphide scrambled conformations. In addition, proteins produced in *E. coli* are contaminated with endotoxins traces that, especially in the case of proteins with medical applications, must be removed. To overcome these hurdles, as well as to improve the expression and purification yield, the yeast *Pichia pastoris*, an endotoxin-free host system, has been selected to produce the scFv-h3D6.

Apart from changing the expression system of the scFv-h3D6*,* an easy and efficient purification system, easy to scale-up in a bioreactor for manufacturing purposes, has been developed. To discern which are the properties of the novel protein in comparison with that from *E. coli*, thermal stability by biophysical techniques and therapeutic effects in the neuroblastoma cell line SH-SY5Y and in the 3xTg-AD mouse model have been determined.

MATERIALS AND METHODS

Cloning. *ScFv-h3D6* gene was inserted in the pPicZαA vector (Invitrogen) in restriction sites *EcoRI* and *NotI* (New England Biolabs). To do so, an *EcoRI* target site had to be generated by PCR upstream of the *scFv-h3D6* gene (Oligonucleotides were purchased at Invitrogen). Single nucleotide mutations were performed using Quickchange Lightning Site-Directed Mutagenesis kit (Agilent Technologies). Ligation and PCR products were transformed into XL1Blue *E.coli* strain and grown on low-salt LB-Zeocine (Ibian Technologies) (vector resistance) agar plates. After extraction and purification of the plasmid, it was linearized by *PmeI* (New England Biolabs) restriction before transformation into *P. pastoris*.

P. pastoris *transformation and selection.* The linearized DNA was transformed into competent *P. pastoris* KM71H cells by electroporation using *Electro Cell Manipulator Precision Plus* (BTX ECM 630). Transformant cells were grown on YPDS-Zeocine agar plates and screened for their ability to grow in increasing concentrations of Zeocine up to 10 mg/mL.

Protein expression in **P. pastoris.** For protein expression tests, transformed *P. pastoris* cells with high resistance to Zeocine were grown in shake flasks containing 100 mL of buffered glycerol complex medium (BMGY, 1% yeast extract, 2% peptone, 100 mM potassium phosphate buffer at pH 6.0, 13.4 g/L YNB, $4x10^{-4}$ g/L biotin, 10 g/L glycerol and 100 µg/mL Zeocine) at 30˚C and 250 rpm until an OD_{600} of 2-6 was reached. Then, the cell culture was centrifuged (3,000xg, 5 min, room temperature (RT)) and resuspended in 20 mL of BMMY (methanol instead of glycerol in BMGY). The medium was supplemented with methanol at a final concentration of 0.5% (v/v) every 24h. Expression was followed for five days. In the case of larger volumes of expression, 10 mL of BMGY were inoculated with transformed KM71H cells. After 16-18h of growing at 30˚C and 250 rpm, these 10 mL were transferred to 1L of BMGY. When the OD_{600} reached 2-6, the cell culture was centrifuged (3,000xg, 5 min, RT) and resuspended in 200 mL of BMMY. Methanol was supplemented every 24h and expression was carried out for 48h.

Large-scale production in **P. pastoris.** Fermentation was carried out at Bioingenium SL facilities. Fresh colonies were picked from YPD-Zeocine plates and grown overnight in 300 mL of BMGY medium. A 100-mL culture was transferred to a bioreactor (Applikon biobundle 5L, Applikon biotechnology), with 3L of fermentation basal salts medium supplemented with PTM_1Trace Salts. The bioreactor conditions were optimized by modification of [158]. The temperature and pH were set at 30˚C and 6, respectively. Dissolved oxygen levels were fixed to a setpoint of 25% of

saturation by regulating agitation at approximately 800 rpm. After complete consumption of glycerol in the medium (24h), a methanol fed-batch phase was initiated by adding methanol to reach a maximum concentration of 1% (v/v) (7.9 g/L). After 48 of induction (72h of total production), the culture was harvested and supernatant was kept for protein purification.

***ScFv-h3D6-Pp purification*.** Protein was expressed in the extracellular space. After 48h of expression, cell culture was centrifuged (3,000xg, 10 min, RT). Supernatant was kept and ammonium sulfate was slowly added in agitation up to 50% (w/v). After 14-16h (o/n) at 4˚C, the sample was centrifuged at 100,000xg for 1h at 4˚C (Optimal LT X-100 Ultracentrifuge. Beckman Coultier). The pellet was resuspended in 10mM Na_2HPO_4, pH 6.5, and dialyzed for 24h (4 X 5L buffer changes). Then, a cationic exchange chromatography with a linear gradient of increasing NaCl concentration was performed. Finally, the protein was dialyzed to PBS, pH 7.4, and stored at -20˚C until its use.

Proteomics. Mass spectrometry (MS) analyses were carried out in the Proteomics facility at the UAB using a MALDI-TOF UltrafleXtreme (Bruker Daltonics). Sample preparation for each test was performed as follows:

Peptide Mass Fingerprinting: SDS-PAGE bands were cut and unstained with 50 mM ammonium bicarbonate/50% ACN. For disulphide bond reduction, samples were incubated with 10 mM DTT for 30 min at RT. For aquilation, samples were incubated with 25 mM iodoacetamide for 30 min at RT in the dark. Then, samples were digested with trypsin: 50 ng/sample (sequencing grade-Promega), 4h at 37˚C. Finally, samples were eluted with H_2O/50% acetonitril/0.2% TFA.

Detection of disulphide bridges: 30 µL of protein samples at 1.5 µg/µL were partially denatured with urea: 30 µL of sample +15 µL 4M urea, 2h at 30˚C. Then, the samples were digested with 800 ng of trypsin, dissolved in 25 µL of 0.1M ammonium bicarbonate, for 4h at 30˚C, and matrix-assisted laser desorption/ionization time-of-flight (MALDI-TOF) analysis was performed. Then, 2-µL samples were reduced with 0.05M DTT for 1h at RT and MALDI-TOF analysis was performed again.

Mass spectrometry: Protein samples were dialyzed by drop dialysis: 2-µL samples were dialyzed against 20 mL of 50 mM $(NH_4)HCO_3$ for 30 min at RT using a 0.025 µm pore membrane (Millipore). Then, samples were diluted 1/5 with milliQ-H_2O, mixed 1:1 sample:matrix (2,6-

dihidroxiacetophenone acid), and 1 µL deposited onto a ground steel plate. Analyses were performed using a lineal method and an accelerating voltatge of 25kv.

For peptide mass fingerprint (PMF) analyses samples were directly mixed 1:1 sample:matrix (α-cyano-4-hydroxycinnamic acid) and 1 µL of sample was deposited onto a ground steel plate. Samples were analyzed using a reflectron method with an accelerating voltatge of 25kv. All the MALDI-TOF analyses were calibrated using external references (Bruker Daltonics).

Lipopolysaccharides detection. Endotoxin units (EU) concentration (EU/mL) of the purified protein was determined by Pierce LAL Chromogenic Endotoxin Quantitation Kit (Thermo Scientific), following manufacturer's instructions.

ScFv-h3D6-Ec expression and purification. Protein expression was carried out using pET28a (+) vector and *E. coli* BL21 strain. Induction with 0.5 mM IPTG (isopropyl *β*-D-thiogalactopyranoside) was performed at OD_{600} = 0.7 and incubation in the shaker at 20˚C for 18h. After three freeze–thaw cycles, the cellular pellet was sonicated for 5 min, at 70% duty cycle and output 9 (Sonifier 450, Branson). The protein was obtained by solubilizing the insoluble fraction in denaturing buffer (100 mM Tris-HCl, 10 mM GSH, pH 8.5, and 8M urea) and refolding by dilution (1:10) in ice-cold refolding buffer (100 mM Tris/HCl, 100 mM L-arginine and 0.15 mM GSSG, pH 8.5) for 48h. Then a cationic exchange chromatography (Resource S6, GE Healthcare) using 5 mM Na_2HPO_4 pH 6.5 buffer and a gradient up to 15% of 5 mM Na_2HPO_4, 1M NaCl, pH 6.5 was performed. This chromatography was used to completely purify the protein and also to fractionate the native state and the disulphide scrambled forms. Finally, because proteins purified from *E. coli* contain lipopolysaccharides that are toxic to cell cultures, these were removed from the protein by using Detoxi-Gel Endotoxin Removing columns (Thermo Scientific). The buffer was changed to PBS using PD-10 Desalting Columns (GE).

Secondary structure determination by Circular Dichroism (CD). Protein secondary structure was monitored at different temperatures by far-UV CD spectroscopy from 260 nm to 190 nm in a Jasco J-715 spectrophotopolarimeter. Protein concentration was 20 µM, and 20 scans were recorded at 50 nm min^{-1} (response 2s) in a 0.2 cm pathlength cuvette.

Thermal denaturation. Thermal denaturation was followed up by far-UV CD spectroscopy at 218 nm (Jasco J-715) and tryptophan fluorescence emission at 338 nm (Cary Eclipse, Varian), both at 20 µM protein concentration and 1°C min^{-1} heating rate.

Transmission Electron Microscopy (TEM). To visualize the aggregation extent and morphology of the scFv-h3D6-Ec and scFv-h3D6-Pp aggregates, incubation of 100-µM samples was carried out at 37°C for 48h. Then, samples were 1:10 diluted in PBS and quickly adsorbed onto glow-discharge carbon-coated grids. TEM was performed in a Jeol 120-kV JEM-1400 microscope, using 1% uranyl acetate for negative staining.

Aβ preparations. $A\beta_{1-42}$ synthetic lyophilized peptide (Bachem), was dissolved at 1 mM in HFIP (1,1,1,3,3,3-hexafluoro-2-isopropanol) (Sigma-Aldrich). Then, aliquots of 30 µL were prepared and HFIP was removed by vacuum drying in a SpeedVac (Savant instruments), and stored at −20°C. For TEM analysis, each aliquot was resuspended with 6 µL of DMSO (Sigma-Aldrich) and subsequently diluted to 300 µL (100 µM) with PBS and co-incubated with scFv-h3D6 variants at 37°C for 48h. For cell-culture cytotoxicity assays, phenol-red free DMEM (Gibco) was used instead of PBS and resuspended Aβ was incubated for 24h at 4˚C before the addition to the wells [150], and then incubated at 37°C for 48h in the cell culture alone or together with the scFv-h3D6 variants.

Cell culture and viability assays. The SH-SY5Y human neuroblastoma cell-line was grown in serum-supplemented medium in 5% CO_2 at 37ºC. DMEM/F-12 (1:1) +GlutaMAX™ (Gibco) was supplemented with 10% fetal bovine serum (Sigma), 1% MEM non-essential amino acids (Gibco) and 1% mix of antibiotics: penicillin, streptomycin and anti-fungal amphotericin (Gibco). 10,000 cells/well were plated in 96-well plates (Life Technologies) and incubated for 24h to allow cell attachment. Then, medium was changed and cells were treated with Aβ oligomers (10 µM) and/or scFv-h3D6 variants (0, 2.5, 5, 7.5 and 10 µM). Because of the method of preparation of the Aβ peptide, 2% (v/v) DMSO remained in the initial solution (0.2% in the well) and all samples, including controls, contained the same percentage of DMSO during incubation, as well as the same medium and buffer composition. After 48h of incubation, viability assay EZ4U (Biomedica) was performed following the manufacturer's instructions. Each condition consisted of three replicas per experiment, and four independent experiments were performed. Data are presented as the percentage of viability for each condition compared to the untreated cells.

Mice treatment. All the experiments were approved by the UAB Animal Research Committee and the Government of Catalonia, and performed in accordance with the Guide for the Care and Use of Laboratory Animals published by the US National Institutes of Health. Five-month-old triple-transgenic (3xTg-AD) mice females harboring PS1/M146V, APPSwe and tauP301L transgenes and non-transgenic (NTg) mice with the same genetic background (B6129SF2/J)

(both purchased from the Jackson Laboratories and stablished at the UAB animal facility) were used. Animals of the same genotype and sex were maintained in cages (Makrolon, 35 × 35 × 25 cm) under standard laboratory conditions (food and water *ad lib*, 22 ± 2°C, 12h light:dark cycle starting at 08:00). Animals (n = 6 each group) received a single intraperitoneal dose of 100 µg of scFv-h3D6-Ec, scFv-h3D6-Pp or vehicle (PBS). Five days after administration, animals were anesthetized with inhaled isofluorane (1% in O_2), sacrificed, and brains were collected and dissected. One hemisphere was kept for histological analysis and the other was used for protein extraction.

Protein Extracts. Protein extraction was performed by centrifugation of brain subregions homogenates. Briefly, frozen tissues of cortex and hippocampus from 5-mo-old 3xTg-AD and NTg mice were weighted and mechanically homogenized in ice-cold TBS-1% Triton X-100 solution supplemented with protease inhibitors (Roche tablets, reference 1836153) (8 µL solution/mg tissue). Then, samples were gently sonicated (1 cycle of 35 sec, at 35% duty cycle and output 4 in a Dynatech Sonic Dismembrator ARTEK 300 with the smallest tip) and centrifuged at 100,000g for 1h at 4°C. Supernatants were aliquoted and stored at −80°C until its use.

Aβ$_{42}$ ELISA. Brain extracts were used to analyze differences in Aβ levels of each group by $Aβ_{42}$ ELISA (Invitrogen). Procedure was performed according to the manufacturer's protocol. Data obtained were normalized by the total amount of protein in each extract measured by BCA assay (Pierce).

Immunohistochemistry*.* Paraformaldehyde-fixed sections (cut at 10 µM) were deparaffined and treated with 70% formic acid for 20 min for epitope retrieval. To quench endogenous peroxidase, sections were incubated with 3% H_2O_2 in methanol for 10 min. Then, sections were washed and permeabilized in 0.1% Tween-PBS followed by blocking in 5% normal goat serum (Sigma-Aldrich), 5% BSA (Sigma-Aldrich) and 0.1% Tween-PBS. After blocking, sections were incubated with primary antibody 6E10 (Biolegend) overnight at 4ºC. The next day, sections were washed and immunostained with Mouse Extravidin Peroxidase Staining kit (Sigma-Aldrich) and developed by diaminobenzidine (DAB) substrate and stained with hematoxylin. Sections were cover-slipped using DPX mounting medium (Sigma-Aldrich) and examined in a Leica DMRB Microscope equipped with the Leica Application Suite (LAS) software.

Statistics. Statistical analysis was performed using Graphpad 6 software. For cell viability assays, differences due to the treatment with scFv-h3D6-Ec or scFv-h3D6-Pp were assessed by two-way ANOVA test, analyzing changes due to protein concentration and protein variant. For comparisons of control groups (Aβ alone for cell viability assays or 3xTg-Vehicle in the *in vivo* experiment) with treated conditions, unpaired t-test with Welch's correction was performed. All data were expressed as means ± SEM values and a *P* value of <0.05 was considered to reflect statistical significance.

RESULTS AND DISCUSSION

Study of protein expression.

Heterologous expression in *P. pastoris* can be either intracellular or secreted. Secretion requires the presence of a signal sequence on the expressed protein to target it to the secretory pathway. The vector used for the expression of scFv-h3D6 in *P. pastoris* was pPicZαA, which has a native *Saccharomyces cerevisiae* α-factor secretion signal (α-MF) that allows for efficient secretion of most proteins from *P. pastoris*. The processing of the α-MF signal sequence in pPicZαA occurs in two steps: the preliminary cleavage of the signal sequence by the *kex2* gene product and the subsequent shortening by the *STE13* gene product. Kex2 cleavage occurs between arginine and glutamic acid residues within the sequence Glu-Lys-Arg*-Glu-Ala-Glu-Ala, where * is the site of cleavage [159,160]. The Glu-Ala repeats are further removed by the *STE13* gene product [161], but there are some cases where this cleavage is not efficient, and Glu-Ala repeats are left in the N-terminus of the expressed protein.

To insert the *scFv-h3D6* gene in the pPicZαA vector, an *EcoRI* target was generated by PCR upstream of the *scFv-h3D6* gene. Then, the *scFv-h3D6* gene was introduced in the pPicZαA vector through *EcoRI* and *NotI* restriction sites. As a consequence of this procedure, a Phe residue was generated in the protein sequence (…EKREAEAE**F**EVQL…). Due to the bulky dimensions and hydrophobicity of this residue, and the difficulties these features could generate, mainly in terms of folding and immunogenicity, sequence modification was performed. Two variants were constructed: EAEA (…EKREA**EA**QL…) and EAEV (…EKREA**EV**QL…). In both variants, the EFEV sequence, which is not necessary for the protease processing, was removed, leading to a much closer location of the scFv-h3D6 N-terminus to the protease target site.

Both constructs were transformed into the Mut^S strain KM71H and zeocine selection was performed. Protein expression tests were carried out and both proteins were efficiently expressed in the extracellular space. From both variants (EAEA and EAEV) two forms of protein were detected depending on the efficiency of the STE13 cleavage (not shown).

To discern which of the two variants (EAEA or EAEV) was a better approach for obtaining a homogenous and pure scFv-h3D6, a longitudinal study of protein expression during five days was performed. Figure 3.1A-B show that while the molecular weight of the EAEV variant changed during the time-course of expression, as assessed by MALDI-TOF-MS, the molecular weight of the EAEA variant was always the same. This indicated that in the case of the EAEV

variant, after the KEX2 processing, the STE13 cleavage was heterogeneously performed. On the other hand, the fact that the molecular weight of the EAEA variant was maintained indicated that the STE3 cleavage was either not performed or performed to an undetectable extent. Although both variants rendered a similar expression yield, as assessed by SDS-PAGE (Figure 3.1C), we decided to focus on the study of the EAEA variant to ensure homogeneity among batches.

Protein purification from P. pastoris*.*

When designing the protein constructs, no C-terminal *myc* epitope or polyhistidine tag for purification were added, as it is usually the case for proteins expressed in *P. pastoris*. Then, a stop codon was used just downstream the protein sequence to avoid the expression of C-terminal peptides included in the pPicZαA vector. As a therapy intended to treat AD patients, protein composition must be limited to the original sequence, without any other additional parts that could interfere with its the therapeutic effect or induce an immunologic response.

The major advantage of expressing heterologous proteins to the extracellular space is that *P. pastoris* secretes very low levels of its own proteins. Then, the secreted heterologous protein comprises the vast majority of the total protein in the medium [162], as was also the case for scFv-h3D6 (Figure 3.1C). The easiest way to purify the protein in this case was to centrifuge the cell culture and precipitate the protein in the supernatant with ammonium sulfate. Apart from a quick way to concentrate the protein, it is also a suitable manner to preserve it in case large volumes have been expressed and cannot be purified at once.

After centrifugation, pellet resuspension, and dialysis, a single cationic exchange chromatography was performed. As can be observed in Figure 3.2A, two differentiated peaks were eluted. PMF analysis indicated that the two fractions corresponded to the two possible variants depending on the STE13 protease cleavage site (Figure 3.2B), with the first eluted and most abundant peak corresponding to the EAEA variant and the second one to the EA one. Therefore, the small proportion of protein that was cleaved by STE13 could be fractioned from the most abundant EAEA form. This makes possible to easily achieve the isolation of a pure and conformationally homogenous protein. Then, as it constituted the majority of the production, we decided to focus our study on the EAEA variant, from now on called scFv-h3D6-Pp.

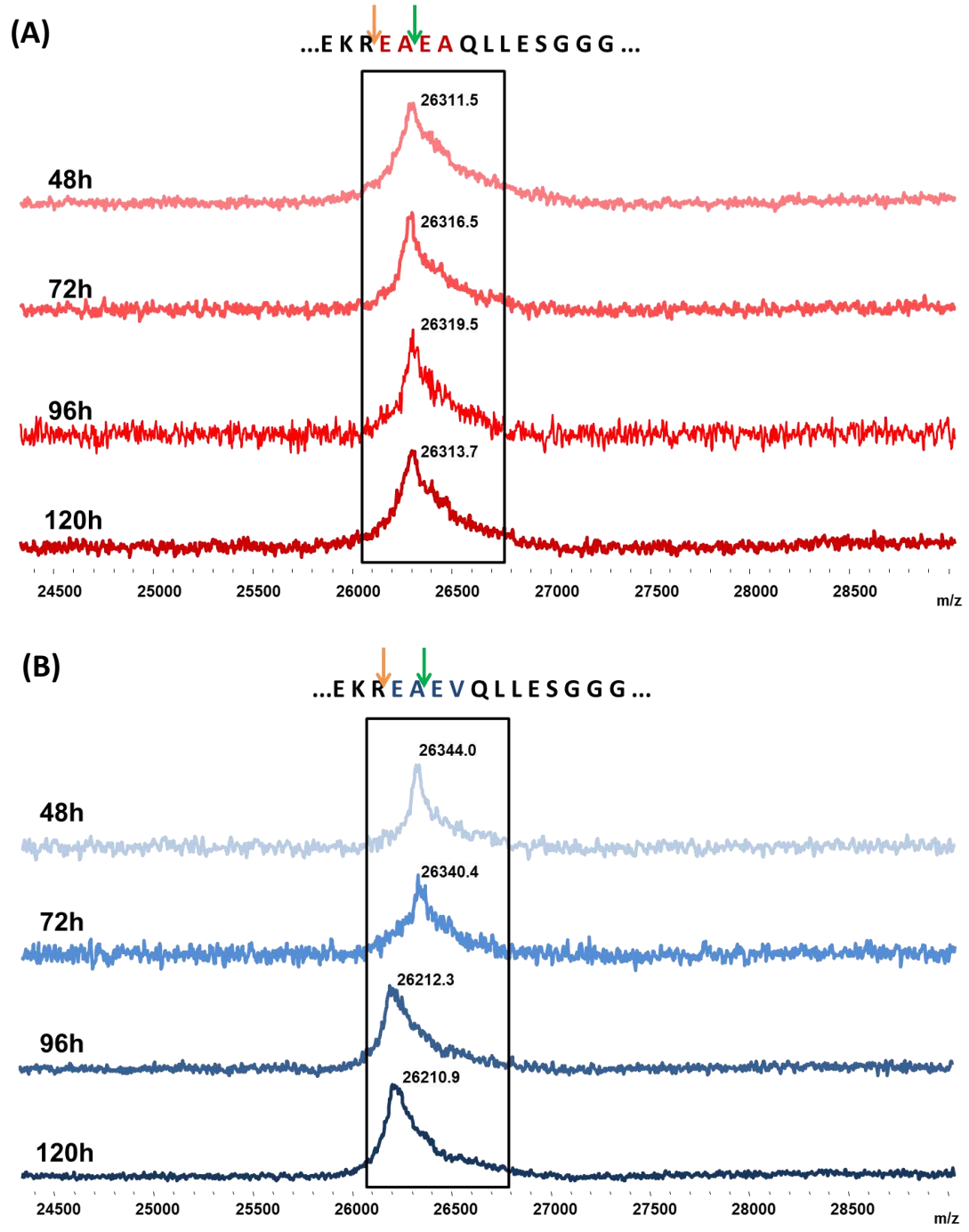

Figure 3.1. Mass spectometry MALDI-TOF analysis of protein expression at 48h, 72h, 96h and 120h after induction of EAEA (A) and EAEV (B) variants. Orange arrows indicate the Kex2 cleavage site and green arrows indicate the STE13 one. While the molecular weight of the EAEV variant (26142.0 or 26342.2 Da depending on the protease cleavage site) changed during the induction period, the EAEA variant (26114.0 or 26314.2 Da) maintained an homogenous population. **(C) SDS-PAGE of the samples analyzed by mass spectrometry.** Secreted proteins rendered a good and similar expression yield.

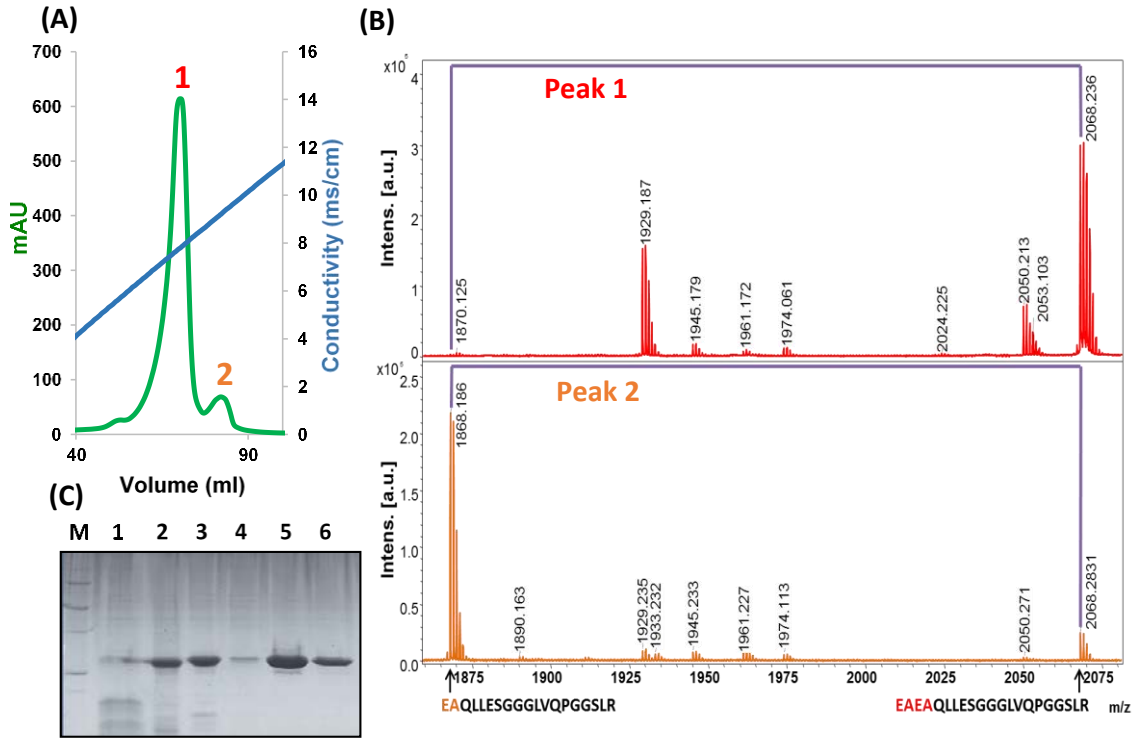

Figure 3.2. ScFv-h3D6-Pp purification. (A) Cation Exchange Chromatography (CEX); (B) Peptide Mass Fingerprinting (PMF) analysis of each peak. PMF analysis of the two differentiated peaks eluted after CEX indicated that the two fractions corresponded to the two possible protein variants depending on the STE13 protease cleavage site. **(C) SDS-PAGE of scFv-h3D6-Pp purification.** (M) Molecular weight marker; (1) Supernatant after ammonium sulfate precipitation; (2) Pellet after ammonium sulfate precipitation; (3) Sample before Cationic Exchange chromatography (CEX); (4) CEX flow through; (5) CEX elution of the mean peak; (6) PBS-dialyzed scFv-h3D6-Pp.

ScFv-h3D6-Pp large scale production in P. Pastoris.

To demonstrate that the production of scFv-h3D6-Pp could be easily scaled-up, so that translation to production for manufacturing purposes would become achievable, fermentation was performed in a 5L-bioreactor and then the protein was purified. Culture conditions were maintained as described in the Materials and Methods section. Fermentation was performed in two phases. First, a batch phase with glycerol in the medium allowed for an exponential cell growth, and after 24h (OD_{600}=148), when glycerol was almost exhausted, a 48h fed-batch phase started with the injection of methanol for inducing protein expression (Figure 3.3). Methanol was injected periodically depending on its concentration in the medium to avoid cell toxicity. After 48h of induction (72h of total production), the culture was harvested and the protein in the supernatant precipitated with ammonium sulfate. After purification by CEX chromatography, the final purification yield was 13.3 mg per initial L of growth culture.

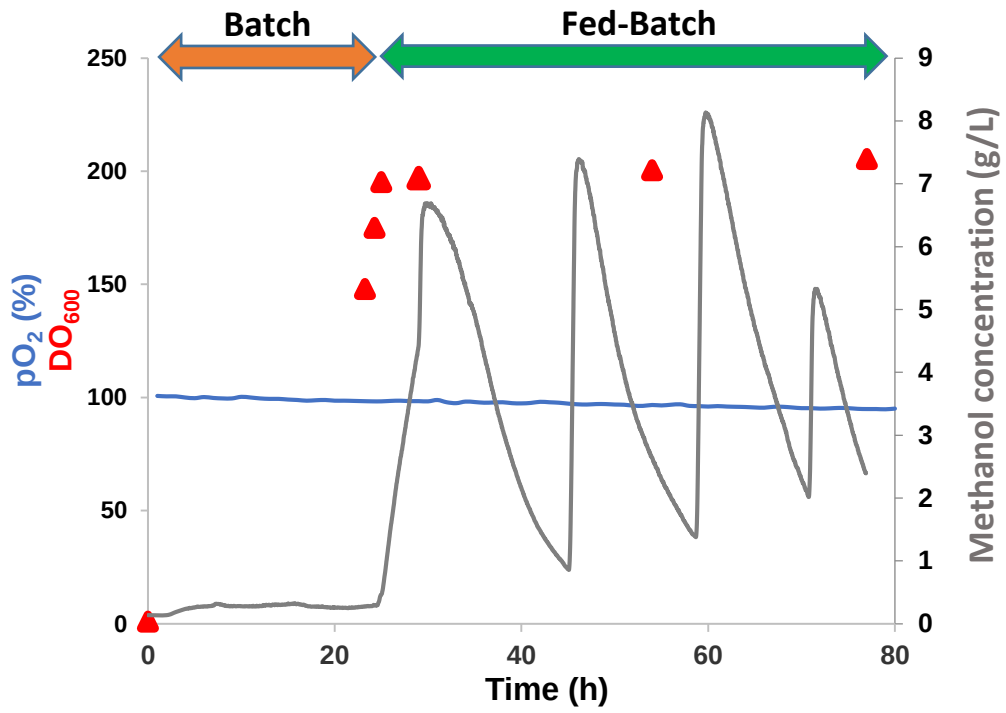

Figure 3.3. Large-scale fermentation profile. Oxygen concentration (expressed as the percentage of air saturation), Cell grow (OD_{600}) and methanol concentration (mg/mL of culture) during batch and feed-batch phases. Culture was induced 24h after the batch phase started. During the fed-batch phase, methanol was added periodically to reach a maximum concentration of 1% (v/v) (7.9 g/L).

Biophysical properties of scFv-h3D6-Pp compared to scFv-h3D6-Ec.

To characterize the novel protein purified from *P. pastoris*, scFv-h3D6-Ec was used for comparative purposes. It is described that the CD spectra of the scFv-h3D6-Ec shows a peculiar minimum at 230 nm and a positive shoulder at 237 nm, corresponding to the interference of the Trp residue in the core of the V_L and V_H domain, respectively [99,163]; apart from the characteristic minimum at 218 nm and maximum at around 200 nm for a β-fold (Figure 3.4A). These interferences are more intense for scFv-h3D6-Pp; however, it is rather difficult to find the rationale behind the effect in the far-UV region (260-190 nm) of an aromatic residue that typically renders ellipticity in the near-UV region (at around 290 nm). So, our hypothesis is just that differences between the N-terminus of both proteins, which contain the sequence MEVQLL for the *E. coli* variant and EAEAQLL for the *P. pastoris* one, could somehow affect the packing of the molecule, accounting for such an effect. In any case, the β-conformation characteristic of the immunoglobulin fold is kept.

To check whether these differences might affect conformation, thermal denaturation was followed by CD and Trp-fluorescence spectroscopies (Figure 3.4 B-C). The profiles were the same in both cases, indicating that the protein obtained from *P. pastoris* shows no differences with

that from *E. coli* in terms of thermal stability and, therefore, we can assume that both molecules are equally folded. As expected, worm-like fibrils, behind the protective effect of scFv-h3D6, are formed upon thermal denaturation in both cases (Figure 3.4 D-E), so the therapeutic effect should remain.

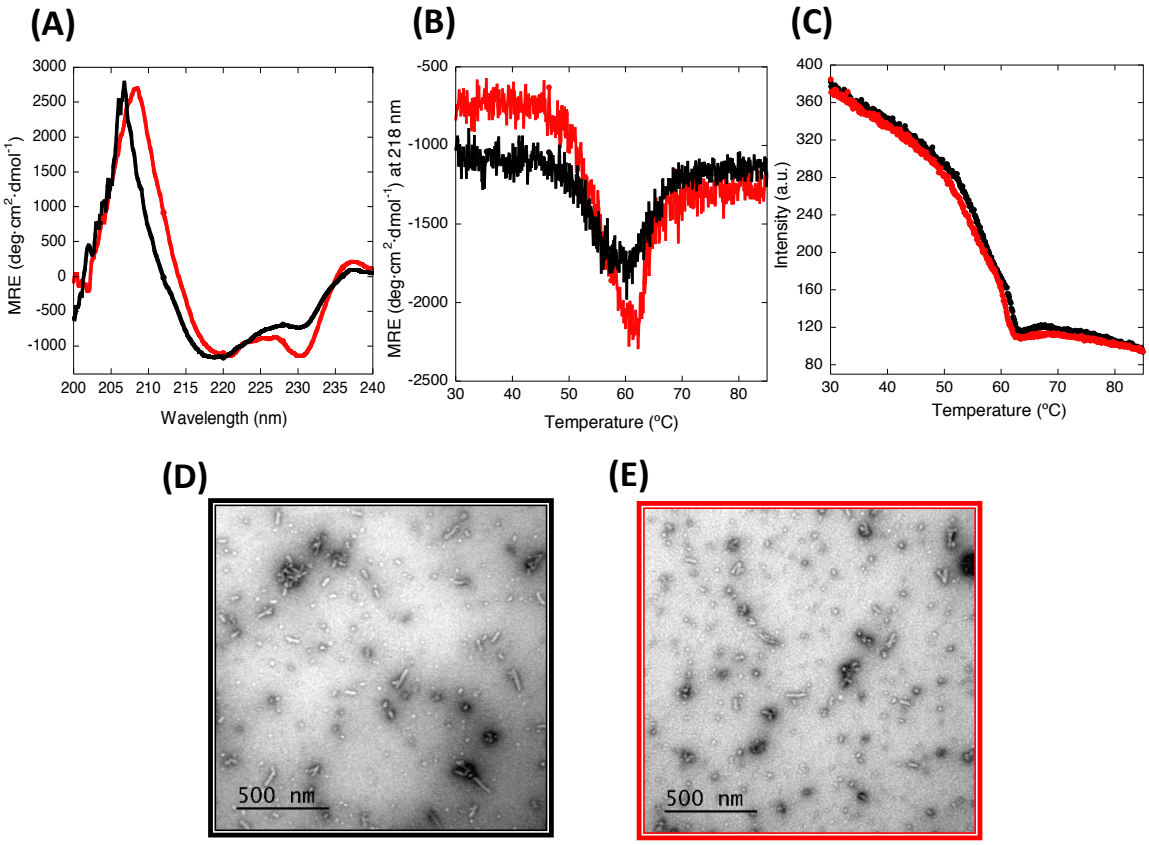

Figure 3.4. Protein Characterization. (A) Circular Dichroism (CD) spectra at 25˚C; (B) Thermal denaturation followed by CD; (C) Thermal denaturation followed by Trp fluorescence; (D) and (E) TEM micrographs. Black: scFv-h3D6-Ec, Red: scFv-h3D6-Pp. CD analysis showed that the β-conformation characteristic of the immunoglobulin fold is maintained, albeit some differences in the interferences due to the Trp residues in the core of each domain are somehow higher in the scFv-h3D6-Pp spectrum. However, no differences in terms of thermal stability were observed and, therefore, it can be assumed that both molecules are equally folded. As expected, worm-like fibrils, behind the protective effect of scFv-h3D6, are formed upon thermal denaturation in both cases, so that the therapeutic effect should remain.

Advantages of scFv-h3D6-Pp as a therapeutic approach.

One of the main drawbacks of *E. coli* as a host organism for protein expression and purification is due to protein expression in the insoluble fraction, as is the case for most scFvs in the literature [99,102,164–166] and also for scFv-h3D6-Ec. In this case, the insoluble fraction needs to be chemically solubilized and proteins, which are denatured, must be refolded. In this process, some disulphide scrambled conformations can occur. Separating scrambled conformations can become an arduous process, especially due to changes in conformation and the subsequent decrease in the purification yield. In addition, some traces of scrambled conformations can remain in the sample or, even after a good fractionation of the native state, appear as a consequence of the reshuffling of the disulphide bonds. These scrambled conformations, even in a very-low concentration, are prone to aggregation and consequently are thermodynamically trapped so that the equilibrium shifts from the native state to the scrambled forms. *P. pastoris* has many of the advantages of higher eukaryotic expression systems such as protein processing and protein folding. In this case, scFv-h3D6-Pp was expressed in the extracellular fraction as a soluble form. In order to ensure that this soluble form corresponded to the native conformation, we checked the configuration of its disulphide bridges by analyzing the tryptic digestion of the non-reduced protein by MALDI-TOF-MS. Only the peptides corresponding to the native disulfide bonding were detected (Figure 3.5), indicating that after purification, scfv-h3D6-Pp was perfectly folded, and no scrambled conformations traces were present.

On the other hand, one of the main drawbacks of expressing heterologous proteins in eukaryotic systems can be the posttranslational modifications carried out by the host organism, especially glycosylation. Contrary to *Saccharomyces cerevisiae, Pichia* may not hyperglycosylate secreted proteins. In the case of N-linked glycosylation, both *Saccharomyces* and *Pichia* have a majority of the N-linked glycosylation as high-mannose type; however the length of the oligosaccharide chains post-translationally added to proteins in *Pichia* is much shorter than those in *Saccharomyces* [167]. On the other hand, very little O-glycosylation has been observed in *Pichia* [168]. Predictor NetNGlyc 1.0 Server showed no targets for N-glycosilation within the sequence of scFv-h3D6-Pp, but predicted one signal sequence for O-glycosilation. Molecular weight analysis by MS (Figure 3.6) determined that no glycosylation was added to the protein as a posttranslational modification, as the molecular weight corresponded to the amino acid sequence alone.

(A)

```
         10         20      a  30         40         50         60
EAEAQLLESG GGLVQPGGSL RLSCAASGFT FSNYGMSWVR QAPGKGLEWV ASIRSGGGRT

                                          b
         70         80         90        100        110        120
YYSDNVKGRF TISRDNSKNT LYLQMNSLRA EDTAVYYCVR YDHYSGSSDY WGQGTLVTVS

                                         c
        130        140        150        160        170        180
SGGGGSGGGG SGGGGSDVVM TQSPLSLPVT PGEPASISCK SSQSLLDSDG KTYLNWLLQK

                                                   d
        190        200        210        220        230        240
PGQSPQRLIY LVSKLDSGVP DRFSGSGSGT DFTLKISRVE AEDVGVYYCW QGTHFPRTFG

QGTKVEIK
```

(B)

Disulfide bonding		Bonded Peptides	
		Expected Mw	Observed Mw
1	a-b	3373,7 Da	√
	c-d	7950,5 Da	√
2	a-d	4340,8 Da	x
	b-c	6983,4 Da	x
3	a-c	3545,9 Da	x
	b-d	7778,4 Da	x

Figure 3.5. (A) Sequence of scFv-h3D6-Pp protein. Cysteine residues are indicated in bold red; tryptic peptides containing cysteine residues are highlighted in a blue rectangle**. (B) Disulfide bonds present in the scFv-h3D6-Pp.** Expected Mw of the tryptic peptides involved in disulfide pairing for each possible disulfide bonding conformation. The peptides detected by MALDI-TOF MS are indicated.

Finally, using Gram-negative bacteria, such as *E. coli*, to obtain recombinant proteins with biomedical applications presents a great obstacle: the presence of endotoxins. Although systems for removal of lipopolysaccharide (LPS) are implemented [169–171], they deeply decrease the purification yield and increase the purification costs. The yeast *P. pastoris* is considered an endotoxin-free cell factory for recombinant protein production. To demonstrate that the scFv-h3D6-Pp is a secure medical device in terms of purity, the level of endotoxins in the purified protein was determined. According to FDA [172], the endotoxins limit for a medical device is dependent on the intended use of the device and what the device contacts (e.g., blood, the cardiovascular system, cerebrospinal fluid, intrathecal routes of administration, permanently implanted devices, and devices implanted subcutaneously). For medical devices, the limit is 0.5 EU/mL or 20 EU/device for products that directly or indirectly contact the cardiovascular and lymphatic systems. In the *in vivo* experiment (following section) the protein was administered

intraperitoneally at a concentration of 0.5 mg/mL and a total volume of 0.2 mL (100 µg). The testing of remaining LPS traces was also performed at this concentration of protein. The concentration of endotoxins in the protein was EU/mL=56.46±1.24, what supposes 11.29 EU in the administration, and consequently, is under the limit. Therefore, scFv-h3D6-Pp can be safely used for therapeutic purposes.

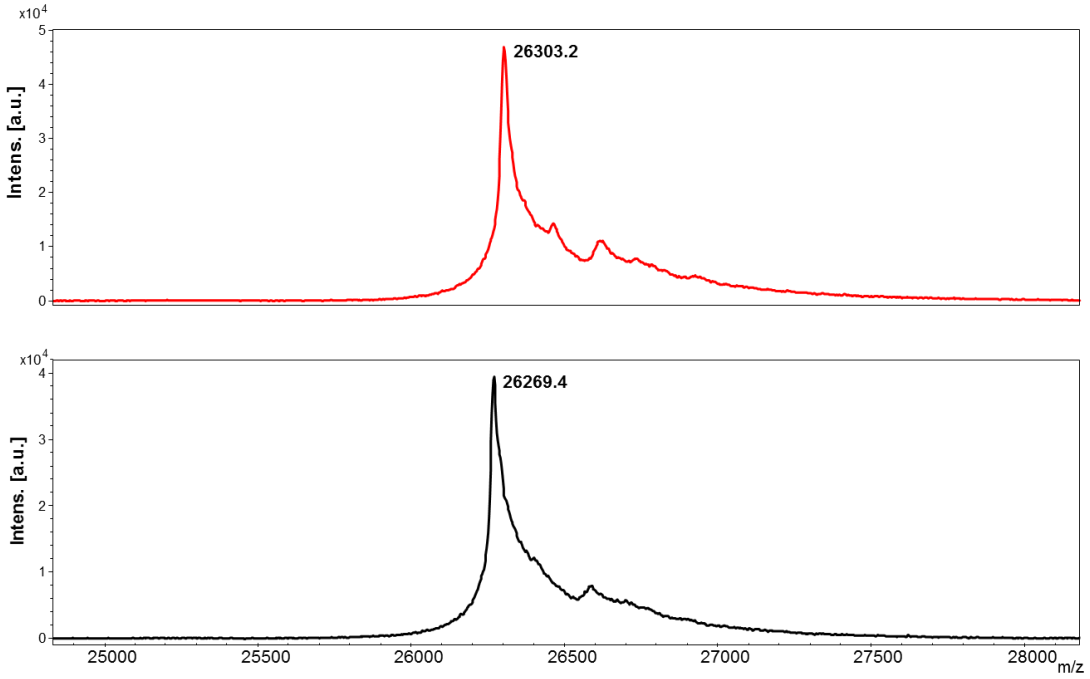

Figure 3.6. **Mass spectrometry analysis of scFv-h3D6-Pp (red) and scFv-h3D6-Ec (black).** Molecular weight analysis determined that no N-glycosylation either O-glycosilation was added to the protein as a posttranslational modification, as the molecular weight corresponded to the amino acid sequence alone (scFv-h3D6-Pp: 26314.2 Da and scFv-h3D6-Ec: 26273.2 Da).

Therapeutic effects of scFv-h3D6-Pp: protective effects in cell culture and reduction of Aβ burden in the 3xTg-AD mouse-model.

Aβ oligomeric species are the crucial toxic species in AD [26,27]. To test the therapeutic effects of the scFv-h3D6-Pp we studied its protective effect against Aβ oligomers neurotoxicity in the SH-SY5Y neuroblastoma cell-line. Aβ concentration was fixed to 10 µM (previously reported as toxic [99]) and protein concentration was tested in a range of concentrations (0, 2.5, 5, 7.5 and 10 µM). Figure 3.7A shows how both variants, from *E. coli* and from *P. pastoris*, are capable of blocking Aβ-induced toxicity in a concentration-dependent manner (two-way ANOVA *P*=0.0016) with a marginal significance due to differences among mutants (two-way ANOVA *P*=0.0508). On the other hand, when comparing each concentration of scFv-h3D6-Ec or scFv-h3D6-Pp with Aβ alone (unpaired t-test with Welch's correction), statistical significance was reached in both cases for

7.5 and 10 μM concentrations (scFv-h3D6-Ec: for 7.5 μM *P*=0.026 and for 10 μM *P*=0.049; scFv-h3D6-Pp: for 7.5 μM *P*=0.017 and for 10 μM *P*=0.0067). These results indicated that both proteins are capable of recovering Aβ-induced toxicity, with scFv-h3D6-Pp showing a tendency to be more effective than scFv-h3D6-Ec.

Both proteins were also tested in the treatment of the 3xTg-AD mouse model. A single intraperitoneal dose of 100 μg of protein was administered to the following groups (n=6): scFv-h3D6-Ec, scFv-h3D6-Pp and vehicle (PBS). A non-transgenic group (NTg) was also administered with vehicle in order to have a control of non-pathological levels of Aβ. After five days, animals were sacrificed. ELISA of brain extracts (Figure 3.7B) indicated that $A\beta_{42}$ levels were decreased in cortex and hippocampus by both scFv-h3D6-Ec and scFv-h3D6-Pp. Statistical analysis of $A\beta_{42}$ levels to determine differences was performed using unpaired t-test with Welch's correction. Comparisons of the treated groups or NTg with 3xTg-AD-vehicle group showed *P*-values for cortex and hippocampus as follows: 3xTg-AD-scFv-h3D6-Ec (Cortex *P*=0.011, Hippocampus *P*=0.084), 3xTg-AD-scFv-h3D6-Pp (Cortex *P*=0.005, Hippocampus *P*=0.037), and NTg-vehicle (Cortex *P*=0.075, Hippocampus *P*=0.006). Therefore, scFv-h3D6-Ec was efficient in decreasing Aβ in the cortex and showed a tendency in the hippocampus, whereas scFv-h3D6-Pp was clearly efficient in both areas. It must be mentioned, however, that the Aβ levels in the cortex of the NTg-vehicle group did not reach significance when compared to the 3xTg-AD-vehicle ones, albeit the former were lower. On the other hand, no significance was reached when comparing 3xTg-AD-scFv-h3D6-Ec and 3xTg-AD-scFv-h3D6-Pp to NTg-vehicle, which indicates that treatments recovered the non-pathological $A\beta_{42}$ levels in both areas.

Finally, immunohistological analysis of brain slices with the anti-Aβ antibody 6E10 (figure 3.7C) also corroborated these results. Aβ-immunoreactivity decreased to similar levels as those in non-transgenic animals when 3xTg-AD were treated with scFv-h3D6-Ec or scFv-h3D6-Pp. Therefore, these results demonstrate that scFv-h3D6-Pp shows the same therapeutic benefits, or slightly better, as those already known for scFv-h3D6 obtained from *E. coli* [100,101]. It is capable of withdrawing Aβ oligomers from the amyloid pathway and, this way, prevent their cytotoxicity. *In vivo*, scFv-h3D6-Pp significantly reduces Aβ burden, the increase of which is the most important hallmark of AD. This work validates scFv-h3D6-Pp as a therapy for AD with multiple advantages in terms of recombinant production and safety.

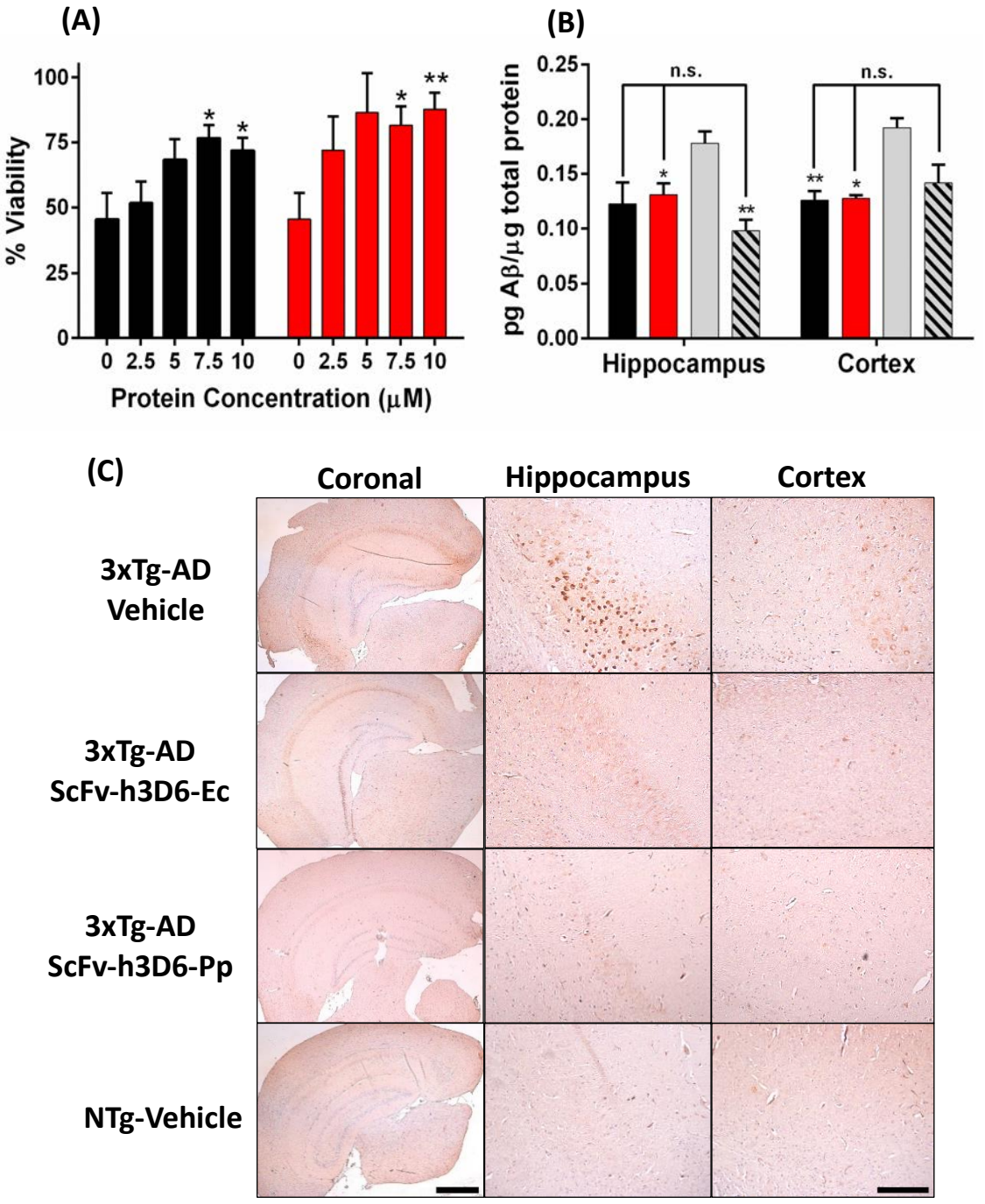

Figure 3.7. **Therapeutic effects of scFv-hD6-Ec and scFv-h3D6-Pp**. **(A) Viability assays in SH-SY5Y neuroblastoma cell line.** Cells were exposed to Aβ oligomers (10 μM) and different concentrations of scFv-h3D6-Ec or scFv-h3D6-Pp. Black: scFv-h3D6-Ec, Red: scFv-h3D6-Pp. Comparisons of each concentration of scFv-h3D6-Ec or scFv-h3D6-Pp with Aβ alone showed statistical significance for 7.5 and 10 μM in both cases, indicating efficiency of both treatments (unpaired t-test with Welch's correction, * P<0.05. ** P<0.01). **(B) $A\beta_{42}$ ELISA of brain homogenates (Hippocampus and Cortex)**; Black: scFv-h3D6-Ec, Red: scFv-h3D6-Pp, Grey: 3xTg-AD-Vehicle, Stripped: NTg-vehicle. Both treatments recovered the non-pathological levels of Aβ. *, ** indicate significance compared to the 3xTg-AD-vehicle group (Unpaired t-test with Welch's correction, * P<0.05, ** P<0.01). Arrows indicate comparisons with NTg-vehicle group (n.s. indicates no significance). **(C) Aβ Immunohistochemistry of coronal sections.** Aβ-immunoreactivity decreased to similar levels as those in non-transgenic animals when 3xTg-AD were treated with scFv-h3D6-Ec or scFv-h3D6-Pp Bar in panoramic coronal sections (2.5x zoom in) corresponds to 1 mm and in hippocampus and cortex sections (16x zoom in) to 200 μm.

CONCLUSIONS

The scFv-h3D6 has been demonstrated to be a promising approach to treat AD. It has been proven to prevent Aβ-induced cytotoxicity by withdrawing Aβ oligomers from the amyloid pathway towards the worm-like one. In addition, it was shown to be effective at the behavioral, cellular, and molecular levels in the treatment of 3xTg-AD after a single intraperitoneal dose. Although its potential properties, scFv-h3D6 production in *E.coli* is limited by some bottlenecks like the presence of disulphide scrambled conformations generated in the refolding process and its contamination with endotoxins. In the present study, we present a simple and efficient system for production of scFv-h3D6 in *P.pastoris*.

One of the hurdles of expressing proteins in *P.pastoris* to the extracellular space is the variability of protease action. Here we demonstrate that it is possible to obtain a pure and homogenous protein. Moreover, with an easy protein purification system, even though the protein sequence has no tags to facilitate purification. The scale-up process was also possible, what is important if this therapeutic approach is eventually used in the treatment of AD patients.

The obtained protein was demonstrated to be well-folded. In addition, LPS traces were under the limits set by FDA and no N either O-glycosylation was performed by the posttranscriptional machinery of *P.pastoris*, assuring safety of the treatment in terms of avoiding an inflammatory response.

Finally, viability experiments with the neuroblastoma cell line SH-SY5Y demonstrated that the novel protein purified from *P.pastoris* is capable of avoiding Aβ-induced cytotoxicity as well as the protein from *E.coli*. *In vivo* experiments corroborated that there are no differences with the already known benefits of scFv-h3D6 obtained from *E. coli*. Therefore, *P. pastoris* constitutes an improved expression system to obtain scFv-h3D6 with therapeutic purposes. This new system must allow the limitations of scFv-h3D6 production not to interfere with its great potential as a therapy to treat AD.

CHAPTER 4:

Effects of scFv-h3D6 on Aβ aggregation and astrocytic uptake are modulated by apolipoprotein E and J mimetic peptides.

AIMS

Albeit Aβ-immunotherapy has long been studied in the treatment of AD, how other molecules involved in the disease could affect the antibody action remains elusive. The present work aimed to test the influence of scFv-h3D6 on Aβ aggregation and cellular uptake by primary human astrocytes, alone or in combination with apolipoproteins E and J. To do so, and as an eventual therapeutic approach, we have combined scFv-h3D6 with apolipoprotein E and J mimetic peptides (MP) composed of essential structures within these apolipoproteins for binding to other molecules. The apoE mimetic peptide (MP) is composed of the receptor binding site (residues141-150) sequence within apoE, linked to a Class A lipid associating domain similar to the lipid binding site of apoE [173]. The apoJ-MP corresponds to the 6th predicted helix of the 17 potential G* amphipathic helices in the mature apoJ protein, residues 113 to 122, and to prevent degradation of such a short peptide is built by D-isomers [174]. The apoE-MP, although initially intended to treat arthrosclerosis [175–177] is already reported in the literature to improve cognition, decrease amyloid plaque deposition and reduce the number of activated microglia and astrocytes in the APP/PS1ΔE9 mice [173]. The apoJ-MP, also intended to treat atherosclerosis [174], has been suggested as a therapy for inflammatory disorders other than atherosclerosis [178], but this is the first study assessing its effect in AD.

Firstly, we have studied the interactions among scFv-h3D6, Aβ, and apoE-MP or apoJ-MP by circular dichroism (CD) and transmission electron microscopy (TEM) to next study the influence of scFv-h3D6 in Aβ aggregation and cellular uptake by primary human astrocytes alone or in combination with these MPs (flow cytometry).

As AD pathology starts long before the symptoms appear, immunotherapy should aim at halting the disease progression in these early stages. Immunotherapy has long been studied in the treatment of AD, but studies have focused on microglia as facilitator instead of astrocytes, the much more abundant scavenger cell type. Therefore, and because astrocytes are the first in line in the physiologic clearance of Aβ and represent the major cell type mediating clearance of Aβ from the extracellular space in the brain [179], we focus on astrocytes in this study.

MATERIALS AND METHODS

***ScFv-h3D6 expression and purification*.** ScFv-h3D6 expression and purification were carried out as described in Chapter 3 for scFv-h3D6-Ec.

***Apolipoprotein E and J mimetic peptides*.** The apoE mimetic peptide (MP) has the sequence: LRKLRKRLLRDWLKAFYDKVAEKLKEAF [173,175] and the apoJ-MP is formed by D-isomers of residues LVGRQLEEFL [174]. Both MPs were synthesized, protected at both termini and at >95% purity, by Caslo laboratories (Denmark).

Aβ$_{1-42}$ Peptide.

Aβ$_{1-42}$ Preparations for Cell culture and FACS analysis. Aβ$_{1-42}$ (Bachem) was dissolved in hexafluoro-isopropanol (HFIP) (Fluka) to obtain a monomeric Aβ$_{1-42}$ solution. Next the solution was aliquoted, nitrogen flow dried and stored at -80˚C until further use, as previously described [180]. For FACS analysis, separate fluorescent (FAM labelled) Aβ$_{1-42}$ preparations enriched in oligomers (Aβoligo) or fibrils (Aβfib) were prepared essentially as described before [150]. Briefly, 100 µg aliquots of Aβ were resuspended, while vortexing, in DMSO that already contained (0.1mg/mL) FAM labelled Aβ (Anaspec). After sonication for 10 min, the sample with an Aβ concentration of 2.5 mM, was split in two. One was dissolved in phenol-red DMEM to 100 µM and incubated at 4˚C for 24 hours to obtain oligomers. The other was dissolved to the same concentration in 10 mM HCl and incubated at 37˚C for 24h to obtain fibrils.

Aβ$_{1-42}$ Preparations for Biophysical studies. The DMSO used to dissolve the Aβ for cell culture studies interferes with UV spectra. As previously described [181], Aβ peptide for biophysical experiments was resuspended in 20% (v:v) NH_4OH, aliquoted and stored at -80ºC. The Aβ in NH_4OH was further diluted to 60 mM NaOH for aggregation and further diluted in either PBS (oligomers) or HCl (fibrils). Therefore, although proportions and procedures were the same as in Aβ for cell culture, no FAM-labelled Aβ or DMSO was used and NH_4OH instead of HFIP was initially used to resuspend the peptide.

In both cases, and in order to assess the effect of scFv-h3D6, apoE-MP and apoJ-MP on Aβ oligomerization and fibrillation, the Aβ monomer preparation was allowed to form either Aβoligo (24h at 4ºC) or Aβfibrils (24h at 37ºC) in the presence or absence of combinations of the different compounds.

Secondary structure and interaction determinations by Circular Dichroism (CD). To analyze the interaction among the molecules studied, equimolar combinations were prepared at 50 µM in

PBS and coincubated for 24h at 4˚C. Incubation and measurement at low temperature limits aggregation and decreases the molecular dynamics characteristic of small peptides, both necessary to get an acceptable signal-to-noise ratio. Protein secondary structure was monitored at 4˚C by far-UV CD spectroscopy from 260 nm to 190 nm in a Jasco J-715 spectrophotopolarimeter. Protein concentration was set to 50 µM, and 20 scans were recorded at 50 nm min^{-1} (response 1s) in a 0.1 cm pathlength cuvette.

Secondary structure determination by Attenuated-Total Reflectance (ATR)-Fourier Transform Infrared (FTIR). Protein/peptides at 50µM in deuterated PBS were N_2-dried onto an ATR-cell and 250 spectra were acquired at a resolution of 2 cm^{-1} and at room temperature in a Variant Resolutions Pro spectrometer.

Transmission Electron Microscopy (TEM). To visualize the extent of aggregation and morphology of the different combinations, samples were diluted to 10 µM in PBS and quickly adsorbed on to glow-discharge carbon-coated grids. TEM was performed in a Jeol 120-kV JEM-1400 microscope, using 1% uranyl acetate for negative staining.

***Cell isolation and culture*.** Adult primary human astrocytes were isolated from brain specimens obtained at surgery (medication-refractory epilepsy) as described before [150,182]. The tissue had to be removed to reach the epileptic focus and was not needed for diagnostic purposes. Normal temporal cortex specimens from 5 patients were used (Table 4.1).

Permission for the use of human brain tissue for in vitro research was granted by the Ethical Medical Committee of the VU University Medical Center (VUmc) in Amsterdam, where the operations took place. Brain tissue specimens were obtained with written informed consent and patient information was treated in accordance with the Declaration of Helsinki.

Isolated astrocytes were cultured in medium containing a mixture of DMEM and HAM-F10 (Gibco) (1:1) supplemented with 10%(v/v) fetal calf serum (Hycult), L-glutamin (2 mM; Gibco), penicillin(100 IU/mL) and streptomycin (50 g/mL) (both Gibco) at 37˚C and 5% CO2[150]. Astrocytes were used up to passage 7.

***Cell Treatment and Flow Cytometry*.** Astrocytes were plated at a density of 25-50,000 cells per well in a 24-well plate. Cells were allowed to adhere for 48h before exposure to different preincubation mixtures of scFv-h3D6/apoE-MP/apoJ-MP and Aβ. After 18h, cell culture supernatant was collected, centrifuged (300xg for 5 min) and stored at -20˚C until further analysis. Cells were rinsed with PBS and 0.2 % trypan blue was added (for 2 minutes) to quench the signal of extracellular Aβoligo and Aβfib. Then, cells were rinsed again with PBS and

harvested using 0.25% trypsin (w:v), centrifuged for 5 min at 300xg and washed three times in cold FACS buffer (0.25% BSA in PBS(w:v). Cellular Aβ-uptake of FAM-labeled $A\beta_{1-42}$ was quantified using flow cytometry (FACS) as described before[150]. The percentage of Aβ positive astrocytes, 10,000 counted cells per condition, was quantified using the FACS Calibur (BD Biosciences, San Jose, CA) with the CellQuest software. Cells were gated based on morphological appearance (forward and side scatter) to count all viable cells and exclude cellular debris and dead cells.

Statistics. Statistical analysis was performed using Graphpad 6. Differences among the various treatments were assessed with a paired t-test using raw data. All data were expressed as means ±SEM values and a *P* value of <0.05 was considered to reflect statistical significance.

RESULTS

Secondary structure of scFv-h3D6, Aβ, apoE-MP and apoJ-MP.

Characterization of the secondary structure of each of the molecules involved in this study is required to next identify interacting partners. CD was recorded at 4˚C to decrease the molecular dynamics characteristic of small peptides, to get an acceptable signal-to-noise ratio, and to partially prevent aggregation of the Aβ peptide. ATR-FTIR allows the measurement of protein aggregates. Figure 4.1A shows far-UV CD spectra at 4˚C for these molecules. ScFv-h3D6 spectrum displays the canonical signatures for an all-β protein, a minimum at 218 nm and a maximum at around 200 nm. In addition, the spectrum shows a minimum at 230 nm and a positive shoulder at 237 nm that have been previously assigned to the particular contribution of the Trp residues in the core of the variable domains to the far-UV region[163]. The Aβ peptide spectrum has a very low signal, but undoubtedly its shape is that of the combination of random coil (minimum at 198 nm) and β-sheet (minimum at 218 nm) conformations (see inset in Figure 4.1A)[183]. As expected from the NMR structure of the full-length apoE [45], the apoE-MP spectrum shows a pure α-helix conformation, with the typical minima at 222 nm and 208 nm. The apoJ-MP spectrum is singular, the signal is positive, because it was synthetized from D-aa to prevent proteolysis *in vivo* of this short and unstructured peptide. Therefore, the spectrum is the mirror-image of the expected for an L-isomer and corresponds to a random coil conformation. This concurs with a minimal helicity previously described for this peptide in the same conditions (13%)[174], which is reported to increase in the presence of lipids [184].

Figure 4.1B shows ATR-FTIR spectra in the amide I' region for the different molecules studied. Samples were pre-incubated at either 4˚C or 37˚C to get oligomers or fibrils, respectively, before acquiring the spectra at room temperature. When pre-incubated at 4˚C, the scFv-h3D6 spectrum is centered at 1638 cm^{-1}, which is indicative of the prevalence of the native β-sheet component, as we previously described in depth[99,102]. The Aβ peptide spectrum is rather flat, and assignment of its components is challenging. The apoE-MP spectrum is centered at 1650 cm^{-1}, which fits with the prevalence of an α-helix component. The apoJ-MP spectrum is wider and could fit a random coil conformation. The spectra changed their shape depending on the temperature at which previous incubation was done in the case of Aβ (Figure 4.1C) and apoJ-MP (Figure 4.1F) but not for scFv-h3D6 nor apoE-MP (Figure 4.1D-E). This fact makes sense since the conformation of small or unstructured peptides is quite temperature-dependent. For Aβ, pre-incubation of the preparation at 37˚C induced the appearance of two separate components characteristic of amyloid fibrils, located at around 1680 and 1620 cm^{-1}. ApoJ-MP spectrum

slightly shifted to lower frequencies, which could be indicative of some extent of aggregation at 37˚C.

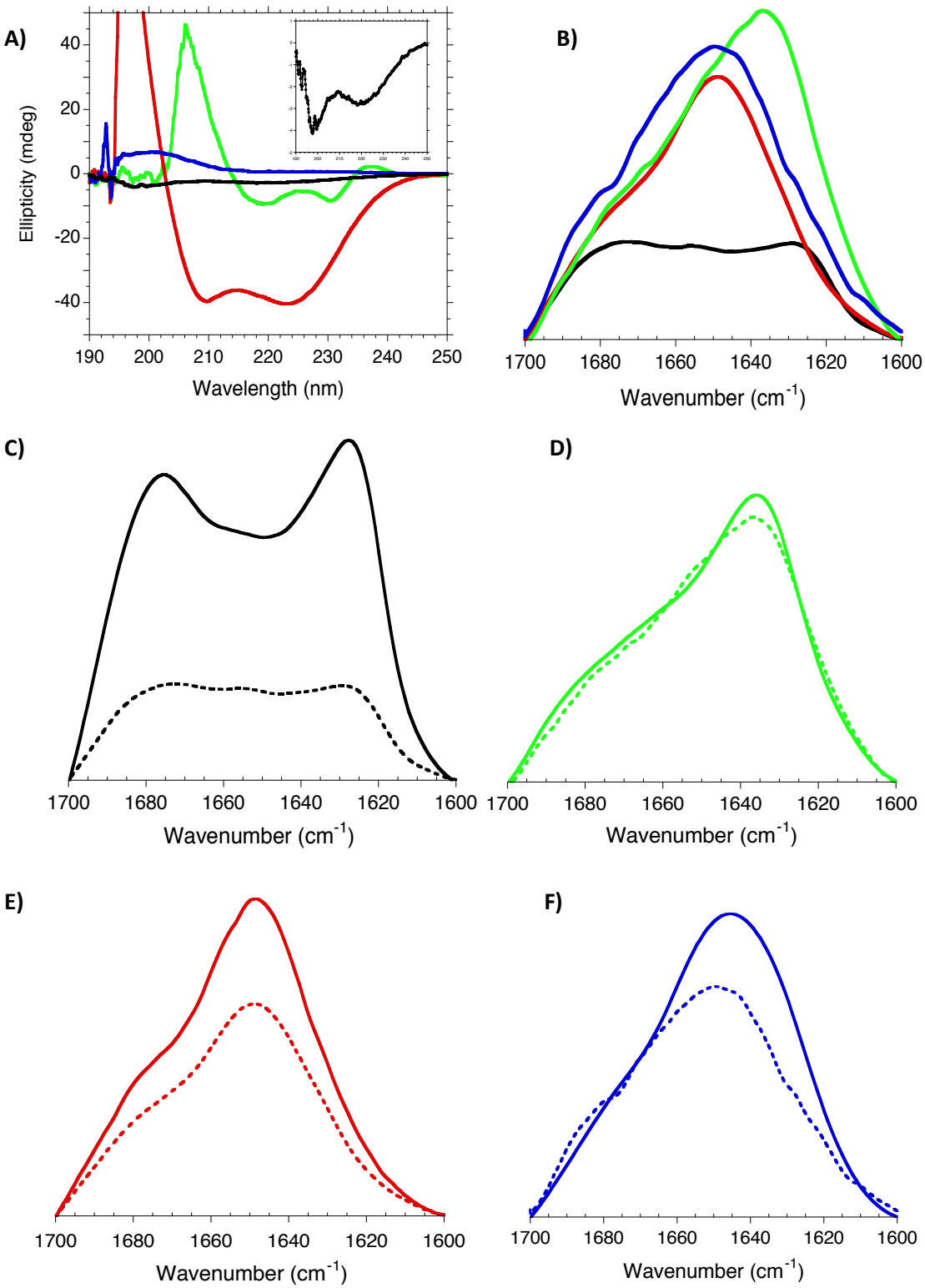

Figure 4.1. Secondary structure of the different molecules assayed. (A) Circular Dichroism and (B) ATR-FTIR spectra of Aβ peptide (black), scFv-h3D6 (green), apoE-MP (red) and apoJ-MP (blue) at 4˚C. The inset in (A) shows the CD spectrum of the Aβ peptide in a smaller scale. (C-F) ATR-FTIR spectra of samples incubated at 4˚C (dotted lines) and 37˚C (continuous lines) of (C) Aβ, (D) scFv-h3D6, (E) apoE-MP and (F) apoJ-MP.

Interactions among scFv-h3D6, Aβ, and apoE-MP or apoJ-MP.

One of the advantages of CD spectroscopy is that the arithmetic sum of two spectra may overlap the experimental spectrum of the equimolar mixture if there is no interaction. If interaction exists, the docking of both molecules may change their conformation so that the experimental and the arithmetic spectra would differ. It is important to note that the conformational change induced by binding can be too small to be detected by this methodology, and it does not correlate with the strength of the interaction. However, when the conformational changes are detected by CD, the interaction unequivocally exits. On the other hand, differences between the experimental CD-spectrum and the arithmetic sum are indicative of aggregation of the complex if the experimental spectrum is similar in shape but less intense than the sum. Figure 4.2 shows the spectra for several combinations of scFv-h3D6, apoE-MP, apoJ-MP and Aβ assayed.

ScFv-h3D6 was not detected interacting with either apoE- or apoJ-MP (Figure 4.2A-B), but as expected it was with Aβ (Figure 4.2C). ApoE-MP also interacted with Aβ (Figure 4.2D). The conformational change was faint when mixing apoJ-MP and Aβ, plausibly due to the small size of the apoJ-MP (10 residues) and/or to a weak interaction (Figure 4.2E).

When combining scFv-h3D6, apoE-MP and Aβ, the obtained spectrum is different from the sum of the three individual spectra (Figure 4.2F). To hypothesize on the nature of the complex, we compared the sums of the experimental spectra for the different pairs assayed and the third component. Only the sum of the spectra for apoE-MP+Aβ and scFv-h3D6 differed from the other spectra (Figure 4.2F). This would indicate that apoE-MP sequesters Aβ and does not allow it to interact with scFv-h3D6, which may prevent the formation of protective WL fibrils (see below). When combining scFv-h3D6, apoJ-MP and Aβ, the obtained spectrum differs from the sum of the three individual spectra (Figure 4.2G). When comparing the sum of the experimental spectra for the different pairs and the third component, the differences are displayed by the sum of the spectra for scFv-h3D6+Aβ and apoJ-MP, which, at first glance, would indicate that the interaction scFv-h3D6/Aβ predominates. However, because the previous observation of the possibility that the small size of apoJ-MP does not induce a huge conformational change, makes other complementary information necessary (see below).

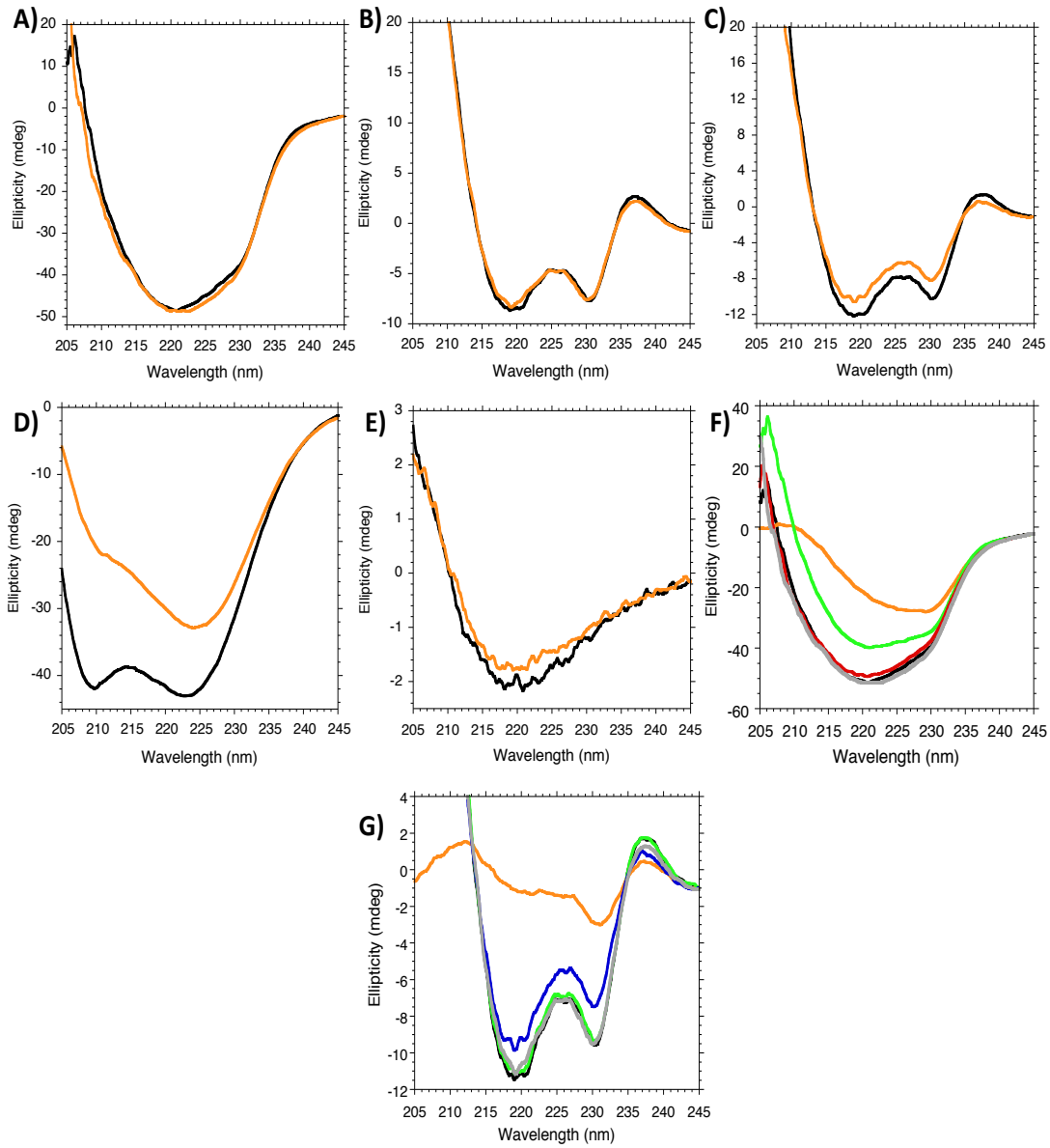

Figure 4.2. Interactions assessed by Circular Dichroism. Arithmetic sum of the spectra of each molecule alone (black) *vs* experimental spectra of different mixtures (orange). (A) scFv-h3D6+apoE-MP; (B) scFv-h3D6+apoJ-MP; (C) scFv-h3D6+Aβ; (D) apoE-MP+Aβ; (E) apoJ-MP+Aβ; the conformational change is evident for apoE-MP+Aβ (D); clear for scFv-h3D6+Aβ (C), and faint for apoJ-MP+Aβ (E). The sum of the experimental spectra for the different pairs assayed and the third component are compared in F-G. (F) Arithmetic sum scFv-h3D6+apoE-MP+Aβ, black; Experimental scFv-h3D6+apoE-MP+Aβ, orange; Experimental (scFv-h3D6+Aβ) + apoE-MP, red; Experimental (apoE-MP +Aβ) + scFv-h3D6, green; Experimental (apoE-MP+scFv-h3D6) + Aβ, grey. The sum of the experimental spectra for the apoE-MP+Aβ mixture and scFv-h3D6 (grey) is the different one, indicating that apoE-MP sequesters Aβ and does not allow it to interact with scFv-h3D6. (G) Arithmetic sum scFv-h3D6+apoJ-MP+Aβ, black; Experimental scFv-h3D6+apoJ-MP+Aβ, orange; Experimental (scFv-h3D6+Aβ) + apoJ-MP, blue; Experimental (apoJ-MP +Aβ) + scFv-h3D6, dotted line; Experimental (apoJ-MP+scFv-h3D6) + Aβ, dotted/dashed line. The sum of the experimental spectra for the scFv-h3D6+Aβ mixture and apoJ-MP (dashed line) is the different one, indicating that the interaction scFv-h3D6/Aβ predominates.

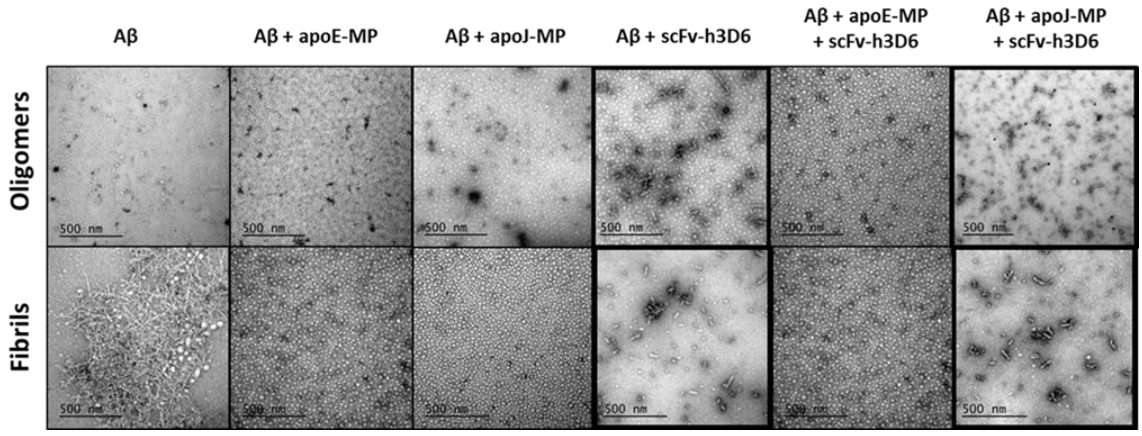

Figure 4.3. TEM micrographs. To visualize the extent of aggregation and the morphology of the different combinations, samples were diluted to 10µM in PBS and quickly adsorbed on to glow-discharge carbon-coated grids. Transmission electron microscopy was performed in a Jeol 120-kV JEM-1400 microscope, using 1% uranyl acetate for negative staining. Worm-like fibrils are outlined.

As mentioned above, the scFv-h3D6/Aβ complex aggregates as WL fibrils and this is the molecular basis of its protective effect [31]. It is interesting to notice that the formation of WL fibrils is an intrinsic property of the scFv-h3D6, and that such an aggregation pathway is thermodynamically and kinetically favoured when the scFv-h3D6 and Aβ form a complex, explaining how the scFv-h3D6 withdraws Aβ oligomers from the amyloid pathway and, consequently, how cytotoxicity is avoided. Therefore, we aimed at assessing the formation of WL fibrils in preparations of Aβ oligomers or fibrils and all combinations of scFv-h3D6, apoJ-MP and apoE-MP by TEM (Figure 4.3). In the presence of apoE-MP and scFv-h3D6, Aβ oligomers had a globulomer-like appearance, supporting the CD experiments conclusion that apoE-MP sequesters Aβ and precludes the scFv-h3D6/Aβ interaction and the subsequent formation of WL fibrils. ApoJ-MP induced a faint conformational change when binding to Aβ and no such a change was observed when mixing with scFv-h3D6. When the three molecules were together the interaction between scFv-h3D6 and Aβ was the strongest one, as judged from the formation of WL fibrils (Figure 4.3 (oligomers)). The Aβ peptide alone clearly formed amyloid fibrils, when incubated according to the protocol for fibril formation. No amyloid fibrils could be observed (Figure 4.3 (fibrils)), when Aβ was allowed to form fibrils in the presence of apoE-MP or apoJ-MP. This means that both MPs bind Aβ. When scFv-h3D6 and Aβ were preincubated, WL fibrils were formed, also in the presence of apoJ-MP, but not when apoE-MP was involved, as was seen with oligomers. Therefore, TEM results were the same for oligomers than for fibrils and concur with CD data, showing that apoE-MP interferes WL fibril formation by binding the Aβ peptide whereas apoJ-MP does not. As a consequence, the faint conformational change detected by CD when mixing apoJ-MP and Aβ would be due to a weak interaction rather than to a small conformational change upon binding.

Uptake of Aβoligo by astrocytes in the presence of scFv-h3D6 and apoE-MP or apoJ-MP.

To assess the effect of scFv-h3D6, apoE-MP and apoJ-MP in Aβ oligomerization and fibrillation, and their consequences in Aβ uptake, the preparations of Aβoligo and Aβfibrils were prepared as in the TEM experiments (Figure 4.3). Aβoligo and Aβfibrils were tested at a 10 μM concentration, and apoE-MP and apoJ-MP at a concentration of 1 μM (ratio 10:1), found to be the most effective concentration to test full-length human apolipoproteins E and J in previous studies [182]. ScFv-h3D6 was tested in a range of different concentrations (0, 1, 5, and 10 μM), and a dose-dependent effect on Aβ uptake by adult human astrocytes was observed (data not shown). One μM concentration of ScFv-h3D6 was chosen for further experiments, because it reduced Aβ uptake to levels in which additional effects of apolipoprotein E and J could still be detected.

Table 4.1. Brain Tissue Donor Characteristics. Demographics of patients who underwent surgery for therapy resistant epilepsy where normal. Neocortex was removed to reach the epileptic focus and was not needed for diagnostic purposes. Astrocytes isolated from these specimens were used for the Aβ uptake experiments.

ADULT HUMAN PRIMARY ASTROCYTE CULTURES				
CASE #	**GENDER**	**AGE (YEARS)**	**APOE GENOTYPE**	**PASSAGE NUMBER**
1	**Female**	**42**	**E2/E3**	**5**
2	**Male**	**19**	**E3/E4**	**4**
3	**Female**	**21**	**E3/E3**	**4**
4	**Female**	**53**	**E3/E3**	**3**
5	**Female**	**31**	**E3/E3**	**5**

Five independent experiments were performed using human primary astrocytes from five different patients (Table 4.1). By use of flow cytometry, we quantified the fraction of Aβ-positive astrocytes after 18h of exposure to either fluorescently labelled Aβ oligomers or fibrils, formed in either absence or presence of the different peptides and/or protein. Figure 4.4A shows how oligomeric Aβ uptake is reduced when Aβ was preincubated with either scFv-h3D6, apoE-MP or apoJ-MP. ScFv-h3D6 was shown to be more effective in reducing uptake (7.6%±2.3) than apoE-MP (22.6%±6.5) or apoJ-MP (38.0%±7.6), probably because it has higher affinity for Aβ than any of the apo-MPs.

When Aβ was preincubated to form oligomers in the presence of scFv-h3D6 and apoE-MP simultaneously, Aβ uptake was significantly increased (17.7%±3.9) compared to scFv-h3D6 alone

(7.6%±2.3), suggesting that apoE-MP is precluding the interaction between scFv-h3D6 and Aβoligo, which makes scFv-h3D6 less effective in reducing Aβ uptake (Figure 4.4A). This concurs with the CD and TEM data above: (i) strong conformational change was induced by apoE-MP and Aβ interaction, and (ii) apoE-MP sequestered Aβ and did not allow it to interact with scFv-h3D6 and, consequently, protective WL fibrils were not observed.

ApoJ-MP did not affect the effect of scFv-h3D6 on uptake (scFv-h3D6 alone (7.6%±2.3) and apoJ-MP+scFv-h3D6 (7.1%±2.7)) (Figure 4.4A). This is consistent with the fact that apoJ-MP was not observed to interact with Aβ in the presence of scFv-h3D6, as inferred by CD and TEM. However, the addition of scFv-h3D6 significantly decreased uptake compared to apoJ-MP alone (38.0%±7.6). Thus, whereas apoE-MP interferes with the scFv-h3D6-induced reduction in Aβoligo uptake by astrocytes, apoJ-MP does not.

Uptake of Aβfibrils by astrocytes in the presence of scFv-h3D6 and apoE-MP or apoJ-MP.

In a previous study, astrocytes were shown bind and ingest Aβoligo more avidly than Aβfibrils[182]. In the current study, we focused on ingested Aβ only, and used trypan blue for quenching the signal of the extracellular Aβ. This reduced the signal (% fluorescence positive astrocytes and mean fluorescence per cell) more pronounced for Aβ fibrils compared to oligomers, probably because fibrils are not easily taken up by astrocytes and remain attached extracellularly. Figure 4.4B shows that in the case of fibrils (Aβ alone) the percentage of Aβ positive astrocytes was 3.8%±0.7, rather low when compared to Aβoligo uptake (Aβ alone in Figure 4.4A: 44.5%±7.7).

When scFv-h3D6, apoE-MP and apoJ-MP were preincubated, alone or combined, with Aβ monomers to form amyloid fibrils, Aβ uptake was increased to much higher levels than uptake of Aβ fibrils alone (Figure 4.4B). Values of the % Aβ positive cells ranged from 30% to 50%, similar to uptake levels of Aβoligo alone. The biggest effect was observed for scFv-h3D6, followed by apoJ-MP, and last apoE-MP. Slightly different results were obtained with Aβ oligomers, where scFv-h3D6 again was most potent, but apoE-MP was more effective than apoJ-MP (Figure 4.4A). This means that apoE-MP more intensely affected the formation of oligomers than fibrils, whereas apoJ behaved opposite. Combinations of scFv-h3D6 and either apoE-MP or apoJ-MP did not enhance Aβ uptake to an equal extent as either factor alone incubated with Aβ fibril preparations. This could be indicative of some competition between these molecules to preclude Aβ fibrillation.

Whether the main species remaining after incubation were monomers, was investigated by increasing the concentration of scFv-h3D6, apoE-MP and apoJ-MP from 1 µM to 2.5 µM, and their effect on Aβ uptake and fibrillation was monitored. At 2.5 µM, scFv-h3D6 reduced Aβoligo uptake from 50.7%±5.9 to 1.8%±0.4, apoE-MP to 2.6%±0.6, and apoJ-MP to 34.6%±10.4 (Figure 4.4C), effects more pronounced than those obtained with 1 µM. The effect of the combination of scFv-h3D6+apoJ-MP (3.7%±2.0) was not significantly different from that of scFv-h3D6 alone, corroborating the small effect of apoJ-MP on Aβ oligo uptake. However, the combination of scFv-h3D6+apoE-MP (8.7%±1.5) increased the uptake with respect to the values obtained with each of the molecules alone. This again points to a competition phenomenon between scFv-h3D6 and apoE-MP for binding Aβ.

No effect of any of these molecules on Aβ fibril was observed, possibly because Aβ fibrils were hardly taken up (1.9%±0.8 Aβ positive cells, when exposed to Aβfibril alone; Figure 4.4D). This suggests that at higher concentrations, scFv-h3D6, apoE-MP, and apoJ-MP, apart from interfering with Aβ fibrillation, also more effectively bind Aβ oligomers and reduce uptake. Therefore, what we are seeing is the interplay between two opposite phenomena: the interference in fibrillation, increasing the concentration of oligomers with respect to the Aβfibrils alone, and the binding of such oligomers precluding uptake.

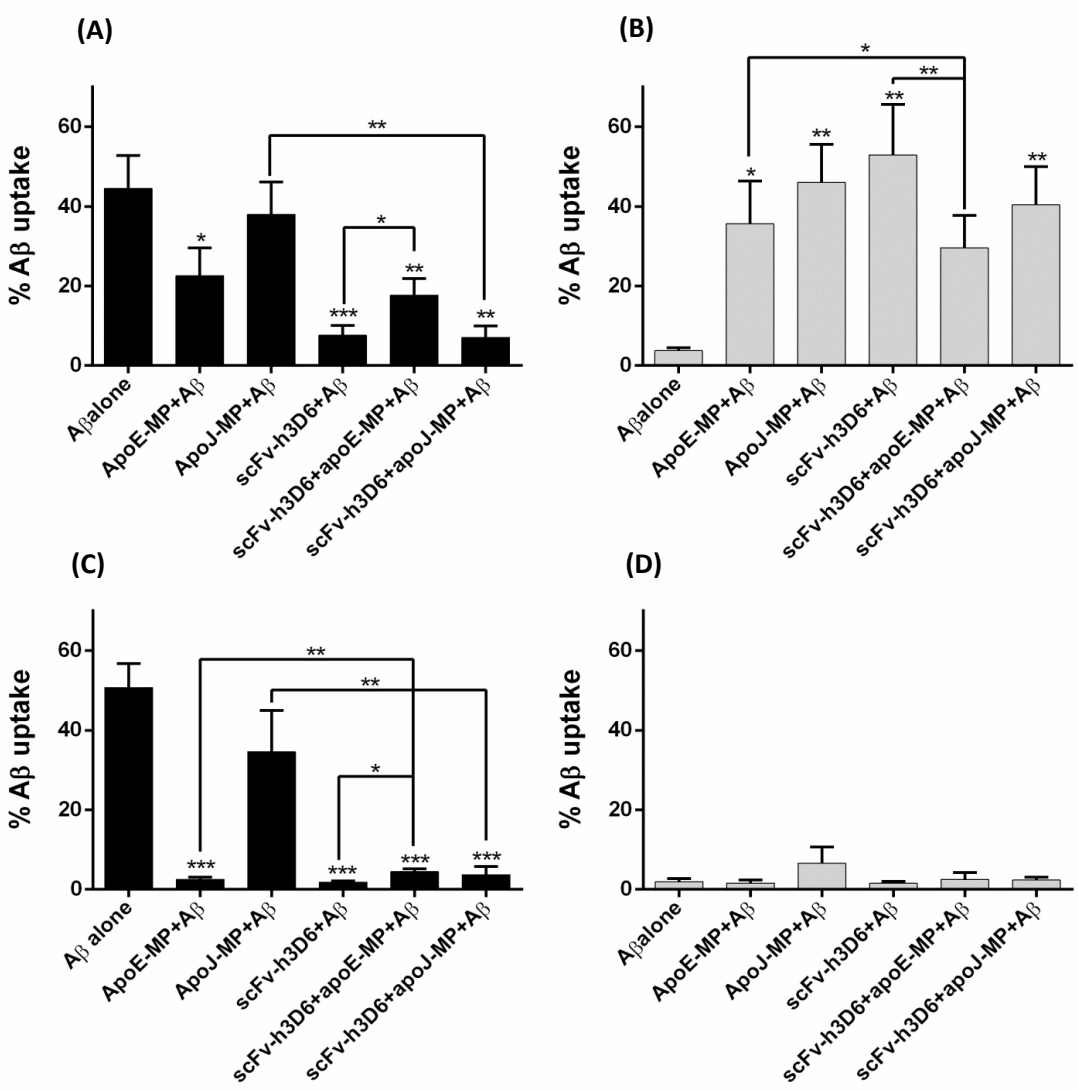

Figure 4.4. Effects of apoE-MP, apoJ-MP and scFv-h3D6 on Aβoligo or Aβfibrils uptake by adult human astrocytes. Effects of apoE-MP, apoJ-MP and scFv-h3D6, either alone or in combination, on Aβoligo (A, C) or Aβfibrils (B, D) uptake by astrocytes. Monomeric Aβ (100 µM) was allowed to aggregate into Aβoligo (24h at 4ºC in phenol-red free DMEM) and Aβfibrils (24h at 37ºC in 10 mM HCl) in the absence and presence of the peptides and/or the antibody fragment. Aβoligo and Aβfibrils were applied to the cells at a fixed concentration of 10µM, as in previous studies, and scFv-h3D6, apoE-MP and apoJ-MP were either tested on the cells at a 1 µM concentration (A and B), or at a 2.5 µM concentration (C and D). Results from a minimum of five individual astrocytes cultures from different patients are presented as means with standard error. Paired t-test was performed. **P*<0.05, ***P*<0.01, ****P*<0.001. Symbols above each column indicate significant changes due to the treatment compared to Aβ alone. Arrows show significance comparing two concrete treatments.

DISCUSSION

ScFv-h3D6 is an Aβ-directed antibody fragment, shown to have therapeutic efficacy in the 3xTg-AD mouse model [100]. Among other beneficences, one single intraperitoneally-administered dose was sufficient to recover the non-pathological levels of the main apolipoproteins in the brain, apoE and apoJ, whose concentrations are rather high in this mouse model [100]. Both apolipoproteins are involved in Aβ clearance [185,186], and we previously hypothesized that they could also be involved in the clearance of the scFv-h3D6/Aβ complex [100]. Astrocytes produce most of the apoE and apoJ in the CNS [38]. Astrocytes are known to also be involved in Aβ clearance, predominantly of small sized oligomers [150]. Because the ingested Aβ above a certain threshold may be toxic, it has been postulated that apoJ and apoE secretion may be a protective mechanism, as apoE [65] and apoJ [187] readily form complexes, and in their presence Aβoligo uptake by astrocytes was found to be strongly reduced [182]. In this work, we have studied the interaction among scFv-h3D6, the Aβ peptide, and apoE or apoJ-MPs to next test the influence of scFv-h3D6 in combination with these MPs on Aβ aggregation and cellular uptake by primary human astrocytes.

The conformation of the molecules used in this study was characterized by CD and ATR-FTIR and all of them were correctly folded. ScFv-h3D6 was not observed to interact with either apoE-MP or apoJ-MP. ApoE-MP clearly interacted with Aβ, but minor effects of apoJ-MP on conformation were observed. This may either have resulted from a very weak interaction between apoJ-MP and Aβ, or even if there was a strong interaction in terms of K_D, minor effects, because the small size of the apoJ-MP is not likely to induce a huge conformational change upon binding. When mixing Aβ, scFv-h3D6 and apoJ-MP, scFv-h3D6/Aβ complexes and ultimately WL fibrils are formed, indicating that the interaction between Aβ and apoJ-MP is rather weak. On the contrary, apoE-MP certainly interacted with Aβ and precluded the formation of WL fibrils. Therefore, at first glance, the combination of scFv-h3D6 with apoE-MP should result in the loss of function of the scFv-h3D6, whereas with apoJ-MP the therapeutic potential remains.

ScFv-h3D6 was more efficient in reducing Aβoligo uptake than apoE-MP or apoJ-MP, as expected from the high affinity of an antibody fragment. In addition to this strong interaction, it is described that the scFv-h3D6/Aβ complex irreversibly aggregates in the form of WL fibrils and thus the trapped Aβoligo cannot be taken up. In the binding of the mimetic peptides to Aβ, apart from displaying lower affinities than scFv-h3D6, the reaction should present some degree of reversibility so that a fraction of Aβoligo could be dissociated from the complex and in that way become free for being taken up. It is already described that apoE significantly decrease uptake

of soluble Aβ by astrocytes [179,182], so that apoE-MP is emulating the function of the full-length apolipoprotein. When scFv-3D6 treatment was combined with apoE-MP, apoE-MP partially precluded the interaction between scFv-h3D6 and Aβoligo and therefore scFv-h3D6 was not so effective in reducing Aβ uptake. ApoJ-MP, which alone decreased Aβoligo uptake although not significantly, showed a value similar to scFv-h3D6 when both molecules were combined so apoJ-MP does not substantially affect Aβoligo uptake by astrocytes.

It is already known that astrocytes take up Aβoligo more avidly than Aβfibrils [150,182]. Here, the uptake of Aβfibrils was 10% that of Aβoligo. In contrast to the inhibitory effects of the peptides on Aβoligo uptake, apoE-MP, apoJ-MP, and scFv-h3D6 at 1 μM increased the uptake of Aβ fibrils by astrocytes. This implies that in the presence of these three molecules, Aβ monomers cannot aggregate to form fibrils probably due to the interaction of the molecules with low molecular weight Aβ aggregates, or even monomers. It is tempting to propose that Aβoligo are neither properly formed in such conditions and therefore free monomers and/or very small-sized oligomers are being taken up. The effect was bigger for scFv-h3D6, than apoJ-MP, and last apoE-MP and this could be related to their capability for precluding fibrillation. It is worth mentioning that apoJ-MP had a significant effect on the formation of fibrils but not of oligomers, which suggests that its chaperone function is more efficient in precluding fibrillation than oligomerization. In this sense, it has been suggested that apoJ can influence transthyretin fibril formation but may not modulate toxicity [188]. In AD, some authors have pointed out that apoJ facilitates amyloid formation [64], while others have shown that it inhibits Aβ fibrillation *in vitro* and promotes the clearance of protein aggregates via endocytosis [65]. ApoE has also been described to prevent Aβ fibrillogenesis [189], as Aβ is able to interact with both the lipid-binding site and the receptor-binding site within apoE [190]. ApoE inhibits Aβ fibril formation regardless its isoform [191,192], but two-fold more Aβ oligomers are formed when the Aβ is coincubated with the pathogenic apoE4 isoform compared to the prevalent apoE3 isoform [193], which suggests that the protective potential of apoE related to prevention of toxic Aβ oligomers formation is impaired in the E4 variant. This would indicate that stabilization of toxic Aβ oligomers at the expense of decreasing protective amyloid fibrils is harmful [194] When combining scFv-h3D6 with apoE or apoJ-MP the increase in Aβ uptake was lower than with each of the three molecules alone, especially for the combination with apoE-MP. This would indicate that the mechanism by which scFv-h3D6 interferes with fibrillation is different from that by the peptides and that both mechanisms are somehow antagonistic.

When the concentration of scFv-h3D6 and MPs was increased from 1 to 2.5 μM, strikingly Aβfibril uptake was reduced to similar levels as Aβfibril alone. Therefore, a higher concentration

of scFv-h3D6, apoE-MP, and apoJ-MP, apart from better preventing Aβ fibrillation, could also more effectively reduce Aβ uptake. This makes sense, since the number of molecules is higher in a preparation of monomers than in a preparation of Aβoligo or Aβfibrils, and so concentration has a great effect because it favors the binding of monomers and/or small-sized oligomers to scFv-h3D6, apoE-MP, and apoJ-MP. In any case, the overall conclusion is that these molecules more intensely interfere with the formation of fibrils than oligomers.

The fact that apoE and apoJ interfere with Aβ fibril formation explains why they are co-localized with Aβ amyloid plaques in AD brain [195]. However, the consequences of preventing fibril formation and how it affects astrocytes, which are also found in amyloid plaques, still remains elusive. In this work, it has been shown that molecules previously described to improve Aβ pathology *in vivo*, apoE-MP and scFv-h3D6, reduce Aβ uptake. Apart from the impaired function generated by an overload of Aβ inside the cell [196,197], it has to be considered that glial cells lose their capability of degrading Aβ with aging and, in the case of AD, with the chronic neuroinflammation associated with the disease [198,199]. Both facts point to a negative effect when inducing Aβ ingestion as an approach to reduce Aβ overburden. Therefore, the traditional idea of designing therapeutic approaches to promote Aβ clearance by glial cells should be carefully re-evaluated. Deviation of Aβ clearance from a cellular uptake pathway towards clearance through BBB or brain-CSF barriers may be more advantageous. ScFv-h3D6, already demonstrated to be effective in the 3xTg-AD treatment, was also shown to reduce astrocytic Aβ uptake in the current study. ScFv-h3D6 possibly does not enhance microglial uptake of Aβ, as complete monoclonal antibodies do, because it lacks the Fc region and because no specific receptors for scFv have been described. This also means that it will probably not compete with receptor-mediated uptake of Aβ, as is the case for apoE with LRP1[179], but presumably acts through the formation of small scFv-h3D6/Aβ complexes that are eliminated by other mechanisms such as drainage from the interstitial fluid from the brain parenchyma towards the CSF.

CHAPTER 5:

Effects on Aβ-induced inflammation of apolipoproteins E and J in combination with scFv-h3D6.

AIMS

Once the apolipoproteins E and J mimetic peptides have been presented, and their interaction with scFv-h3D6 and Aβ determined, in this chapter we aimed to test if these shortened variants had the same effect as the full-length versions. We compared apoE-MP and apoJ-MP with full-length apolipoproteins E and J and also scFv-h3D6 with the complete monoclonal antibody 3D6. In order to have a broader perspective, not only Aβ uptake but also Aβ-induced inflammation have been studied. Accumulation of Aβ peptide is reported to start a chronic glial activation and neuroinflammation that contribute to AD pathology [29–31]. In the brain of both AD individuals and transgenic animal models, Aβ plaques are surrounded by activated glial cells. Activated microglia and astrocytes strongly secrete inflammatory components such as pro-inflammatory cytokines, chemokines, complement components, macrophage inflammatory proteins, reactive oxygen species (ROS), nitric oxide (NO), etc [200,201]. These secreted inflammatory mediators, in turn, activate more microglia and astrocytes to produce inflammatory molecules [202].

Aβ uptake has been determined by flow cytometry and Aβ-induced inflammation, studied by measuring the levels of IL-6 and MCP-1 released by human primary astrocytes, following the research line of the previous chapter. Finally, we combined the different treatments in order to observe mutual effects. In this case, molecules have not been preincubated, as in Chapter 4, but directly added to the well to avoid effects of preformed interacting partners on inflammation.

MATERIALS AND METHODS

Primary human astrocyte cultures. Brain specimens for cell isolations were obtained at surgery through cooperation with the Neurosurgery Department of VU university medical center Amsterdam (VUmc) as described in Chapter 4. Adult primary human astrocytes were isolated from normal temporal cortex specimens from 5 patients, as described before [150,180,182]**.** Isolated astrocytes were cultured as described in Chapter 4 and [180].

Aβ$_{1-42}$ Preparations. Aβ$_{1-42}$ oligomers and fibrils were prepared and characterized by Western blotting as described [150,180]. In short, Aβ$_{1-42}$ (Bachem) was dissolved in hexafluoro-isopropanol (Fluka) to obtain a monomeric Aβ$_{1-42}$ solution, which subsequently was aliquoted, nitrogen flow dried and stored at -80˚C until further use. To obtain fluorescent (FAM labelled) Aβ$_{1-42}$ preparations enriched in oligomers and fibrils, aliquots of 100 ug of Aβ were resuspended in 20 µM FAM labelled Aβ$_{1-42}$ (Anaspec) dissolved in DMSO, resulting in an Aβ concentration of 2.5 mM, and further diluted (100 µM) and incubated, either in phenol-red free DMEM (at 4ºC for 24h) to obtain oligomers, or in HCl (10 mM) (incubation at 37ºC for 24h) to form fibrils.

Humanized monoclonal antibody 3D6. Recombinantly expressed humanized bapineuzumab (3D6; hu-IgG1) was kindly provided by Dr. Mario Losen (Division Neuroscience, Maastricht University, The Netherlands).

ScFv-h3D6 expression and purification**.** ScFv-h3D6 expression and purification were carried out as described in Chapter 3 for scFv-h3D6-Ec.

Apolipoproteins and apolipoprotein-mimetic peptides**.** ApoE (plasma derived; from human VLDL) was obtained from rPeptide (Bogart, GA) and ApoJ was isolated in house from human plasma by affinity chromatography, as described [203].The apoE-MP [173,175] and the apoJ-MP [174], were synthetized by Caslo ApS (Lyngby, Denmark).

Cell Treatment and Flow Cytometry**.** Astrocytes were plated at a density of 25,000-50,000 cells per well in a 24-well plate. Cells were allowed to adhere for 48h and then, exposed to treatment. All compounds to be tested were added directly to the well without preincubation. Fluorescently labeled Aβ oligomers and fibrils at a 10 µM final concentration were added to the cells in the presence of either medium alone, mAb-h3D6 at 1 µM, or scFv-h3D6 at 4 µM, and the % cells containing labeled Aβ, determined. The 4-fold difference in concentration of mAb-h3D6 and scFv-h3D6 used, was based on the difference in number of antigen binding sites and the stability of both molecules. ApoE and apoJ (full-length or mimetics) were added at final concentration of

0, 0.1 and 1 μM, as in previous studies [182]. Aβ and mAb-h3D6/scFv-h3D6/apoE/apoE-MP/apoJ/apoJ-MP were added directly to the cell culture without any previous co-incubation, apart from the formation of Aβ oligomers or Aβ fibrils. The cells were harvested after 18h, and cellular uptake of FAM-labeled $A\beta_{1-42}$ was quantified, using flow cytometry as described before [150,180,182]. In addition, cell-free conditioned culture medium was collected, centrifuged (300xg for 5 min) and stored at -20˚C until further analysis. The percentage of Aβ-positive astrocytes, 10,000 counted cells per condition, was quantified using the FACS Calibur (BD Biosciences, San Jose, CA) with the CellQuest software. Cells were gated based on morphological appearance (forward and side scatter) to count all viable cells and exclude cellular debris and dead cells. For visualization purposes, the results on Aβ uptake alone were set to 100% and the effects of different treatments on Aβ uptake were normalized to Aβ uptake alone.

Enzyme Linked Immuno-Sorbent Assays for IL-6 and MCP-1.To determine astrocytic pro-inflammatory activation and production and secretion of inflammatory factors, conditioned medium from the astrocyte cultures used for flow cytometry analyses was collected and analyzed for MCP-1 release, using the Human CCL2/MCP-1 DuoSet enzyme linked immuno-sorbent assay (ELISA) (R&D Systems), and IL-6 release, assayed with the Pelipair IL-6 ELISA kit (Sanquin). Results are presented as % of MCP-1 or IL-6 release compared to non-treated cells.

Cytotoxicity assay. In order to test toxicity of the compounds used in the current study, LDH levels of the collected supernatants were determined by Pierce LDH cytotoxicity assay kit (ThermoScientific). Results are expressed as percentage considering non-treated cells as 100% viable.

Statistics. Differences among the various treatments were assessed with a paired t-test using raw data. Correlations were investigated using the Pearson correlation test. All data were expressed as means ±SEM values and a *P* value of <0.05 was considered to reflect statistical significance.

RESULTS

Aβ uptake and Aβ-induced inflammation in primary human astrocytes.

The uptake capacity of adult human astrocytes for Aβ oligomers and Aβ fibrils was determined by flow cytometry, after quenching the signal from extracellularly attached Aβ using trypan blue. The percentage of astrocytes that ingested Aβ was higher when exposed to Aβ oligomers (42.7% ±7.5) compared to Aβ fibrils (3.0%±0.6) (Figure 5.1A), in line with earlier findings [150,182].

Human astrocytes secreted higher levels of IL-6 (27.8 fold) and MCP-1 (2.4 fold) upon exposure to Aβ oligomers, but no effect on activation was found for exposure to Aβ fibrils (1.2 and 1.1 folds, respectively; Figures 5.1B-C).

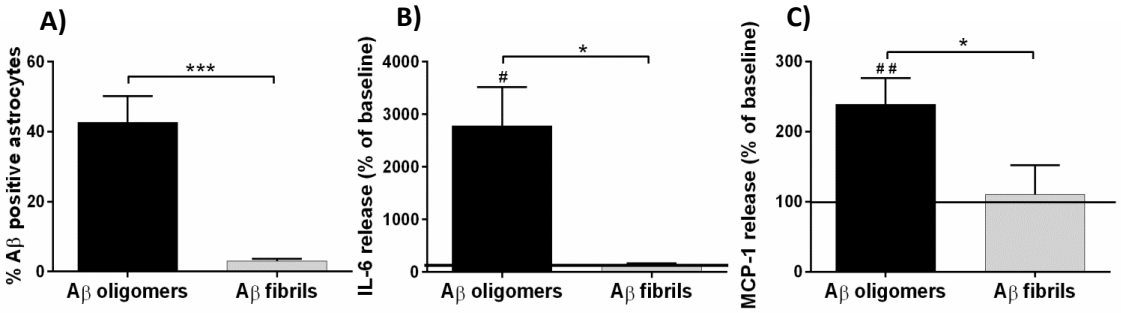

Figure 5.1. Uptake and stimulatory effects of Aβoligo or Aβfibrils on adult human astrocytes. (A) Astrocytes take up Aβoligo more avidly than Aβfibrils. Aβoligo, but not Aβfibrils, induce proinflammatory activation of astrocytes as shown by astrocytic release of IL-6 (B) and MCP-1 (C). In (A) not normalized data is represented for comparing purposes. In (B) and (C) cell-responses from treated cells were compared to baseline levels of cells exposed to medium alone (solid line 100%). In both, results from a minimum of five individual astrocyte cultures are presented as means and standard error (paired t-test). # indicates significance compared to untreated cells and * indicates significance compared to Aβoligo or Aβfibrils.* or # $P<0.05$, ** or ## $P<0.01$, *** or ### $P<0.001$.

Effects of mAb-h3D6 and scFv-h3D6 on Aβ uptake and *on Aβ-induced inflammation.*

First, we tested if the scFv-h3D6, derived from the humanized monoclonal antibody bapineuzumab (mAb-h3D6), has similar effects on Aβ oligomers and Aβ fibrils uptake by primary human astrocytes as intact mAb-h3D6. We found mAb-h3D6 and scFv-h3D6 to reduce Aβ oligomers uptake by human primary astrocytes to 19.3%±5.6 and 8.6%±2.7, respectively, when the percentage of Aβ positive cells in the absence of either mAb-h3D6 or scFv-h3D6 was set at 100%. No significant effect of either mAb-h3D6 (153.7%±25.1) or scFv-h3D6 (84.4%±18.9) on Aβ fibrils uptake was observed compared to uptake of Aβ fibrils alone (set at 100%; Figure 5.2A).

When the inflammatory response was analyzed (Figures 5.2B and 5.2C), no significant effects of either mAb-h3D6 or scFv-h3D6 on Aβ oligomer-induced IL-6 and MCP-1 release were observed.

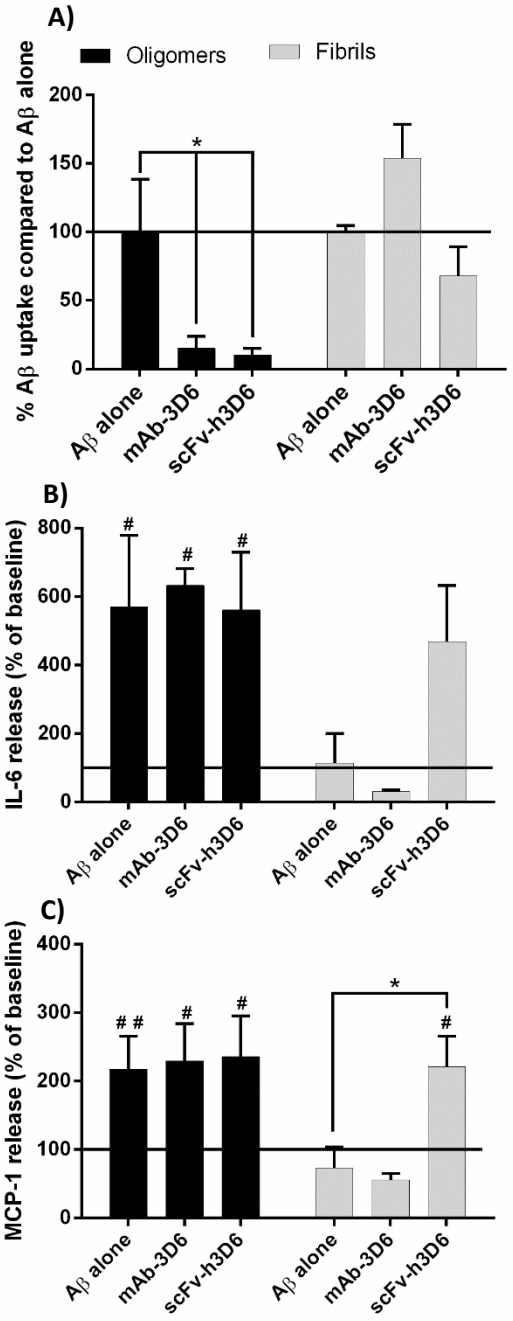

Whereas Aβ fibrils alone had no stimulatory effects on either MCP-1 or IL-6 secretion by the astrocytes, secretion of MCP-1 was significantly increased in the presence of scFv-h3D6 and a trend (*P*=0.14) towards increased IL-6 secretion was observed (Fig. 5.2B,C).

Taken together, both molecules behaved similar in terms of reducing Aβ oligomers uptake, without affecting the Aβ oligomers-induced activation of the astrocytes. In contrast, neither full-length 3D6, nor scFv-h3D6 had significant effects on Aβ fibrils uptake, but scFv-h3D6, and not mAb-h3D6, seemed to induce astrocyte activation (Figure 5.2B and 5.2C).

Figure 5.2. Comparison of the effects of the full-length mAb-3D6 *vs* scFv-h3D6 on adult human astrocytes. (A) Effects on the uptake of Aβ oligomers and Aβ fibrils by adult human astrocytes. Intact mAb-3D6 as well as scFv-h3D6 inhibit the uptake of Aβ oligomers, but have no effect on Aβ fibril uptake. The % fluorescent Aβ-positive cells upon incubation with either Aβ oligomers, or Aβ fibrils, was set at 100%. Effects on the release of IL-6 (B) and MCP-1 (C), as indicators of proinflammatory activation. The IL-6 and MCP-1 release by treated cells was compared to baseline levels of medium-treated cells (set at 100%; solid line). Results from a minimum of three individual astrocyte cultures are presented as means and standard error. $^{\#}P < 0.05$ compared to untreated cells, $^{*}P < 0.05$ compared to cells treated with either Aβ oligomers or Aβ fibrils, $^{\#\#}P < 0.01$.

Effects of mimetic peptides and full-length apoE and apoJ on Aβ uptake.

Previous studies had already demonstrated that Aβ oligomers and Aβ fibrils uptake by astrocytes is reduced in the presence of apolipoproteins E and J [182]. Here, we compared the effect of apoE-MP and apoJ-MP with the full-length apolipoproteins on Aβ uptake by primary adult human astrocytes in order to assess their therapeutic potential.

Aβ oligomers or Aβ fibrils preparations (10 μM) were applied to the cells simultaneous with apoJ or apoE full-length or mimetic peptides (MP). ApoE-MP and apoJ-MP were tested in concentrations ranging from 0.01 to 1μM (similar to full-length apoE and apoJ in previous studies [150,180,182]).

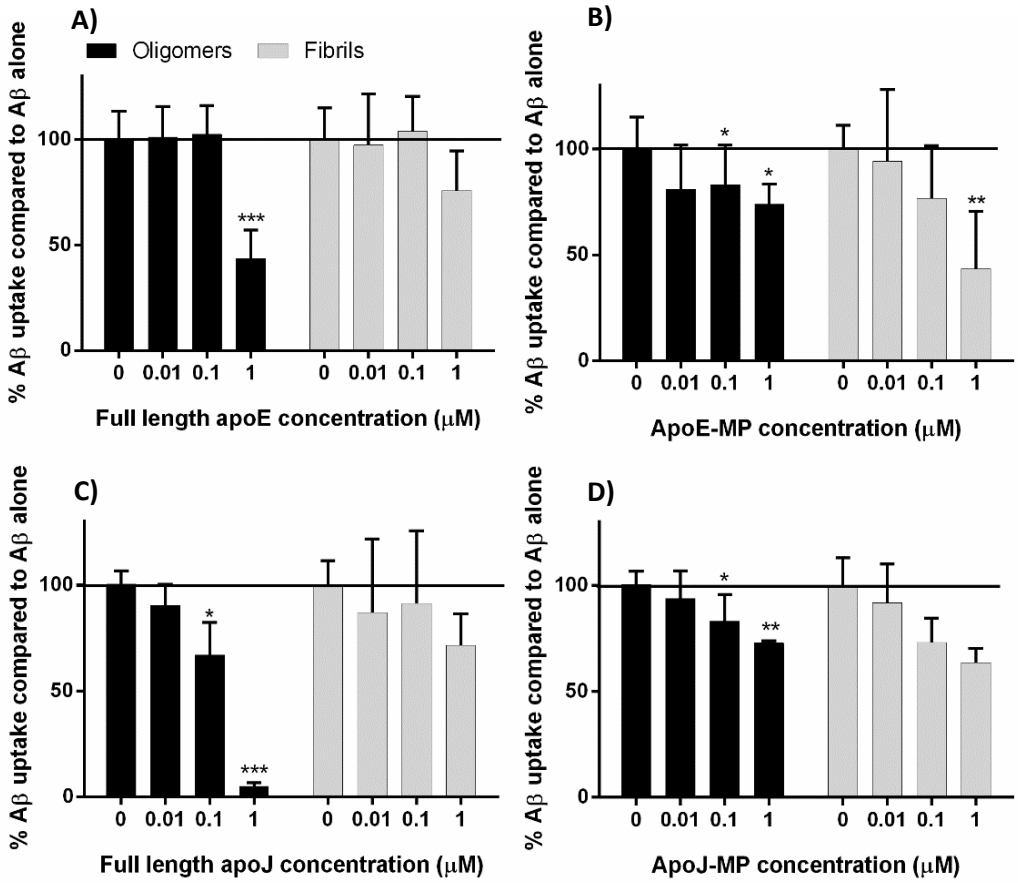

Figure 5.3. Comparison of the effects of full-length apolipoproteins and mimetic peptides on Aβ oligomer and Aβ fibril uptake by primary human astrocytes. Aβ oligomers (black) and Aβ fibrils (grey) were added to the astrocytes either in the absence or the presence of (A) full-length apoE, (B) ApoE-MP, (C) full-length apoJ, or (D) ApoJ-MP. The Aβ oligomers and Aβ fibrils (final concentration of 10 μM) were added to the cell culture simultaneously with the apolipoproteins and mimetic peptides, tested at a range from 0.01 to 1 μM, without any previous preincubation. Uptake of Aβ alone was set to 100%. Results from a minimum of five individual astrocytes cultures are presented as means with standard error. **P*<0.05, ***P*<0.01, ****P*<0.001.

All four apolipoprotein variants dose-dependently inhibited Aβ oligomers uptake, with the highest concentration (1 μM apolipoprotein variants *vs* 10 μM Aβ; ratio 1:10) having the most

pronounced effects (Figure 5.3). Plasma-derived apolipoproteins and the mimetic peptides had similar, but not exactly the same effects. Full-length apolipoproteins showed a higher reduction in uptake at the same concentration than the mimetic peptides. ApoE and apoJ at a concentration of 1 μM reduced Aβ oligomers uptake by astrocytes to 43.4% and 10.8%, respectively (Figure 5.3A,C), whereas apoE-MP and apoJ-MP reduced uptake to 73.7% and 72.8%, respectively (Figure 5.3B,D). Although the effect of mimetic peptides is less pronounced at 1 μM, it is noteworthy that in the case of apoE, the mimetic peptide reduced uptake of Aβ oligomers to 81% at a lower concentration (0.1 μM), whereas the full-length apoE had no effect (100%). Also in this sense, the lowest concentration of apoE-MP assayed (0.01 μM) showed a trend (*P*= 0.062) towards reducing Aβ oligomers uptake.

When apoE and apoJ, as well as their MP, were tested for effects on Aβ fibrils uptake, no significant effects on Aβ uptake were seen, except for significantly reduced Aβ fibrils uptake in the presence of apoE-MP at 1 μM (Figure 5.3B).

Effects of mimetic peptides and full-length apoE and apoJ on Aβ-induced inflammation.

To determine if inhibition of Aβ uptake by the astrocytes also leads to changes in their pro-inflammatory response induced by Aβ aggregates, the effect of apolipoproteins and mimetic peptides on the Aβ aggregate-induced IL-6 and MCP-1 release was determined.

The increased secretion of IL-6 by astrocytes upon treatment with Aβ oligomers was to a large extent abolished by treatment with both apoE and apoE-MP (from 500% activation to 200% activation; at 1 μM) (Figure 5.4A,B). No such decrease was seen with either full length or MP apoJ; instead, full-length apoJ induced IL-6 release at the highest dose assayed (1 μM) (Figure 5.4C,D). ApoE and apoE-MP had no significant effect on Aβ fibril-induced IL-6 release by the astrocytes, neither did apoJ-MP, but, as in the case of Aβ oligomers uptake, full-length apoJ-MP induced IL-6 release at the highest dose assayed (1 μM) (Figure 5.4).

In contrast to IL-6, MCP-1 release was not significantly affected when the astrocytes were exposed to Aβ oligomers in the presence of either apoE or apoE-MP, except for the downregulatory effect at the highest dose of apoE-MP (1 μM) (Fig 5.5B).

Only astrocytes treated with Aβ oligomers at the highest dose of apoJ (1 μM) secreted higher amounts (266.5% of baseline values) of MCP-1 compared to cells exposed to Aβ oligomers alone,

whereas apoJ-MP inhibited the Aβ oligomers-induced MCP-1 release at all the concentrations assayed (Fig. 5C,D).

No clear effects on MCP-1 secretion in the presence of Aβ fibrils were observed, except for an increase in MCP-1 release when in combination with full length apoJ at the highest dose (1 μM) (Figure 5.5C).

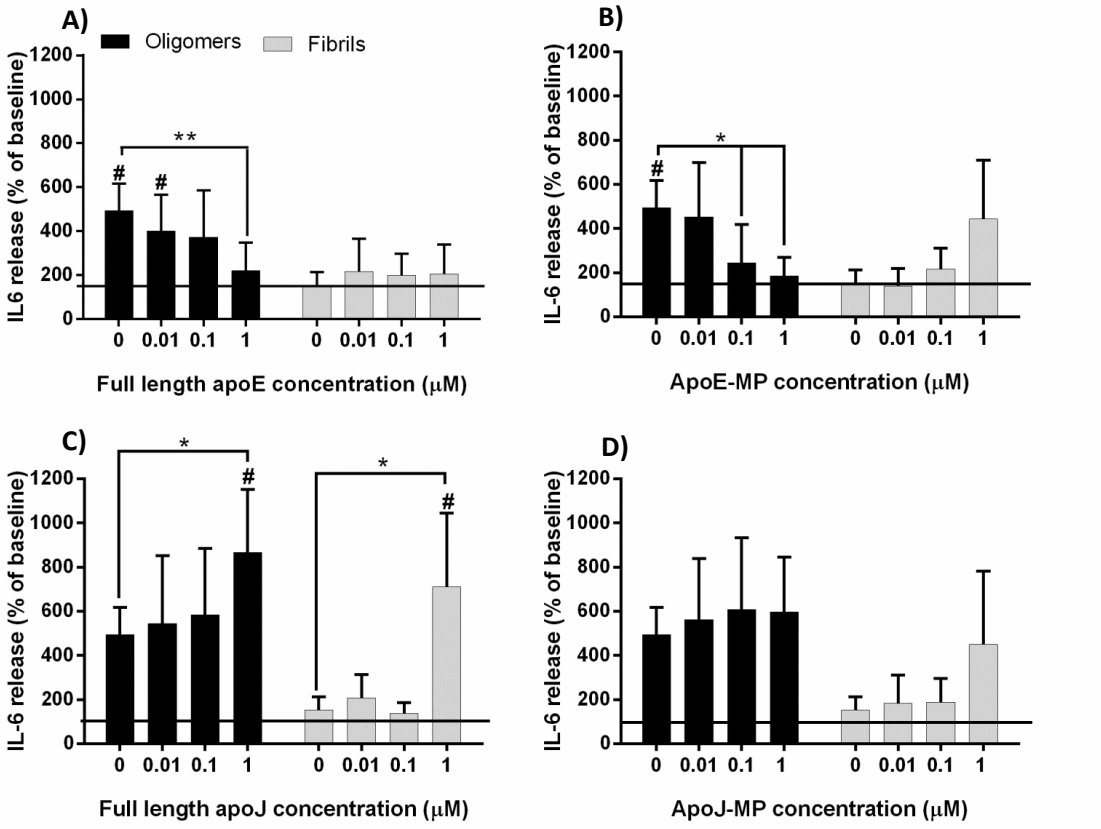

Figure 5.4. Comparison of the effects of full-length apolipoproteins compared to mimetic peptides on IL-6 release by primary human astrocytes. Astrocytes were exposed to Aβ oligomers (black) or Aβ fibrils (grey), either in the absence or presence of (A) full-length apoE, (B) ApoE-MP, (C) full-length apoJ, or (D) ApoJ-MP. IL-6 release by treated cells was compared to baseline levels secreted by cells exposed to medium alone (set at 100%; solid line). Results from a minimum of five individual astrocytes cultures are presented as means with standard error. $^{\#}P < 0.05$ compared to untreated cells, $^{*}P < 0.05$ compared to Aβ oligomer or Aβ fibril exposed cells, $^{**}P < 0.01$.

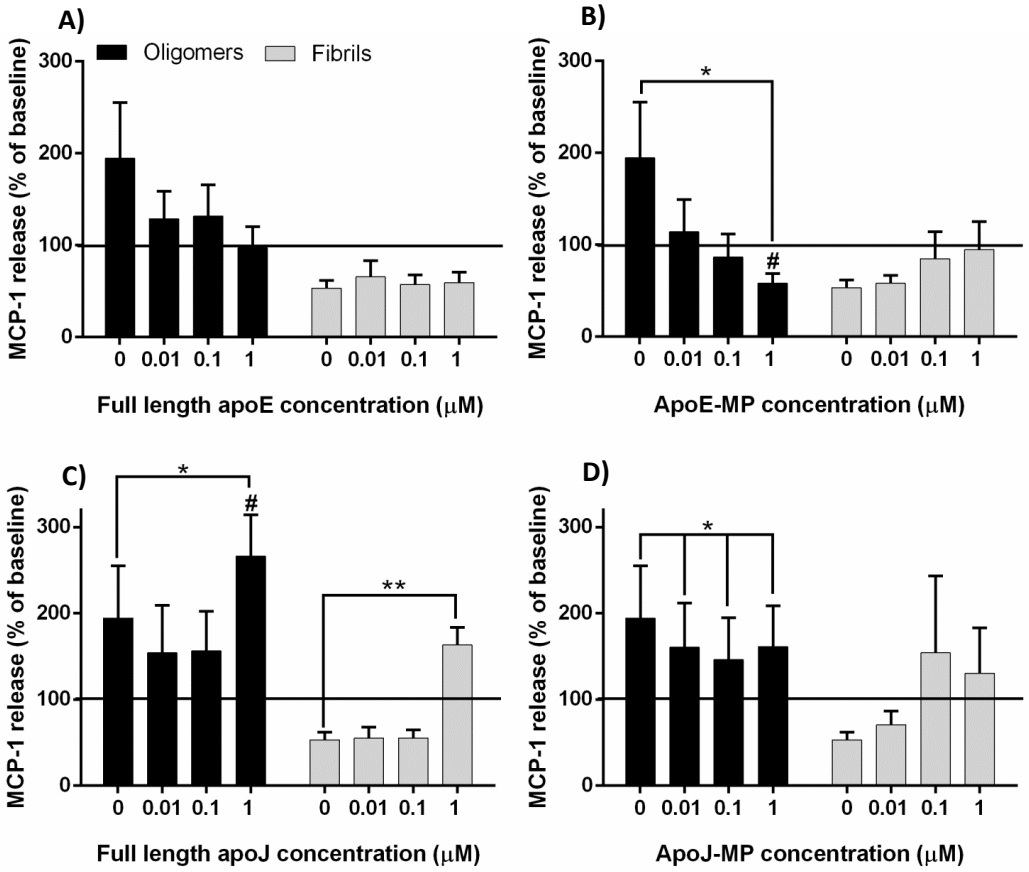

Figure 5.5. Comparison of the effects of full-length apolipoproteins compared to mimetic peptides on MCP-1 release by adult human astrocytes. MCP-1 release by astrocytes exposed to Aβ oligomers (black) or Aβ fibrils (grey), in combination with either (A) full-length apoE, (B) ApoE-MP, (C) full-length apoJ, or (D) ApoJ-MP, was compared to baseline levels of cells exposed to medium alone (set at 100%; solid line). Results from a minimum of five individual astrocytes cultures are presented as means with standard error. Paired t test was performed. $^{\#}P < 0.05$ compared to untreated cells, $^{*}P < 0.05$ compared to Aβoligo or Aβfibrils alone, ** $P < 0.01$.

Combined effects of scFv-h3D6, apoE-MP and apoJ-MP on Aβ uptake and Aβ-induced inflammation.

Because apoE-MP and apoJ-MP had similar effects on Aβ uptake and Aβ-mediated astrocyte activation as full-length apoE and apoJ, we used the MPs in further studies to determine their effect in combination with scFv-h3D6.

Aβ fibrils or Aβ oligomers were added (10 μM) to the human astrocytes simultaneously with different combinations of scFv-h3D6, apoE-MP or apoJ-MP (all at 1 μM), and effects on Aβ oligomers and Aβ fibrils uptake, as well as on Aβ-induced activation of the astrocytes were determined. Figures 5.6A and 5.6B show how Aβ uptake was affected by the presence of scFv-h3D6, apoE-MP and apoJ-MP, alone or combined. All of them show a decrease in Aβ oligomers uptake, as previously mentioned. No additive effects on Aβ uptake were observed when scFv-

h3D6, apoE-MP or apoJ-MP (all at 1 μM) were added to the cells simultaneously with Aβ oligomers or Aβ fibrils.

The activation of astrocytes by Aβ oligomers was not affected by treatment with scFv-h3D6 or apoJ-MP, as judged from the unchanged levels of secreted IL-6 and MCP-1 (Figures 5.6C and 5.6E). In contrast, apoE-MP reduced IL-6 and MCP-1 release to levels similar to those secreted by untreated cells (119.8% and 85%, respectively), as was previously observed with the full-length apoE (Figures 5.4A and 5.5A). When apoE-MP was added to the cell culture in combination with scFv-h3D6, the lowering effects of the apoE-MP on IL-6 and MCP-1 release (138.0% and 94.4%, respectively) remained similar, which demonstrates that the anti-inflammatory effect of apoE-MP is not abrogated in the presence of scFv-h3D6 in this conditions.

Aβ fibrils alone did not significantly induce activation of the astrocytes, however in combination with scFv-h3D6, Aβ fibrils induced the secretion of IL-6, an effect that was counteracted by the presence of apoE-MP, but not of apoJ-MP (Fig 5.6 D), suggesting different functional properties of the apoE-MP and apoJ-MP.

To investigate if variations in cell viability account for the observed effects, LDH release from the exposed astrocytes was determined in the culture supernatants collected after 18h. No differences in LDH release were appreciated between cells untreated and treated with scFv-h3D6, apoE-MP and/or apoJ-MP at 1 μM concentrations (Figure 5.7).

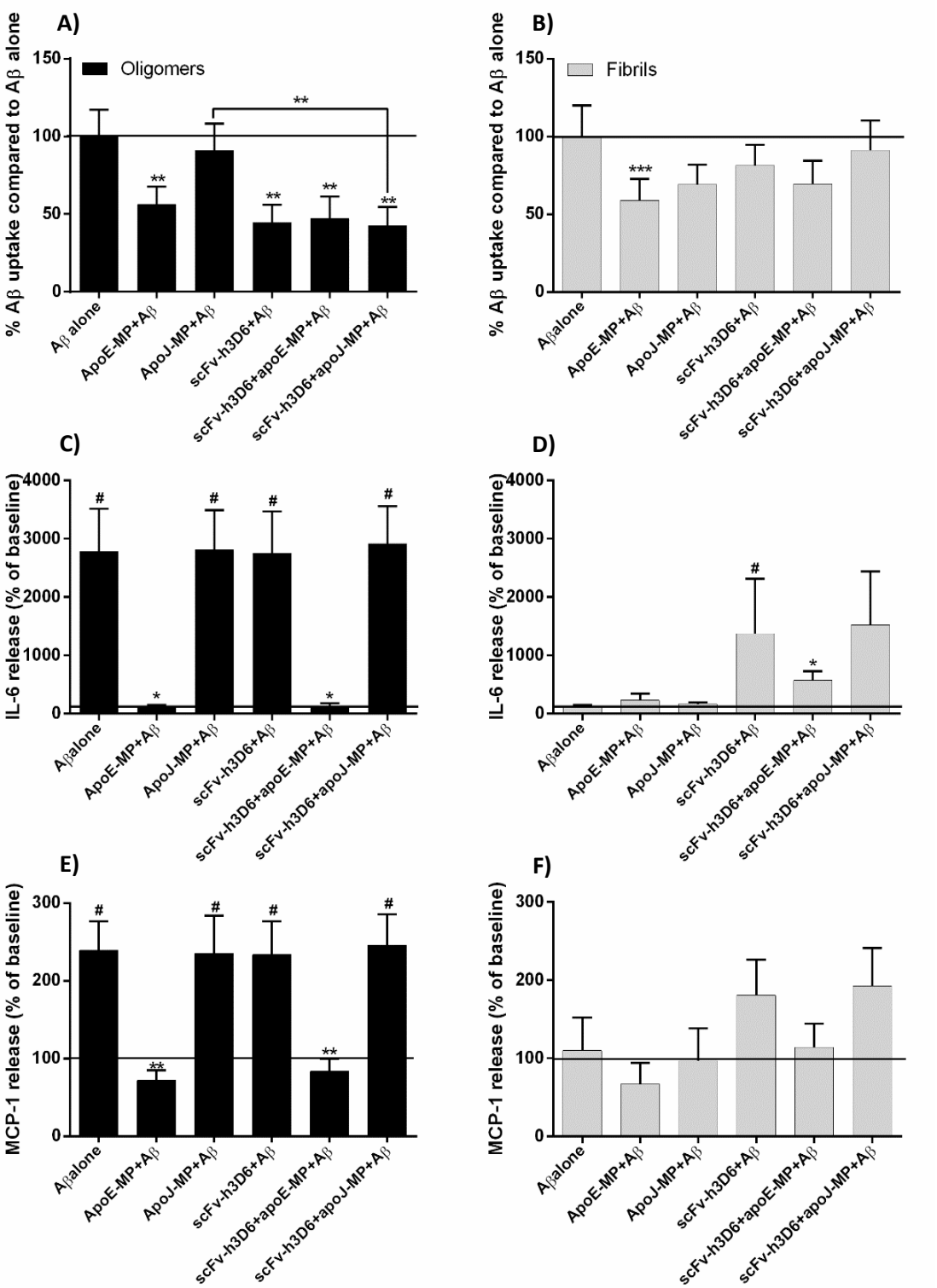

Figure 5.6. Effects of scFv-h3D6, apoE-MP and apoJ-MP, alone or combined, on the uptake of Aβ oligomers and Aβ fibrils as well as on the release of inflammatory mediators by primary human astrocytes. (A) Uptake of oligomers, (B) uptake of fibrils, (C) IL-6 release in the presence of oligomers (D) IL-6 release in the presence of fibrils, (E) MCP-1 release in the presence of oligomer, and (F) MCP-1 release in the presence of fibrils. In (A) and (B) the % fluorescent Aβ - positive cells upon incubation with either Aβ oligomers, or Aβ fibrils, was set at 100%. In (C), (D), (E) and (F) cell-responses from treated cells were compared to those of untreated cells (baseline value set at 100%; solid line). Results from a minimum of five individual astrocytes cultures are presented as means with standard error. $^{\#}P < 0.05$ compared to untreated cells and *P < 0.05 compared to Aβ oligomer or Aβ fibril treated cells, ** $P < 0.01$, *** $P < 0.001$.

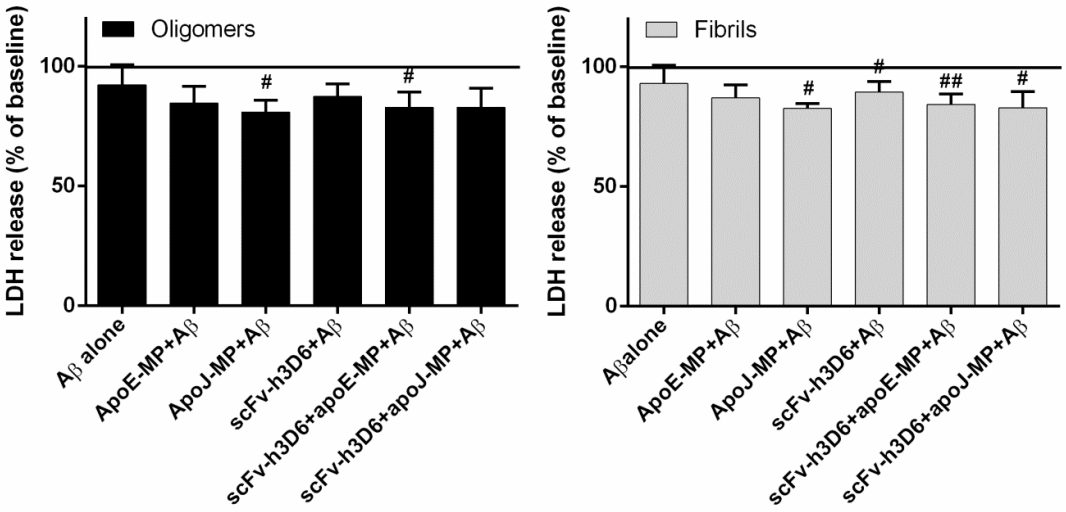

Figure 5.7. LDH release as indicator of toxicity. To determine possible effects on cell viability, the LDH release of astrocytes exposed to Aβ oligomers (A), and Aβ Fibrils (B) in the presence or absence of scFv-h3D6 and /or MPs was compared to that of medium treated cells (set at 100%; solid line). Results from a minimum of five individual astrocyte cultures are presented as means and standard error. # $P < 0.05$ compared to untreated cells, $^{\#\#}P < 0.01$. No significant increase in LDH release was observed effects on cell viability was observed with any of the treatments.

DISCUSSION

Long term exposure to increased levels of Aβ may lead to impairment of astrocyte and neuronal functioning and to reduced synapse functioning, which are early events in AD etiology [204]. The increase in local levels of Aβ results from decreased Aβ clearance from the brain parenchyma, rather than an increase in Aβ formation in sporadic, late onset AD [33]. Clearance mechanisms include diffusion towards CSF and choroid plexus, transport across the BBB, and uptake and lysosomal degradation by glial cells [196,205]. Therapeutic strategies aimed at increasing the uptake of Aβ by especially microglia, upon either passive or active immunization against Aβ, have yielded disappointing results because, despite positive effects on Aβ load and cognition, side effects including meningoencephalitis and vasogenic edema were encountered [81,206,207]. Since these effects were related to the FcγR-dependent activation of glial cells, we engineered a single chain antibody fragment (scFv-h3D6) composed of the variable domain of the heavy chain linked to the variable domain of the light chain of bapineuzumab [99,102]. This scFv-h3D6 was found to be neuroprotective *in vitro* when SH-SY5Y neuroblastoma cells were exposed to Aβ and *in vivo* in the 3xTg-AD mouse model, where Aβ load was reduced and learning and memory deficits ameliorated. In addition, scFv-h3D6 administration reduced the apoE and apoJ levels that are raised in the 3xTg-AD mice, to normal [100,101].

The aim of the current study was to investigate the effects on Aβ uptake by human astrocytes and on Aβ-mediated astrocyte activation of scFv-h3D6 alone or in combination with mimetic peptides (MP) of the AAPs apoE and apoJ, because there is an urgent need for therapeutic compounds that enhance oligomeric Aβ clearance without initiating an inflammatory process, and because astrocytes are the first in line to clear Aβ from the brain parenchyma.

Astrocytes are the predominant cell type in the brain and have traditionally been described as playing a supportive role for neurons [205], including glucose transporter (GLUT1)-mediated uptake of glucose and conversion into lactate to be utilized by neurons as an energy source [208]. Aβ binding to and uptake by astrocytes down-regulates GLUT1 expression on the astrocytic end feet in the synaptic area, which affects glutamate reuptake and synaptic glutamate levels, and triggers excitotoxic pathways [209–211]. In the present study, adult human astrocytes were found to more readily ingest Aβ oligomers than Aβ fibrils (Figure 5.1A), in line with previous findings [150,180,182].

When clearance mechanisms are impaired, the accumulation of Aβ aggregates initiates a neuroinflammatory process, as can be concluded from the increased levels of the pro-

inflammatory factors IL-6 and MCP-1 in AD brain tissues extracts and their co-localization with neurons as well as astrocytes [212]. A study on rat astrocytes suggested differential effects of oligomeric and fibrillar $A\beta_{1-42}$ on astrocyte-mediated inflammation [213]. We now also observed in human primary astrocytes that the cells are activated to release the pro-inflammatory factors IL-6 and MCP-1, when incubated with Aβ oligomers but not in the presence of Aβ fibrils (Figures 5.1B and 5.1C). This also correlates with the fact that the oligomeric and protofibril forms of Aβ are the crucial toxic species, as several studies have pointed out that soluble Aβ levels are better correlated with cognitive deficits than amyloid plaques [25,26].

Aβ-Immunotherapy aims to reduce Aβ toxic species burden in order to prevent the progress of the pathological alterations caused by Aβ accumulation. In the current work, we have studied the effect of a full-length monoclonal antibody (mAb-h3D6, bapineuzumab) and its single-chain variable fragment (scFv-h3D6). We have observed that scFv-h3D6 reduces Aβ oligomers uptake and shows a trend to reduce Aβ fibrils, while mAb-h3D6 reduces oligomer uptake by primary human astrocytes but shows a trend to increasing fibril uptake. Therefore, it is likely that the binding of the mAb-3D6 and scFv-h3D6 to the relatively small Aβ oligomers prevents their uptake. The increase in Aβ fibrils uptake induced by the full-length mAb-3D6 could be indicative of the ability of the mAb to remove those fibrils attached to cell receptors without being internalized, or alternatively that the full-length mAb intercalates with the Aβ fibrils, in such a way that smaller sized oligomeric and monomeric Aβ are generated and can be ingested by the cells. This does not seem the case for the scFv-h3D6. Also in this sense, albeit no differences were observed in the presence of Aβ oligomers, mAb-3D6 shows a tendency in reducing IL-6 and MCP-1 release in the presence of Aβ fibrils, while scFv-h3D6 increased it. The mechanism behind the activation of astrocytes in the presence of scFv-h3D6 and Aβ fibrils could be related to the decrease in uptake, but further experiments should be performed to unravel this question. In any case, immunotherapy is aimed to prevent the disease progression rather than treat patients in an advanced stage of the disease, which symptoms seem to be irreversible, as demonstrated in recent studies [70]. Effectiveness in trapping toxic oligomers must be the key of the protective effect behind these molecules.

Astrocytes are the main producers of apoE and apoJ in the CNS [214,215]. In previous studies, Aβ clearance by glial cells was found to be negatively affected by apoE and apoJ [182]. In the present study, we used mimetic peptides instead of full-length apoE and apoJ because of their higher potential as therapeutics for AD. This is so because apoE-MP and apoJ-MP are homogenous in composition and easily obtained by chemical synthesis, while keeping characteristics. In contrast, plasma derived apolipoproteins exist in different isoforms and degrees of

posttranslational modification, and obtaining them for therapeutic purposes is not a straightforward procedure.

Here, we have observed that both, full-length or mimetic peptide, apoE variants reduce Aβ oligomers uptake, although the full-length apoE was more efficient that its mimetic peptide. Aβ fibrils uptake was found to be reduced in the presence of apoE-MP, but not with the full-length apoE. Full-length apoE as well as apoE-MP reduced the Aβ oligomers-induced IL-6 and MCP-1 release by astrocytes (Figures 5.4 and 5.5), similarly to the effect observed in previous cell culture and *in vivo* studies [173,177,216]. ApoE was shown in the bibliography to downregulate CNS production of TNFα, IL-1β and IL-6 following stimulation with LPS [217], and Aβ-induced activation was attenuated by the addition of exogenous apoE-containing particles. In addition, glial cells cultured from apoE-knockout mice exhibited an enhanced production of several pro-inflammatory markers in response to treatment with Aβ and other activating stimuli [218]. Also, administration of apoE-MP to APP/PS1ΔE9 mice significantly reduced the numbers of activated microglia and astrocytes in immunostained brain sections [173].

Although apolipoprotein J is clearly implicated in AD and *APOJ* repeatedly identified in high-throughput genotyping analyses as a genetic determinant of AD [219,220], little is known about the exact role this apolipoprotein plays in AD pathogenesis. The apoJ-MP was found to exert similar effects as the full-length apoJ on Aβ uptake and Aβ-induced inflammation (increased IL-6 and MCP-1 release), however apoJ-MP was far less potent than the full-length apoJ concerning the inhibitory effect on Aβ oligomers uptake (Figure 5.3).These results suggest that in the case of Aβ oligomers, mimetic peptides cannot block Aβ interaction with cell surface receptors as efficiently as the full-length apolipoproteins; probably due to their smaller size and stability, but, in the case of Aβ fibrils, their smaller size probably allows them to better interact and disrupt the fibrils' architecture.

When combinations of Aβ, scFv-h3D6 and apolipoproteins-MP were directly added to the well, no influence of molecules on each other's effect was observed in uptake, as it happened in Chapter 4; where apoE-MP partially interfered with the scFv-h3D6-induced reduction in Aβ-uptake by astrocytes, whereas apoJ-MP did not. However, this study cannot be directly compared, since in Chapter 4 extensive preincubation of the involved molecules was required in order to assess interactions among them and their effect on amyloid fibril formation *in vitro*.

The Aβ oligomers-induced cytokine release by astrocytes was only reduced in the presence of apoE-MP, also when apoE-MP was combined with scFv-h3D6. The fact that all molecules studied inhibit Aβ uptake, whereas only apoE (full-length or MP) reduces Aβ-induced inflammation,

suggests that apoE exerts its effect by a mechanism that does not involve blocking uptake of Aβ oligomers. Probably apoE is inducing its anti-inflammatory effect by interacting with specific receptors. Experiments using receptor associated protein (RAP), an inhibitor of apoE receptors with a differential affinity for the low-density lipoprotein receptor (LDLR) and the LDLR-related protein receptor (LRP1), revealed that LRP1 mediates Aβ-induced glial activation, while LDLR mediates the Aβ-induced changes in apoE levels [218]. However, Tai *et al.* recently proposed the hypothesis that apoE modulates Aβ-induced effects on inflammatory receptor signaling; specifically, impaired apoE4 function and signaling via the apoE receptors causes amplification of detrimental TLR4-p38α, and suppression of beneficial IL-4R nuclear receptor, resulting in an adverse neuroinflammatory profile [221].

From previous data and data obtained in the current study, it can be concluded that apoE reduces Aβ uptake probably by blocking receptors rather than interacting with Aβ and this may probably be the mechanism by which it protects against neuroinflammation. On the other hand, scFv-h3D6 and apoJ-MP might reduce uptake by interacting with Aβ. In the case of scFv-h3D6, it is already demonstrated that a single intraperitoneal dose dramatically reduces oligomers in the cortex of 3xT-AD young females [100] . In the case of apoJ, this idea is supported by the fact that apoJ/Aβ complexes are found in the CSF [222], while apoE and Aβ have been found to hardly associate in physiological conditions [179]. In addition, preparations of human cortical synaptosomes were shown to contain lower apoE/Aβ levels in AD patients compared with controls [223].

The combination of scFv-h3D6, which transforms potentially synaptotoxic Aβ oligomers into harmless worm-like fibrils, with apoE or apoJ MPs that prevent the uptake of the Aβ-complexes by glial cells, holds potential for further testing. This is especially worthy for the combination of scFv-h3D6 with apoE-MP, whose anti-inflammatory properties have been evidenced.

CHAPTER 6:

In vivo study of the effect of scFv-h3D6 in combination with apolipoprotein E or J mimetic peptides on Aβ pathology and inflammation.

AIMS

Previous chapters have described which are the interactions among Aβ, scFv-h3D6, and apoE-MP or apoJ-MP, and their effects in Aβ uptake and Aβ-induced activation in human primary astrocytes. This chapter aims to extrapolate these results to the *in vivo* level.

Four and a half month-old 3xTg-AD mice females have been treated for six weeks with either scFv-h3D6, apoE-MP or apoJ-MP, and the combinations of scFv-h3D6 with each of the mimetic peptides, and compared to non-transgenic (NTg) mice as to refer to non-pathological conditions. Determination of how the different treatments affect Aβ pathology, glial inflammation and endogenous apolipoproteins E and J levels is presented.

As previously explained, apoE-MP and apoJ-MP have been used *in vivo* with different animal models. ApoE-MP is already reported in the literature to improve cognition, decrease amyloid plaque deposition and reduce the number of activated microglia and astrocytes in the APP/PS1ΔE9 mice[173]. The apoJ-MP, has been suggested as a therapy for inflammatory disorders [224] and shown to be effective in reducing inflammation and atherosclerosis in apoE-null mice [174]. As far as we know, this is the first work testing a combined therapy of these mimetic peptides with an anti-Aβ antibody fragment.

MATERIALS AND METHODS

Mice and treatment. All the experiments were approved by the UAB Animal Research Committee and the Government of Catalonia, and performed in accordance with the Guide for the Care and Use of Laboratory Animals published by the US National Institutes of Health. Triple-transgenic (3xTg-AD) mice females harboring PS1/M146V, APPSwe and tauP301L transgenes and non-transgenic (NTg) mice with the same genetic background (B6129SF2/J) (both purchased from Jackson Laboratories and stablished at the UAB animal facility) were used. Animals of the same genotype and sex were maintained in cages (Makrolon, 35 × 35 × 25 cm) under standard laboratory conditions (food and water *ad lib*, 22 ± 2°C, 12 h light: dark cycle starting at 08:00). Animals received intraperitoneal (i.p.) injections three times per week for 6 weeks, beginning at the age of 4.5 months. Thirty-six 3xTg-AD animals were distributed in six groups (n=6) as follows: apoE-MP, apoJ-MP, scFv-h3D6, apoE-MP+scFv-h3D6, apoJ-MP+scFv-h3D6 and vehicle (PBS). A NTg group (n=6) was administered vehicle (PBS) for the same period and frequency in order to have a reference of non-pathological conditions. Doses for each treatment were calculated based on previous studies in the literature: 80 μg of apoE-MP per week (40 μg/day, twice a week), 50 μg of apoJ-MP per week (25 μg/day, twice a week) and 100 μg of scFv-h3D6 (100 μg/day, once a week) (Table 6.1). Taking into account that two groups required three administrations per week (apoE-MP+scFv-h3D6 and apoJ-MP+scFv-h3D6), all groups were injected three times per week (saline in absence of treatment) so that all groups were subjected to the same stress.

Table 6.1. Mice treatment in this experiment.

GENOTYPE	GROUPS	DAY 1	DAY 2	DAY 3	DAY 4	DAY 5
3xTg-AD	**ApoE-MP**	ApoE-MP	Vehicle	-	-	ApoE-MP
	ApoJ-MP	ApoJ-MP	-	-	Vehicle	ApoJ-MP
	ScFv-h3D6	-	Vehicle	ScFv-h3D6	Vehicle	-
	ApoE-MP+scFv-h3D6	ApoE-MP	-	ScFv-h3D6	-	ApoE-MP
	ApoJ-MP+scFv-h3D6	ApoJ-MP	-	ScFv-h3D6	-	ApoJ-MP
	Vehicle	-	Vehicle	Vehicle	Vehicle	-
NTg	**Vehicle**	-	Vehicle	-	Vehicle	Vehicle

All protein and peptides injections were prepared in saline under sterile conditions. During the treatment, veterinary staff monitored animals for any signs of toxicity, such as changes in body weight, physical appearance, and altered behavior. Five days after the last administration, animals were anesthetized with inhaled isofluorane (1% in O_2), sacrificed (at the age of 6 months), and brains were collected and dissected. One hemisphere was kept for histological analysis and the other one was used for protein extraction.

ScFv-h3D6 expression and purification. ScFv-h3D6 expression and purification were carried out as described in Chapter 3 for scFv-h3D6-Ec.

Lipopolysaccharides detection. Endotoxin units (EU) concentration (EU/mL) of the purified protein was determined by Pierce LAL Chromogenic Endotoxin Quantitation Kit (Thermo Scientific), following manufacturer's instructions. The concentration of endotoxins in the scFv-h3D6 was EU/mL=25.02±4.45. Protein was administered intraperitoneally at a concentration of 0.5 mg/mL and a total volume of 0.2 mL (5.0 EU/injection). According to FDA, for medical devices that directly or indirectly contact the cardiovascular and lymphatic systems the limit is 20 EU/device, consequently, the administrated protein presents an endotoxin level that is under the limit.

***Apolipoprotein E and J mimetic peptides*.** The apoE-MP has the sequence: LRKLRKRLLRDWLKAFYDKVAEKLKEAF [173,175] and the apoJ-MP is formed by D-isomers of residues LVGRQLEEFL [174]. Both MPs were synthesized protected at both terminus and at >95% purity by Caslo laboratories (Denmark).

Protein Extracts. The extraction was prepared by sequential centrifugation of brain subregions homogenates as previously described [100]. Briefly, frozen tissues of hippocampus and cortex from 5-mo-old 3xTg-AD and NTg mice used in the experiment were weighted and mechanically homogenized in ice-cold TBS supplemented with protease inhibitors (Roche tablet 1836153) (8 µL TBS/mg tissue). Then, samples were gently sonicated (1 cycle of 35 sec, at 35% duty cycle and output 4 in a Dynatech Sonic Dismembrator ARTEK 300 with the smallest tip), centrifuged at 100,000 g for 1h at 4°C, and the collected supernatant was labeled as the extracellular protein TBS fraction. Subsequently, the insoluble pellet was dissolved to the same volume and rehomogenized in cold TBS-1% Triton X-100 solution supplemented with protease inhibitors and centrifuged again; the supernatant was labeled as the intracellular protein 1% Triton fraction. All of the fractions were aliquoted and stored at −80°C until its use.

Cholesterol and hepatic enzymes determination. Cholesterol, Aspartate aminotransferase (AST) and Alanine aminotransferase (ALT) levels in plasma were determined by a commercial enzyme-colorimetric method (CHO2, ASTL and ALTL; Roche Diagnostics) and a autoanalyzer (Cobas c501/6000), according to manufacturer's instructions.

Aβ$_{42}$, IL-33, apoE and apoJ ELISA. Brain extracts were used to analyze differences in Aβ, IL-33, apoE and apoJ levels in the cortex and hippocampus of each experimental group. Kits were purchased to Invitrogen (Aβ$_{42}$), R&D systems (IL-33), and USCN Life (apoE and apoJ). Procedures were performed according to the manufacturer's protocols. Data obtained were normalized by the total amount of protein in each extract, as measured by BCA assay (Pierce).

Immunohistochemistry*.* Paraformaldehyde-fixed sections (cut at 10 µM) were deparaffined and treated with citrate buffer at 100˚C for 20 min for antigen retrieval. To quench endogenous peroxidase, sections were incubated with 3% H_2O_2 in methanol for 10 min. Then, sections were washed and permeabilized in 0.1% Tween-PBS followed by blocking in 5% normal goat serum (Sigma-Aldrich), 5% BSA (Sigma-Aldrich) and 0.1% Tween-PBS. After blocking, sections were incubated with primary antibody GFAP (Wako) or Iba-1 (Wako) overnight at 4ºC. The next day, sections were washed and immunostained with Rabbit Extravidin Peroxidase Staining kit (Sigma-Aldrich) and developed by diaminobenzidine (DAB) substrate. Sections were cover-slipped using DPX mounting medium (Sigma-Aldrich) and examined in a Leica DMRB Microscope equipped with the Leica Application Suite (LAS) software.

Image Quantification. ImageJ was used for image quantification. Anti-GFAP immunostained sections were quantified at 5x zoom in and Iba-1 at 10x. Light Background was subtracted and images were converted to 8bit images. Then, light background was subtracted again and images were converted to binary. Next, particles were analyzed with limits for size and circularity. Mean of marked area percentage is given.

Statistics. Statistical analysis was performed using Graphpad 6 software. Mann-Whitney test was performed to compare effects of each treatment against the control 3xTg-AD-Vehicle. All data are expressed as means ± SEM values and a *P* value of <0.05 was considered to reflect statistical significance.

RESULTS

Cholesterol and hepatic enzymes levels in plasma.

Because apolipoproteins E and J are also involved in systemic lipid metabolism, we determined total cholesterol levels in plasma of each animal. No significant differences were observed with any of the treatments, not even between the 3xTg-AD-vehicle and NTg-vehicle groups (Table 6.2). Previous studies already reported no alteration of lipid metabolism in this mouse model [225,226]. Hepatic enzymes such as aspartate aminotransferase (AST) and alanine aminotransferase (ALT) were also investigated in order to report any toxicity caused by the repeated administration of any of the treatments. No significant differences among the groups were detected either.

Table 6.2. Cholesterol and hepatic enzymes levels in plasma. Values are presented as mean±SEM.

GROUP	TOTAL CHOLESTEROL (mM)	AST[1] (U/L)	ALT[2] (U/L)
ApoE-MP	0.91±0.06	117.26±14.09	22.92±2.83
ApoJ-MP	1.27±0.12	145.15±19.34	50.28±11.50
ScFv-h3D6	1.13±0.06	139.0±11.38	35.73±1.40
ApoE-MP+scFv-h3D6	1.19±0.10	76.75±5.35	20.35±6.83
ApoJ-MP+scFv-h3D6	0.80±0.11	112.27±20.76	25.53±8.58
3xTg-AD-Vehicle	1.08±0.23	178.22±54.72	25.65±3.68
NTg-Vehicle	1.22±0.10	93.55±13.80	21.45±4.62

[1]Aspartate aminotransferase (AST), [2]Alanine aminotransferase (ALT).

Determination of Aβ burden in the hippocampus and cortex.

Previous studies demonstrated that a single intraperitoneal dose of scFv-h3D6 globally decreased Aβ oligomers burden in the 3xTg-AD mouse model. In this Thesis Dissertation, we also showed that scFv-h3D6, apoE-MP and apoJ-MP reduce Aβ uptake by human primary astrocytes. Here, total $A\beta_{42}$ burden in the brain homogenates of hippocampus and cortex was quantified by ELISA (Figure 6.1). The protein extracts were prepared by sequential centrifugation of brain subregions homogenates, first with ice-cold TBS and, after ultracentrifugation, the pellet was resuspended with Triton X-100 in TBS. TBS fraction will be called extracellular fraction and TBS Triton X-100, intracellular fraction.

At first sight, it can be observed that the intracellular levels of $A\beta_{42}$ of the 3xTg-AD-vehicle group, especially in the hippocampus, were higher than those in the extracellular fraction (P=0.03).

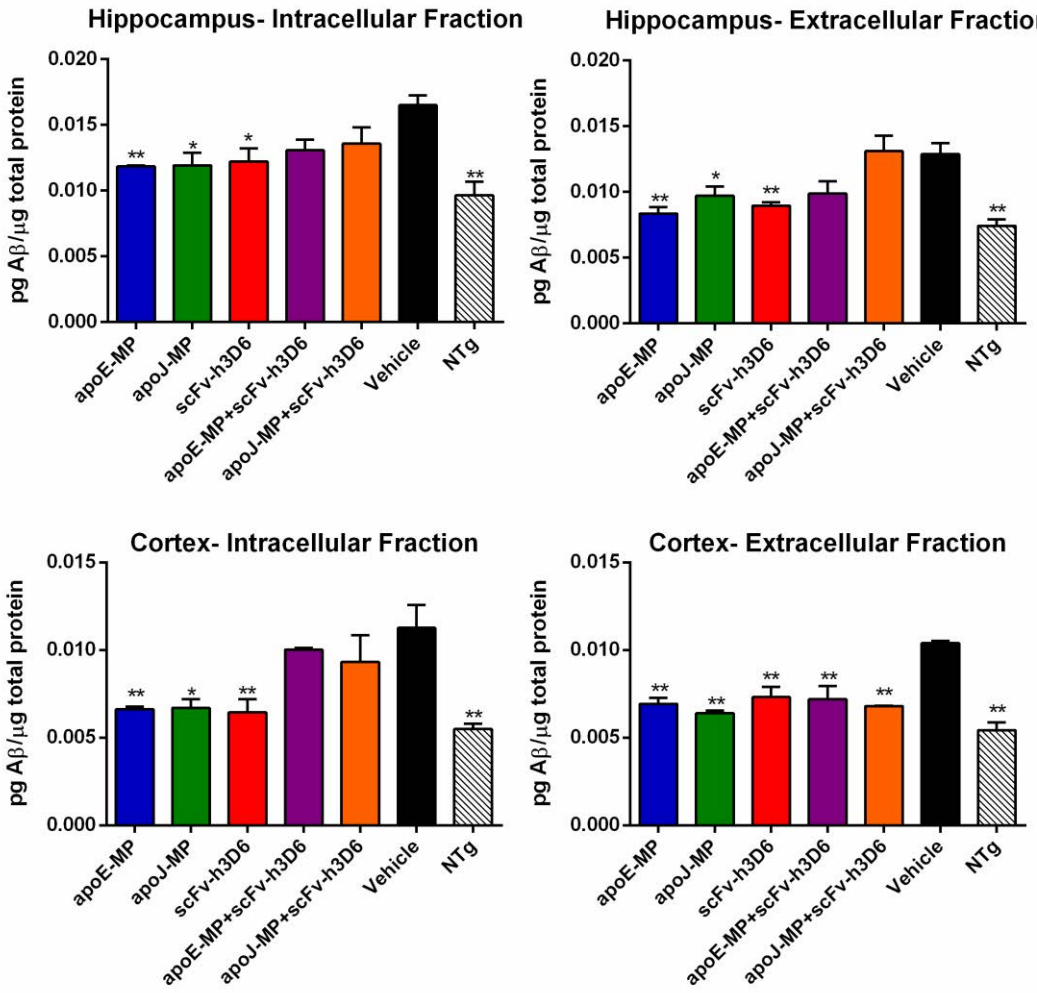

Figure 6.1. AB levels in the intracellular and extracellular fractions of the hippocampus and cortex. Except for the extracellular fraction from the cortex, apoE-MP, apoJ-MP and scFv-h3D6 alone had a greater effect in reducing $A\beta_{42}$ burden than when they were combined. Intracellular and extracellular levels of $A\beta_{42}$ in cortex and hippocampus extracts were measured by ELISA. Data are normalized by the total amount of protein in the brain extracts. Results from six animals per group are presented as means with standard error (Mann Whitney test). * indicates significance of each treatment or NTg group compared to 3xTg-AD-vehicle (*P<0.05; **P<0.01).

In the four fractions, there was a significant difference between $A\beta_{42}$ burden in the 3xTg-AD-vehicle and NTg-vehicle groups (Hippocampus: intracellular (P=0.002) and extracellular (P=0.002); Cortex: intracellular (P=0.002) and extracellular (P=0.009)). It was also shown that, except for the extracellular fraction from the cortex, apoE-MP, apoJ-MP and scFv-h3D6 alone had a greater effect (statistical significance) in reducing $A\beta_{42}$ burden than when they were combined. All three molecules presented similar efficiencies in reducing $A\beta_{42}$ levels by their own, but combination with each other seemed to interfere with their action. However, it is noteworthy to mention that this did not happen in the extracellular fraction of the cortex, where apoE-MP+scFv-h3D6 and apoJ-MP+scFv-h3D6 treatments also had a significant effect (P=0.003 and P=0.004 respectively).

Effects of the different treatments on inflammation.

Interleukin IL-33

IL-33, an alarmin of the IL-1 family, has been described as protective in AD. In LOAD, IL-33 is decreased, but how IL-33-mediated AD pathology works is still unclear. Quantification of IL-33 levels in the extracellular fractions of hippocampus and cortex revealed that the 3xTg-AD-vehicle group had lower levels of this interleukin compared to the NTg-vehicle group (hippocampus *P*=0.003; cortex *P*=0.079), in consonance with the literature [227,228] and suggesting a protective role for this interleukin (Figure 6.2). ApoE-MP and apoJ-MP significantly increased IL-33 levels in the hippocampus and cortex, even to higher levels than those in the NTg-vehicle group. ScFv-h3D6, alone or combined with apoE-MP and apoJ-MP, also significantly recovered the non-pathological levels in the hippocampus, but not in the cortex.

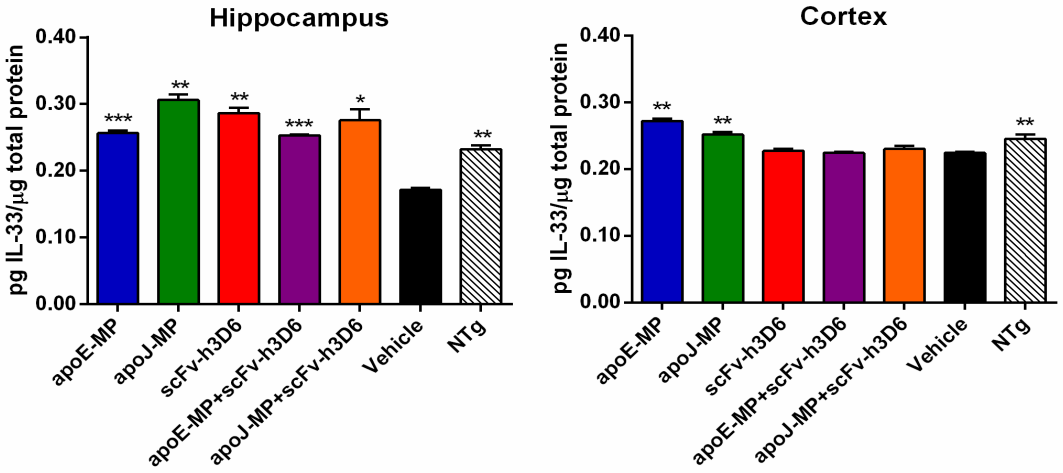

Figure 6.2. IL-33 levels in the extracellular fractions of hippocampus and cortex. ApoE-MP and apoJ-MP significantly increased IL-33 levels in the hippocampus and cortex, and scFv-h3D6, alone or combined with apoE-MP and apoJ-MP, also significantly recovered the non-pathological levels in the hippocampus, but not in the cortex. IL-33 levels in cortex and hippocampus extracts were measured by ELISA. Data are normalized by the total amount of protein in the brain extracts. Results from six animals per group are presented as means with standard error (Mann Whitney test). * indicates significance of each treatment or NTg group compared to 3xTg-AD-vehicle (**P*<0.05; ***P*<0.01; ****P*<0.001).

Astrogliosis

To evaluate the effect of the treatments on brain inflammation, we quantitively examined the extent of astrogliois in brain regions of the cortex and hippocampus by immunohistochemical analysis (Figure 6.3). An antibody against glial fibrillary acidic protein (GFAP) was used as a specific immunostainner of astrocytes. Figure 6.3 (Top) shows the mean of the percentage of the area stained by GFAP in the hippocampus and cortex.

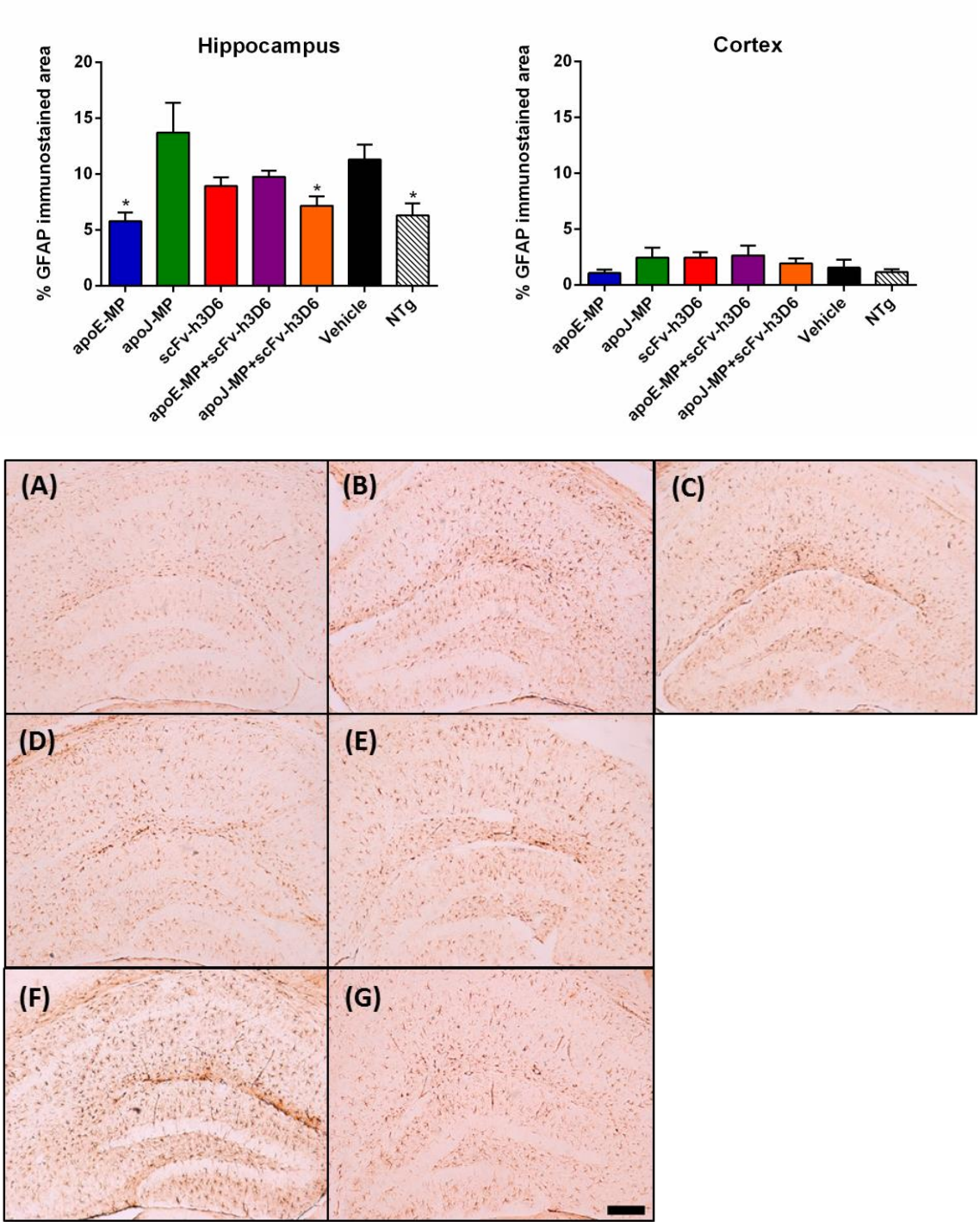

Figure 6.3. Effect of the different treatments on astrogliosis in the hippocampus and cortex. Significant results were only obtained in the hippocampus, where apoE-MP and apoJ-MP+scFv-h3D6 treatments reduced astroglial inflammation to similar levels to the NTg group**.** An antibody against glial fibrillary acidic protein (GFAP) was used as a specific marker of astrocytes. TOP: GFAP-Immunostained area was quantified using ImageJ. Results from six animals per group are presented as means with standard error (Mann Whitney test). * indicates significance of each treatment or NTg group compared to 3xTg-AD-Vehicle (* *P*<0.05). BOTTOM: Representative images of coronal GFAP-immunostained sections of hippocampus are presented: (A) apoE-MP; (B) apoJ-MP; (C) scFv-h3D6; (D) apoE-MP+scFv-h3D6; (E) apoJ-MP+scFv-h3D6; (F) Vehicle and (G) NTg**.** Zoom in is the same for all images (8x), bar corresponds to 200µm.

The first thing that can be observed is that there is a great difference between the levels in hippocampus and cortex, with very low levels in the cortex. This can be attributed to the fact that GFAP-immunoreactivity is thought to be due to different regional proliferation of the embryonic neuroepithelium of the diencephalon, and is not so effective in staining cells in the cortex [229,230], that is probably why no differences among the different treatments or 3xTg-AD and NTg mice were observed. In the hippocampus, a significant difference between 3xTg-AD-vehicle and NTg-vehicle groups was revealed (*P*=0.031), indicating that the 3xTg-AD mouse model shows symptoms of inflammation at six months of age. This can be easily seen just comparing panels F and G in Figure 6.3 (Bottom).

When looking at the effect of the different treatments in the hippocampus, apoE-MP (*P*=0.016) as well as apoJ-MP+scFv-h3D6 (*P*=0.032) significantly decreased astrocyte inflammation to similar levels as the non-pathological ones. Interestingly, while apoJ-MP treatment seemed to increase astrogliosis (not significant, *P*=0.29), when combined with scFv-h3D6 significantly reduced inflammation. On the contrary, apoE-MP alone reduced astrogliosis, but when combined with scFv-h3D6, no effect was observed (*P*=0.68). On the other hand, although scFv-h3D6 administration did not recover the NTg levels (scFv-h3D6: 8.95%±0.76; NTg: 6.76%±1.11), it did not induce astrogliosis and activation was even at lower levels than the 3xTg-AD-vehicle (11.20%±1.32).

Microgliosis

The assessment of activation of microglia in the hippocampus and cortex was based on Iba-1 antibody immunodetection (Figure 6.4). Significant differences between the 3xTg-AD-vehicle and NTg-vehicle groups were revealed in both areas (hippocampus *P*=0.016; cortex *P*=0.008), indicating microglia activation in the transgenic control (Figure 6.4, Top). In the hippocampus, none of the treatments induced a significant reduction in the percentage of Iba-1 immunostained area, although all of them showed a tendency to lower microgliosis. Especially, apoJ-MP and scFv-h3D6 effects were marginally significant (*P*=0.056 and *P*=0.055, respectively).

In the cortex, differences between 3xTg-AD-vehicle and NTg-vehicle were more evident and all the different treatments also seemed to reduce microglia activation (Figure 6.4, Bottom). Concretely, apoE-MP (*P*=0.015), scFv-h3D6 (*P*=0.016) and apoJ-MP+scFv-h3D6 (*P*=0.032) had a significant anti-inflammatory effect (Figure 6.4, Top). As it happened with astrogliosis, here it was also observed that although apoE-MP alone reduced microgliosis, this was not the case when combined with scFv-h3D6 (*P*=0.11). However, for apoJ-MP, anti-inflammatory effects were only observed in combination with scFv-h3D6.

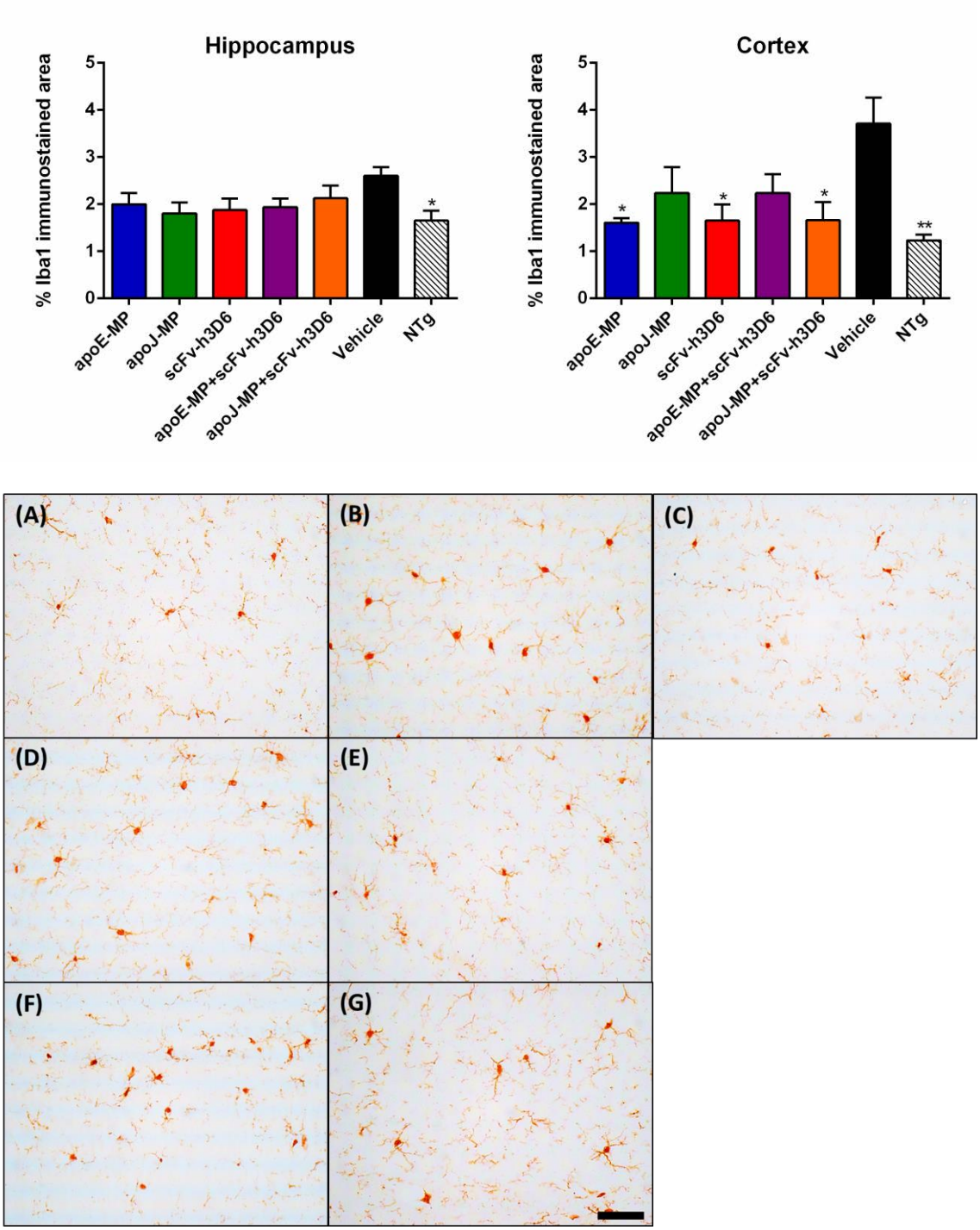

Figure 6.4. Effect of the different treatments in microgliosis in the hippocampus and cortex. . Significant results were only obtained in the cortex, where apoE-MP, scFv-h3D6 and apoJ-MP+scFv-h3D6 treatments reduced microglial inflammation to similar levels to the NTg group**.** An antibody against Iba-1 protein was used as a specific marker of microglia. TOP: Iba-1-Immunostained area was quantified using ImageJ. Results from six animals per group are presented as means with standard error (Mann Whitney test). * indicates significance of each treatment or NTg group compared to 3xTg-AD-Vehicle (* *P*<0.05). BOTTOM: Representative images of coronal Iba-1-immunostained sections of cortex are presented: (A) apoE-MP; (B) apoJ-MP; (C) scFv-h3D6; (D) apoE-MP+scFv-h3D6; (E) apoJ-MP+scFv-h3D6; (F) Vehicle and (G) NTg**.** Zoom in is the same for all images (40x), bar corresponds to 50µm.

Apolipoproteins E and J levels in the hippocampus and cortex.

The extracellular fractions of the hippocampus and cortex were analyzed to determine how apoE-MP, apoJ-MP, and scFv-h3D6 affect endogenous apolipoprotein E and J levels. For both apolipoproteins, levels in the hippocampus showed no significant differences among any of the treatments, and not even between 3xTg-AD-vehicle and NTg-vehicle (Figure 6.5). In the cortex, as previously described [100], the 3xTg-AD transgenic model showed increased levels of both apolipoproteins with respect to the NTg (apoE *P*=0.008 ; apoJ *P*=0.002).

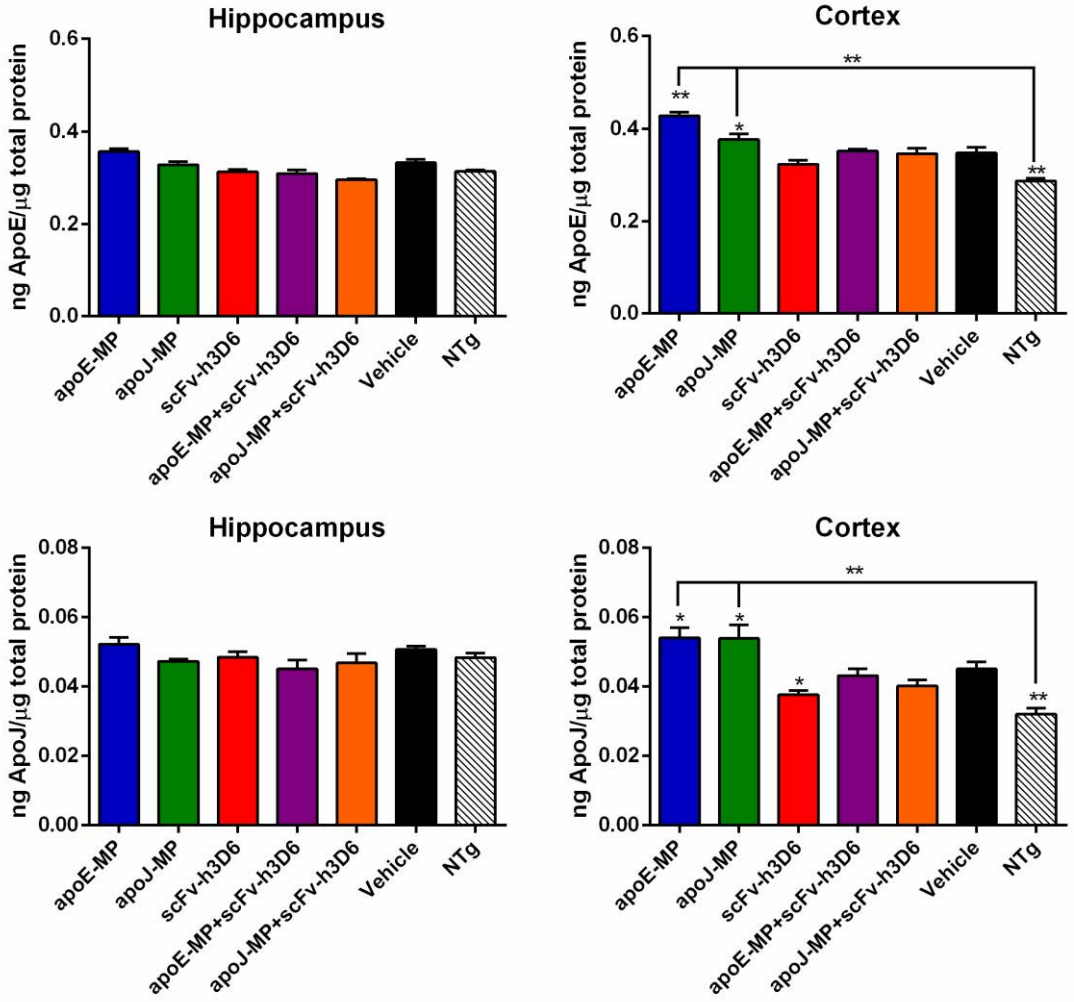

Figure 6.5. Apolipoprotein E and J levels in the extracellular fractions of the hippocampus and cortex. ApoE-MP and apoJ-MP significantly increased both apoE and apoJ levels in cortex, while scFv-h3D6 reduced them. ApoE and apoJ levels in hippocampus and cortex extracts were measured by ELISA. Results from six animals per group are presented as means with standard error (Mann Whitney test). * indicates significance of each treatment or NTg group compared to 3xTg-AD-Vehicle (**P*<0.05; ***P*<0.01). Arrows indicate significance compared to the NTg group (***P*<0.01).

Among treatments, scFv-h3D6 restored apoE and apoJ levels to similar values as NTg-Vehicle group (apoE (ns), apoJ *P*=0.015). As previously described [173], apoE-MP increases apoE levels (*P*=0.008), but interestingly it also rised apoJ expression (*P*=0.045). This also happened for apoJ-MP, which increased apoJ levels (*P*=0.041), but also apoE (*P*=0.026). Therefore, there is a mutual effect on the expression of these apolipoproteins. Combination of scFv-h3D6 with any of the mimetic peptides did not achieve to significantly lower apoE or apoJ concentrations, probably due to an opposed effect.

DISCUSSION

ScFv-h3D6 was demonstrated, after a single intraperitoneal dose, to ameliorate learning and memory deficits, reduce Aβ oligomers levels, and recover the non-pathological levels of apolipoproteins E and J in the 3xTg-AD mouse model [100,101]. Previous work presented in this Thesis (Chapters 4-5) described which are the interactions among Aβ, scFv-h3D6, and apoE-MP or apoJ-MP, and their effects, alone or combined, in Aβ uptake and Aβ-induced activation in human primary astrocytes. The aim of this chapter was to test *in vivo* what we had observed in our biophysical and cellular studies. To do so, we treated the 3xTg-AD mouse model with all different combinations of these molecules: apoE-MP, apoJ-MP, scFv-h3D6, apoE-MP+scFv-h3D6, apoJ-MP+scFv-h3D6 and vehicle. A NTg group was used as a reference of non-pathological conditions.

In 2003, Oddo *et al.* developed the 3xTg-AD transgenic mouse model harboring PS1M146V, APPSwe, and tauP301L transgenes (see General Methods). The 3xTg-AD mouse model was described to show a progressive age-related increase in Aβ deposition. Intraneuronal Aβ immunoreactivity was firstly shown between 3 and 4 months of age, and extracellular Aβ deposits from 6 months [133]. In this work, animals were treated for 6 weeks, from 4.5 to 6 months of age. $A\beta_{42}$ levels of the intracellular and extracellular fractions of the hippocampus and cortex were quantified by ELISA. The intracellular levels of $A\beta_{42}$ of the 3xTg-AD-vehicle group, especially in the hippocampus, were higher than those in the extracellular space, probably due the young age of the mice. Although all treatments seemed to have a greater effect on the extracellular fraction, $A\beta_{42}$ levels were also reduced in the intracellular one, probably because of a "sink effect". ApoE-MP, apoJ-MP and scFv-h3D6 showed high efficiencies in reducing $A\beta_{42}$ levels, but combinations decreased their potential; except for the extracellular cortex, where scFv-h3D6 combined with the mimetic peptides, both apoE-MP and apoJ-MP, also had a significant effect. In a published study, the combination of a N-terminal Aβ antibody and a synthetic agonist for the liver X receptor (LXR), a receptor that controls apoE expression, showed no interaction between immunotherapy and the agonist, suggesting no synergism [231]. Our previous biophysical work showed that, although scFv-h3D6 and apoE-MP did not interact, worm-like fibrils could not be formed in the presence of apoE-MP (Chapter 4), indicating that apoE-MP can interfere on scFv-h3D6 action.

Neuroinflammation plays a significant role in neurodegenerative diseases, whereas a debate is ongoing about its precise role, whether it is protective or harmful [232]. For the first time in the literature, we show how IL-33 levels are modulated after the administration of a putative

therapy to treat AD. Transcriptional analysis of brain tissue from patients with AD revealed that IL-33 expression was decreased compared to control tissues [233,234]. We also observed this difference here: the 3xTg-AD-vehicle had lower levels of IL-33 compared to the NTg-vehicle group. In an interesting study, Fu *et al.* demonstrated that IL-33 treatment reversed synaptic plasticity and cognitive deficits in APP/PS1mice. IL-33 reduced soluble Aβ and amyloid plaque load by promoting the recruitment and phagocytic activity of microglia, modulated the immune response of APP/PS1 mice and polarized microglia/macrophages toward an anti-inflammatory phenotype [228]. Although all treatments in this work increased IL-33 levels, apoE-MP and apoJ-MP had a greater effect, probably in line with the protective effects this interleukin has shown in cardiovascular diseases such as atherosclerosis, obesity, type 2 diabetes and cardiac remodeling [235].

Microglial and astrocytic cells have been described as the principal modulators in the neuroinflammation process underlying the development of AD [236]. Glial inflammation was studied determining astrogliosis (by measuring GFAP immunoreactivity) and microgliosis (by measuring Iba-1). In both cases, apoE-MP showed a potent anti-inflammatory effect that was inhibited in the presence of scFv-h3D6, probably due to the same negative mutual effect as observed in relation with Aβ burden. Previous works in the literature already described the anti-inflammatory properties of apoE-MP [173,177,216], and Chapter 5 of the current Thesis also showed this effect in primary human astrocytes. On the contrary, apoJ-MP alone rather shows a tendency to be pro-inflammatory, at least in astrocytes, as it also happened in Chapter 5. ApoJ-MP was initially designed as an anti-inflammatory peptide to treat atherosclerosis [174], but was also suggested to treat other disorders [178]. Its mechanism of action was demonstrated to involve the conversion of HDL into anti-inflammatory HDL (with a doubling in HDL paraoxonase activity) [174,224]. Here, apoJ-MP has been used to treat AD *in vivo* for the first time. As demonstrated that cholesterol levels, and likely lipid metabolism, is not affected in this mouse model, at least at this early stage, probably apoJ-MP cannot exert any anti-inflammatory effect. Surprisingly, combination of apoJ-MP with scFv-h3D6 seemed to be synergic in terms of inflammation (contrary to apoE-MP), both for astrogliosis and microgliosis. This clearly describes a differential role of apoE-MP and apoJ-MP, as we (Chapters 4 and 5) and others[237] previously suggested.

ScFv-h3D6 was predicted not to induce microglial activation because it lacks the Fc region of a complete antibody. Clearance of Aβ from the brain by anti-Aβ full-length antibodies has been proposed to be mediated by microglia through FcγR-dependent uptake. There is evidence that the activation of microglia and/or perivascular macrophages through FcγR, and the subsequent neuroinflammation, may be partly responsible of the side-effects observed in the treatment

with complete antibodies (reviewed in [81]). In addition, it has been shown that reduced binding to FcγR can decrease the incidence of vascular damage in mice [238,239]. In this work, scFv-h3D6 not only did not induce microgliosis but significantly reduced microglial activation and showed a tendency for reducing astrogliosis. The fact that apoE-MP reduced microgliosis and astrogliosis in such a significant way (as it also happened in previous chapters) seems to be related with a specific mechanism as postulated by Tai *et al*. [221]: apoE modulates Aβ-induced effects on inflammatory receptor signaling; specifically, TLR4-p38α and IL-4R receptors. On the other hand, scFv-h3D6 did not generate an inflammation as happened with the corresponding full-length monoclonal antibody, but rather showed a tendency to reduce it. Probably, not because it initiates an anti-inflammatory pathway (since it lacks specific receptors), but rather because the reduction in Aβ levels translates in the long run to a decrease in Aβ-induced inflammation.

Tai *et al.* recently proposed the hypothesis that apoE modulates Aβ-induced effects on inflammatory receptor signaling; specifically, impaired apoE4 function and signaling via the apoE receptors causes amplification of detrimental TLR4-p38α, and suppression of beneficial IL-4R nuclear receptor, resulting in an adverse neuroinflammatory profile [221].

In a recent study, comparison of three monoclonal antibodies against Aβ showed 3D6 to be the most effective in clearing Aβ plaques, but also the one causing higher microglia activation as measured by the increase in CD11B and proinflammatory cytokines, IL-1β and TNFα [240]. As scFv-h3D6 is derived from 3D6, we postulate that it may maintain its high affinity for Aβ, with the advantage of avoiding microglial activation.

Finally, determination of apolipoproteins E and J levels, especially in the cortex, showed that scFv-h3D6 was able to decrease the non-pathological levels, as previously described [100]. In addition, apoE-MP significantly increased endogenous apoE, as previously described [173], but strikingly also endogenous apoJ. This interplay also happened the other way around, suggesting a linked metabolism in which one apolipoprotein induces the expression of the other.

But whether increasing or decreasing, especially apoE levels, as a therapeutic strategy for AD is controversial. Concretely in the 3xTg-AD mouse model, harboring mutations that only affect Aβ and tau, apoE and apoJ levels are increased [100], which suggests a pathological role for the increase of these molecules. In addition, it has been shown that AD transgenic mice lacking apoE have decreased plaque deposition [241–243] and that an excessive apoE accumulation within Aβ plaques impairs the ability of microglia to contain plaque load [244]. Therefore, some authors have pointed out to the reduction in apoE levels as a therapeutic approach to treat AD. Administration of an anti-apoE antibody reduced apoE levels, prevented the formation of new amyloid deposits,

limited their growth and was associated with occasional clearance of plaques by a process likely associated with direct binding to amyloid aggregates. Interestingly, microglial activation was reduced and there was no effect on total plasma cholesterol or cerebral amyloid angiopathy [245].

This is in apparent contradiction with the numerous studies with LXR agonists [246–248], shown to decrease Aβ deposition in the brain while modestly increasing apoE expression, and the positive results obtained with the apoE-MP administration (here and in previous studies [173]). Maybe an explanation of this lies on the different stages of the disease. Sakai *et al*. demonstrated that apoE is involved in the removal of plaques and transport of Aβ to the cerebral vasculature induced by Aβ immunotherapy. When the antibody removes the plaques, the Aβ that becomes soluble is transported to the blood vessels together with apoE and is when CAA and ARIA appear [249].

As a general conclusion, Aβ levels decreased upon treatment with scFv-h3D6, apoE-MP or apoJ-MP, but the effect was not so evident in combined therapy. All treatments in this work recovered IL-33 levels, and apoE-MP showed a potent anti-inflammatory effect in terms of glia activation that was inhibited in the presence of scFv-h3D6, whereas apoJ-MP behaved the opposite. This fact points to a differential role of apoE-MP and apoJ-MP, as we also described in Chapters 4 and 5. Finally, endogenous apolipoproteins E and J levels were decreased to non-pathological levels by scFv-h3D6, but the mimetic peptides induced a simultaneous increase of both apolipoproteins that reflects a coordinated expression between them. After analyzing our data, we consider that the increase of, especially apoE, might be harmful in terms of Aβ deposition and appearance of CAA and ARIA.

V-GENERAL DISCUSSION

Alzheimer's disease (AD) is the major cause of dementia, affecting some 44 million people globally; this number is expected to almost double in the next 15 years and more than triple by 2050 [250]. Current therapies to treat AD patients are focused on ameliorating symptoms instead of targeting the underlying causes of the disease. With an aging population and an increase in disease incidence, it is imperative to develop disease-modifying therapies for AD [251].

The scFv-h3D6 was demonstrated to be a promising approach to treat the underlying causes of AD. It was proven to prevent Aβ-induced cytotoxicity by withdrawing Aβ oligomers from the amyloid pathway towards the non-toxic worm-like one and, in this way, prevent Aβ-induced toxicity in neuroblastoma SH-SY5Y [99]. In addition, it was shown to be effective at the behavioral, cellular, and molecular levels in the treatment of 3xTg-AD after a single intraperitoneal dose. Treatment improved cognition and reversed BPSD-like symptoms, protected from cell-death, decreased extracellular Aβ oligomers levels and restored apolipoprotein E and J concentrations to non-pathological levels [100,101].

Although its great potential, scFv-h3D6 production was limited by some bottlenecks like the presence of scrambled conformations generated in the refolding process and its contamination with endotoxins, which dramatically reduce the production yield and increase the cost. The first three chapters of this Thesis aimed to improve the folding and stability properties of the scFv-h3D6, as well as to establish a protein expression and purification system with a higher production yield. They constitute an exhaustive study and a great effort to improve different aspects of scFv-h3D6 folding, stability and production.

Firstly, disulphide bridges were eliminated in order to avoid scrambled conformations and, in this way, improve protein purification yield and assure a homogenous protein conformation. ScFv-h3D6 did not endure the elimination of the disulphide bridge of the less stable domain, V_L. However, elimination of the disulphide bridge of the V_H domain improved purification yield, ensuring one conformation, but generated a drastic change in the conformational landscape of the protein. Destabilization of the V_H domain induced by the removal of its disulphide bridge changed the folding behavior from a Class I scfv, with one domain being much more stable than the sum of the other plus interface contribution, to a Class II, where the intrinsic stability of one domain is in the same range as the total stability of the other domain [104]. The second main effect of removing the V_H disulfide bridge was that the aggregation pathway changed from a WL morphology, through the formation of a β-rich intermediate, to an amyloid morphology, through the formation of a partially-unfolded intermediate. These conformational changes had a great effect because, apart from avoiding the formation of the protective WL fibrils, the

addition of previously described as stabilizing mutations (C1, C2 and C3) had no effect. These mutations were found to stabilize the native fold by stabilizing the intermediate state in the folding pathway of scFv-h3D6. The main conclusion is that if the intermediate state cannot be formed, no stabilization of the native state can be achieved.

Although protein production improved, new mutants could not be used with therapeutic approaches because of their incapacity to form worm-like fibrils, which are behind the therapeutic effect of scFv-h3D6. Then, we decided to explore and find new stabilizing mutations. We tried to improve scFv-h3D6 by introducing the mutation V_H-K64R [146], intended to stabilize the βC''-βD loop, and combined this mutation with the previously described C3. Urea denaturation demonstrated that the three mutants (V_H-K64R, K64R/C3 and C3) maintained a three state model of denaturation curve. V_H-K64R mutation mainly affected the second transition, stabilizing the V_H domain, whereas the C3 elongation shifted the first transition to higher temperatures, thus stabilizing the V_L domain. However, when combining V_H-K64R with the elongation mutation C3, no additivity but rather a negative effect that made both mutations partially cancel each other was observed. DSC also showed that enthalpic effects were not additive since combination of both mutations had lower increase than when incorporating both separately. What it could be observed was that all these mutants (V_H-K64R, K64R/C3 and C3) conserved the WL aggregation pathway, contrary to disulfide bridge mutants. It could also be determined that a correlation between protein stability and therapeutic effectiveness exists, as it was revealed by viability assays with the neuroblastoma cell line SH-SY5Y.

Strikingly, in these two studies, the C3 elongating mutation, previously described as stabilizing, had no additional effect when combined with other mutations. In the case of disulphide bridge less mutants, no stabilization could be achieved because the folding intermediate state was not formed, and in the K64R/C3 mutant, K64R and C3 mutations partially cancelled each other.

Finally, a change in the expression system of the wild-type scFv-h3D6 was performed. The novel protein obtained in the eukaryotic system *Pichia Pastoris* maintained the same thermodynamic properties as the protein obtained from *Escherichia coli*. However, other properties were improved: homogeneity of the sample, absence of scrambled conformations, endotoxin free sample, improved protein yield, easy purification and extrapolation to a larger scale. Therapeutic effectiveness of scFv-h3D6-Pp was also demonstrated *in vitro* and *in vivo* in comparison with scFv-h3D6-Ec, showing the same or slightly better effects. Although this system did not involve an increase in protein stability, it definitely supposes a great advance in the development of scFv-h3D6 as a future therapy to treat AD.

The second part of this Thesis has been focused on the effects of apolipoproteins E and J in scFv-h3D6 action. Even though Aβ-immunotherapy has long been studied in the treatment of AD, how other molecules involved in the disease could affect the antibody action remains elusive. Both Aβ fibrillar and diffuse plaques include components that co-localize with Aβ-deposits [39] and modulate fibril formation [40], known as amyloid-associated proteins (AAPs). AAPs include apolipoproteins E and J, both genetic determinants for sporadic AD as assessed in genome-wide association studies (GWAS) [150,219,252]. The best characterized of these proteins is apolipoprotein E (apoE), a key protein involved in lipid metabolism. Human apoE is a 299-residue glycoprotein composed of two separate domains joined by a flexible hinge region: the N-terminal domain, which constitutes the receptor-binding region, and the C-terminal domain, the lipid-binding region [46]. Human apoE exists in three isoforms, apoE2, apoE3 and apoE4, with apoE3 as the most common form and apoE4 being the major genetic risk factor for AD [253]. Epitope mapping of the apoE-Aβ complex revealed that Aβ can interact with both the lipid-binding site and the receptor-binding site within apoE [57]. But, not only apoE and Aβ can interact with each other, they also share common receptors including LRP1 (Low density lipoprotein receptor-related protein 1), LDLR (Low density lipoprotein receptor) and HSPG (heparan sulfate proteoglycans) on cell surface [47].

Apolipoprotein J (apoJ, clusterin) is a multifunctional protein normally associated with lipids in plasma and cerebrospinal fluid (CSF), and secreted as lipoproteins by hepatocytes and astrocytes [254]. In conjunction with apoE and some other AAPs, apoJ has been found associated with parenchymal and vascular Aβ peptide deposits in AD, already in early stages when Aβ deposits are diffuse [39,255]. Furthermore, apoJ can form soluble complexes with Aβ which are readily detectable in the CSF [187]. ApoJ facilitates transport of Aβ across the blood brain barrier by mechanisms that involve megalin (also known as LRP-2) [252,256].

To completely understand the possible interactions and effects among Aβ, scFv-h3D6, apoE and apoJ, we present a complete study from all different perspectives: biophysical, cellular and *in vivo*. Because our work is aimed to a combined therapy, instead of full-length apolipoproteins, we have combined scFv-h3D6 with apolipoproteins E and J mimetic peptides (MP) composed of essential structures within these apolipoproteins for binding to other molecules. The apoE-MP, although initially intended to treat arthrosclerosis [175–177] is already reported in the literature to improve cognition, decrease amyloid plaque deposition and reduce the number of activated microglia and astrocytes in the APP/PS1ΔE9 mice [173]. The apoJ-MP, also intended to treat atherosclerosis [174], has been suggested as a therapy for inflammatory disorders other than atherosclerosis [178]. Both apoE-MP and apoJ-MP were shown in Chapter 5 to resemble full-length apolipoproteins effect.

On the other hand, this is the first work where scFv-h3D6 and its full-length mAb are compared (Chapter 5), showing that both scFv-h3D6 and mAb-h3D6 reduced Aβ oligomers uptake by human primary astrocytes, but had opposite effects on fibrils uptake. In the case of Aβ fibrils, scFv-h3D6 showed an increase in inflammation, maybe related to a stronger interference on amyloid fibril formation compared to the full-length mAb, increasing the concentration of Aβ oligomers that can readily be ingested.

Biophysical studies presented in Chapter 4 showed that apoE-MP precluded the formation of protective WL fibrils by the scFv-h3D6/Aβ complex and partially interfered with the scFv-h3D6-induced reduction in Aβ-uptake by astrocytes, whereas apoJ-MP allowed the formation of WL fibrils and did not interfere with the reduction in Aβ uptake. In Chapter 5, flow cytometry studies did not show interferences in any of the combined treatments, probably because the molecules were directly added to the cell culture, without any previous incubation.

In vivo results in Chapter 6 were more similar to those in Chapter 4 (preincubated to study interactions in the steady state), even though the treatment with the different molecules was separated two days to avoid possible interactions. It could be observed that the apoE-MP+scFv-h3D6 treatment was not so effective in reducing Aβ burden as treatments with the scFv-h3D6 or MPs alone, and apoE-MP anti-inflammatory effect was inhibited in the presence of scFv-h3D6. This would imply that the mechanism behind Aβ burden reduction is different between the scFv-h3D6 and the MPs. On the other hand, in Chapter 5 (no preincubated) anti-inflammatory effect of apoE-MP was not inhibited in the presence of scFv-h3D6. The main experimental difference between both procedures is the period and repetition of administration. In Chapter 5, cells were exposed to the different treatments for 18h and in Chapter 6, animals were treated for 6 weeks. Probably, a repeated administration facilitates the same conditions as if the molecules were preincubated. It can be possible that the competition of scFv-h3D6 and apoE-MP for binding Aβ, increase free Aβ levels, which should cause a slight increase in inflammation. When the molecules are directly added, as apoE-MP suffers a huge conformational change upon Aβ binding (Chapter 4) and the incubation time is shorter, this competition process is not so clearly observed.

ApoE has been demonstrated to have an anti-inflammatory role. It was shown to downregulate CNS production of TNFα, IL-1β and IL-6 following stimulation with lipopolysaccharide (LPS) [217], and Aβ-induced activation was attenuated by the addition of exogenous apoE-containing particles. In addition, glial cells cultured from apoE-knockout mice exhibit an enhanced production of several pro-inflammatory markers in response to treatment with Aβ and other

activating stimuli [218]. Also, administration of apoE-MP to APP/PS1ΔE9 mice significantly reduced the numbers of activated microglia and astrocytes in immunostained brain sections [173].

Although its determination as a risk factor in several GWAS [219,257], little has been described in the literature about apoJ role in AD pathogenesis, especially in terms of inflammation. In this work, apoJ seemed to have an opposed effect to apoE: proinflammatory profile alone but anti-inflammatory when combined with scFv-h3D6. Although apoJ has been described to have an anti-inflammatory role in arthrosclerosis and suggested to modulate activation in AD [258], no pro/anti-inflammatory role has been established. In Chapter 5, full-length apoJ exerted an activation effect, but no apoJ-MP. As explained in Chapter 6, probably an anti-inflammatory effect of apoJ-MP could not be observed because lipid metabolism is not likely to be affected in the 3xTg-AD mouse model, at least at this early age. Interestingly, in Chapter 6, apoJ-MP exerted an anti-inflammatory effect when combined with scFv-h3D6. As we previously postulated [100], also here, apoJ-MP may be helping to eliminate the scFv-h3D6/Aβ complex and probably is not that it initiates an anti-inflammatory pathway, but helping to eliminate Aβ avoids Aβ-induced inflammation, as it also happened with scFv-h3D6 alone.

ScFv-h3D6 induced a decrease in microglial activation in Chapter 6, probably because of its dramatic effect in reducing Aβ burden. Surprisingly, instead of an anti-inflammatory profile a proinflammatory one was observed in Chapter 5. This was not the case in the presence of Aβ oligomers, but Aβ fibrils. This apparent contradiction may be explained because: 1) Chapter 6 shows the results of a repeated administration, while Chapter 5 shows the results of a 18h incubation; 2) the *in vivo* experiment was performed at early stages of the disease, when Aβ fibrillar forms are still not present. In relation with the first point, it has been shown in the literature that short-term administration with certain anti-Aβ antibodies increases reactive microglia whereas long-term administration has a decreasing effect [259]. On the other hand, several studies have reported that anti-Aβ antibodies administrated at an advanced stage of the disease are ineffective in reversing cognitive symptoms and more prone to provoke side-effects [81]. Three consortia are working to test different antibodies in younger patients in order to prevent the disease development: the Alzheimer's Prevention Initiative (API), the Dominantly Inherited Alzheimer's Network (DIAN) and the Anti-Amyloid treatment in Asymptomatic Alzheimer's (A4). API tests crenezumab in individuals from a large Colombian family which carries the $PS1_{E280A}$ mutation [260]; DIAN tests immunotherapy with solanezumab or gantenerumab in adult children of a parent with the same mutation; and, finally, A4 tests solanezumab in asymptomatic elderly patients with amyloid positive PET [261,262]. Also in this sense, it has been demonstrated that antibodies are capable of removing Aβ plaques and

redistribute Aβ. It is though that some ARIAs have been generated because of the mobilization of this Aβ and deposition in the peripheral vasculature, together with apoE previously deposited in the plaques [249]. That's why we consider that an increase in apoE levels by apoE-MP and apoJ-MP (Chapter 6) might be detrimental for the antibody action.

In addition, as observed in Chapter 4, scFv-h3D6, like apoE-MP and apoJ-MP, interfere in Aβ fibrillation, so probably at early stages of the disease when Aβ oligomers are increased, but Aβ fibrils still not formed, is the best time for antibody administration.

Apart from the moment for antibody administration, the results in the current Thesis lead us to a relevant consideration about the strategy to follow when designing a therapeutic approach for reducing Aβ burden. It has been demonstrated that scFv-h3D6, as well as apoE-MP and apoJ-MP, reduce Aβ uptake by human primary astrocytes and also Aβ burden in the 3xTg-AD mouse model. Up to now, anti-Aβ antibodies have been designed to promote glial uptake to degrade Aβ. In an interesting work, Spangenberg *et al.* demonstrated that chronic microglial elimination did not alter Aβ levels or plaque load; however, it did rescue dendritic spine loss and prevented neuronal loss in 5xFAD mice, as well as reduced overall inflammation. These results demonstrated that microglia contribute to neuronal loss, as well as to memory impairments, in 5xFAD mice, but do not mediate or protect from amyloid pathology [263]. On the other hand, although astrocytes have been reported to be resistant to Aβ cytotoxicity, unless their glycolysis mechanism is down-regulated [264], they have been described to be severely affected by high loads of Aβ, which alter their normal functions. As described by Sölvander *et al*., astrocytes degradation system is ineffective, and when they are overwhelmed Aβ degradation is not completed and partly degraded Aβ is left, which may, instead of being beneficial promote the spreading of AD pathology [197]. Glial cells in AD patients, whether it is because of aging, Aβ overburden or chronic neuroinflammation, are damaged and not so effective in developing their functions such as Aβ degradation [198,265,266]. So, strategies for AD therapeutics should shift to promote Aβ elimination somehow else, i.e. by CSF drainage as postulated for the scFv-h3D6/Aβ complex.

Finally, we can conclude that this work unravels some of the important questions in AD pathology, but especially anti-Aβ immunotherapy. We hope these results help to better understand and improve one of the most promising therapies to treat this devastating disease.

VI-CONCLUSIONS

The **general conclusions** for the current Thesis are:

PART 1 (Chapters 1-3): Folding and stability properties of the scFv-h3D6 have been engineered. Several ways to improve them and scFv-h3D6 production yield have been explored.

General conclusion: The removal of the disulphide bridge of the more stable domain, V_H, increases the production yield and avoids scrambled conformations but abolished its therapeutic effect, whereas stabilizing mutations showed improved therapeutic effect. Expression in *Pichia pastoris* improved the production and safety of the recombinant scFv-h3D6 while keeping, or slightly improving, the therapeutic effect *in vivo*.

PART 2 (Chapters 4-6): -The role of scFv-h3D6, apoE-MP and apoJ-MP on Aβ uptake and Aβ-induced inflammation has been determined, as well as their interactions. Their possible application as therapeutic approaches has also been presented.

General conclusion: ScFv-h3D6 treatment decreases Aβ burden, decreases astrocytic Aβ uptake, and restores endogenous apoE and apoJ levels, while ameliorating Aβ-induced inflammation. Although combined therapy with MP should be further analyzed, this work demonstrates that all the effects of scFv-h3D6 are addressed to preclude AD pathology, without eliciting the detrimental effects shown by bapineuzumab in clinical trials.

The **specific conclusions** for each chapter are:

<u>Chapter 1</u>: Understanding the contribution of disulphide bridges to the folding and misfolding of scFv-h3D6.

1.1. ScFv-h3D6 does not endure the elimination of the disulphide bridge of the less stable domain, V_L.
1.2. Elimination of the disulphide bridge of the V_H domain, improved purification yield ensuring conformational homogeneity.
1.3. Destabilization of the V_H domain induced by the removal of its disulphide bridge changed the folding behavior from a Class I scFv molecule to a Class II.
1.4. Removing the V_H disulfide bridge shifted the worm-like aggregation pathway characterized by the presence of a β-rich intermediate state, towards an amyloid pathway populated by a partially unfolded intermediate state.
1.5. The addition of previously described as stabilizing mutations (C1, C2 and C3) had no effect on the V_H-DF mutant because these mutations were found to stabilize the native fold by stabilizing the intermediate state in the folding pathway of scFv-h3D6. Since this state could not be formed, no stabilization of the native state could be achieved.

Chapter 2: Towards the improvement in stability of scFv-h3D6 as a way to enhance its therapeutic potential.

2.1 Urea denaturation demonstrated that the three mutants (V_H-K64R, K64R/C3 and C3) maintained a three-state model for protein folding.
2.2 V_H-K64R mutation mainly affected the second transition, stabilizing the V_H domain, whereas the C3 elongation shifted the first transition to higher temperatures, thus stabilizing the V_L domain.
2.3 When combining V_H-K64R with the elongation mutation C3, no additivity but rather a negative effect that made both mutations partially cancel each other was observed.
2.4 All these mutants (V_H-K64R, K64R/C3 and C3) conserved the worm-like aggregation pathway, in line with the presence of a β-rich intermediate state.
2.5 A correlation between protein stability and therapeutic effectiveness exists, as observed in the viability assays with the neuroblastoma cell line SH-SY5Y.

Chapter 3: A simple *Pichia pastoris* production of scFv-h3D6 and *in vitro* and *in vivo* validation of its therapeutic effect.

3.1 To avoid several drawbacks of the expression of scFv-h3D6 in *Escherichia coli*, the change to a *Pichia Pastoris* was successfully performed.
3.2 The novel protein obtained in the eukaryotic system maintained the same thermodynamic properties as the protein obtained from *E. coli.*
3.3 However, other properties were improved: homogeneity of the sample, absence of scrambled conformations, endotoxin-free sample, improved protein yield, easy purification, and extrapolation to a larger scale.
3.4 Therapeutic effectiveness of scFv-h3D6-Pp was also demonstrated *in vitro* and *in vivo* in comparison with scFv-h3D6-Ec, showing the same or slightly better effects.

Chapter 4: Effects of scFv-h3D6 on Aβ aggregation and astrocytic uptake are modulated by apolipoprotein E and J mimetic peptides.

4.1 ApoE-MP and scFv-h3D6 strongly interacted with Aβ, while apoJ-MP did it very weakly.
4.2 ScFv-h3D6 did not interact with apoE-MP, neither apoJ-MP.
4.3 ScFv-h3D6 and Aβ were allowed to form the protective worm-like fibrils in the presence of apoJ-MP, but not in the presence of apoE-MP.
4.4 ScFv-h3D6, apoE-MP and apoE-MP, to a different extent, reduced Aβ-uptake by astrocytes, and apoE partially interfered with the reduction by scFv-h3D6.
4.5 ScFv-h3D6, apoE-MP and apoJ-MP prevented Aβ fibrillation.

<u>Chapter 5</u>: Effects on Aβ-induced inflammation of apolipoproteins E and J in combination with scFv-h3D6.

5.1 ApoE-MP and apoJ-MP had similar effects as the full-length apolipoproteins on Aβ uptake by adult human primary astrocytes, and also on the Aβ-mediated pro-inflammatory response.
5.2 This also was the case for scFv-h3D6 when compared to the full-length antibody bapineuzumab, especially considering oligomers assays.
5.3 The presence of Aβ fibrils did not induce an inflammatory response, but Aβ oligomers did increase IL-6 and MCP-1 release, which was prevented by apoE-MP but not apoJ-MP neither scFv-h3D6.

<u>Chapter 6</u>: *In vivo* study of the effect of scFv-h3D6 in combination with apolipoproteins E or J mimetic peptides on Aβ pathology and inflammation.

1.1 ApoE-MP, apoJ-MP and scFv-h3D6 reduce Aβ burden both in the cortex and hippocampus, but when they are combined they are not so effective. This shows again the different mechanism behind the action of the scFv and the MPs.
1.2 ApoE-MP has a potential anti-inflammatory effect.
1.3 ScFv-h3D6 does not induce microglial activation but rather reduces it.
1.4 ApoJ-MP has a potential anti-inflammatory effect when combined with scFv-h3D6 but not alone.
1.5 Apolipoprotein E and J levels are reduced by scFv-h3D6, but simultaneously increased by apoE-MP or apoJ-MP, showing an evident link in apolipoprotein regulation.
1.6 ScFv-h3D6 reduced the level of endogenous apolipoproteins E and J.

VII-REFERENCES

1. Martin Prince, A. *et al.* World Alzheimer Report 2015 The Global Impact of Dementia An analysis of prevalence, incidence, cost and Trends. (2015).

2. Sperling, R. a. *et al.* Toward defining the preclinical stages of Alzheimer's disease: Recommendations from the National Institute on Aging and the Alzheimer's Association workgroup. *Alzheimer's Dement.* **7,** 280–292 (2011).

3. Albert, M. S. *et al.* The diagnosis of mild cognitive impairment due to Alzheimer's disease: Recommendations from the National Institute on Aging and Alzheimer's Association workgroup. *Alzheimer's Dement.* **7,** 270–279 (2011).

4. McKhann, G. M. *et al.* The diagnosis of dementia due to Alzheimer's disease: Recommendations from the National Institute on Aging-Alzheimer's Association workgroups on diagnostic guidelines for Alzheimer's disease. *Alzheimer's and Dementia* **7,** 263–269 (2011).

5. Yang, T. *et al.* A highly sensitive novel immunoassay specifically detects low levels of soluble Aβ oligomers in human cerebrospinal fluid. *Alzheimers. Res. Ther.* **7,** 14 (2015).

6. Hardy, J. & Selkoe, D. J. The amyloid hypothesis of Alzheimer's disease: progress and problems on the road to therapeutics. *Science* **297,** 353–6 (2002).

7. Solomon, B. Immunotherapeutic strategies for Alzheimer's disease treatment. *ScientificWorldJournal.* **9,** 909–919 (2009).

8. Karran, E., Mercken, M., Strooper, B. De & De Strooper, B. The amyloid cascade hypothesis for Alzheimer's disease: an appraisal for the development of therapeutics. *Nat. Rev. Drug Discov.* **10,** 698–712 (2011).

9. Wolfe, M. S. *et al.* Two transmembrane aspartates in presenilin-1 required for presenilin endoproteolysis and gamma-secretase activity. *Nature* **398,** 513–7 (1999).

10. Kojro, E. & Fahrenholz, F. The non-amyloidogenic pathway: structure and function of alpha-secretases. *Subcell. Biochem.* **38,** 105–27 (2005).

11. Haass, C., Hung, A. Y., Schlossmacher, M. G., Teplow, D. B. & Selkoe, D. J. beta-Amyloid peptide and a 3-kDa fragment are derived by distinct cellular mechanisms. *J. Biol. Chem.* **268,** 3021–4 (1993).

12. Montoliu-Gaya, L. & Villegas, S. Protein structures in Alzheimer's disease: The basis for rationale therapeutic design. *Arch. Biochem. Biophys.* **588,** 1–14 (2015).

13. LaFerla, F. M., Green, K. N. & Oddo, S. Intracellular amyloid-beta in Alzheimer's disease. *Nat. Rev. Neurosci.* **8,** 499–509 (2007).

14. Benilova, I., Karran, E. & De Strooper, B. The toxic Aβ oligomer and Alzheimer's disease: an emperor in need of clothes. *Nature Neuroscience* **15,** 349–357 (2012).

15. Jarrett, J. T., Berger, E. P. & Lansbury, P. T. The carboxy terminus of the beta amyloid protein is critical for the seeding of amyloid formation: implications for the pathogenesis of Alzheimer's disease. *Biochemistry* **32,** 4693–7 (1993).

16. Marr, R. A. & Hafez, D. M. Amyloid-beta and Alzheimer's disease: the role of neprilysin-2 in amyloid-beta clearance. *Front. Aging Neurosci.* **6,** 187 (2014).

17. Pimplikar, S. W. Reassessing the amyloid cascade hypothesis of Alzheimer's disease. *Int. J. Biochem. Cell Biol.* **41,** 1261–8 (2009).

18. Morishima-Kawashima, M. Molecular mechanism of the intramembrane cleavage of

the β-carboxyl terminal fragment of amyloid precursor protein by γ-secretase. *Front. Physiol.* **5,** 463 (2014).

19. Zhao, G. *et al.* Identification of a new presenilin-dependent zeta-cleavage site within the transmembrane domain of amyloid precursor protein. *J. Biol. Chem.* **279,** 50647–50 (2004).

20. Sato, T. *et al.* Potential link between amyloid beta-protein 42 and C-terminal fragment gamma 49-99 of beta-amyloid precursor protein. *J. Biol. Chem.* **278,** 24294–301 (2003).

21. Morley, J. E. & Farr, S. A. The role of amyloid-beta in the regulation of memory. *Biochem. Pharmacol.* **88,** 479–85 (2014).

22. Abramov, E. *et al.* Amyloid-beta as a positive endogenous regulator of release probability at hippocampal synapses. *Nat. Neurosci.* **12,** 1567–76 (2009).

23. Koo, E. H., Park, L. & Selkoe, D. J. Amyloid beta-protein as a substrate interacts with extracellular matrix to promote neurite outgrowth. *Proc. Natl. Acad. Sci. U. S. A.* **90,** 4748–52 (1993).

24. Knowles, T. P. J., Vendruscolo, M. & Dobson, C. M. The amyloid state and its association with protein misfolding diseases. *Nat. Rev. Mol. Cell Biol.* **15,** 384–96 (2014).

25. Näslund, J. *et al.* 2000.Correlation between elevated levels of amyloid beta-peptide in the brain and cognitive decline. *JAMA* **283,** 1571–7

26. Wang, J., Dickson, D. W., Trojanowski, J. Q. & Lee, V. M. The levels of soluble versus insoluble brain Abeta distinguish Alzheimer's disease from normal and pathologic aging. *Exp. Neurol.* **158,** 328–37 (1999).

27. McLean, C. A. *et al.* Soluble pool of Abeta amyloid as a determinant of severity of neurodegeneration in Alzheimer's disease. *Ann. Neurol.* **46,** 860–6 (1999).

28. Bagyinszky, E. *et al.* Role of inflammatory molecules in the Alzheimer's disease progression and diagnosis. *J. Neurol. Sci.* **376,** 242–254 (2017).

29. Bauer, J. *et al.* Interleukin-6 and alpha-2-macroglobulin indicate an acute-phase state in Alzheimer's disease cortices. *FEBS Lett.* **285,** 111–4 (1991).

30. Cagnin, A. *et al.* In-vivo measurement of activated microglia in dementia. *Lancet (London, England)* **358,** 461–7 (2001).

31. Fillit, H. *et al.* Elevated circulating tumor necrosis factor levels in Alzheimer's disease. *Neurosci. Lett.* **129,** 318–20 (1991).

32. Lu, J.-X. *et al.* Molecular structure of β-amyloid fibrils in Alzheimer's disease brain tissue. *Cell* **154,** 1257–68 (2013).

33. Mawuenyega, K. G. *et al.* Decreased clearance of CNS beta-amyloid in Alzheimer's disease. *Science* **330,** 1774 (2010).

34. Bu, G. Apolipoprotein E and its receptors in Alzheimer's disease: pathways, pathogenesis and therapy. *Nat. Rev. Neurosci.* **10,** 333–44 (2009).

35. Liu, C.-C., Liu, C.-C., Kanekiyo, T., Xu, H. & Bu, G. Apolipoprotein E and Alzheimer disease: risk, mechanisms and therapy. *Nat. Rev. Neurol.* **9,** 106–18 (2013).

36. Poirier, J. *et al.* Apolipoprotein E and lipid homeostasis in the etiology and treatment of sporadic Alzheimer's disease. *Neurobiol. Aging* **35 Suppl 2,** S3-10 (2014).

37. Leduc, V., Jasmin-Bélanger, S. & Poirier, J. APOE and cholesterol homeostasis in Alzheimer's disease. *Trends Mol. Med.* **16,** 469–77 (2010).

38. Bohm, C. *et al.* Current and future implications of basic and translational research on amyloid-β peptide production and removal pathways. *Mol. Cell. Neurosci.* (2015). doi:10.1016/j.mcn.2015.02.016

39. Veerhuis, R., Boshuizen, R. S. & Familian, A. Amyloid associated proteins in Alzheimer's and prion disease. *Curr. Drug Targets. CNS Neurol. Disord.* **4,** 235–48 (2005).

40. Dickson, D. W. The pathogenesis of senile plaques. *J. Neuropathol. Exp. Neurol.* **56,** 321–39 (1997).

41. May, P. C. *et al.* Dynamics of gene expression for a hippocampal glycoprotein elevated in Alzheimer's disease and in response to experimental lesions in rat. *Neuron* **5,** 831–9 (1990).

42. Beffert, U., Stolt, P. C. & Herz, J. Functions of lipoprotein receptors in neurons. *J. Lipid Res.* **45,** 403–9 (2004).

43. Zannis, V. I., McPherson, J., Goldberger, G., Karathanasis, S. K. & Breslow, J. L. Synthesis, intracellular processing, and signal peptide of human apolipoprotein E. *J. Biol. Chem.* **259,** 5495–9 (1984).

44. Rall, S. C., Weisgraber, K. H. & Mahley, R. W. Human apolipoprotein E. The complete amino acid sequence. *J. Biol. Chem.* **257,** 4171–8 (1982).

45. Chen, J., Li, Q. & Wang, J. Topology of human apolipoprotein E3 uniquely regulates its diverse biological functions. *Proc. Natl. Acad. Sci. U. S. A.* **108,** 14813–8 (2011).

46. Hauser, P. S., Narayanaswami, V. & Ryan, R. O. Apolipoprotein E: from lipid transport to neurobiology. *Prog. Lipid Res.* **50,** 62–74 (2011).

47. Kanekiyo, T., Xu, H. & Bu, G. ApoE and Aβ in Alzheimer's disease: Accidental encounters or partners? *Neuron* **81,** 740–754 (2014).

48. Huang, Y. & Mucke, L. Alzheimer mechanisms and therapeutic strategies. *Cell* **148,** 1204–22 (2012).

49. Lane-Donovan, C., Philips, G. T. & Herz, J. More than cholesterol transporters: lipoprotein receptors in CNS function and neurodegeneration. *Neuron* **83,** 771–87 (2014).

50. Winkler, K. *et al.* Competition of Abeta amyloid peptide and apolipoprotein E for receptor-mediated endocytosis. *J. Lipid Res.* **40,** 447–55 (1999).

51. Kanekiyo, T. & Bu, G. The low-density lipoprotein receptor-related protein 1 and amyloid-β clearance in Alzheimer's disease. *Front. Aging Neurosci.* **6,** 93 (2014).

52. Poirier, J. *et al.* Apolipoprotein E and lipid homeostasis in the etiology and treatment of sporadic Alzheimer's disease. *Neurobiol. Aging* **35 Suppl 2,** S3-10 (2014).

53. Deane, R. *et al.* apoE isoform-specific disruption of amyloid beta peptide clearance from mouse brain. *J. Clin. Invest.* **118,** 4002–13 (2008).

54. Castano, E. M. *et al.* Fibrillogenesis in Alzheimer's disease of amyloid beta peptides and apolipoprotein E. *Biochem. J.* **306 (Pt 2,** 599–604 (1995).

55. Hashimoto, T. *et al.* Apolipoprotein E, especially apolipoprotein E4, increases the

oligomerization of amyloid β peptide. *J. Neurosci.* **32,** 15181–92 (2012).

56. Kanekiyo, T., Xu, H. & Bu, G. ApoE and Aβ in Alzheimer's disease: accidental encounters or partners? *Neuron* **81,** 740–54 (2014).

57. Golabek, A. A., Soto, C., Vogel, T. & Wisniewski, T. The interaction between apolipoprotein E and Alzheimer's amyloid beta-peptide is dependent on beta-peptide conformation. *J. Biol. Chem.* **271,** 10602–6 (1996).

58. Wood, S. J., Chan, W. & Wetzel, R. An ApoE-Abeta inhibition complex in Abeta fibril extension. *Chem. Biol.* **3,** 949–56 (1996).

59. Ricciarelli, R. *et al.* Cholesterol and Alzheimer's disease: a still poorly understood correlation. *IUBMB Life* **64,** 931–5 (2012).

60. Hatters, D. M., Peters-Libeu, C. A. & Weisgraber, K. H. Apolipoprotein E structure: insights into function. *Trends Biochem. Sci.* **31,** 445–54 (2006).

61. Reitz, C. Dyslipidemia and the risk of Alzheimer's disease. *Curr. Atheroscler. Rep.* **15,** 307 (2013).

62. Leeb, C., Eresheim, C. & Nimpf, J. Clusterin is a ligand for apolipoprotein E receptor 2 (ApoER2) and very low density lipoprotein receptor (VLDLR) and signals via the Reelin-signaling pathway. *J. Biol. Chem.* **289,** 4161–72 (2014).

63. Ong, W.-Y., Tanaka, K., Dawe, G. S., Ittner, L. M. & Farooqui, A. A. Slow excitotoxicity in Alzheimer's disease. *J. Alzheimers. Dis.* **35,** 643–68 (2013).

64. DeMattos, R. B. *et al.* Clusterin promotes amyloid plaque formation and is critical for neuritic toxicity in a mouse model of Alzheimer's disease. *Proc. Natl. Acad. Sci. U. S. A.* **99,** 10843–8 (2002).

65. Cascella, R. *et al.* Extracellular chaperones prevent Aβ42-induced toxicity in rat brains. *Biochim. Biophys. Acta* **1832,** 1217–26 (2013).

66. Menting, K. W. & Claassen, J. A. H. R. β-secretase inhibitor; a promising novel therapeutic drug in Alzheimer's disease. *Front. Aging Neurosci.* **6,** 165 (2014).

67. Villegas, S. [Alzheimer's disease: New therapeutic strategies.]. *Med. Clin. (Barc).* (2014). doi:10.1016/j.medcli.2014.05.023

68. Weksler, M. E. *et al.* Patients with Alzheimer disease have lower levels of serum anti-amyloid peptide antibodies than healthy elderly individuals. *Exp. Gerontol.* **37,** 943–8 (2002).

69. Spencer, B. & Masliah, E. Immunotherapy for Alzheimer's disease: past, present and future. *Front. Aging Neurosci.* **6,** 114 (2014).

70. Li, Y., Liu, Y., Wang, Z. & Jiang, Y. Clinical trials of amyloid-based immunotherapy for Alzheimer's disease: end of beginning or beginning of end? *Expert Opin. Biol. Ther.* **13,** 1515–22 (2013).

71. Lemere, C. a. Immunotherapy for Alzheimer's disease: hoops and hurdles. *Mol. Neurodegener.* **8,** 36 (2013).

72. Lannfelt, L. *et al.* Perspectives on future Alzheimer therapies: amyloid-β protofibrils - a new target for immunotherapy with BAN2401 in Alzheimer's disease. *Alzheimers. Res. Ther.* **6,** 16 (2014).

73. Gilman, S. *et al.* Clinical effects of A?? immunization (AN1792) in patients with AD in an interrupted trial. *Neurology* **64,** 1553–1562 (2005).

74. Sarazin, M., Dorothée, G., de Souza, L. C. & Aucouturier, P. Immunotherapy in Alzheimer's disease: do we have all the pieces of the puzzle? *Biol. Psychiatry* **74,** 329–32 (2013).

75. Schneeberger, A. . et al. 12th International Conference on Alzheimer's and Parkinson's Diseases and Related Neurological Disorders. March 2015. in

76. Lannfelt, L., Relkin, N. R. & Siemers, E. R. Amyloid-ß-directed immunotherapy for Alzheimer's disease. *J. Intern. Med.* **275,** 284–95 (2014).

77. Arai, H., Suzuki, H. & Yoshiyama, T. Vanutide Cridificar and the QS-21 Adjuvant in Japanese Subjects With Mild to Moderate Alzheimer's Disease: Results from Two Phase 2 Studies. *Curr. Alzheimer Res.* **12,** 242–54 (2015).

78. Wang, Y. J., Zhou, H. D. & Zhou, X. F. Modified immunotherapies against Alzheimer's disease: Toward safer and effective amyloid-?? clearance. *Journal of Alzheimer's Disease* **21,** 1065–1075 (2010).

79. Holliger, P. & Hudson, P. J. Engineered antibody fragments and the rise of single domains. *Nat. Biotechnol.* **23,** 1126–1136 (2005).

80. Waldmann, T. A. Immunotherapy: past, present and future. *Nat. Med.* **9,** 269–77 (2003).

81. Montoliu-Gaya, L. & Villegas, S. Aβ-Immunotherapeutic strategies: a wide range of approaches for Alzheimer's disease treatment. *Expert Rev. Mol. Med.* **18,** e13 (2016).

82. Bard, F. *et al.* Peripherally administered antibodies against amyloid beta-peptide enter the central nervous system and reduce pathology in a mouse model of Alzheimer disease. *Nat. Med.* **6,** 916–919 (2000).

83. Salloway, S. *et al.* Two phase 3 trials of bapineuzumab in mild-to-moderate Alzheimer's disease. *N. Engl. J. Med.* **370,** 322–33 (2014).

84. Sperling, R. A. *et al.* Amyloid-related imaging abnormalities in amyloid-modifying therapeutic trials: recommendations from the Alzheimer's Association Research Roundtable Workgroup. *Alzheimers. Dement.* **7,** 367–85 (2011).

85. https://clinicaltrials.gov/. Accessed 2015-10-01.

86. Black R, Ekman L, Lieberburg I, Grundman M, Callaway J, Gregg K, Jacobsen J, Gill D, Tchistiakova L, W. A. Immunotherapy regimes dependent on ApoE status (US Patent). (2009).

87. Liu, R. *et al.* Single chain variable fragments against beta-amyloid (Abeta) can inhibit Abeta aggregation and prevent abeta-induced neurotoxicity. *Biochemistry* **43,** 6959–6967 (2004).

88. Frenkel, D., Solomon, B. & Benhar, I. Modulation of Alzheimer's β-amyloid neurotoxicity by site-directed single-chain antibody. *J. Neuroimmunol.* **106,** 23–31 (2000).

89. Lafaye, P., Achour, I., England, P., Duyckaerts, C. & Rougeon, F. Single-domain antibodies recognize selectively small oligomeric forms of amyloid β, prevent Aβ-induced neurotoxicity and inhibit fibril formation. *Mol. Immunol.* **46,** 695–704 (2009).

90. Robert, R. *et al.* Engineered antibody intervention strategies for Alzheimer's disease

and related dementias by targeting amyloid and toxic oligomers. *Protein Eng. Des. Sel.* **22,** 199–208 (2009).

91. Habicht, G. *et al.* Directed selection of a conformational antibody domain that prevents mature amyloid fibril formation by stabilizing Abeta protofibrils. *Proc. Natl. Acad. Sci. U. S. A.* **104,** 19232–19237 (2007).

92. Meli, G., Visintin, M., Cannistraci, I. & Cattaneo, A. Direct in Vivo Intracellular Selection of Conformation-sensitive Antibody Domains Targeting Alzheimer's Amyloid-?? Oligomers. *J. Mol. Biol.* **387,** 584–606 (2009).

93. Paganetti, P., Calanca, V., Galli, C., Stefani, M. & Molinari, M. ??-site specific intrabodies to decrease and prevent generation of Alzheimer's A?? peptide. *J. Cell Biol.* **168,** 863–868 (2005).

94. Rangan, S. K. *et al.* Degradation of beta-amyloid by proteolytic antibody light chains. *Biochemistry* **42,** 14328–14334 (2003).

95. Taguchi, H. *et al.* Exceptional amyloid ?? peptide hydrolyzing activity of nonphysiological immunoglobulin variable domain scaffolds. *J. Biol. Chem.* **283,** 36724–36733 (2008).

96. Taguchi, H. *et al.* Catalytic antibodies to amyloid ?? peptide in defense against Alzheimer disease. *Autoimmunity Reviews* **7,** 391–397 (2008).

97. Robert, R. & Wark, K. L. Engineered antibody approaches for Alzheimer's disease immunotherapy. *Archives of Biochemistry and Biophysics* **526,** 132–138 (2012).

98. Kasturirangan, S. & Sierks, M. Targeted hydrolysis of Beta-amyloid with engineered antibody fragment. *Curr. Alzheimer Res.* **7,** 214–22 (2010).

99. Marín-Argany, M., Rivera-Hernández, G., Martí, J. & Villegas, S. An anti-Aβ (amyloid β) single-chain variable fragment prevents amyloid fibril formation and cytotoxicity by withdrawing Aβ oligomers from the amyloid pathway. *Biochem. J.* **437,** 25–34 (2011).

100. Giménez-Llort, L., Rivera-Hernández, G., Marin-Argany, M., Sánchez-Quesada, J. L. & Villegas, S. Early intervention in the 3xTg-AD mice with an amyloid β-antibody fragment ameliorates first hallmarks of alzheimer disease. *MAbs* **5,** 665–677 (2013).

101. Esquerda-Canals, G., Marti, J., Rivera-Hernández, G., Giménez-Llort, L. & Villegas, S. 2013. Loss of deep cerebellar nuclei neurons in the 3xTg-AD mice and protection by an anti-amyloid β antibody fragment. *MAbs* **5,** 660–4

102. Rivera-Hernández, G. *et al.* Elongation of the C-terminal domain of an anti-amyloid β single-chain variable fragment increases its thermodynamic stability and decreases its aggregation tendency. *MAbs* **5,** 678–689 (2013).

103. Wörn, A. & Plückthun, A. Different equilibrium stability behavior of ScFv fragments: identification, classification, and improvement by protein engineering. *Biochemistry* **38,** 8739–50 (1999).

104. Wörn, A. & Plückthun, A. Stability engineering of antibody single-chain Fv fragments. *J. Mol. Biol.* **305,** 989–1010 (2001).

105. Polymerase Chain Reaction (PCR). at <https://www.ncbi.nlm.nih.gov/probe/docs/techpcr/>

106. PCR - Introduction | ABM Inc. at

<https://www.abmgood.com/marketing/knowledge_base/polymerase_chain_reaction_introduction.php>

107. Demain, A. L. & Vaishnav, P. Production of recombinant proteins by microbes and higher organisms. *Biotechnol. Adv.* **27,** 297–306 (2009).

108. Adrio, J.-L. & Demain, A. L. Recombinant organisms for production of industrial products. *Bioeng. Bugs* **1,** 116–31 (2010).

109. Sahdev, S., Khattar, S. K. & Saini, K. S. Production of active eukaryotic proteins through bacterial expression systems: a review of the existing biotechnology strategies. *Mol. Cell. Biochem.* **307,** 249–64 (2008).

110. Greenfield, N. J. Using circular dichroism spectra to estimate protein secondary structure. *Nat. Protoc.* **1,** 2876–90 (2006).

111. HOLZWARTH, G. & DOTY, P. THE ULTRAVIOLET CIRCULAR DICHROISM OF POLYPEPTIDES. *J. Am. Chem. Soc.* **87,** 218–28 (1965).

112. Greenfield, N. & Fasman, G. D. Computed circular dichroism spectra for the evaluation of protein conformation. *Biochemistry* **8,** 4108–16 (1969).

113. Venyaminov SYu, Baikalov, I. A., Shen, Z. M., Wu, C. S. & Yang, J. T. Circular dichroic analysis of denatured proteins: inclusion of denatured proteins in the reference set. *Anal. Biochem.* **214,** 17–24 (1993).

114. Sreerama, N. *et al.* Tyrosine, phenylalanine, and disulfide contributions to the circular dichroism of proteins: circular dichroism spectra of wild-type and mutant bovine pancreatic trypsin inhibitor. *Biochemistry* **38,** 10814–22 (1999).

115. Royer, C. A. in *Protein Stability and Folding* 65–90 (Humana Press). doi:10.1385/0-89603-301-5:65

116. Vivian, J. T. & Callis, P. R. Mechanisms of Tryptophan Fluorescence Shifts in Proteins.

117. Zandomeneghi, G., Krebs, M. R. H., McCammon, M. G. & Fändrich, M. FTIR reveals structural differences between native beta-sheet proteins and amyloid fibrils. *Protein Sci.* **13,** 3314–21 (2004).

118. Arrondo, J. L., Muga, A., Castresana, J. & Goñi, F. M. Quantitative studies of the structure of proteins in solution by Fourier-transform infrared spectroscopy. *Prog. Biophys. Mol. Biol.* **59,** 23–56 (1993).

119. Arrondo, J. L. & Goñi, F. M. Structure and dynamics of membrane proteins as studied by infrared spectroscopy. *Prog. Biophys. Mol. Biol.* **72,** 367–405 (1999).

120. What is Electron Microscopy? at <https://www.jic.ac.uk/microscopy/intro_EM.html>

121. De Carlo, S. & Harris, J. R. Negative staining and cryo-negative staining of macromolecules and viruses for TEM. *Micron* **42,** 117–31 (2011).

122. Martínez, J., Cobos, E., Luque, I. & Ruiz-Sanz, J. in *Protein Folding. Eric C. Walters* (2011).

123. Singhal, N., Kumar, M., Kanaujia, P. K. & Virdi, J. S. MALDI-TOF mass spectrometry: an emerging technology for microbial identification and diagnosis. *Front. Microbiol.* **6,** 791 (2015).

124. Doke, S. K. & Dhawale, S. C. Alternatives to animal testing: A review. *Saudi Pharm. J.* **23,** 223–229 (2015).

125. Kovalevich, J. & Langford, D. Considerations for the use of SH-SY5Y neuroblastoma cells in neurobiology. *Methods Mol. Biol.* **1078,** 9–21 (2013).

126. Riss, T. L. *et al. Cell Viability Assays*. *Assay Guidance Manual* (Eli Lilly & Company and the National Center for Advancing Translational Sciences, 2004).

127. *EZ4U. Nonradioactive cell proliferation and cytotoxicity assay. Biomedica. Cat. No. BI-5000*.

128. Human Primary Cells. at <https://www.lgcstandards-atcc.org/Products/Cells_and_Microorganisms/Cell_Lines/Human_Primary_Cells.aspx?geo_country=es>

129. De Groot, C. J. A. *et al.* Isolation and characterization of adult microglial cells and oligodendrocytes derived from postmortem human brain tissue. *Brain Res. Protoc.* (2000). doi:10.1016/S1385-299X(99)00059-8

130. Jahan-Tigh, R. R., Ryan, C., Obermoser, G. & Schwarzenberger, K. Flow Cytometry. *J. Invest. Dermatol.* **132,** 1–6 (2012).

131. *Introduction to Flow Cytometry: A Learning Guide*. (2000).

132. Sandwich ELISA. at <http://www.elisa-antibody.com/ELISA-Introduction/ELISA-types/sandwich-elisa>

133. Oddo, S. *et al.* Triple-transgenic model of Alzheimer's disease with plaques and tangles: intracellular Abeta and synaptic dysfunction. *Neuron* **39,** 409–21 (2003).

134. Oddo, S., Caccamo, A., Kitazawa, M., Tseng, B. P. & LaFerla, F. M. Amyloid deposition precedes tangle formation in a triple transgenic model of Alzheimer's disease. *Neurobiol. Aging* **24,** 1063–70 (2003).

135. Billings, L. M., Oddo, S., Green, K. N., McGaugh, J. L. & LaFerla, F. M. Intraneuronal Aβ Causes the Onset of Early Alzheimer's Disease-Related Cognitive Deficits in Transgenic Mice. *Neuron* **45,** 675–688 (2005).

136. Duraiyan, J., Govindarajan, R., Kaliyappan, K. & Palanisamy, M. Applications of immunohistochemistry. *J. Pharm. Bioallied Sci.* **4,** S307-9 (2012).

137. Bulaj, G. Formation of disulfide bonds in proteins and peptides. *Biotechnol. Adv.* **23,** 87–92 (2005).

138. Wörn, A. & Plückthun, A. An intrinsically stable antibody scFv fragment can tolerate the loss of both disulfide bonds and fold correctly. *FEBS Lett.* **427,** 357–61 (1998).

139. Schmid, F. in *Protein Structure: A Practical Approach. 2ond ed. IRL Press, Oxford University Press* 261–267 (1997).

140. Wörn, A. & Plückthun, A. Mutual stabilization of VL and VH in single-chain antibody fragments, investigated with mutants engineered for stability. *Biochemistry* **37,** 13120–7 (1998).

141. Zandomeneghi, G., Krebs, M. R. H., McCammon, M. G. & Fändrich, M. FTIR reveals structural differences between native β-sheet proteins and amyloid fibrils. *Protein Sci.* **13,** 3314–3321 (2009).

142. Gosal, W. S. *et al.* Competing pathways determine fibril morphology in the self-assembly of beta2-microglobulin into amyloid. *J. Mol. Biol.* **351,** 850–64 (2005).

143. Ramm, K., Gehrig, P. & Plückthun, A. Removal of the conserved disulfide bridges from the scfv fragment of an antibody: effects on folding kinetics and aggregation. *J. Mol. Biol.* **290,** 535–546 (1999).

144. Frisch, C. *et al.* Contribution of the intramolecular disulfide bridge to the folding stability of REIv, the variable domain of a human immunoglobulin kappa light chain. *Fold. Des.* **1,** 431–40 (1996).

145. Chiti, F. *et al.* Kinetic partitioning of protein folding and aggregation. *Nat. Struct. Biol.* **9,** 137–143 (2002).

146. Proba, K., Wörn, A., Honegger, A. & Plückthun, A. Antibody scFv fragments without disulfide bonds made by molecular evolution. *J. Mol. Biol.* **275,** 245–53 (1998).

147. Villegas, S., Rivera-Hernandez, G., Marín-Argany, M. & Blasco-Moreno, B. Patent. International Application Number PCT/EP2014/060047. (2014).

148. Marin-Argany, M., Candel, A. M., Murciano-Calles, J., Martinez, J. C. & Villegas, S. The Interconversion between a Flexible β-Sheet and a Fibril β-Arrangement Constitutes the Main Conformational Event during Misfolding of PSD95-PDZ3 Domain. *Biophys. J.* **103,** 738–747 (2012).

149. Galisteo, M. L., Mateo, P. L. & Sanchez-Ruiz, J. M. Kinetic study on the irreversible thermal denaturation of yeast phosphoglycerate kinase. *Biochemistry* **30,** 2061–6 (1991).

150. Nielsen, H. M. *et al.* Astrocytic A beta 1-42 uptake is determined by A beta-aggregation state and the presence of amyloid-associated proteins. *Glia* **58,** 1235–46 (2010).

151. Kabat, E. A., Wu, T. T., Perry, H. M., Gottesman, K. S.& Foeller, C. Variable region heavy chain sequences. In Sequences of Proteins of Immunological Interest. *National Technical Information Service (NTIS). NIH Publication No. 91-3242* (1991).

152. Sanchez-Ruiz, J. M. Theoretical analysis of Lumry-Eyring models in differential scanning calorimetry. *Biophys. J.* **61,** 921–35 (1992).

153. Fincke, A., Winter, J., Bunte, T. & Olbrich, C. Thermally induced degradation pathways of three different antibody-based drug development candidates. *Eur. J. Pharm. Sci.* **62,** 148–60 (2014).

154. Viguera, A. R., Martínez, J. C., Filimonov, V. V, Mateo, P. L. & Serrano, L. Thermodynamic and kinetic analysis of the SH3 domain of spectrin shows a two-state folding transition. *Biochemistry* **33,** 2142–50 (1994).

155. Freire, E. *Protein stability and folding: Theory and practice*. (Shirley, B. A., Ed. Humana Press Inc., 1995).

156. Privalov, P. L. & Makhatadze, G. I. Heat capacity of proteins. II. Partial molar heat capacity of the unfolded polypeptide chain of proteins: protein unfolding effects. *J. Mol. Biol.* **213,** 385–91 (1990).

157. Gupta, S. K. & Shukla, P. Microbial platform technology for recombinant antibody fragment production: A review. *Crit. Rev. Microbiol.* **43,** 31–42 (2017).

158. Invitrogen. Life Technologies. *Pichia Fermentation Process Guidelines Overview Introduction*.

159. Brake, A. J. *et al.* Alpha-factor-directed synthesis and secretion of mature foreign

proteins in Saccharomyces cerevisiae. *Proc. Natl. Acad. Sci. U. S. A.* **81,** 4642–6 (1984).

160. Julius, D., Brake, A., Blair, L., Kunisawa, R. & Thorner, J. Isolation of the putative structural gene for the lysine-arginine-cleaving endopeptidase required for processing of yeast prepro-alpha-factor. *Cell* **37,** 1075–89 (1984).

161. Daly, R. & Hearn, M. T. W. Expression of heterologous proteins inPichia pastoris: a useful experimental tool in protein engineering and production. *J. Mol. Recognit.* **18,** 119–138 (2005).

162. Higgins, D. R., Higgins & R., D. in *Current Protocols in Protein Science* 5.7.1-5.7.18 (John Wiley & Sons, Inc., 1995). doi:10.1002/0471140864.ps0507s02

163. Montoliu-Gaya, L., Martínez, J. C. & Villegas, S. Understanding the contribution of disulphide bridges to the folding and misfolding of an anti-Aβ scFv. *Protein Sci.* (2017). doi:10.1002/pro.3164

164. Song, H.-N. *et al.* Refolded scFv antibody fragment against myoglobin shows rapid reaction kinetics. *Int. J. Mol. Sci.* **15,** 23658–71 (2014).

165. Arakawa, T. & Ejima, D. Refolding Technologies for Antibody Fragments. *Antibodies* **3,** 232–241 (2014).

166. Chen, L.-H. *et al.* Expression, purification, and in vitro refolding of a humanized single-chain Fv antibody against human CTLA4 (CD152). *Protein Expr. Purif.* **46,** 495–502 (2006).

167. Grinna, L. S. & Tschopp, J. F. Size distribution and general structural features of N-linked oligosaccharides from the methylotrophic yeast, Pichia pastoris. *Yeast* **5,** 107–15 (1989).

168. Gemmill, T. R. & Trimble, R. B. Overview of N- and O-linked oligosaccharide structures found in various yeast species. *Biochim. Biophys. Acta* **1426,** 227–37 (1999).

169. Liu, S. *et al.* Removal of endotoxin from recombinant protein preparations. *Clin. Biochem.* **30,** 455–63 (1997).

170. Petsch, D. & Anspach, F. B. Endotoxin removal from protein solutions. *J. Biotechnol.* **76,** 97–119 (2000).

171. Magalhães, P. O. *et al.* Methods of endotoxin removal from biological preparations: a review. *J. Pharm. Pharm. Sci.* **10,** 388–404 (2007).

172. Research, C. for D. E. and. Guidances (Drugs) - Guidance for Industry: Pyrogen and Endotoxins Testing: Questions and Answers.

173. Handattu, S. P. *et al.* In vivo and in vitro effects of an apolipoprotein e mimetic peptide on amyloid-β pathology. *J. Alzheimers. Dis.* **36,** 335–47 (2013).

174. Navab, M. *et al.* An oral apoJ peptide renders HDL antiinflammatory in mice and monkeys and dramatically reduces atherosclerosis in apolipoprotein E-null mice. *Arterioscler. Thromb. Vasc. Biol.* **25,** 1932–7 (2005).

175. Sharifov, O. F. *et al.* Apolipoprotein E mimetics and cholesterol-lowering properties. *Am. J. Cardiovasc. Drugs* **11,** 371–81 (2011).

176. Nayyar, G. *et al.* Two adjacent domains (141-150 and 151-160) of apoE covalently linked to a class A amphipathic helical peptide exhibit opposite atherogenic effects. *Atherosclerosis* **213,** 449–57 (2010).

177. Datta, G. *et al.* Anti-inflammatory and recycling properties of an apolipoprotein mimetic peptide, Ac-hE18A-NH(2). *Atherosclerosis* **208,** 134–41 (2010).

178. Navab, M., Anantharamaiah, G. M. & Fogelman, A. M. The Effect of Apolipoprotein Mimetic Peptides in Inflammatory Disorders Other Than Atherosclerosis. *Trends Cardiovasc. Med.* **18,** 61–66 (2008).

179. Verghese, P. B. *et al.* ApoE influences amyloid-β (Aβ) clearance despite minimal apoE/Aβ association in physiological conditions. *Proc. Natl. Acad. Sci. U. S. A.* **110,** E1807-16 (2013).

180. Nielsen, H. M., Veerhuis, R., Holmqvist, B. & Janciauskiene, S. Binding and uptake of A beta1-42 by primary human astrocytes in vitro. *Glia* **57,** 978–88 (2009).

181. Ryan, T. M. *et al.* Ammonium hydroxide treatment of Aβ produces an aggregate free solution suitable for biophysical and cell culture characterization. *PeerJ* **1,** e73 (2013).

182. Mulder, S. D., Nielsen, H. M., Blankenstein, M. A., Eikelenboom, P. & Veerhuis, R. Apolipoproteins E and J interfere with amyloid-beta uptake by primary human astrocytes and microglia in vitro. *Glia* **62,** 493–503 (2014).

183. Bruggink, K. A., Müller, M., Kuiperij, H. B. & Verbeek, M. M. Methods for analysis of amyloid-β aggregates. *J. Alzheimers. Dis.* **28,** 735–58 (2012).

184. Mishra, V. K. *et al.* Structure and lipid interactions of an anti-inflammatory and anti-atherogenic 10-residue class G(*) apolipoprotein J peptide using solution NMR. *Biochim. Biophys. Acta* **1808,** 498–507 (2011).

185. Deane, R., Bell, R., Sagare, A. & Zlokovic, B. Clearance of Amyloid-β Peptide Across the Blood-Brain Barrier: Implication for Therapies in Alzheimers Disease. *CNS Neurol. Disord. - Drug Targets* **8,** 16–30 (2009).

186. Kline, A. Apolipoprotein E, amyloid-ß clearance and therapeutic opportunities in Alzheimer's disease. *Alzheimers. Res. Ther.* **4,** 32 (2012).

187. Ghiso, J. *et al.* The cerebrospinal-fluid soluble form of Alzheimer's amyloid beta is complexed to SP-40,40 (apolipoprotein J), an inhibitor of the complement membrane-attack complex. *Biochem. J.* 27–30 (1993).

188. Magalhães, J. & Saraiva, M. J. Clusterin overexpression and its possible protective role in transthyretin deposition in familial amyloidotic polyneuropathy. *J. Neuropathol. Exp. Neurol.* **70,** 1097–106 (2011).

189. Wood, S. J., Chan, W. & Wetzel, R. An ApoE-Abeta inhibition complex in Abeta fibril extension. *Chem. Biol.* **3,** 949–56 (1996).

190. Winkler, K. *et al.* Competition of Abeta amyloid peptide and apolipoprotein E for receptor-mediated endocytosis. *J. Lipid Res.* **40,** 447–55 (1999).

191. Wood, S. J., Chan, W. & Wetzel, R. Seeding of Aβ Fibril Formation Is Inhibited by All Three Isotypes of Apolipoprotein E. *Biochemistry* **35,** 12623–12628 (1996).

192. Naiki, H. *et al.* Apolipoprotein E and antioxidants have different mechanisms of inhibiting Alzheimer's beta-amyloid fibril formation in vitro. *Biochemistry* **37,** 17882–9 (1998).

193. Cerf, E., Gustot, A., Goormaghtigh, E., Ruysschaert, J.-M. & Raussens, V. High ability of apolipoprotein E4 to stabilize amyloid- peptide oligomers, the pathological entities

responsible for Alzheimer's disease. *FASEB J.* **25,** 1585–1595 (2011).

194. Cheng, I. H. *et al.* Accelerating amyloid-beta fibrillization reduces oligomer levels and functional deficits in Alzheimer disease mouse models. *J. Biol. Chem.* **282,** 23818–28 (2007).

195. Liu, C.-C., Liu, C.-C., Kanekiyo, T., Xu, H. & Bu, G. Apolipoprotein E and Alzheimer disease: risk, mechanisms and therapy. *Nat. Rev. Neurol.* **9,** 106–18 (2013).

196. Thal, D. R. The role of astrocytes in amyloid β-protein toxicity and clearance. *Exp. Neurol.* **236,** 1–5 (2012).

197. Söllvander, S. *et al.* Accumulation of amyloid-β by astrocytes result in enlarged endosomes and microvesicle-induced apoptosis of neurons. *Mol. Neurodegener.* **11,** 38 (2016).

198. Davies, D. S., Ma, J., Jegathees, T. & Goldsbury, C. Microglia show altered morphology and reduced arborization in human brain during aging and Alzheimer's disease. *Brain Pathol.* (2016). doi:10.1111/bpa.12456

199. Rodríguez, J. J., Butt, A. M., Gardenal, E., Parpura, V. & Verkhratsky, A. Complex and differential glial responses in Alzheimer's disease and ageing. *Curr. Alzheimer Res.* **13,** 343–58 (2016).

200. Akiyama, H. *et al.* Cell mediators of inflammation in the Alzheimer disease brain. *Alzheimer Dis. Assoc. Disord.* **14 Suppl 1,** S47-53 (2000).

201. Tuppo, E. E. & Arias, H. R. The role of inflammation in Alzheimer's disease. *Int. J. Biochem. Cell Biol.* **37,** 289–305 (2005).

202. Zhang, Z.-G., Li, Y., Ng, C. T. & Song, Y.-Q. Inflammation in Alzheimer's Disease and Molecular Genetics: Recent Update. *Arch. Immunol. Ther. Exp. (Warsz).* **63,** 333–44 (2015).

203. Jongbloed, W., Herrebout, M. A. C., Blankenstein, M. A. & Veerhuis, R. Quantification of clusterin in paired cerebrospinal fluid and plasma samples. *Ann. Clin. Biochem.* **51,** 557–67 (2014).

204. Hardy, J. The amyloid hypothesis for Alzheimer's disease: a critical reappraisal. *J. Neurochem.* **110,** 1129–1134 (2009).

205. Lai, A. Y. & McLaurin, J. Clearance of amyloid-β peptides by microglia and macrophages: the issue of what, when and where. *Future Neurol.* **7,** 165–176 (2012).

206. Bohrmann, B. *et al.* Gantenerumab: a novel human anti-Aβ antibody demonstrates sustained cerebral amyloid-β binding and elicits cell-mediated removal of human amyloid-β. *J. Alzheimers. Dis.* **28,** 49–69 (2012).

207. Ostrowitzki, S. *et al.* Mechanism of amyloid removal in patients with Alzheimer disease treated with gantenerumab. *Arch. Neurol.* **69,** 198–207 (2012).

208. Benarroch, E. E. Neuron-astrocyte interactions: partnership for normal function and disease in the central nervous system. *Mayo Clin. Proc.* **80,** 1326–38 (2005).

209. Matos, M., Augusto, E., Oliveira, C. R. & Agostinho, P. Amyloid-beta peptide decreases glutamate uptake in cultured astrocytes: involvement of oxidative stress and mitogen-activated protein kinase cascades. *Neuroscience* **156,** 898–910 (2008).

210. Scimemi, A. *et al.* Amyloid-β1-42 slows clearance of synaptically released glutamate by

mislocalizing astrocytic GLT-1. *J. Neurosci.* **33,** 5312–8 (2013).

211. Talantova, M. *et al.* A induces astrocytic glutamate release, extrasynaptic NMDA receptor activation, and synaptic loss. *Proc. Natl. Acad. Sci.* **110,** E2518–E2527 (2013).

212. Sokolova, A. *et al.* Monocyte chemoattractant protein-1 plays a dominant role in the chronic inflammation observed in Alzheimer's disease. *Brain Pathol.* **19,** 392–8 (2009).

213. White, J. A., Manelli, A. M., Holmberg, K. H., Van Eldik, L. J. & Ladu, M. J. Differential effects of oligomeric and fibrillar amyloid-beta 1-42 on astrocyte-mediated inflammation. *Neurobiol. Dis.* **18,** 459–65 (2005).

214. Boyles, J. K., Pitas, R. E., Wilson, E., Mahley, R. W. & Taylor, J. M. Apolipoprotein E associated with astrocytic glia of the central nervous system and with nonmyelinating glia of the peripheral nervous system. *J. Clin. Invest.* **76,** 1501–1513 (1985).

215. Pitas, R. E., Boyles, J. K., Lee, S. H., Foss, D. & Mahley, R. W. Astrocytes synthesize apolipoprotein E and metabolize apolipoprotein E-containing lipoproteins. *Biochim. Biophys. Acta* **917,** 148–61 (1987).

216. Vitek, M. P. *et al.* APOE-mimetic peptides reduce behavioral deficits, plaques and tangles in Alzheimer's disease transgenics. *Neurodegener. Dis.* **10,** 122–6 (2012).

217. Lynch, J. R., Morgan, D., Mance, J., Matthew, W. D. & Laskowitz, D. T. Apolipoprotein E modulates glial activation and the endogenous central nervous system inflammatory response. *J. Neuroimmunol.* **114,** 107–13 (2001).

218. LaDu, M. J. *et al.* 2001. Apolipoprotein E and apolipoprotein E receptors modulate A beta-induced glial neuroinflammatory responses. *2001. Neurochem. Int.* **39,** 427–34

219. Harold, D. *et al.* Genome-wide association study identifies variants at CLU and PICALM associated with Alzheimer's disease. *Nat. Genet.* **41,** 1088–93 (2009).

220. Lambert, J.-C. *et al.* Genome-wide association study identifies variants at CLU and CR1 associated with Alzheimer's disease. *Nat. Genet.* **41,** 1094–1099 (2009).

221. Tai, L. M. *et al. APOE* -modulated Aβ-induced neuroinflammation in Alzheimer's disease: current landscape, novel data, and future perspective. *J. Neurochem.* **133,** 465–488 (2015).

222. Matsubara, E., Frangione, B. & Ghiso, J. Characterization of apolipoprotein J-Alzheimer's A beta interaction. *J. Biol. Chem.* **270,** 7563–7 (1995).

223. Tai, L. M. *et al.* Levels of Soluble Apolipoprotein E/Amyloid- (A) Complex Are Reduced and Oligomeric A Increased with APOE4 and Alzheimer Disease in a Transgenic Mouse Model and Human Samples. *J. Biol. Chem.* **288,** 5914–5926 (2013).

224. Reddy, S. T. *et al.* Oral amphipathic peptides as therapeutic agents. *Expert Opin. Investig. Drugs* **15,** 13–21 (2006).

225. Phivilay, A. *et al.* High dietary consumption of trans fatty acids decreases brain docosahexaenoic acid but does not alter amyloid-beta and tau pathologies in the 3xTg-AD model of Alzheimer's disease. *Neuroscience* **159,** 296–307 (2009).

226. Hohsfield, L. A., Daschil, N., Orädd, G., Strömberg, I. & Humpel, C. Vascular pathology of 20-month-old hypercholesterolemia mice in comparison to triple-transgenic and APPSwDI Alzheimer's disease mouse models. *Mol. Cell. Neurosci.* **63,** 83–95 (2014).

227. Xiong, Z. *et al.* Alzheimer's disease: evidence for the expression of interleukin-33 and its

receptor ST2 in the brain. *J. Alzheimers. Dis.* **40,** 297–308 (2014).

228. Fu, A. K. Y. *et al.* IL-33 ameliorates Alzheimer's disease-like pathology and cognitive decline. *Proc. Natl. Acad. Sci.* **113,** E2705–E2713 (2016).

229. Kálmán, M. & Hajós, F. Distribution of glial fibrillary acidic protein (GFAP)-immunoreactive astrocytes in the rat brain. I. Forebrain. *Exp. brain Res.* **78,** 147–63 (1989).

230. Tissue expression of GFAP - Staining in cerebral cortex - The Human Protein Atlas. at <http://www.proteinatlas.org/ENSG00000131095-GFAP/tissue/cerebral+cortex>

231. Fitz, N. F. *et al.* Improvement of memory deficits and amyloid-β clearance in aged APP23 mice treated with a combination of anti-amyloid-β antibody and LXR agonist. *J. Alzheimers. Dis.* **41,** 535–49 (2014).

232. Calsolaro, V. & Edison, P. Neuroinflammation in Alzheimer's disease: Current evidence and future directions. *Alzheimer's Dement.* **12,** 719–732 (2016).

233. Chapuis, J. *et al.* Transcriptomic and genetic studies identify IL-33 as a candidate gene for Alzheimer's disease. *Mol. Psychiatry* **14,** 1004–16 (2009).

234. Tian, M. *et al.* Association of IL-1, IL-18, and IL-33 gene polymorphisms with late-onset Alzheimer's disease in a Hunan Han Chinese population. *Brain Res.* **1596,** 136–145 (2015).

235. Fulgheri, G. & Malinowski, B. The Role of IL-33 in the Inflammation Process of Asthma and Atherosclerosis. *EJIFCC* **22,** 79–91 (2011).

236. Hensley, K. Neuroinflammation in Alzheimer's Disease: Mechanisms, Pathologic Consequences, and Potential for Therapeutic Manipulation. *J. Alzheimer's Dis.* **21,** 1–14 (2010).

237. Xu, Q., Li, Y., Cyras, C., Sanan, D. A. & Cordell, B. Isolation and characterization of apolipoproteins from murine microglia. Identification of a low density lipoprotein-like apolipoprotein J-rich but E-poor spherical particle. *J. Biol. Chem.* **275,** 31770–7 (2000).

238. Freeman, G. B., Brown, T. P., Wallace, K. & Bales, K. R. Chronic administration of an aglycosylated murine antibody of ponezumab does not worsen microhemorrhages in aged Tg2576 mice. *Curr. Alzheimer Res.* **9,** 1059–68 (2012).

239. Wilcock, D. M. Deglycosylated Anti-Amyloid-beta Antibodies Eliminate Cognitive Deficits and Reduce Parenchymal Amyloid with Minimal Vascular Consequences in Aged Amyloid Precursor Protein Transgenic Mice. *J. Neurosci.* **26,** 5340–5346 (2006).

240. Fuller, J. P. *et al.* Comparing the efficacy and neuroinflammatory potential of three anti-abeta antibodies. *Acta Neuropathol.* **130,** 699–711 (2015).

241. Bales, K. R. *et al.* Lack of apolipoprotein E dramatically reduces amyloid beta-peptide deposition. *Nat. Genet.* **17,** 263–4 (1997).

242. Bales, K. R. *et al.* Apolipoprotein E is essential for amyloid deposition in the APP(V717F) transgenic mouse model of Alzheimer's disease. *Proc. Natl. Acad. Sci. U. S. A.* **96,** 15233–8 (1999).

243. DeMattos, R. B. Apolipoprotein E dose-dependent modulation of beta-amyloid deposition in a transgenic mouse model of Alzheimer's disease. *J. Mol. Neurosci.* **23,** 255–62 (2004).

244. Chakrabarty, P. *et al.* IL-10 alters immunoproteostasis in APP mice, increasing plaque burden and worsening cognitive behavior. *Neuron* **85,** 519–33 (2015).

245. Liao, F. *et al.* Anti-ApoE Antibody Given after Plaque Onset Decreases A Accumulation and Improves Brain Function in a Mouse Model of A Amyloidosis. *J. Neurosci.* **34,** 7281–7292 (2014).

246. Fitz, N. F. *et al.* Liver X Receptor Agonist Treatment Ameliorates Amyloid Pathology and Memory Deficits Caused by High-Fat Diet in APP23 Mice. *J. Neurosci.* **30,** 6862–6872 (2010).

247. Zelcer, N. *et al.* Attenuation of neuroinflammation and Alzheimer's disease pathology by liver x receptors. *Proc. Natl. Acad. Sci. U. S. A.* **104,** 10601–6 (2007).

248. Lefterov, I. *et al.* Expression profiling in APP23 mouse brain: inhibition of Aβ amyloidosis and inflammation in response to LXR agonist treatment. *Mol. Neurodegener.* **2,** 20 (2007).

249. Sakai, K. *et al.* Aβ immunotherapy for Alzheimer's disease: effects on apoE and cerebral vasculopathy. *Acta Neuropathol.* **128,** 777–789 (2014).

250. Alzheimer's Disease International. *World Alzheimer Report 2014: Dementia and Risk Reduction*. (2014).

251. Alzheimer's Disease International. *World Alzheimer report 2013: journey of caring*. (2013).

252. Zlokovic, B. V *et al.* Glycoprotein 330/megalin: probable role in receptor-mediated transport of apolipoprotein J alone and in a complex with Alzheimer disease amyloid beta at the blood-brain and blood-cerebrospinal fluid barriers. *Proc. Natl. Acad. Sci. U. S. A.* **93,** 4229–34 (1996).

253. Corder, E. H. *et al.* Gene dose of apolipoprotein E type 4 allele and the risk of Alzheimer's disease in late onset families. *Science* **261,** 921–3 (1993).

254. Calero, M. *et al.* Functional and structural properties of lipid-associated apolipoprotein J (clusterin). *Biochem. J.* **344 Pt 2,** 375–83 (1999).

255. Choi-Miura, N. H. *et al.* SP-40,40 is a constituent of Alzheimer's amyloid. *Acta Neuropathol.* **83,** 260–4 (1992).

256. Zlokovic, B. V *et al.* Brain uptake of circulating apolipoproteins J and E complexed to Alzheimer's amyloid beta. *Biochem. Biophys. Res. Commun.* **205,** 1431–7 (1994).

257. Villegas-Llerena, C., Phillips, A., Garcia-Reitboeck, P., Hardy, J. & Pocock, J. M. Microglial genes regulating neuroinflammation in the progression of Alzheimer's disease. *Curr. Opin. Neurobiol.* **36,** 74–81 (2016).

258. Troakes, C. *et al.* Clusterin expression is upregulated following acute head injury and localizes to astrocytes in old head injury. *Neuropathology* **37,** 12–24 (2017).

259. Wilcock, D. M. *et al.* Passive amyloid immunotherapy clears amyloid and transiently activates microglia in a transgenic mouse model of amyloid deposition. *J. Neurosci.* **24,** 6144–51 (2004).

260. Panza, F. *et al.* Amyloid-based immunotherapy for Alzheimer's disease in the time of prevention trials: the way forward. *Expert Rev. Clin. Immunol.* **10,** 405–19 (2014).

261. Samadi, H. & Sultzer, D. Solanezumab for Alzheimer's disease. *Expert Opin. Biol. Ther.*

11, 787–98 (2011).

262. Doody, R. S. *et al.* Phase 3 trials of solanezumab for mild-to-moderate Alzheimer's disease. *N. Engl. J. Med.* **370,** 311–21 (2014).

263. Spangenberg, E. E. *et al.* Eliminating microglia in Alzheimer's mice prevents neuronal loss without modulating amyloid-β pathology. *Brain* **139,** 1265–81 (2016).

264. Fu, W., Shi, D., Westaway, D. & Jhamandas, J. H. Bioenergetic mechanisms in astrocytes may contribute to amyloid plaque deposition and toxicity. *J. Biol. Chem.* **290,** 12504–13 (2015).

265. Ries, M. & Sastre, M. Mechanisms of Aβ Clearance and Degradation by Glial Cells. *Front. Aging Neurosci.* **8,** 160 (2016).

266. Orre, M. *et al.* Isolation of glia from Alzheimer's mice reveals inflammation and dysfunction. *Neurobiol. Aging* **35,** 2746–60 (2014).